Methodologies for Active Control of Free Shear Flows

By

Chen Ding

A Dissertation submitted to the Faculty of the

Virginia Polytechnic Institute and State University

in partial fulfillment of the requirements for the degree of

DOCTOR OF PHILOSOPHY

IN

MECHANICAL ENGINEERING

APPROVED:

U. Vandsburger, Chair

A. L. Wicks

M. G. Mungal

F. J. Pierce

L. A. Roe

March, 1995

Blacksburg, Virginia

Key Words: Flow Control, Active Control, Jet, Jet Control, Fluid Mechanics

Methodologies for Active Control of Free Shear Flows

By

Chen Ding

Committee Chairman: Dr. U. Vandsburger

Department of Mechanical Engineering

Abstract

The objective of this work is to study the basic mechanism of the active control of free shear flows and look for new concepts in actuation methodologies.

The possibility of controlling the evolution of a triangular jet is discussed in Chapter 2. The piezoceramic actuators were mounted on the flat sides of the nozzle. The flow was fully sheared near the nozzle. Single mode excitation with frequency as the varying parameter was found to be ineffective for controlling the far field evolution. In contrast, excitation of the jet with non-integer and counter propagating azimuthal modes yielded marked changes in the jet evolution.

A new method employing dynamic spatial modes to control the far field of a circular jet is examined in Chapter 3. The basic mechanism that governs the far field control was found to be the non-linear interaction of the instabilities of the standing-waves. This observation agrees with conclusions of former investigators but with a new understanding that the non-linear interaction mechanism and the jet expansion are not to become effective until the potential core ends, after which the jet demonstrates large, directional expansion. It was shown in the experiment that this expansion could be easily predicted and controlled. These results point out a better control mechanism -- the dynamic mode control method. Three schemes were proposed: 1) the phase modulation,

2) the switching modulation, and 3) the spatial mode modulation, where the first two were implemented with great success in controlling the evolution of the jet flow.

Finally, a triangular jet with a top hat initial velocity profile is examined in Chapter 4. The results of excited and unexcited jets were compared with those studies where the initial flow conditions were different. It was found that the initial flow condition affected the flow field in two ways: the axis switching and the jet expansion. The combination of an initial top-hat velocity profile and a non-symmetric nozzle geometry was proved to be the necessary condition to create axis switching. Proper combination of initial velocity profile, nozzle geometry and spatial mode could greatly enhance the jet expansion.

Acknowledgments

I would like to express my gratitude to Professor Uri Vandsburger for his invaluable guidance throughout this endeavor, and to Professors M. G. Mungal, F. J, Pierce, L. Roe, and A. Wicks for their advice and serving as members of my advisory committee. Prof. Pierce suggested the magic cosine curve that had been successfully applied to the designing and building of the contraction sections of two flow facilities. Prof. Mungal provided me much of the insights into the three-dimensional flow structure. Prof. Wicks, through his patience, helped debug the signal processing results.

I am indebted to my wife Fang Lu and my son Yi Ding for the support they have given to me during my Ph. D. study. I am very grateful to the many sacrifices they made during this period.

Nomenclature

The important symbols used in this thesis are identified here in alphabetical order. Latin and Greek alphabet symbols are listed separately:

D	Nozzle Diameter
f_e	Excitation frequency
f_m	The most amplified frequency
$F(m, n)$	Fourier Transform of the phase mean velocity, where m stands for the spatial mode and n stands for frequency harmonics
Q	The integrated volume flux, $Q = \int_{R_{0.1}}^{R_{0.9}} U(x,y)dy$
Q_0	The integrated volume flux at z/D = 0.5
$(Q-Q_0)/Q_0$	Flow entrainment ratio
$R(\phi)$	Radial intercepts of the flow distortion of an excited jet
$R_{1/2}$	Radial intercepts at R = 0.5
R	Velocity ratio of a mixing layer, $R = (U_H - U_L)/(U_H + U_L)$
$R_{0.1}$	Velocity ratio truncated at R = 0.1
$R_{0.9}$	Velocity ratio truncated at R = 0.9
Re_D	Reynolds number based on nozzle diameter
Re_θ	Reynolds number based on initial momentum thickness
U_L, U_H	Low speed side, high speed side velocities
u'	Random turbulent fluctuation
u''	Organized turbulent fluctuation
u_3'	Standing wave fluctuation
u_{int}	Normalized phase mean fluctuation amplitude, $u_{int} = \frac{1}{\theta_i} \int_{R_{0.1}}^{R_{0.9}} u'(f)\,dr$
U	Local time mean velocity
Uj	Jet center time mean velocity

U_0	Time mean velocity at the jet exit
u'_f	Turbulence fluctuation amplitude at the forcing frequency
U_p	Phase Speed
$y_{0.5}$	Lateral coordinates truncated at R = 0.5
z, x, y, t	Streamwise, lateral, time coordinates
z/D	Non dimensionalized streamwise coordinates

Geek Symbols

η	Non dimensionalized coordinate $\eta = (y - y_{0.5}) / \theta$
θ	Momentum thickness
ϕ	Phase shift of the forcing frequency
ω	Angular frequency
λ	Wave length of the forcing frequency
$-\alpha_i\theta$	Amplification rate

Table of Contents

List of Figures

Chapter 1 Introduction

1.1 Review - Instabilities and Orderly Structures in Free Shear Flows

It has been over 100 years since the phenomenon of flow instabilities was first documented. In 1858, Leconte described in his paper "On the influence of musical sounds on the flame of a jet of coal-gas" the flickering of the flame of a gas lamp in response to music. Twenty one years later, Lord Rayleigh (1879) established a theoretical explanation of flow instability using an adaptation of the Normal Mode method. This model was later improved by Helmholtz (1890) and Kelvin (1880, 1887). In this method, the Euler equations were perturbed and linearized by neglecting products of the perturbation terms. It was further assumed that the perturbation of each quantity could be resolved into independent components, or modes, varying with time to a set of constants which are in general complex. The values for the modes were calculated from the linearized equations. If the real part was found to be positive for any mode, the system was deemed unstable because a small perturbation of the system would grow exponentially in time until it was no longer small.

Experimentally, the classic work by Osborne Reynolds (1883) of flow in a pipe best described the behavior of flow instabilities. Further progress in this area was delayed for more than a half century owing to the lack of dynamic data acquisition instrumentation. In 1941 Schubauer and Skramstad measured the laminar to turbulent transition over a flat plate using a hot wire, a dynamic sensor. They discovered the selective amplifications of the random fluctuations during the transition.

Before the Sixties flow instability was treated only as a wave property. The roll-up of traveling instability waves into a periodic array of vortices was first predicted by Michalke (1965) and demonstrated experimentally by Freymuth (1966). Although there had been many other observations and evidences of orderly structures in the flow (Bradshaw (1964), Reynolds (1967), among many), it was not until 1971 that Crow and

Champane confirmed both their existence and relationship to the local instability and the global feedback mechanism. They found that the coherent structures can be strengthened and stabilized by periodic stimulation. This discovery of the flow structure pointed to an instability mechanism involved in their creation and provided a tool for their detailed analysis and handling. The efforts in this direction reached new heights in the mid 1970's and early 1980's. The term "active control" was proposed, Ho, C. M. (1981). This term has been used to refer to any small perturbation method employing relatively small energy to achieve global effects in the flow.

In mixing layer studies, Ho and Huang (1982) and Ho and Huerre (1984) demonstrated the basic mechanisms of the instabilities of the vortex sheet leaving a trailing edge. These include the amplification of instabilities, the roll up and the formation of vortices, and vortex merging. The active control of the vortex merging using external perturbations was also demonstrated. It was found that there exists a most amplified frequency in the flow which scales with the local momentum thickness, θ. The measured amplification rate of the most amplified frequency agreed with their theoretical results. Subharmonic forcing of the most amplified frequency was able to make several vortices merge simultaneously and increased the spreading rate of the shear layer dramatically. A resonant effect or "collective interaction" where multiple vortex merging took place was also reported. In this case, the process of sequential vortex merging is shortened through the coalescence of a large number of vortices.

The most amplified frequency is a very important concept in both planar mixing layer and jet shear layer control. Both of the shear layers have a thin mixing layer in the near flow field. However, unless the flow can be assumed parallel the most amplified frequency is not unique along the streamwise direction. Moreover, the assumption of a non-divergent shear layer is rather restrictive because it implies that at some distance downstream only the most amplified wave will dominate the flow. In practice, the width of the shear layer increases in the streamwise direction, resulting in a continuous shift of the most amplified instability waves towards lower frequencies. This effect was realized

by Mattingly & Chang (1974), and later by workers such as Crighton & Gaster (1976) and Gaster, Kit & Wygnanski (1985), who tried to adapt the quasi-parallel stability calculations or expansion methods to simulate the flow divergence.

Additional difficulties arise when attempting to determine the most amplified frequencies in a turbulent mixing layer. First, there is no steady mean velocity field in existence upon which small perturbations may be superimposed. Hence, the linear stability analysis is questionable. Second, there is strong background noise over a wide band of frequencies from which it is difficult to experimentally detect the most amplified frequency, Wygnanski (1987). The determination of the most amplified frequencies in such instances is rather complex.

In jet studies, the most amplified frequency has been considered as the local instability mode. The jet column instability, termed as the preferred mode, was observed to scale approximately with the jet diameter and velocity and characterized as a single scale that dominates the turbulent region, Crow and Champagne (1971). The frequency associated with the preferred mode was usually based on spectral measurements made near the end of the potential core. There have been ambiguities in defining the preferred mode over the past twenty years that resulted in scattering of reported values, see Gutmark and Huang, (1983). Crow and Champagne (1971) introduced $St_{De} = 0.85$ as the preferred mode, since the total centerline turbulence level u_c' became the highest at this St_{De}. The concept of the preferred mode was redefined by Zaman & Hussain (1977, 1980) as that which produced maximum amplification of the fundamental amplitude u_f' rather than the total turbulence level. The fundamental amplitude was determined using artificial forcing at a single frequency at a time so that the background noise was well suppressed. The location of measurement also requires agreement. Zaman & Hussain (1980) defined it on the center line of the jets. Using this definition the measured preferred mode was $St_{De} = 0.4$, which is independent of the nozzle geometry as long as the "momentum flux equivalent diameter" is used. Recently, Peterson (1988) argued against the existence of a single preferred mode. The most amplified shear-layer

instability depends on the streamwise location and on the streamwise distribution of shear-layer thickness. Therefore, the preferred mode defined by Crow and Champagne (1971) was nothing but the most amplified shear layer mode at x/D=4.

Despite the above mentioned controversies, this author would like to argue that in active shear flow control one may still use the preferred mode as the characteristic scale in the jet flow. It is the author's opinion, based on the personal experiences in jet study, that the definition of Zaman & Hussain's (1980) best defines the preferred mode.

There are similarities in behavior between mixing layer and jets. The momentum thickness used in mixing layer as the length scale is also the appropriate length scale for the near-field jet dynamics (note: further downstream, greater than three or four diameters of the jet exit, the jet diameter generally governs the evolution, Corke (1993)). However, there are differences in control methods between mixing layers and jets. In planar mixing layers frequency is the only control parameter while in jet flow there is additional parameter -- the spatial mode. This flexibility is attributed to the additional dimension -- the jet diameter, which makes azimuthal perturbations possible. The spatial-mode can be employed in jets to control the excitation amplitude along the azimuthal direction, thus, achieving the desired resonant interactions between different azimuthal modes. This method, termed as the spatial mode control method, has been proven much more effective than the methods that employ only frequency control. Next, a review of the spatial mode and its control will be addressed.

In the near field of a top hat jet, the thin axisymmetric shear layer is unstable to a large number of discrete azimuthal modes, Plaschko, (1979). At some distance beyond the termination of the potential core, however, the fully developed jet was reported to be unstable to the first helical mode only, Bachelor & Gill (1961). This conclusion has been accepted and repeatedly proven by subsequent researchers. However, in 1989 Tso & Hussain reported seeing the axisymmetric, helical, and double helical modes in the far-

field of a turbulent air jet from conditionally sampled multi-point velocity measurements. Recently, Yoda (1992) proposed the existence of helical modes in the far field of the jet. Depending on the projections one may infer the existence of axisymmetric or helical shapes. Her results suggest that helical modes are unstable in the far field.

In 1983, Strange systematically studied an axisymmetric high-Reynolds-number jet excited at three modes (m = 0, 1, 2) and showed that the growth rates of modes m = 0 and 1 were comparable. His work was later extended by Cohen and Wygnanski (1987) Peterson (1990) and Corke (1993). They were able to prove theoretically and experimentally that in the near field of circular jets, where the shear layer surrounding the nozzle is usually thin, many azimuthal modes are equally unstable. The distortion or control of the mean velocity field can be realized by excitation of multiple modes expressed as frequencies, wave-numbers or azimuthal modes. The condition for those modes to interact with each other is that their phase velocity be the same and that there should be sufficient time for them to interact. It was shown in the paper by Cohen and Wygnanski (1987) that many modes are not dispersive over a broad range of frequencies at z/D <3 which permits resonant interactions to occur. It was found in their paper that single mode excitation maintains the axisymmetric structure of the jets, thus has little effect over the jet. However, by standing wave excitation, which consists of two counter rotating waves with the same azimuthal mode value, the directional jet expansion, depicted by the shape of the iso-velocity contours of the jet, can be exactly predicted and controlled (For example, the iso-velocity contours for m = ± 1 excitation are elliptic; m = ± 1.5, triangular and m = ± 2, square).

There has been renewed interest in non-circular jets in the late 1980's. These geometries appear to be capable of entraining surrounding fluid more efficiently than the corresponding circular jets. One of the interesting phenomena associated with these jets is a switch-over between axes of the mean flow occurring downstream of the nozzle. Several investigations of unforced non-circular jets, in cold flows, have been reported

including the following: elliptical jets by Ho & Gurmark (1987) and Hussain & Husain (1989); rectangular with various aspect ratios by Sforza, Steiger & Trentacoste (1966) and Trentacoste & Sforza (1967); Square by DuPlessis, Wang & Kahawita (1974), Quinn & Militzer (1988) and Wiltse & Glezer (1993); triangular by Gutmark el. al. (1985). While non-circular nozzles have shown advantages with respect to the flow field evolution, their implementation is not very practical. It would seem desirable to achieve similar results with round jets, necessarily excited. This argument is supported by the fact that one can generate a quasi-elliptic jet by exciting a circular jet at modes ± 1, Cohen and Wygnanski (1987). External excitation of jets may therefore be combined with non-circular nozzle designs in augmenting the mixing produced by nozzle shapes.

In summary of this section, it is known that shear flows, including mixing layers and jets, are unstable to small perturbations. The disturbances are known to amplify non-linearly if they are fed at the most amplified frequency or its sub-harmonics. In jets, besides the most amplified frequency or the preferred mode (the most amplified frequency at the end of potential core) the flow is also unstable to spatial instability modes. It has been found that the spatial-mode excitation is the most effective way to control the jet to enhance jet expansion and mixing. Studies of the basic mechanisms of free shear flows have improved our understanding of their intrinsic nature. Next, approaches for their control are explored.

1.2 Active Shear Flow Control Methods

Active control has been considered as the second generation of flow control methods (as compared with the passive control methods, termed as the first generation) which may open a new era to aerodynamics, Wu (1985). It is the author's view that the proper design of actuators is the key for the success of this revolution.

An active control system is composed of hardware: sensors and actuators, and software: control methodology and algorithm.

Actuators used to date can be divided into four groups: 1) mechanical devices: oscillating flaps, vibrating ribbons, piezoelectric materials; 2) hydrodynamic techniques: periodic suction or blowing; 3) thermal techniques: heating strips, electrical discharge, and 4) acoustical excitation.

An oscillating flap is usually driven by stepper motors that run at a frequency under 30 Hz depending on the oscillation amplitude. The frequency range restricts its usage to low Reynolds number flows. Therefore, it is only suitable for academic purposes. Piezoceramic actuators can reach a much higher frequency, but their frequency response diminishes outside a narrow band around the resonance frequency. This shortcoming can be overcome by introducing the method of Amplitude Modulation developed by Wiltse M. & Glezer (1993). In this method the actuators are resonantly driven with a time-harmonic carrier wave train which is amplitude modulated with the desired excitation waveform. However, the excitation waveform frequency usually is one or two orders lower than the carrier, which again, results a low excitation frequency. Furthermore, current piezoceramic material can only withstand temperatures below 400 ^0C. The temperature limitation hinders its applications in high temperature environments. Almost all the mechanical devices have vibrating parts that are exposed to the flow. Therefore, it may not suitable to use them in compressible flows.

Hydrodynamic techniques are, typically, employed in the areas of jet vectoring, separation elimination and retarded boundary layer energization. At present the energy required for this kind of control to operate effectively is about one third or one half of the total energy in the flow. This is impractical for real flow applications.

Thermal devices also require relatively high power to actuate the flow. However, because of their non intrusive nature and ease of placement in complex geometries they have been widely used in basic flow studies, Glezer, Katz and Wygnanski (1989).

One may call the above types of actuators as "externally excited", since they require external energy input which, generally, is not insignificant when compared to the total energy of the flow. On the other hand, the flow can be self excited by appropriate

configurations. For instance, the well-known sound-vortex resonance phenomenon was applied in an experiment conducted by Parker (1966). A thin flat plate with blunt trailing edge was located midway between the wind tunnel walls at zero incidence. As the incoming flow velocity U_∞ increased from zero, vortices would shed near the plate with a natural frequency depending on U_∞, and induce a fluctuating pressure field which behaved as a sound source. When U_∞ increased to a certain value the vortex shedding frequency suddenly increased and locked-on to the sound frequency. The resonance then started and the sound became much louder, until a maximum sound pressure level was reached. With further increase in U_∞ the shedding frequency suddenly unlocked and increased to its natural Strouhal value again, the resonant sound ceased. The resonant effect was also observed when the co-flow density ratio was below 0.9 in reacting flows, Yu and Monkewitx (1993). Other applications using self-excitation mechanism are the whistling nozzle, Hasan and Hussain, (1982), the self excited music wire method, Vandsburger and Ding (1992), the externally controlled flip-flop jet, Raman (1993), and the suppression of the separation in the diffuser, Ding and Zhang (1989) (both of the later two cases utilize the Coanda effects). Self excitation methods are attractive because they offer a natural way of organizing the flow structure and the possibility of obtaining the most enhanced vortical flow with the least energy input. This approach reminds one of the old Chinese proverb: "With the right method, one may move a ton of weight by four ounces' force." However, the shortcoming of current self-excitation devices is that they are hard to adapt to real flow geometries.

As a design guide, the ideal actuator should have fast dynamic response, low power consumption, easy adaptation to real flow geometries and durability in severe working conditions. Unfortunately, there are few systems that can meet all these demands. As a result, these requirements pose the major challenge to actuator design.

The other challenge comes from the active control methodology. Present actuation methods are unable to control the far field since the actuation signal has only a limited region of influence. Within that region, the coherent structures are phase locked

to the excitation signals and the flow structure is greatly altered. Beyond this region the phase between the coherent structure and the excitation is no longer locked (decorrelated), and the forcing loses its influence, Ho (1991). This phenomenon implies that outside this zone active control is not effective at all.

1.3 Objectives and Approach of Present Study

The main objectives set for the work concluded in this dissertation have been:

1. Look for new concepts in actuation methodologies that can both extend the region of influence the actuation may exert and increase the controllability of the far field of jets.
2. Investigate the effects of initial flow conditions on the characteristic flow evolution, e.g., the possible influence of the nozzle geometry and initial velocity profile on axis switching and on the flow entrainment rate.
3. Develop a new type of actuator that is both effective in flow control and requires the least energy.

These studies were motivated by the fact that the real control of the shear flow (especially in the far field) could be realized only by overcoming the phase decorralation limitations; that the amplification of the spatial modes was mostly influenced by the initial flow conditions; and that any new actuator design had to be guided by the principle of efficiency in energy consumption and effectiveness in flow control.

The study of the control of jet fields, in accomplishment of the first objective, had been done in two stages. First, a triangular jet with a fully sheared initial velocity profile was investigated and the possibility to control the far field considered, this work is discussed in chapter 2. Second, a circular jet with initial top hat velocity profile was studied. The controllability of the jet in both near and far field was investigated in a more detailed manner and new actuation methods were sought for jet flows. This work is discussed in Chapter 3.

In fulfillment of the second objective, the influence of the initial flow conditions on the jet evolution were investigated and are discussed in Chapter 4. A triangular jet with an initial top hat velocity profile was studied and the excited and unexcited results were compared with those that presented in Chapter 2 and 3 where the initial flow conditions were different.

The 'music wire' method was introduced in Appendix A as result of the third objective. A planar mixing layer was employed in this study. The relatively simple configuration of the mixing layer and its similarities in behavior to jets in the axisymmetric mixing region made it an ideal starting point for active flow control research.

Chapter 2 Spatial Modulation of a Forced Triangular Jet with a Fully-Sheared Exit Velocity Profile

2.1 Introduction

This chapter includes a description of a study that addresses one of the key issues of jet control -- the control of the far field. Based on the extensive investigations reviewed for this study, it was determined that frequency control alone was ineffective for the flow conditions posed in this experiment, while spatial mode control was a better choice. This reasoning showed that the spatial mode is more flexible and versatile to control. As mentioned in Chapter 1, a number of studies have been conducted on the near field of jets, employing the spatial mode control method. Examples were Cohen and Wygnanski (1987), Peterson and Samet (1991), Corke and Kusek (1993), Wiltse and Glezer (1994). However, very few of the above enumerated examples dealt with the far field and none had a combination of a non-circular geometry and a initially fully-sheared velocity profile. Driven by practical interests this chapter examines a highly turbulent jet flow. It was decided to combine the virtues of non-circular nozzles with spatial mode excitation in order to achieve the best control over the evolution of jets.

Several issues are addressed in this Chapter:

1. What is the response of a jet, with a fully sheared turbulent velocity profile at the nozzle exit, to excitation?
2. What are the combined effects of flow excitation and non-circular nozzles?

Generally, excited jets are well organized in the near field. The forcing signal and the response frequency have a well defined phase relationship. Further downstream, the forcing looses its influence because of the decorrelation of the phase between the forcing signal and the passing structures, see Ho *et al.* (1991). Therefore, a key question to be addressed in this Chapter is:

3. Can the evolution of a turbulent jet be controlled well into the far field?

In order to answer these questions, in section 2.2 the experimental methods are discussed, in section 2.3 the method of spatial mode control is analyzed and its ability to control the far field examined.

2.2 Experimental Facilities and Techniques

2.2.1 Experimental Systems

The experiments on jet flows were conducted using an equilateral triangular nozzle, 12 mm on each side, Figure 2.1, corresponding to a hydraulic diameter of about 7 mm. The results reported in this chapter are for a jet of air, issuing into stagnant room air, with a Reynolds number of 8000 based on the hydraulic diameter. Brass shims, 0.009" in thickness, were mounted on the flat sides of the nozzle, flush with the nozzle walls. A patch of piezoceramic monomorph material, Ni alloy, 0.012" thick (Piezoelectric Products, Metuchen NJ), was bonded to each brass shim using electrically conducting epoxy. This way the brass shim serves as one electrode and the upper surface of the piezoceramic as the other. The actuators were driven by a PC-486 computer which sent out three signals to the three channels. The signals were then amplified using audio amplifiers and coupled to the actuators via a transformer network. A D/A board, Cyber Research model CYDDA 06, which drove the three actuators and enabled the control of the relative phase between the actuators also triggered the data acquisition by another PC 486 and drove it's clock externally. The phase shifting between the actuators and the signal was less than 5^0. This system enabled collection of phase-locked data, and therefore the acquisition of phase averaged information. The experimental arrangement is shown schematically in Figure 2.2.

2.2.2 Data Acquisition and Processing

Information on the evolution of the jet flow field was obtained using a single hot wire anemometer, TSI type IFA 100. The hot wire probe was mounted on a fully automated stage assembly with four degrees of freedom, x-y-z and the angular position θ. The probe position was controlled by the data acquisition computer. The hot wire was capable of acquiring an effective (axial) velocity or three velocity components at each location, synchronized with the excitation (see appendix C for details). During the study it was determined that the additional data obtained by acquiring all three velocity components did not warrant the very long data collection periods, since the key features of the flow field and the conclusions drawn were found to be identical.

The data collected by the hot wire measurements was used in two ways. The velocities were used to generate iso-value surfaces, two and three dimensional, in order to compare the evolution of the jet flow in the natural and excited cases. The 3-D data was processed on a Silicon Graphic Workstation using AVS version 4.0. The velocity data were also processed to obtain spectral information using a Tektronix 2630 FFT system.

2.3 Results and Discussion

The data acquired are analyzed and presented in three ways: time-mean, phase-mean, and in the frequency domain. These analyses are used to obtain information on the evolution of the jet flow in two and three dimensions.

2.3.1. Time Mean Velocity and Turbulence Characteristics

The mean velocity profile for the axial position of z/D=0.2 is shown in Figure 2.3. In order to examine the similarities of the velocity distributions, measurements were made along three directions, i.e., across the nozzle from each of the flat sides to its opposite apex. As seen from the figure, all the velocity profiles have a broad polynomial shape, with the maximum velocity near the centroid of the triangular cross section. They

are identical along the line from the flat side to the centroid but have a slight difference toward the apex, indicating that the velocity gradient of side 3 is the highest while that of side 1 lowest. These differences may be attributed to minor differences in mechanical mounting of the actuators and also the complexities of the flow. Differences in the velocity slope towards the apex will result in differences in the turbulence level, since a higher velocity gradient means a higher amplification rate. This is, indeed, reflected by the turbulence level of the flow on the same plot. There exist indeed differences in turbulent levels as described above. The turbulence level in the central portion of the flow is about 1% of the mean flow. Near the jet edge the turbulence level is higher, with the highest level at the apex being about 9.5% for side 3, compared with 5.5% on its flat side. The average turbulence intensity, integrated across the jet, is 1.8. Since the excitation level was much higher than the unexcited turbulence intensity, the minor differences among each side in mean velocity and turbulent level did not affect the results of the study and the general conclusions derived in this Chapter.

The power spectra of the jet flow at the nozzle exit, z/D = 0.1 (closest location where the hot wire probe could be placed), was examined and is shown in Figure 2.4. As seen, the jet center exhibits no discernible peak frequency while the sides do. The peak (most amplified) frequency for the flat side is in the 150-200 Hz range, while for the apex it is around 400 Hz. The latter should be expected as the corner is a region of smaller scale turbulence.

The lack of potential core and the high turbulence level in the near region of the jet is an undesirable situation for selective control of shear flows since the excitation may be overpowered by the high level of the background turbulence. This problem, as will be shown later, can only be overcome by spatial mode manipulation.

2.3.2. Spectral Analysis of the Shear Flow

The natural jet flow was examined first. Spectral data was reduced from hot wire measurements at the edge of the shear layer spreading from the flat sides of the nozzle.

The spectra along the axial direction are shown in Figure 2.5. In the near field, the background noise is wide band but one can still see the peak in each power spectrum line. The power spectra peak is at about 200 Hz for z/D = 1 and 2, increases to 300 Hz at z/D = 4 and 8 and falls off afterwards, at z/D = 30 the peak is at about 100 Hz. Based on this data the characteristic frequency of jets termed the "preferred mode" is hard to determine. One would tend to deduce that the preferred mode exists between the range of 200 Hz to 300 Hz since that is the range where the power spectra peak for z/D < 8. However, further evidence is needed to verify this prediction. A method suggested by Hussain et al (1989) is to excite the flow at an amplitude higher than the background noise while varying the excitation frequency. In this way, the most unstable mode can be pinpointed.

The response of the flow to excitation can also be demonstrated in the time domain. Shown in Figure 3.6 is a typical time domain flow response to excitation at 80 Hz. The two sharp peak signals are the triggering signal with an amplitude of 5V. Between the triggering signals one can see three peaks that correspond to the flow response measured by hot wire. The jet response was, therefore, about 240 Hz.

The spectral content of the excited jet flow is examined next. Shown in Figure 2.7 are near field (z/D=4) spectra of the jet for the m=0 (symmetrical) azimuthal mode excitation at increasing excitation amplitude. Several noteworthy features can be seen. With increasing excitation amplitude, (shown as applied voltage), the energy content at the excitation frequency, 80 Hz and its harmonics is increased. This implies that the amplitude of excitation has not reached saturation yet. For small excitation amplitudes, Figure 2.7a, the excitation frequency is absent from the spectrum. With increasing amplitude, the excitation frequency appears in the spectrum, and the ratio of the energy content at the excitation frequency to that at higher frequencies increases. It can be deduced, as in other shear flows (for instance in the case of a music wire excited mixing layer that introduced in chapter 2), that for a large enough excitation amplitude the flow will respond at the excitation frequency rather than at the most unstable frequency, a phenomenon termed "collective interaction" by Ho and Huang (1982).

Proper characterization of the forcing level of the jet shear layer is important in order to optimize the excitation (maximum effect with minimum energy input), and also for the comparison of excitation methods. Unfortunately, there seems to be no common agreeable definition of the forcing level, at least with respect to spatial modes. As a result multiple definitions of forcing levels, that are rather arbitrarily adopted, have been employed.

Quoting from Long and Peterson (1992): "When the forcing is introduced from the plenum it is common to define the forcing level in terms of free-stream fluctuations measured on the centerline in the plane of the nozzle (e.g. Crow & Champagne 1971). When the forcing is introduced from outside the jet as in the present case the disturbance is exponentially damped inside the potential core. Consequently there is some ambiguity in defining the level."

Long and Peterson used a forcing level of $|F_{11}|_{max} / U_j = 0.17$, where $|F_{11}|$ is the Fourier transform of the phase mean velocity. The first subscript stands for fundamental frequency and the second for spatial mode 1. In their important paper that systematically described the spatial mode control methods, Cohen and Wygnanski (1987) did not even mention the excitation amplitude employed. In Y. Y. Chan's experiment (1977), six loudspeakers were used. His definition was: "The forcing amplitude of the drivers was set to 124 dB re. 0.0002 dynes/cm^2 at the exit of the duct with the jet running." There was no mention of whether this amplitude was the individual's or the six loudspeakers' combined. In Corke and Kusek's paper (1993) twelve loudspeakers were used. They defined the forcing amplitude in terms of the rms pressure fluctuations (p') of each loudspeaker at the lip of the jet. The fluctuating pressure was normalized by the dynamic pressure in the jet core. The unsteady pressure was measured using the sound level meter while connected to a pressure port without any flow through the jet. In the case of helical mode this pressure represents the maximum value. Wiltse and Glezer (1993) quantified the excitation amplitude and degree of modulation of each actuator using a broad band miniature microphone on the jet centerline at x/D = 0.11 without flow. Gutmark et. al. in their triangular nozzle paper (1988) used the relative forcing amplitude DP/P which is

similar to Corke and Kusek's definition. Koga and Nagib (1983) used the absolute flap motion amplitude to characterize the excitation level. It was concluded that the flap amplitude should be about the order of the local shear layer thickness.

In the present study the maximum Fourier transform of the phase mean velocity, along the radial direction at z/D = 0.2 was used as the measure for the flow excitation level. This level was about $|F_{11}|_{max} / U_j = 0.15$ where the first subscript stands for the fundamental frequency and the second subscript stands for the spatial mode 1.

The spatial evolution of various azimuthal modes of the excited triangular jet along the streamwise direction is shown in Figures 2.8a-d where $|F_{mn}|_{max}/U_j$ represents the maximum amplitude of the modulus along the radial direction. Examined moduli, for single mode, are 0 and 1; for non-integer mode 0.75, are 0, + 0.75, - 0.75 and 1.5; for mode ± 1, are 0, 1, -1 and 2. As seen, while the excited mode is always the strongest, other modes also appear but only at a fractional level, as seen in all cases. The appearance of other modes may be due to the irregularities of the geometry and the complexities of the flow. For example, the turbulence level at the apex and the flat side are different, which can lead to the generation of additional modes. Noticeable in the case of the m=0 excitation is that this mode decays very rapidly along the streamwise direction and becomes comparable to the secondary mode m = 1. This confirms the predictions (Batchelor (1961)) that an axisymmetric mode is not sustainable in a jet without a potential core. One can notice that except for m = 0 all modes have an amplitude about 0.15 at z/D = 0.5. The effect of these modes on the flow development is considered next.

2.3.3 Jet Evolution in the Near and Far Field

In this section the evolution of the jet flow field structure is described through the examination of 2-D and 3-D iso-velocity surfaces. The two key points to be examined are the response of the jet to different modes of excitation, and whether it is possible to

control the evolution of the jet into the far field. The response of the excited triangular jet is also compared with previous work on the azimuthal excitation of round jets.

In their papers Cohen and Wygnanski (1987) described, analytically and experimentally the single mode excitation. They concluded that single mode excitation results in amplification which is independent of the azimuthal coordinate ϕ. This implies that the axisymmetric jet remains such regardless of the mode of excitation, e.g., m=0, 1, 2, etc. This analytical derivation was, however, not restricted to a circular geometry. The question arises, therefore, about what is the near and far field response of the triangular jet to single mode excitation.

The evolution of the velocity field of an unexcited jet is shown in Figure 2.9. One observes that the cross section changes from triangular to circular in the far field as shown in the Top View.

In previous work on triangular nozzles Sforza *et al.* (1966) and Trentacoste and Sforza (1967) reported the switching of axes of the unexcited jet. This phenomenon was not observed in the present jet with a fully-sheared velocity profile and a high level of turbulence. Execution of the same experiment with a well-controlled top hat velocity profile and low turbulence in a different experimental setup (reported in chapter 5) did, indeed, exhibit axis switching. The lack of axis switching in the present case may be attributed to the absence of a potential core in the near field, the existence of which is essential for the creation of vortex rings, and as argued by Hussain et al (1989), it is the distortion of the vortex ring that causes the switching.

As a consequence of the evolution of the triangular jet into a circular shape in the far field, one may infer that if the jet response was independent of the azimuthal location ϕ, it should also evolve into a circular cross section in the far field when excited. An examination of such a case, m=1 excitation, is shown in Figure 2.10a, which depicts the $U/U_{\max}(z) = 0.5$ contour for $0 \le z/D \le 30$. Two observations can be made. First, the flow responds to the excitation only in the near-field (z/D<10) as evidenced through the presence of large scale structures. Second, the velocity contour evolves into a circular

shape (like the unexcited case) in the far field. The response of the jet, therefore, is independent of ϕ for single integer mode excitation.

The effect of more complex modes of excitation was investigated next, with particular interest in the resulting far field structure. The modes of excitation included standing wave mode (two waves generated with the same frequency, wave number but opposite spatial mode sign), previously examined by Cohen and Wygnanski, 1987 in the near field), and non-integer modes. Iso-velocity surfaces are shown in Figure 2.10b-d for excitation modes m = 0.75, ± 1, and ± 0.5 respectively. The measured distance along the streamwise direction was about $0.5 < z/D < 30$. The distance between the measuring stations was about a quarter of the excitation wavelength (z/D = 0.5), and all data were acquired at the same instance in the excitation cycle. The response of the jet differs significantly from that of the integer mode excitation. The data shows that the effects of the excitation for non-integer and standing wave modes persists into the far field, while for simple integer modes the perturbation decays rapidly. More importantly, as a practical outcome, one notices the large expansion of the iso-velocity contour in the far field. Concurrent with this expansion, indicative of momentum transfer between the jet and the ambient air, the cross sectional shape of the velocity-contour became increasingly non-circular, transforming from circular to elliptical and to a flattened ellipse, with a preferred orientation.

To examine this point further the response of the jet flow, subject to different azimuthal excitation modes was investigated in the far-field, at z/D=30, are shown in Figure 2.11. Comparison of the far-field structure of the jet subject to various excitation modes was done using the criteria of shape of the $U/U_j = 0.5$ iso-velocity contour, its orientation, and the area enclosed within it. As seen in Figure 2.11a, the axisymmetric structure of the jet is maintained in the far field when it is subject to single, integer, mode excitation, be it axisymmetric or non-axisymmetric. Using the area enclosed within the half-velocity contour, one can note that single mode excitation, Figure 2.11a, yields very little change compared with the unexcited case shown in a dashed line. The effect of

other modes of excitation, standing waves and non-integer modes, can be seen in Figure 2.11b - d. The most noticeable characteristics are:

1. the area enclosed by the half velocity contour more than doubles compared with the unexcited case,
2. the velocity contours are close to being elliptic rather than circular, and
3. the inclination angle of the major axis for the elliptic contours varies with excitation mode, being about 35° for the m=0.75 mode (non-integer), single or m= ± , and 90° for the m= ± mode.

The third observation mentioned above has been proven to be potentially important. The fact that the directional jet expansion was formed to correlate with the excitation mode, led to the development of the dynamic excitation methodologies. These methodologies are discussed in Chapter 3.

Another measure, and perhaps of greater practical significance, is the entrainment of the excited jets. The total volume flow rate (gas density remains constant) of the various jets, unexcited and excited with modes m = 1, 0.75, ±1 and ±0.5, was calculated as a function of axial position. The results are shown in Figure 2.12 as the ratio of entrained fluid flow rate to the jet flow rate at the nozzle exit. As shown, for single integer mode, m=1, there is an increase in the amount of entrained fluid by ambient air about 50% compared with the unexcited case, while for fractional and counter propagating modes the ratio is about 300%.

The difference in the behavior of the triangular jet when subject to single versus non-integer and standing wave modes excitation is examined next. In their work on a circular jet Cohen and Wygnanski (1987) pointed out that the azimuthal variation of the velocity contour was determined, in the near field, by $\cos[\phi(m_{11} - m_{22})]$. Long and Peterson (1992) reached similar conclusions at about the near-field (z/D<4). Strange (1981) reported that at about z/D =12 the azimuthal distribution of the mean velocity regained its natural axisymmetric shape. The conclusions drawn from these studies are that although good velocity contour manipulation could be achieved in the near field, the

circular jet could not be controlled in the far field.

As in the case of the circular jet, the far field of the present triangular jet could not be controlled by using frequency excitation alone. The observations listed above, however, indicate that such control may be achieved by azimuthal mode manipulation. The mechanism responsible for this control is explored next.

The temporal evolution of the jet is shown in Figure 2.13 for several spatial modes. The plots show iso-velocity surfaces of $U/U_j = 0.5$ at the streamwise location of $z/D = 4$ in the x-y-ϕ space, with x and y being spatial coordinates in the cross sectional plane and ϕ being the temporal coordinate. Each plot shows three cycles at the flow response frequency of 240 Hz.

When the jet is excited with a single integer modes, Figure 2.13a for m = 1, the response is symmetric. Excitation at m=0.75, shown in Figure 3.13b, exhibits drastically asymmetric motion. With progressing time the fluid column undulates in the *x-y* plane along the ϕ axis direction. The same phenomenon can be observed in the case of $m = \pm 1$ shown in figure 3.13c. The undulation, asymmetric evolution, and spiral motion help explain the large elliptical cross sections observed in the far field for the fractional and standing wave integer and fractional, excitation modes.

Closer inspection of the $U/U_j=0.5$ contours of Figure 2.13 reveals a difference in the temporal evolution of the jet cross sections in the x-y plane.

Excitation with a single integer mode, m = 1 in Figure 2.13a, results in a pulsating axisymmetric evolution, termed as jet column motion. In contrast, excitation with non integer and standing wave modes, m = 0.75 in Figure 2.13b and m=+-1 in Figure 2.13c, shows very different behavior. First, the evolution of the x-y cross section with time is asymmetric. Second, the displacement of the jet fluid in the x-y plane is in a preferred direction, for example, for m = 0.75, this is along the y direction (due to phase inputs along that direction).

This asymmetric and directional motion of the jet column in the near field leads to the observed large directional expansion of the jet in the far field. Further discussion of this observation is presented.

2.3.4 Three Dimensional Views of Spatial Modes

Recently, Yoda (1992) proposed the existence of three dimensional spiral vortical structure in circular jets. Analyzing natural jets she pointed to the possibility of the existence of helical modes that exhibiting axisymmetric and anti-symmetric modes simultaneously in natural jets. This led to a 3-D depiction of the vortical structure of the natural circular jet. For excited jet, Cohen and Wygnanski (1987), by analyzing the phase-locked data, decomposed into azimuthal modes, had concluded that the amplitude of the excited mode was an order of magnitude higher than other modes, the modes detected in the excited jets were those of being excited and the natural coupling among different modes was secondary only.

In the following, the experimental data are represented using iso-velocity contour, depicted as the jet column.

In the present experiments, it was found that either the axisymmetric or asymmetric modes or both existed depending upon the mode excited. Shown in Figure 2.14 are iso-velocity surfaces, U/U_j=0.5 for the streamwise region of $0 \leq z/D \leq 10$ at temporal phase angle of zero, viewed from two orthogonal directions as a sequence comprised of eight velocity contours (in 13 azimuthal degrees increments, viewed from top left to bottom right). For single mode excitation, in the case of m = 1 (shown in figure 2.14.a) the flow structures are basically symmetric, while in the case of m = 0.75 (shown in Figure 2.14b) the flow structures are basically asymmetric. However, viewed from orthogonal directions according to the viewing sequence mentioned above, one can observe in figure 2.14b that the flow structure varies from the asymmetric shape (typically shown in the first velocity contour) to the symmetric shape (typically shown in

the fourth velocity contour) and then back again to asymmetric shape (typically shown in the last velocity contour). It is also noticeable that among the eight velocity contours, there is one that shows the largest jet expansions, the last velocity contour in this case. The mode excitations, m = ±1 and ±0.5, shown in Figure 2.14c and 2.14d, exhibit similar behaviors to that of m=0.75. However, in those later two cases, the flow structure is, at first, symmetric. As the azimuthal angle turned from one orthogonal direction to the other, the flow structure becomes completely asymmetric as shown in their last velocity contour. The jet expansions represented in the figure of m=0.75, ±1 and ±0.5 (in Figure 2.14b, 2.14c, 2.14d) are much larger than the case of m = 1 (shown in Figure 2.14a). It is obvious that in order to enhance jet expansion one has to excite asymmetric structures in the jet.

Figure 2.15 shows one cycle of the temporal developments of the structures (represented by velocity contours for U/Uj=0.5) as they evolve in time under different spatial modes excitations. Four cases are shown m=1, Figure 2.15a, m=0.75, Figure 2.15b, m=±1, Figure 2.15c and m=±0.5, Figure 2.15d. They can be viewed in the same manner as in figure 2.14, i.e., from top left to bottom right of the picture. The individual depictions are temporally 18^0 apart in one cycle. The propagation of the flow structures termed as bulges can be vividly seen in these figures. For example, in Figure 2.15a (m = 1) the bulge that is located at about 1/3 height of the first velocity contour evolves -- as the temporal phase angle increases -- upward to the top end of the last velocity contour. The development is spatially symmetric. In Figure 2.15.b, m = 0.75, one can observe two bulges that propagate in the streamwise direction, one is parallel and one is perpendicular to the plane of the page. The jet column is asymmetric. For instance, the structure that is parallel to the drawing plane is on the left side of the jet column and develops in that direction too. It looks like a protruded bulge. An apparent feature of the bulge is that it not only develops axially but also radially which enables the jet expands faster, leading to a much larger expansion than for m = 1 excitation. Similar observations can be seen in

the case of standing wave excitations in Figure 2.15 c and 2.15d for m=±1 and ±0.5 respectively.

The data presented above shows that the asymmetric movement of the structures induced by m = 0.75 and ± 1 modes excitations results in larger jet expansion compared with its symmetric counterpart. Single integer mode can only generate symmetric flow structures. These types of excitation are, therefore, unable to generate large jet expansion in the far flow field.

2.4 Summary and Conclusions

The possibility of controlling the evolution of a turbulent jet to the far field was investigated. The study was performed on a high turbulence level jet using an active triangular nozzle. Without excitation, the jet in the far field was axisymmetrically shaped. Frequency excitation was found to be ineffective for the purpose of achieving control over the jet evolution into the far field. In contrast, excitation of certain azimuthal modes has been shown to allow the desired control. Excitation of a single integer mode resulted in axisymmetric expansion in the far field, 10 <z/D<30, similar to the case of circular jets. Non-integer mode and ± 1 mode excitation resulted in non-symmetrical evolution of the jet. Even though the far field was still completely decorrelated from the excitation signal, unlike the case of Cohen and Wygnanski (1987), the spreading rate and direction of the iso-velocity contours in the far field were able to be controlled by azimuthal mode manipulation.

The control of jet evolution in the far field was explained in terms of three-dimensional jet column motion in the near field. It was able to show in this chapter that the far field of jet could be affected by spatial mode control. This was validated by the fact that in the far field:

1. The jet column size was increased in size (Figure 2.12);

2. The direction of the jet expansion was modulated according to the mode excited (Figure 2.12);

3. The entrainment ratio was attained a 300% increase by non-integer modes and standing wave modes excitations (Figure 2.13).

The unique dependence of the jet directional expansion to the mode excited points to a better way to control the far field. This will be discussed in the next Chapter.

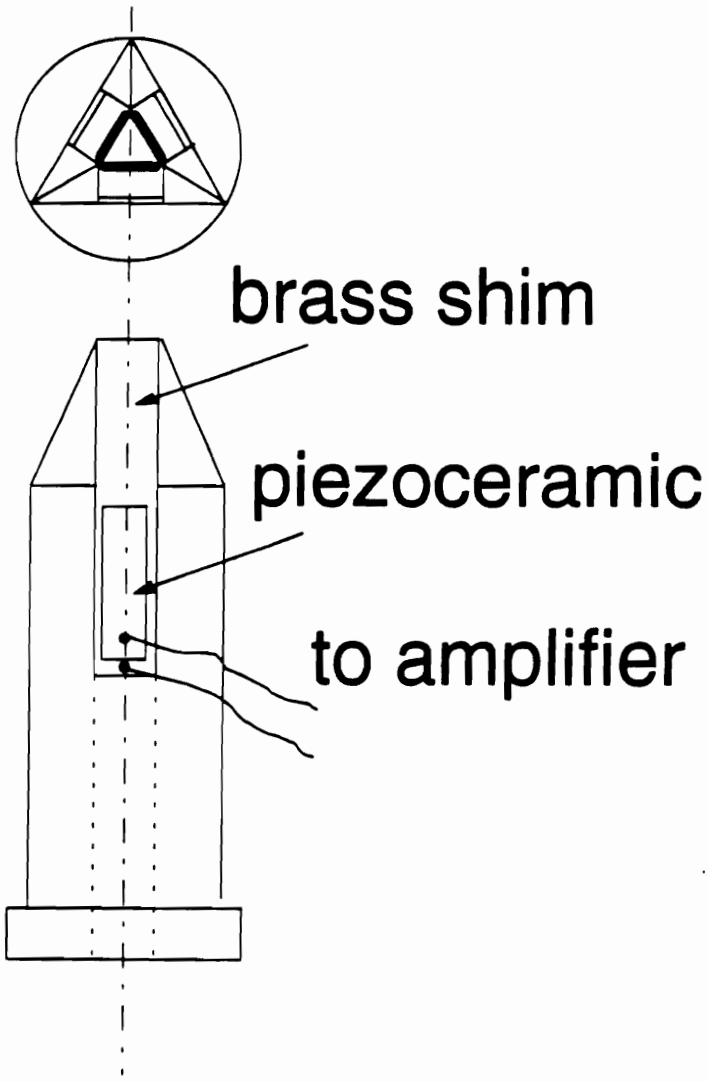

Figure 2.1. Active triangular nozzle (not to scale)

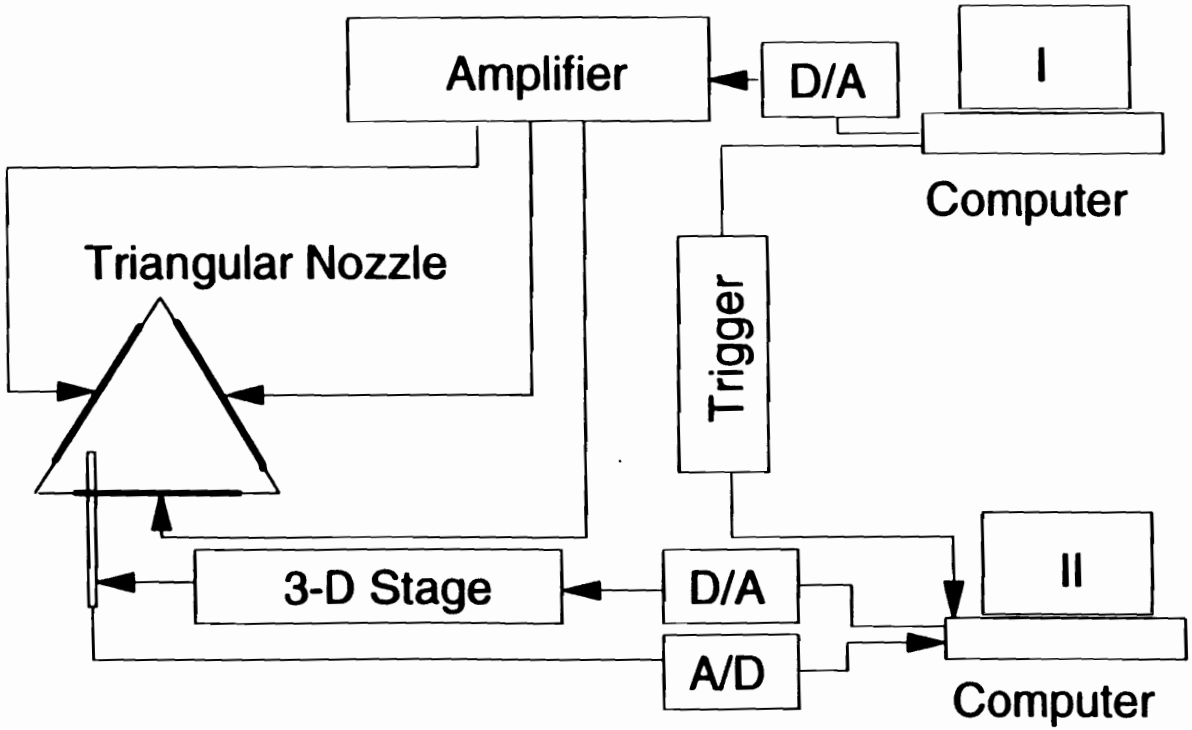

Figure 2.2 Nozzle actuation and data acquisition system

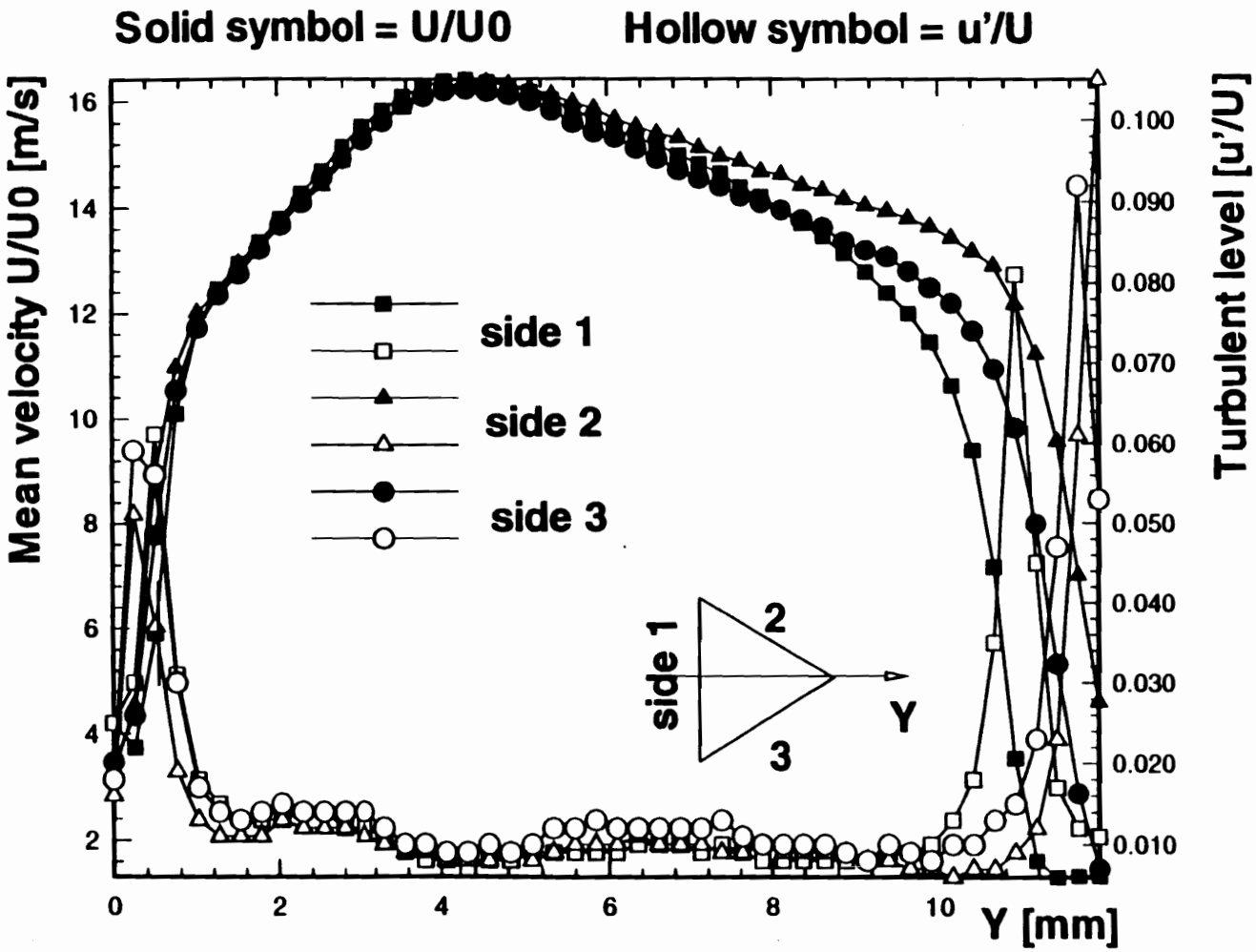

Figure 2.3 Mean jet velocity and turbulence intensity profile (flat side to vertex cross section)

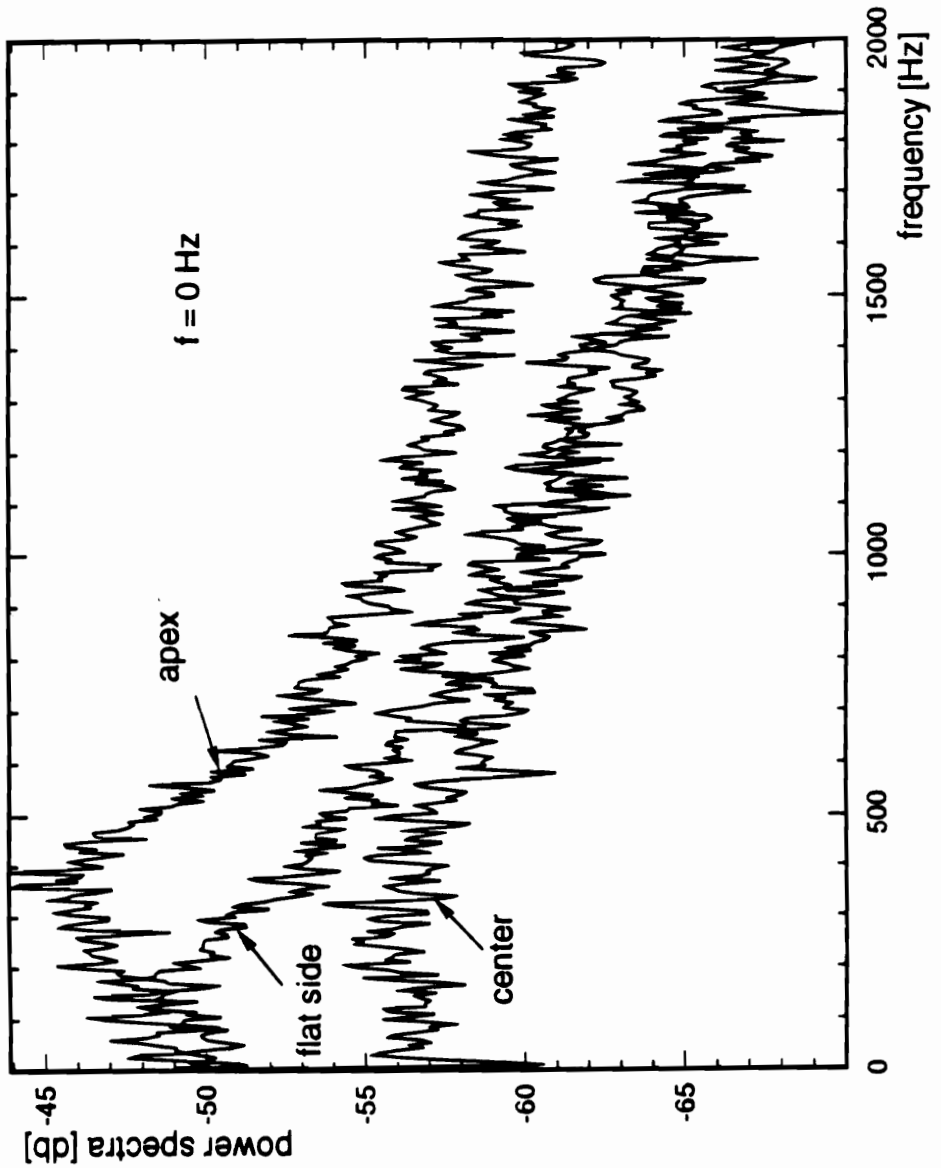

Figure 2.4. Power spectra of unexcited jet at $z/D \approx 0$

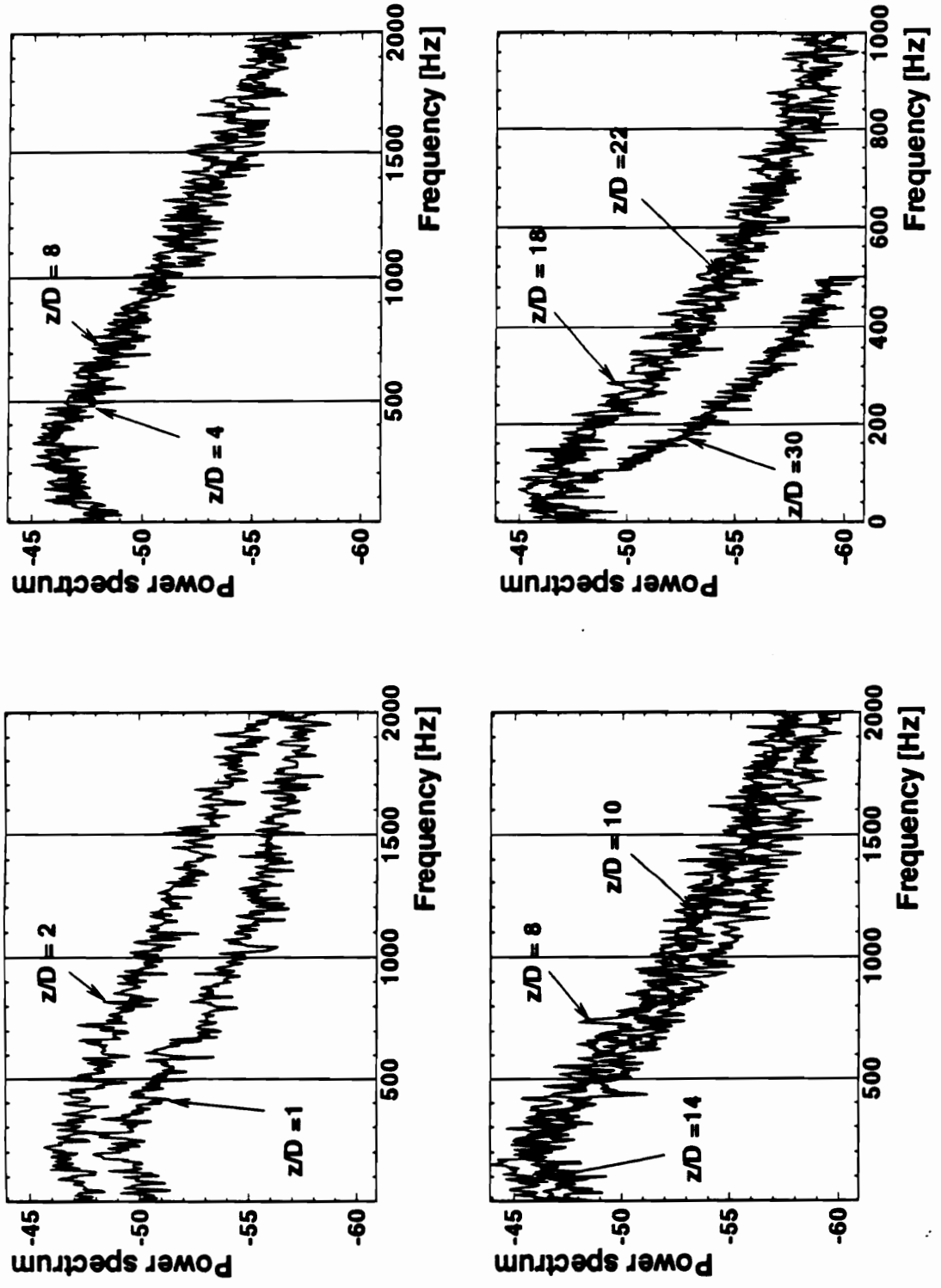

Figure 2.5. Power spectra of the unexcited jet along the streamwise direction $\mathrm{Re}_D = 8000$

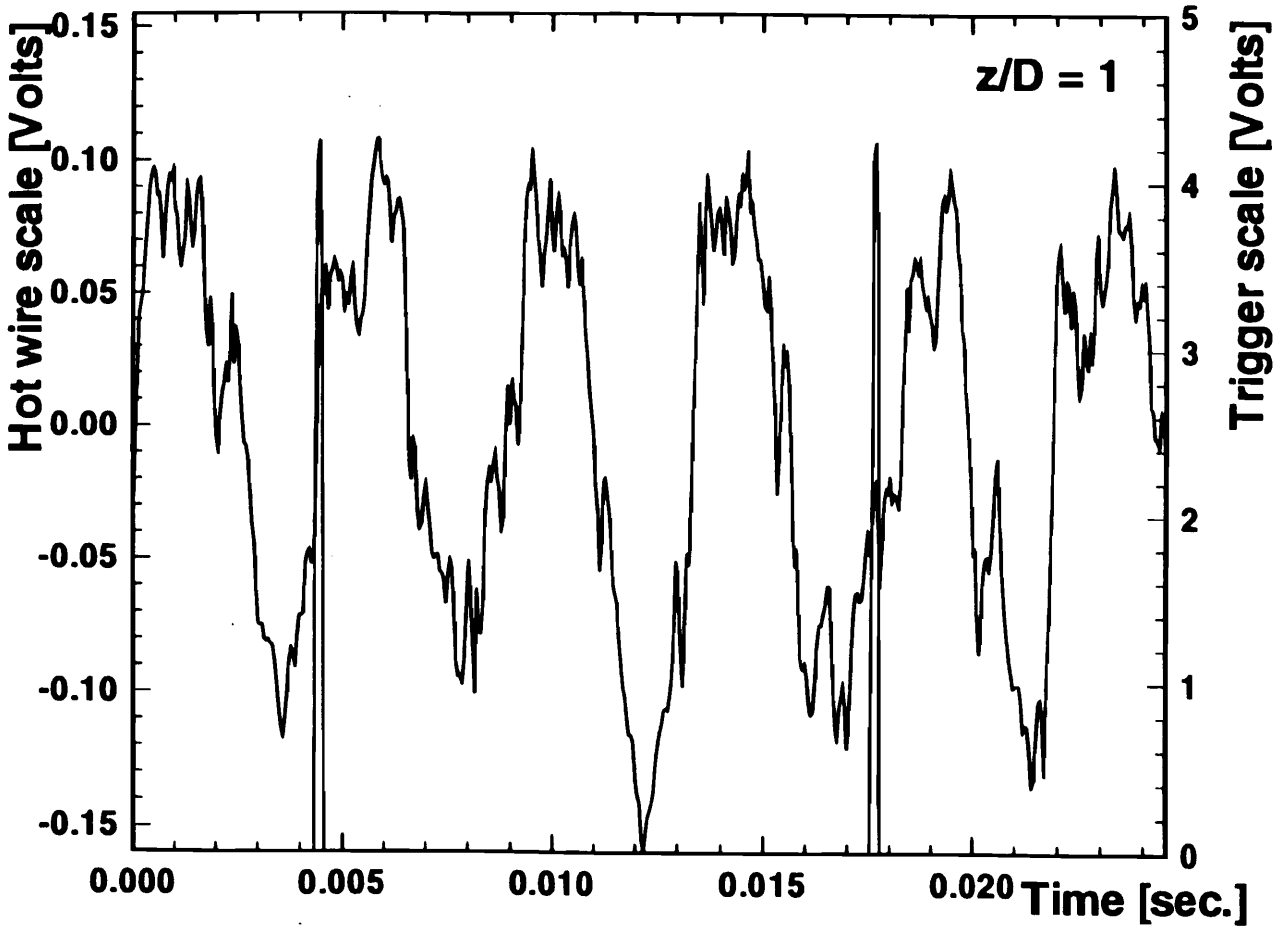

Figure 2.6 Time domain flow response to excitation

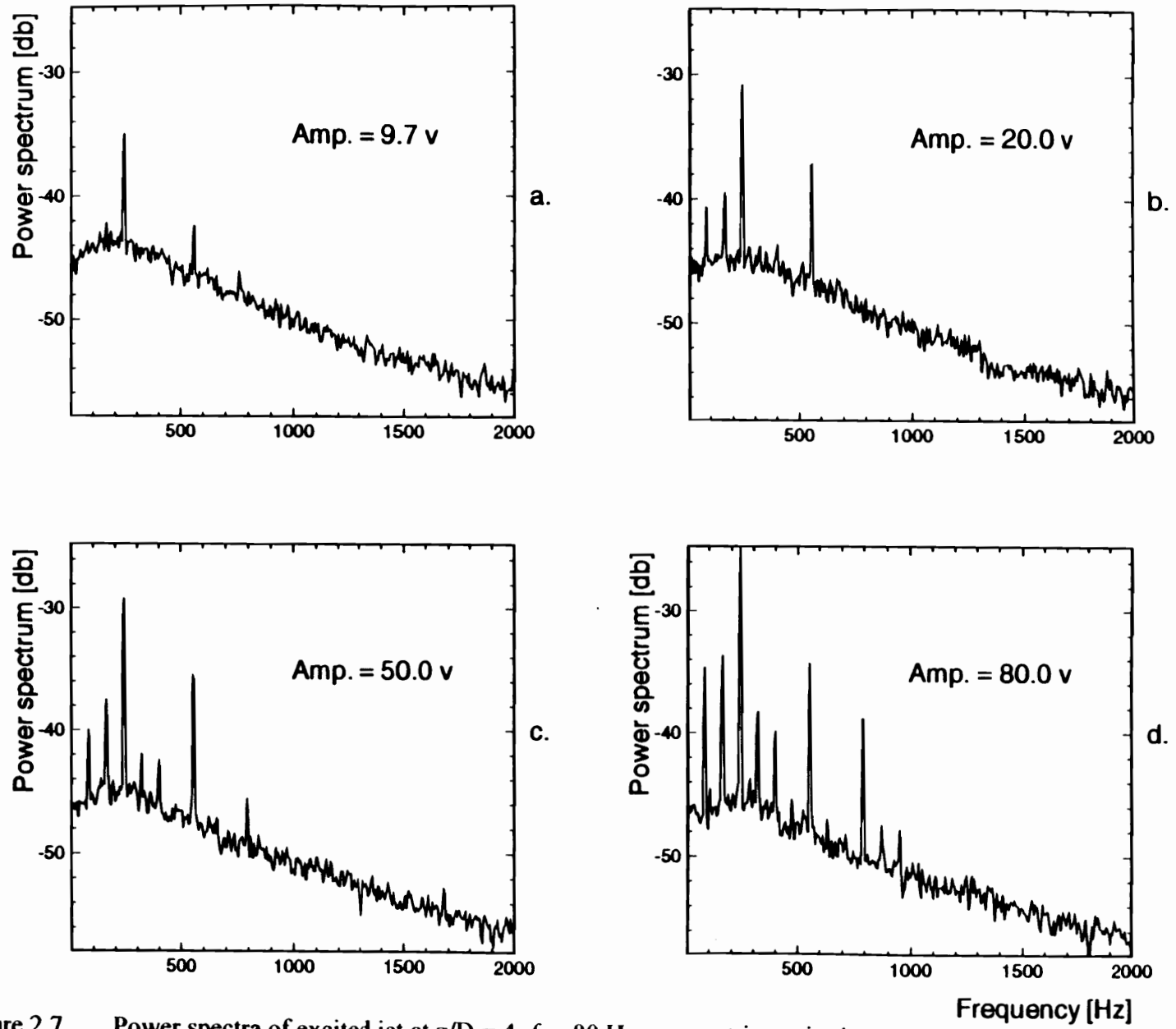

Figure 2.7. Power spectra of excited jet at z/D = 4, f_e = 80 Hz, symmetric excitation m = 0, increasing amplitude

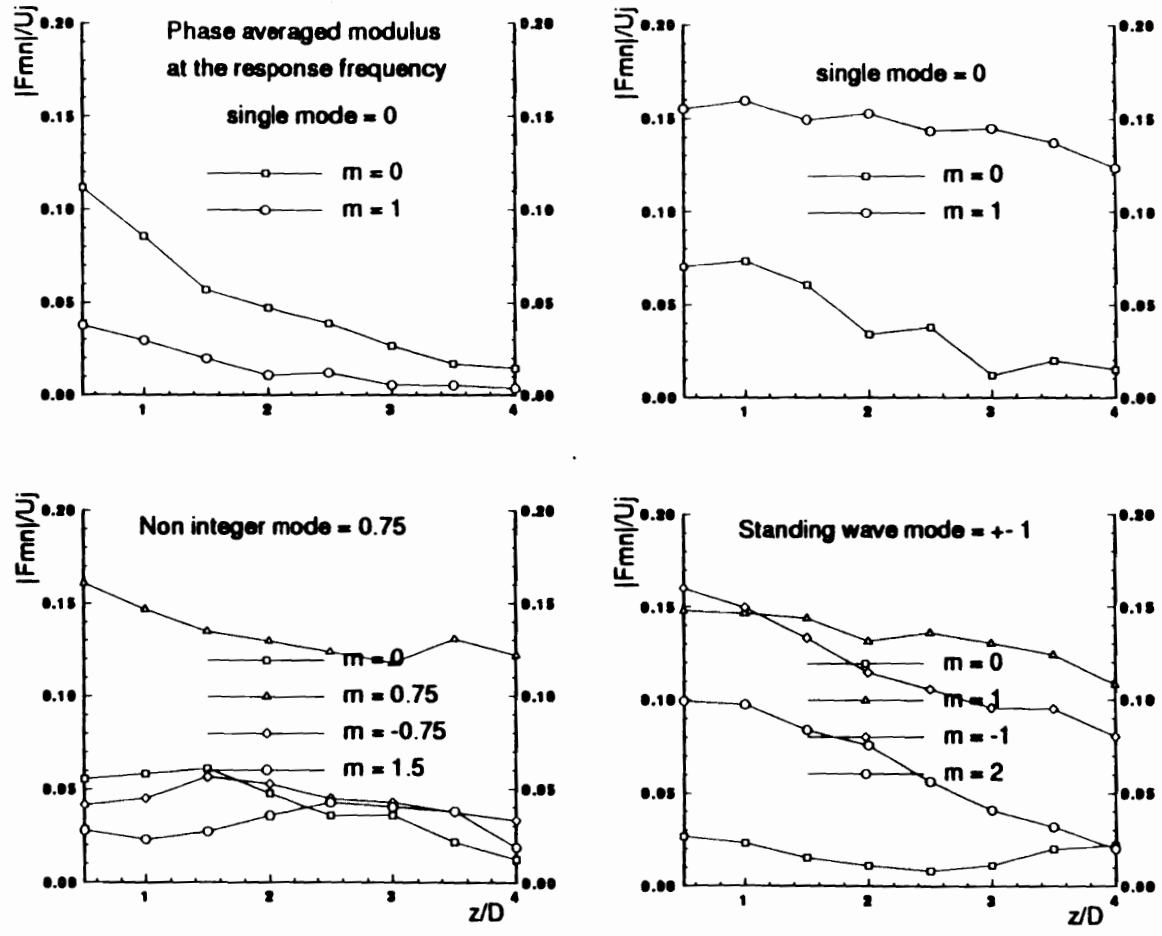

Figure 2.8. Mode spectra of excited triangular jet, f_e = 80 Hz, for $0 \leq z/D \leq 4$ a. m=0; b. m=1; c. m=0.75; d. m=±1

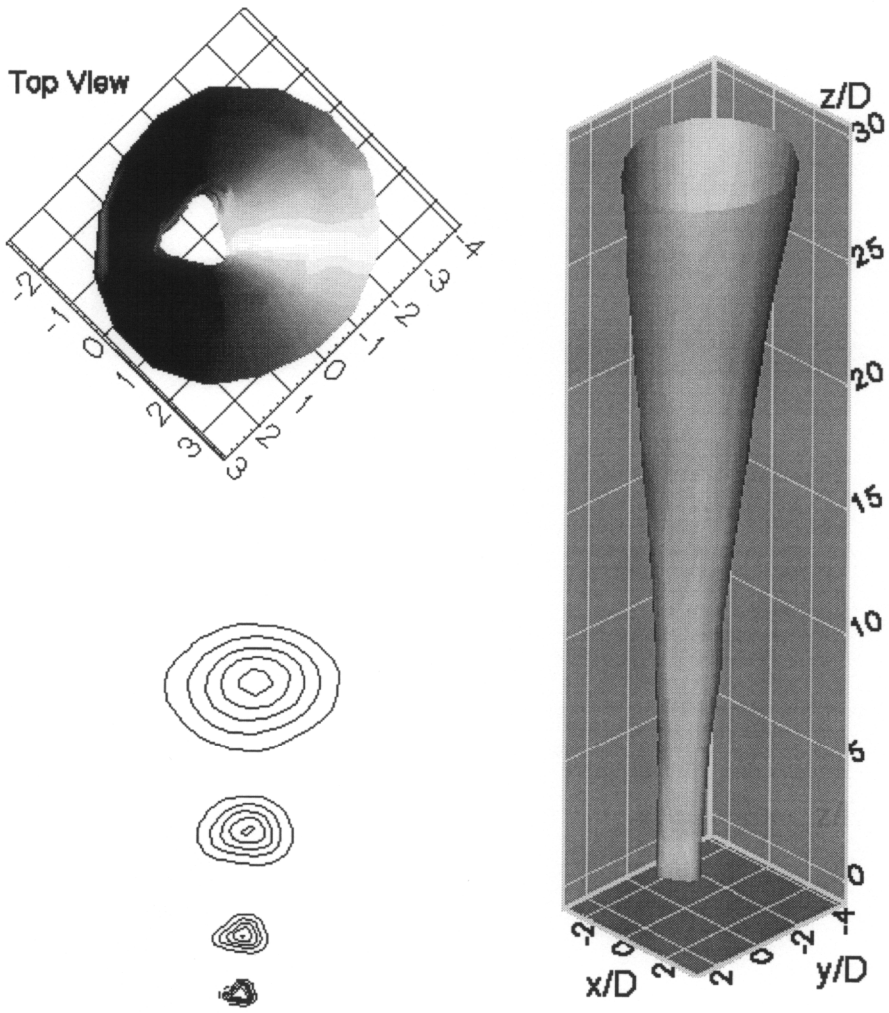

Figure 2.9. Isovelocity contour $U / U_{max}(z) = 0.5$ of unexcited jet, 3D surface, z/D = 0.5 to 30

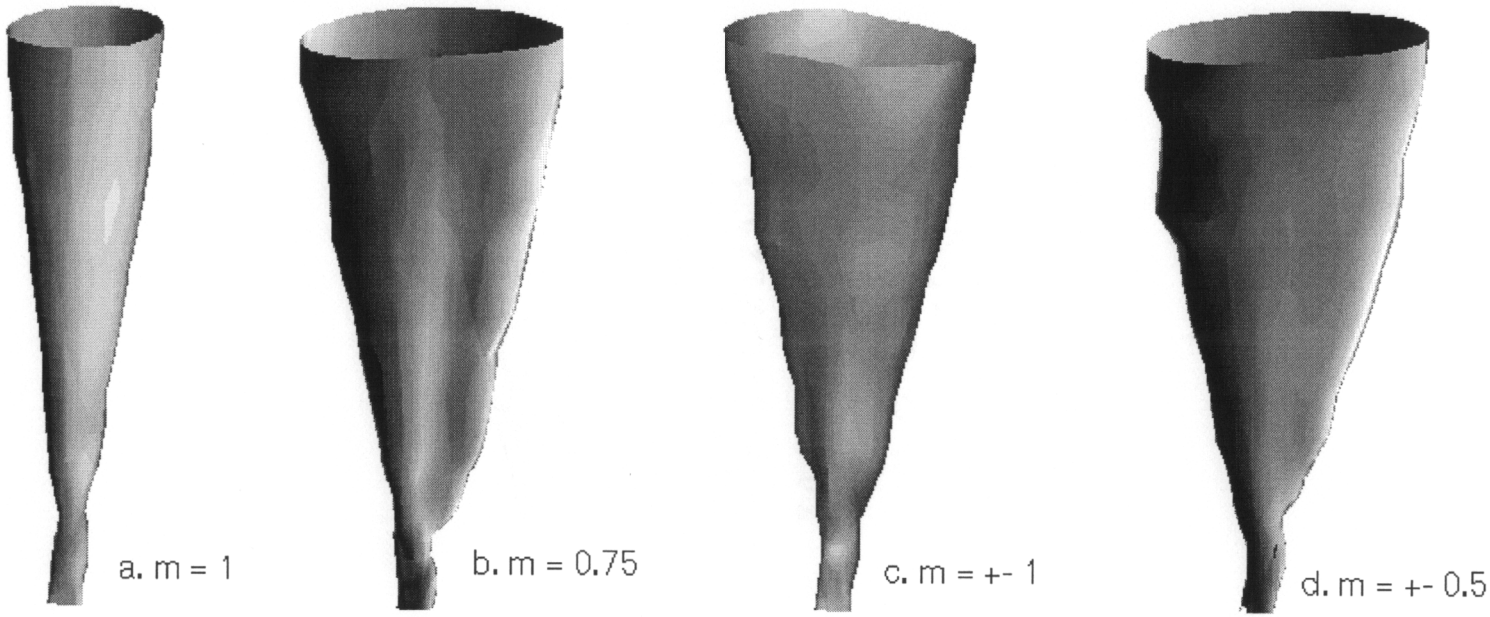

Figure 2.10. Isovelocity surface $U / U_{max}(z)$ for a jet excited at 80 Hz, a: m = 1; b: m = 0.75; m = ±1; d: m = ±0.5 at the same instance in the time cycle

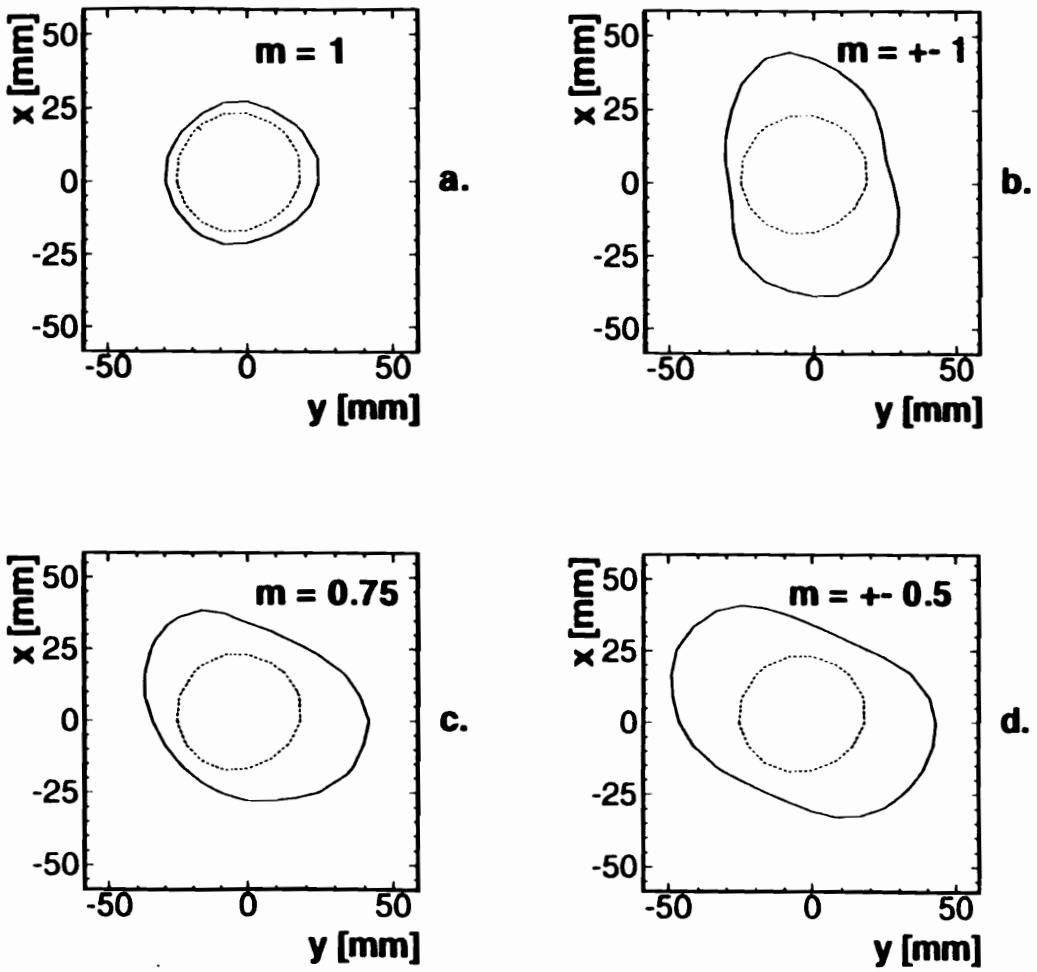

Figure 2.11 Isovelocity contour $U / U_{max}(z)$ at z/D = 30 for different excitation modes. —— indicated mode; ····· unexcited

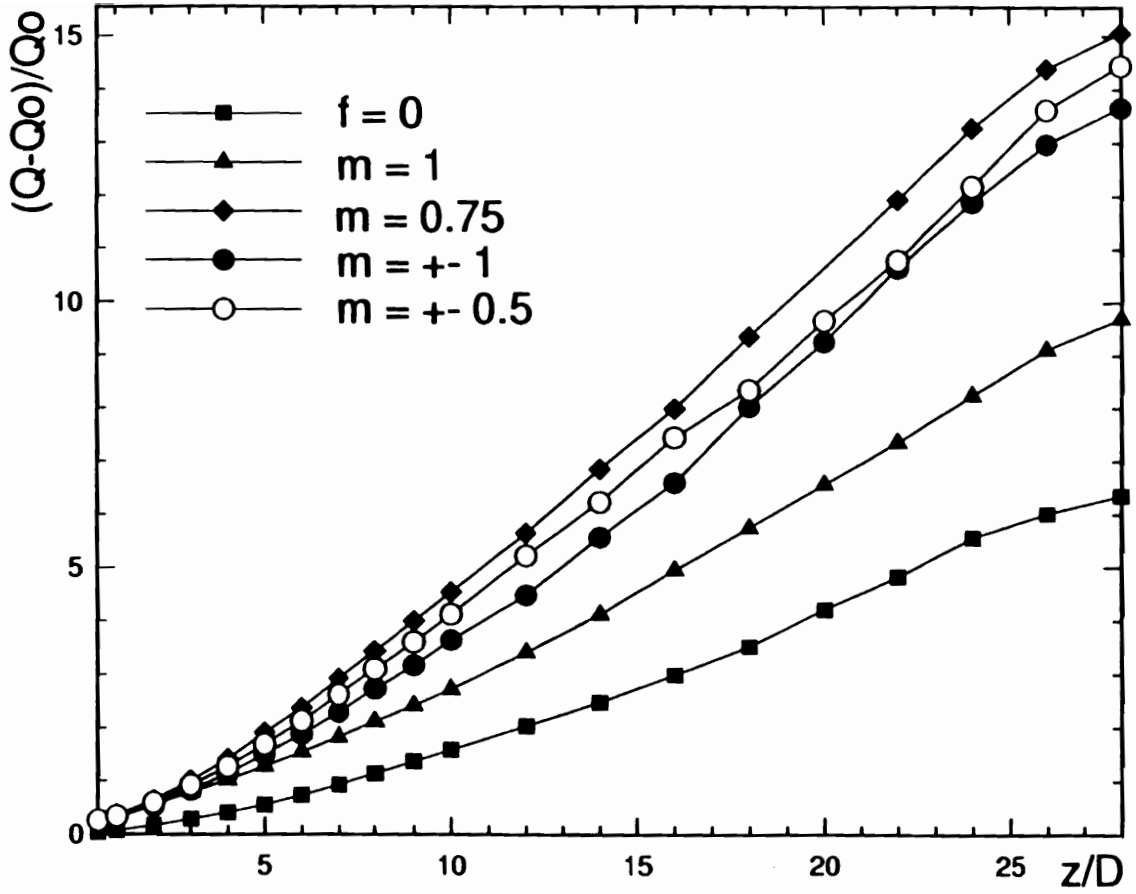

Figure 2.12. Entrainment ratio for the unexcited and the excited jet f_e = 80Hz, m=1; 0.75; ±1; ±0.5

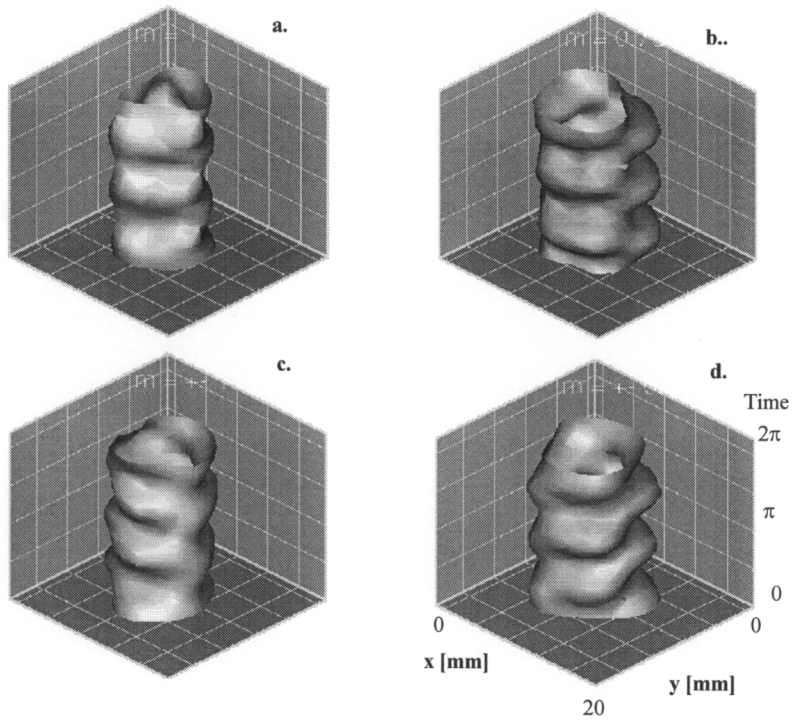

Figure 2.13. Isovelocity surface of u/Uj = 0.5, in the z-y-t space. Shown are four jet response periods, a: m = 1; b: m = 0.75; c: m = ±1; d: m = ±0.5

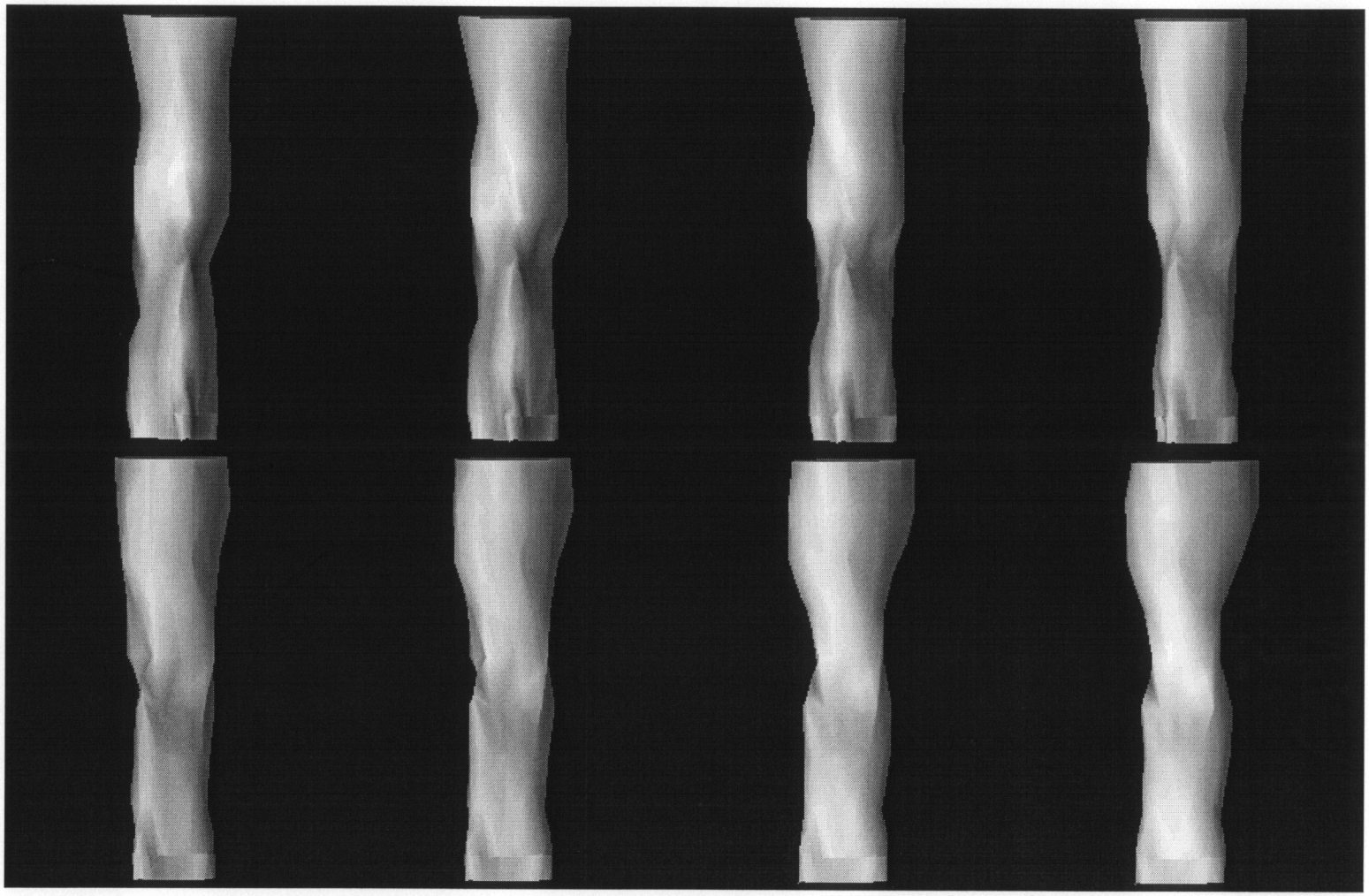

Figure 2.14 a. 3-D view of the isovelocity surface from different projection angles, for m=1 excitation; top left view at 0^0, bottom right view at 90^0 with 13^0 increments, going from left to right

Figure 2.14 b. 3-D view of the isovelocity surface from different projection angles, for m=0.75 excitation; top left view at 0^0, bottom right view at 90^0 with 13^0 increments, going from left to right

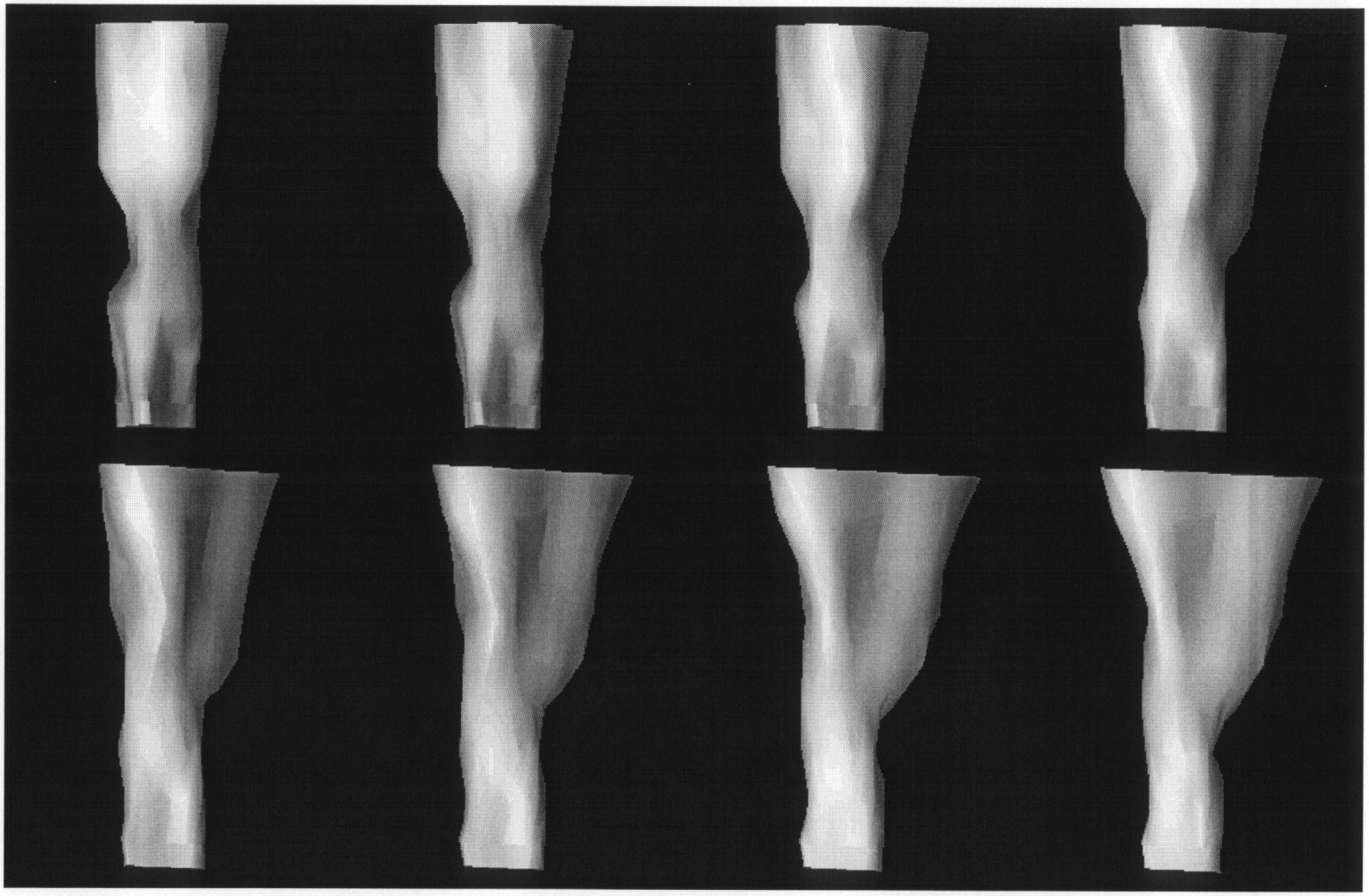

Figure 2.14 c. 3-D view of the isovelocity surface from different projection angles, for m=±1 excitation; top left view at 0^0, bottom right view at 90^0 with 13^0 increments, going from left to right

Figure 2.14 d. 3-D view of the isovelocity surface from different projection angles, for m=±0.5 excitation; top left view at 0^0, bottom right view at 90^0 with 13^0 increments, going from left to right

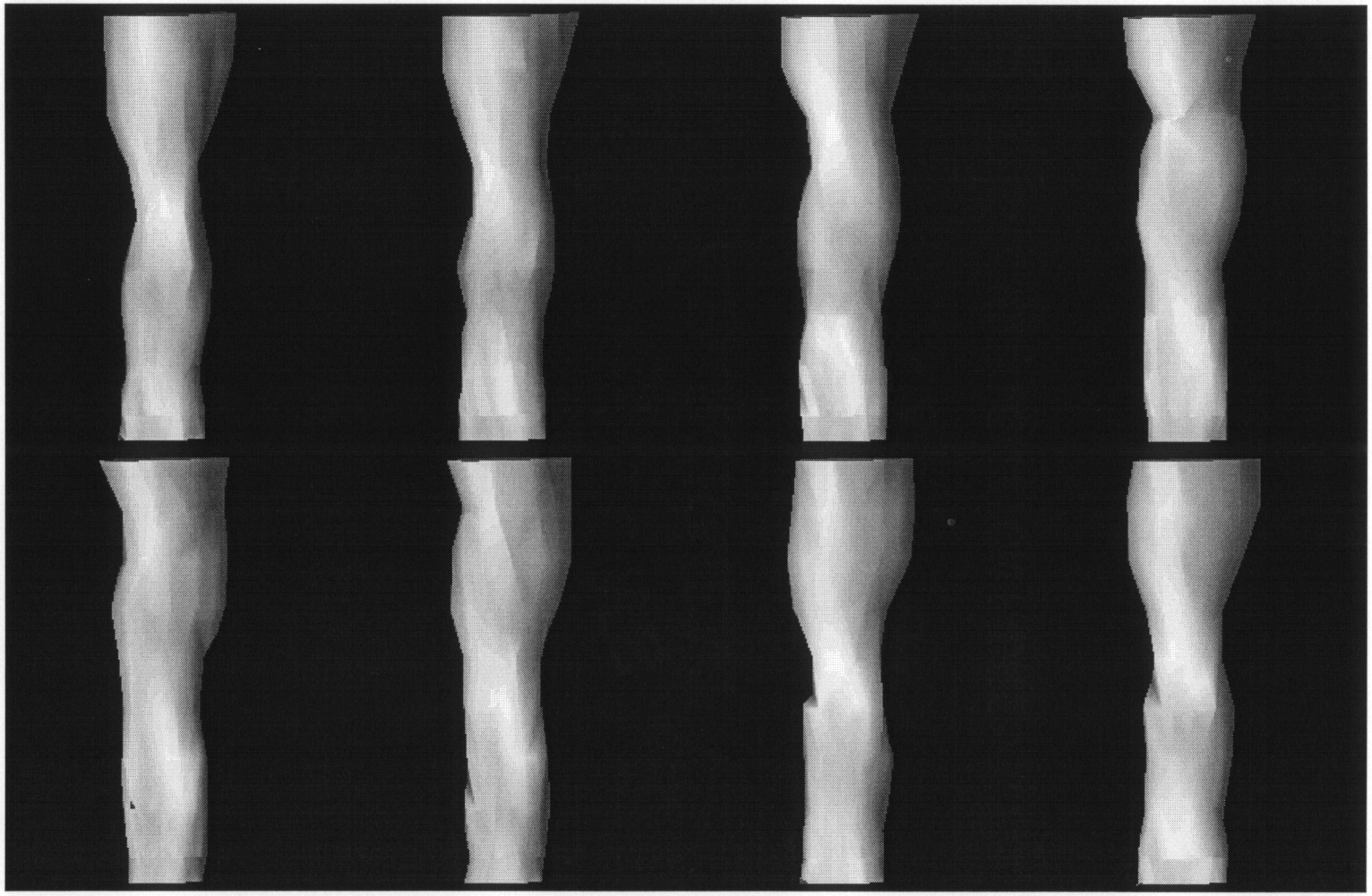

Figure 2.15 a. 3-D view of the isovelocity surface in one temporal cycle , for m=1 excitation; top left view at 0^0, bottom right view at 360^0 with 51^0 increments, going from left to right

Figure 2.15 b. 3-D view of the isovelocity surface in one temporal cycle , for m=0.75 excitation; top left view at 0^0, bottom right view at 360^0 with 51^0 increments, going from left to right

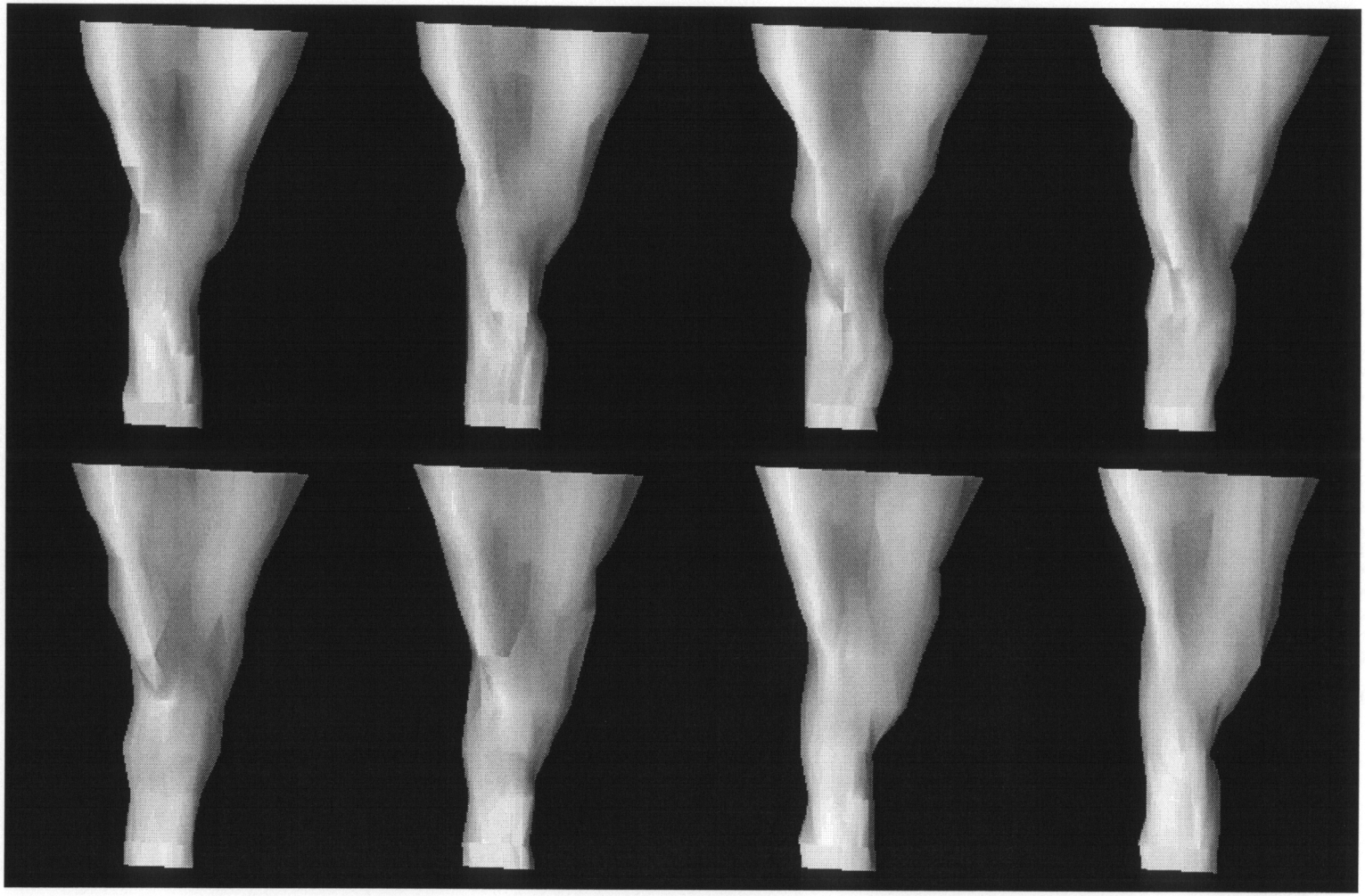

Figure 2.15 c. 3-D view of the isovelocity surface in one temporal cycle , for m=±1 excitation; top left view at 0^0, bottom right view at 360^0 with 51^0 increments, going from left to right

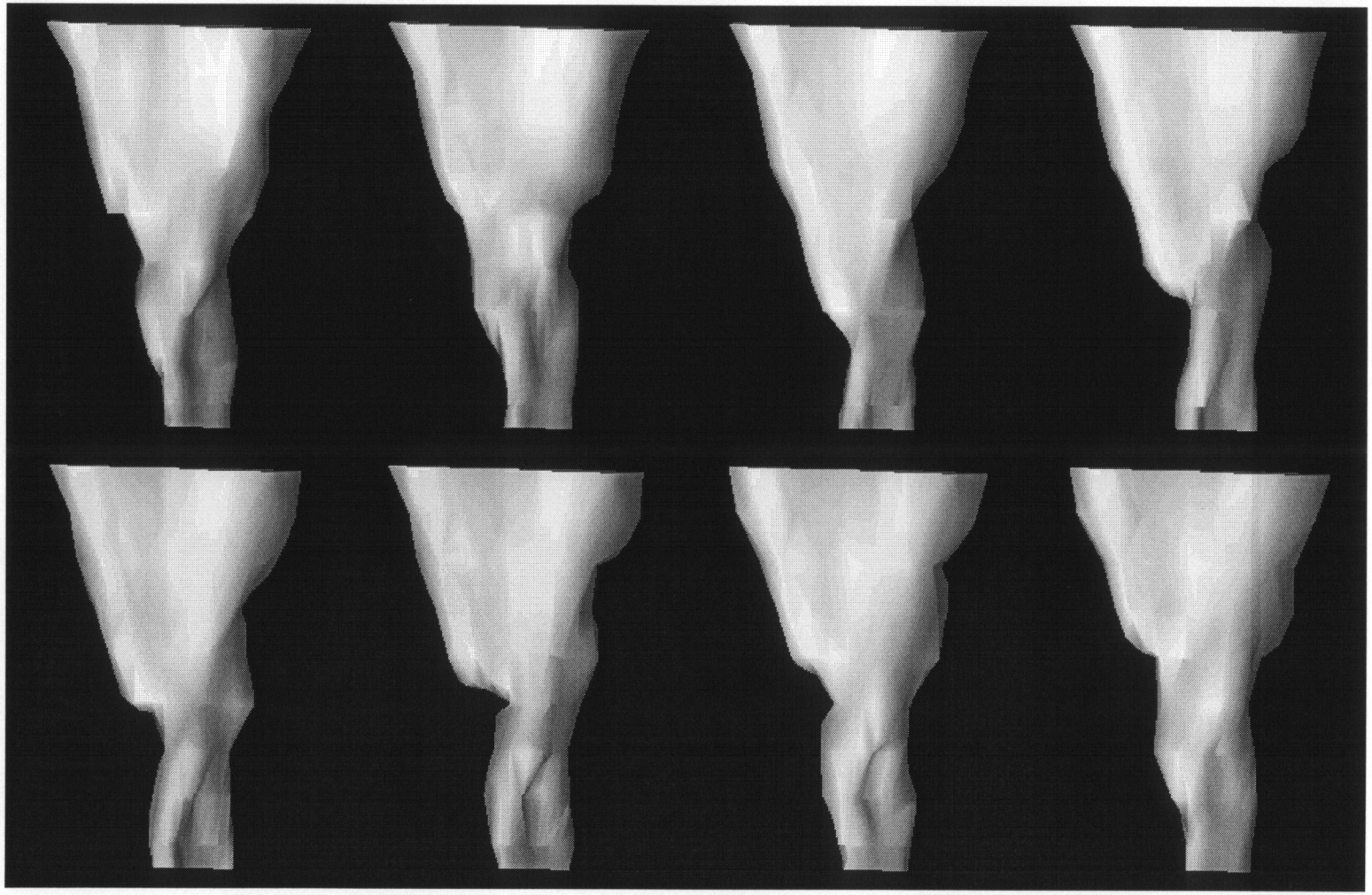

Figure 2.15 d. 3-D view of the isovelocity surface in one temporal cycle , for m=±0.5 excitation; top left view at 0^0, bottom right view at 360^0 with 51^0 increments, going from left to righ

Chapter 3 Circular Jet with Initial Top Hat Velocity Profile

3.1 Introduction

Jet control in the near field can be achieved using spatial mode manipulation. This method was reviewed in Chapter 1, discussed in Chapter 2 and is further examined in this Chapter. As described in Chapter 2, when the same methodology was applied to the far field, the jet was uncontrollable and unlocked to the forcing signal. The goal of the work presented in this chapter was to look for new actuation methods that can enhance the controllability of the far field of jet.

Some of the key results determined in the last chapter, which formed the basis for the work presented in this chapter are:

1. The far field of jet can be affected by spatial mode control.
2. The mechanism used to affect the far field is to excite the jet column instability. This type of instability can only be excited using spatial mode control.
3. In the far field, the direction of the expansion and the cross sectional shape of the jet are uniquely determined by the type of spatial mode excited near the nozzle.

Based on the above results, it was postulated that the phase decorrelation of the flow from the actuation signal can be overcome by dynamically varying the spatial mode in the near field.

In this chapter, a description is given of studies where this postulate was tested.

A circular jet with an initial top hat velocity profile and low turbulent level was employed. This type of jet has several advantages over the triangular jet for spatial mode control studies:

1. The controlled velocity profile can be readily predicted via the theory developed by Cohen and Wygnanski (1987).
2. The effects as a result of non-symmetric geometry as was the case for the triangular nozzle set up need not to be considered.

The experimental methods are discussed in section 3.2. Section 3.2.1 includes a description of the jet facility, the forcing conditions, set to characterize the excited jet, are described in section 3.2.2; and section 3.2.3 includes a description of the data reduction technique used in this and later chapters.

There are still two important issues that were not clarified in the last chapter:

1. The effects of excitation amplitude -- whether there exists a threshold of the excitation amplitude below which the far field control is not achieved.
2. The mechanism of the jet expansion -- where does the non-linear jet expansion take place and how does it happen?

These issues are discussed in Section 3.3, the results are reported.

Finally, in section 3.4 the dynamic mode control method is described in detail while in section 3.5 conclusions are drawn.

3.2 Experimental Methods

3.2.1 Jet Facility

The jet facility was designed to accommodate different geometrical setups, and in all cases exhibit low turbulence levels over the test section.

A schematic diagram of the jet facility is shown in Figure 3.2.1. The air used in the experiment was supplied by a high-pressure compressor (100 p.s.i.). The air passed

through pressure regulators and control valves before entering the apparatus at the bottom of an acoustically dampened circular plenum chamber. There were four air inlets to the plenum chamber arranged 90 degrees apart. However, only one inlet was used because the symmetric arrangement of the air inlets made the incoming air jets impinge on each other, creating excessive noises. After the plenum chamber the air passed through a honeycomb and a series of perforated plates and screens before entering the nozzle.

Design experience shows that the nozzle is the critical part of a jet facility. There are two distinguishing features in the present nozzle design.

1. It is CNC machined using 3D cosine curve contraction which makes it extremely smooth.
2. It is interchangeable, as shown in the schematic view of Figure 3.2.1.

The nozzle is divided into two parts: 1) a contraction from 6″ circular to 2″ circular cross section then 2) a further contraction from 2″ circular cross section to a 1″ circular or momentum flux equivalent triangular and elliptic cross sections.

At the nozzle exit, the flow attained a 'top-hat' velocity profile, except for a thin boundary layer present near the solid surface. The jet velocity U_j could be varied from 0 - 70 m/s. In this study the velocity was kept at 20 m/s with a Reynolds number based on the exit diameter of the nozzle equal to 3.4×10^4. The turbulence level at the exit plane of the jet was less than 0.15%.

A speaker was mounted at the base of the plenum chamber to generate controlled, axisymmetric disturbances at the exit plane of the nozzle. Eight or three speakers were placed, azimuthaly equally spaced, around the circular and triangular nozzle respectively. This setup can generate spatial modes by the pumping action of air from narrow slits located near the lip of the nozzle. These speakers were driven by an AT-DT-10 D/A board via 24 watt amplifiers which were controlled by the software developed by the author. This software is documented in appendix B.

The key to spatial mode control is the control of the phase difference among the azimuthally arranged loudspeakers. The combination of signal generator, amplifiers, loudspeakers and their extensions forms the actuating system. A detailed description of the control mechanism is given in appendix B.

The phase difference between each of the signals was precisely controlled by a computer. Unfortunately, the phase shifting between the loudspeaker and signal source was not zero and varied with frequency, amplitude and from day to day. Also, the performance of extension parts of the loudspeaker and the amplifier varied for each system, making the phase shifting problem even more complicated. Consequently, the whole actuating system had to not only be calibrated before the experiments but the calibration procedure had also to be automated. The calibration method is described in section 3.2.2.

In this experiment the excitation frequency was fixed at 180Hz. At this frequency the speakers were found to have a minimum phase shift. The speakers' phase was calibrated at the location of Z/D = 0.5 and R = 0.4, which was in front of each of the actuators and above the circumference of the exit nozzle. The reason for such a definition will be discussed in the next section. In single mode test, only phase calibration was needed. For the standing wave case, since the amplitude of the excitation varied along the azimuth of the nozzle, amplitude and phase calibrations for each of the eight loudspeakers were necessary. After the calibration was done the calibrated data for each loudspeaker system was incorporated into the control program. In this procedure the corrected phase lag could be extrapolated from each of the eight loudspeaker systems during the control process.

3.2.2 Forcing Conditions

The objective in setting the forcing level is to produce significant changes in the mean flow. A clearly defined forcing level is crucial in evaluating the performance of a

certain control method. Unfortunately, although it is important, there seems to be no single agreed upon way to define the forcing level. Owing to this difficulty, rather arbitrary definitions were employed by previous researchers, as was discussed in section 2.3.2.

In the present study the forcing level is defined as a function of u'_f/U_0 at the location of Z/D = 0.5, R = 0.4. The forcing level was measured with the jet flow on. The loudspeakers were turned on consecutively with a hot wire placed at the corresponding location indicated above.

There are several reasons for choosing such a definition:

1. As documented later in this chapter, the instability modes did not amplify below Z/D = 0.5 at the frequency studied (f = 180 Hz). Therefore, the excitation level measured at Z/D = 0.5 should be close to the forcing level measured at the nozzle exit. The measured difference was within 15%.
2. The location chosen made it much easier for automated calibration, since the hot wire probe can be moved freely at this plane without any interference. Due to the large amount of work involved in the calibration procedure, automation was essential.
3. Modes 1 and ±2 excitations were very sensitive to the excitation level and phase shifting. A variation of 10 % in excitation level or 5^0 in phase shift would invalidate the measured results. As a consequence the measured results for these modes were, in effect a test for the validity of the calibration method.

To excite a spatial mode of a positive wavenumber m (clockwise moving) and angular frequency ω, the periodic time series sent to any individual speaker located at azimuthal angle γ is $A_1=A\sin(m\gamma + \omega t + \phi_1)$. Here ϕ_1 is an arbitrary phase shift. The opposite-going and equal-amplitude mode with wavenumber -m is then by the periodic function $A_2=A\sin(-m\gamma + \omega t + \phi_2)$. The addition of these two periodic functions yields $A=2A_m\sin(\omega t + \frac{1}{2}(\phi_1+\phi_2)\cos(m\gamma + \frac{1}{2}(\phi_1+\phi_2))$. Therefore, to produce equal and opposite helical modes with azimuthal wavenumber ±m and frequency ω, each speaker operates

with a periodic input $\sin(\omega t + \frac{1}{2}(\phi_1 + \phi_2))$, and amplitude determined by its azimuthal position according to $\cos(m\gamma + \frac{1}{2}(\phi_1+\phi_2))$. With 8 speakers it is possible to excite helical modes with azimuthal wavenumbers up to m = ± 4 (i.e., every other speaker is 180° apart in phase).

3.2.3 Data Reduction

Decomposition of phase-locked data by discrete Fourier transform

One of the parameters used to describe the response of the jet to its excitation is the spatial distribution of phase-averaged velocity. Like any other physical quantity, it can also be depicted in the frequency domain and its corresponding spatial domain where it is specified by giving its amplitude F(f, ϕ) (generally a complex number which includes phase also) as a function of frequency and spatial mode.

In data processing, when the Discrete Fourier Transform method (DFT) is employed it is computed with the Fast Fourier Transform (FFT) algorithm which is much faster than to compute the DFT directly.

The phase-averaged velocity in its Fourier form defined over a two-dimensional grid $0 \le n \le N_1 - 1, 0 \le m \le N_2 - 1$ is expressed as:

$$F(m,n) = \sum_{m=0}^{N_2-1} \sum_{n=0}^{N_1-1} \exp(2\pi i t m / N_1) \exp(2\pi i \phi n / N_2) u(t,\phi) \qquad (3.2.1)$$

where m stands for the spatial mode and n stands for the frequency harmonics. In the standing wave case $m = |m_+| + |m_-|$

Flow distortion

In standing wave mode excitation, the distortion of the mean flow is expressed in terms of contours of mean velocity in jet cross-sections at various streamwise locations.

At a certain streamwise location, a velocity level can be derived from the velocity contour and its radial intercepts R_i can be acquired. The spatial position of the particular level can be expressed as:

$$R(\phi) = R_0 + \sum_{m=1}^{4}\left[a_m \cos(m\phi) + b_m \sin(m\phi)\right] \qquad (3.2.2)$$

the superscript above the summation symbol stands for mode m = 4 which is the highest mode that could be acquired without getting aliasing.

The coefficients a_m and b_m are determined from the measured radial intercepts R_i according to

$$\begin{Bmatrix} a_m \\ b_m \end{Bmatrix} = \frac{2}{n}\sum_{i=0}^{n-1} R_i \begin{Bmatrix} \cos(im\pi / n) \\ \sin(im\pi / n) \end{Bmatrix} \qquad (3.2.3)$$

The superscript above the summation symbol stands for the number of excitation sources employed.

The modulus $c_m = \left(a_m^2 + b_m^2\right)^{\frac{1}{2}}$ reflects the contributions of each mode to the distortion of the mean velocity profile.

Flow entrainment calculation

Enhanced entrainment is a more relevant measure of mixing than the velocity contour measurement. Since the flow can be considered incompressible the entrainment of ambient fluid was measured using the volumetric flow rate Q. The integrated volumetric flow flux Q, truncated at $R_{0.1}$, the radius corresponding to U/U_j=0.1, is defined as:

$$Q = \int_0^{R_{0.1}} \int_0^{2\pi} U(r,\phi)\, d\phi\, r\, dr \qquad (3.2.4)$$

The volumetric flow flux was normalized by the exit conditions Q_0 defined as:

$$Q_0 = \frac{1}{4}\pi D^2 U_j \qquad (3.2.5)$$

The fraction of entrained flow at each streamwise station was defined as $(Q-Q_0)/Q_0$.

Phase speed and amplification rate measurements

The phase speed calculation in theoretical or numerical linear instability analysis is straight forward: $U_p = \lambda \times f$. In experimental measurement, the phase speed has to be determined indirectly.

There are two methods to measure phase speed. The first, suggested by Chan (1974), employs a microphone as the sensor. In his experiment the pressure signals from the microphone were fed into narrow-band filters slaved to the forcing frequency. At each position of the traversing probes, the filtered signals were then used to drive the vertical displacement of an oscilloscope. The periodic signal from the oscillator was converted by a stroboscope unit into timing spikes to trigger the oscilloscope intensity modulation at the required phase. Thus, the signal oscillating about vertically would be lit up as a bright spot only at the time triggered by the stroboscope. The probes were then moved to another position, and the process was repeated until a continuous trace was obtained. The displayed trace reflects the spatial variation of the pressure signal at a fixed phase, and the wavelength can thus be obtained. The distance between the second and the fourth zero crossings of the wave form was taken as the average value of the wavelength. The disadvantage of this method is its low spatial resolution and its inability to measure the detailed phase speed variation along the streamwise direction.

The second method was introduced by Corke and Kusek (1992). In this method, the phase variation of the excitation signal is measured along the streamwise direction by cross correlating the well-defined source signal and the sensor signal. The slope of the phase line is proportional to the excited wavelength. With known excitation frequency and wavelength, the phase speed can be calculated.

The amplification rate $-\alpha_i\theta$ is the imaginary part of a complex number which also cannot be measured directly. However, by examining its definition:

$$u / Uj = A(r)\exp[i(\alpha z - \beta t + m\phi)] + (*)$$

taking the natural logarithm of both sides yields:

$$\ln(u / Uj) = \ln[A(r)] + i(\alpha z - \beta t + m\phi) + \ln(*)$$

then

$$\frac{d}{dz}[\ln(u / Uj)] = i\alpha_i + \overline{i\alpha_i} = -2\alpha_i$$

and non-dimensionalizing

$$-\alpha_i\theta = \frac{1}{2}\frac{d}{d(z/\theta)}\ln(u / Uj) \qquad (3.2.6)$$

where u/U_j can be measured using the hot wire. In the above equation u represent the perturbation at a particular frequency. Consequently, $u = u'_f$. The acquisition of u'_f must be obtained via inverse Fourier Transformation.

3.3 Flow Characterization and Spatial Mode Control

The study of a circular jet with a well-defined exit velocity profile and a low turbulence level has a twofold importance. First, comparisons between experimental and theoretical results, between this experiment and experiments done in other laboratories where the nozzles are usually circular and velocity profiles top hat can be made. Second, the circular nozzle is the most basic and suitable nozzle geometry to study the spatial mode control methodology since the additional non-circular geometry need not be considered.

The evolution of a planar mixing layer can be described by a single velocity scale and a single lengthscale, the momentum thickness θ, respectively. In a jet where the flow is fully sheared at the exit of the nozzle, a single velocity scale and a single lengthscale, the jet diameter D, are also enough to describe the jet evolution. In the circular jet used in this experiment there exists an axisymmetric mixing layer in the near field which is constricted by the diameter of the jet column. This constriction introduces the additional

lengthscale $R_{1/2}$, permitting the evolution of an infinite number of discrete helical instability modes. The additional length scale $R_{1/2}$, the lengthscale θ, the phase velocity of the disturbance U_p and the disturbance frequency f are the main independent parameters which need to be defined. In addition, characterization of the predominant frequency of the disturbance (the most amplified frequency f_m in the asymmetric mixing layer), the amplification rate $-\alpha/\theta$ in the near field and the preferred modes at end of the potential core are also essential.

In the near flow field, the most important length-scale is the non-dimensional value of $R_{1/2} / \theta$. Its significance can be appreciated by recalling that, in the two-dimensional mixing layer, a given ratio of θ/λ determines uniquely the solution for an amplified mode. In the axisymmetric case, a whole family of solutions depending on the parameter $R_{1/2} / \theta$ exists, Michalke & Herman (1982).

However, the parameter $R_{1/2} / \theta$ is only important in the very near region of the jet where the shear layer is thin and the momentum thickness θ small, typically before z/D=0.5. In this chapter the focus is on the far field where the jet diameter is more of concern. Therefore, the lengthscale D will be used most.

3.3.1 The Predominant Instability Frequencies in the Axisymmetric Jet

One of the major concerns of active control is to determine the preferred mode or the jet column instability. Since the frequency of the local instability changes along the streamwise direction, determination of the preferred mode is essential for jet control. The purpose of this section is to address this issue.

Before examining the frequency domain, the time mean behavior of the jet is discussed first, since it has been agreed that the instability frequency of the jet can be determined using linear stability analysis over the time mean velocity results, Michalke (1965).

The center line velocity, the momentum thickness and the jet radius for unexcited case are shown in Figure 3.3.1. As seen from the center line velocity graph, Figure 3.3.1.b, the length of the potential core is approximately 4 diameters. The velocity in the potential core is 20 m/s. This corresponds to a $Re_D = U_cD/\nu \cong 3.4\times10^4$. Also seen in Figure 3.3.1c (the momentum thickness curve) is that the mixing layer is almost parallel near the nozzle ($Z/D \leq 0.5$). This pattern shows that the momentum thickness changes relatively slowly close to the nozzle and the parallel flow assumption is valid over this region. After this region the momentum thickness spreads rapidly ($1 \leq Z/D \leq 4$). As further support for this flow behavior is the variation of the ratio $R_{\frac{1}{2}}$ which increases steeply after Z/D = 0.5, Figure 3.3.1 a.

Mean velocity profiles normalized by the local velocity of the jet on the centerline (U_c) are plotted versus $(r - R_{\frac{1}{2}}) / \theta$ for several downstream locations in Figure 3.3.2. The solid lines describe Michalke's profile 2 (1989) with minor modifications that have the form:

$$U/Uc = 0.5\{1 + \tanh[b_2(R/r - r/R)]\} \quad where \quad b_2 = 3.0 \times 0.5 \times R / \theta \qquad (3.3.1)$$

As seen, the experimental velocity data collapsed at each streamwise location and matched the Michalke's profile. However, it can be noted that the farther away from the nozzle, the less accurate Michalke's profile is. The velocity profiles are also not self-similar since θ does not increase linearly with Z (Figure 3.3.1).

Linear stability analysis was applied to the above velocity profile equation for modes 0 and 1 at z/D locations of 0.5, 1, 2, 3 using the code of Huang and Brown (1994). The dimensionless amplification rates $-\alpha_i\theta$ were calculated as a function of the dimensionless frequency $2\pi f\theta/U_c$ for the above streamwise locations as shown in Figure 3.3.3. Shown in Figure 3.3.4 are the experimental data of the normalized fluctuation amplitude, u'_{int} / U_j at location z/D = 0.5. Its relationship with the amplification rate was discussed in section 3.2.3. The figures demonstrate that linear instability theory predicts the streamwise amplification rate very well. Typically, at z/D = 0.5, the linear instability

theory predicts a growth rate of 0.069 at $\omega = 0.12$, while the measured growth rate is about 0.065, at $\omega = 0.128$. These results also agree with Cohen and Wygnanski's (1987), although different mean velocity profiles were assumed. From the above analysis it is obvious that the linear instability theory is able to predict the behavior of the jet with a top hat velocity profile at the nozzle exit. Moreover, the linear instability theory can be used to test the flow conditions of a newly built jet facility, as in the current case, to verify its validity.

The frequency domain analysis is discussed next. As mentioned in Chapter 1, the instability frequencies in a jet can be best determined by artificial forcing at a single frequency at a time. This method was employed in the experiment introduced in this section.

Figure 3.3.5 a and b show the experimental data of u'_{int} / U_j versus z/D in the near field (z/D<=0.5) where parallel flow dominates. The flow was excited using the plenum chamber loudspeaker at a excitation level of 1.0% of U_0 for f > 1000 Hz and 2.5% of U_0 for f ≤1000 Hz. Note that the most amplified frequency peaks at about 2080 Hz at the location z/D = 0.25 (Figure 3.3.5b). At the location z/D = 0.5 it peaks at about the same frequency 2010 Hz (Figure 3.3.5 b), while another peak is observed at a frequency of 860 Hz. As mentioned above, different excitation amplitudes were employed, hence, the amplitude below and above 1000 Hz can not be compared. However, it is still valid to state that the amplification amplitude decreases along the streamwise direction and it decreases very sharply with decreasing frequency. As seen in Figure 3.3.5.a, the amplitude decreases approximately five fold as the frequency drops from 1000 Hz to 200 Hz.

Shown in Figure 3.3.6 are the experimental data u'_{int} / U_j versus z/D over the streamwise interval of $0.1 \leq z/D \leq 4$. Similar to Figure 3.3.5, decreasing the excitation frequency causes the flow instability to peak farther downstream with a much lower amplitude. At z/D = 4 the instability peaks at about 300 Hz and any excitations below

160 Hz (St. = 0.2) will not amplify at all. Also seen is that the amplitude peaking of u'_{int} / U_j does not change very much between z/D= 2 to 4.

An examination of figures 3.3.5 and 3.3.6 reveals that the local most amplified frequency shifts to lower values in a discontinuous way. For example, in the range 0.25<z/D<0.5 the most amplified frequency is about 2050 Hz (Figure 3.3.5b), while in the range of 2<z/D<4 it is about 315 Hz (Figure 3.3.6). The former range corresponds to the instabilities in the axisymmetric mixing layer and the later to the preferred mode. This observation indicates that the jet behaves very differently in the region close to the nozzle where parallel flow dominates (z/D<0.5) than in the region towards the end of potential core (2<z/D<4) where the shear flow is much thicker.

Results were shown that when using a higher excitation level under 500 Hz the position of the maximum disturbance decreases. Typically at 330 Hz, when the excitation level changes from 2.5% to 5% of U_0 the position of the peaking moves from z/D=2 down to z/D<1. This showed that a higher amplitude of excitation results in a faster saturation, which leads to amplitude peaking closer to the nozzle.

An analysis of the evolution of the flow turbulence using turbulent fluctuations u' / U_j as a function of frequency is shown in Figure 3.3.7. Here the turbulent fluctuations is shown along the axial and radial directions for several frequencies. Shown are cases of f=160, 235, 400 and 1000 Hz. The general trends described in Figure 3.3.5 and 3.3.6 are clearly reproduced in Figure 3.3.7. A lower frequency excitation results in a lower amplification that peaks farther away from the nozzle. Most noticeable is the fact that the change of the width of the shear layer along the streamwise direction are not large, compared among the four frequencies examined. This trend further demonstrates that frequency modulation is not an effective way to promote jet expansion.

The behavior of the velocity power spectrum across the shear layer and in the streamwise direction are shown in Figure 3.3.8. Shown in Figure 3.3.8a is the radial spectrum for a 400 Hz excitation at z/D = 2, where the natural frequency peaks at 330 Hz (refer to Figure 3.3.6). As seen, along radial direction, the turbulent level is highest at

about R=0.5 except at f = 400 Hz where the amplitude has the largest value near the potential core and lowest at R=0.5. The measurements along the streamwise direction are shown in Figure 3.3.8b. At each z/D location the maximum power spectrum line was chosen among the spectrum lines acquired along the radial direction. As seen, the amplitude of the excitation frequency increases in the range for z/D < 2; peaks at about z/D = 2; it then decreases for z/D > 2. The power spectrum for 1000 Hz excitation behaves a little differently. Measurements along the radial direction, Figure 3.3.8.c (z/D = 0.2) and 3.3.8d (z/D = 2), show that the 1000 Hz excitation exhibits a very strong fundamental and first harmonics in the very near flow field. Further downstream (z/D = 2) subharmonics appear, indicating the occurrence of vortex merging. As the fundamental frequency becomes weaker along the streamwise direction, the sub-harmonics become weaker too and finally disappear.

3.3.2 The Jet Response to Spatial Mode Forcing

In this study, spatial mode forcing was applied at 180 Hz excitation. As seen both from the linear instability analysis data, Figure 3.3.4, and experimental data, Figures 3.3.6-8, this frequency is lower than the preferred mode (315 Hz) defined at z/D = 4. Although the amplitude was small and the amplification rate almost zero, good results were achieved under this frequency (180 Hz) excitation.

The strong evidence that the most amplified frequency in the axisymmetric mixing layer is not the predominant frequency in the jet justifies that it should not be used as a reference parameter in jet control. The predominant frequency, termed as the preferred mode in the axisymmetric jet, is the most amplified frequency near the end of potential core. This frequency, was shown to be 315 Hz, Figure 3.3.6 and 7. Moreover, even the preferred mode, as evidenced above, is not the controlling factor in spatial mode excitation. Since the preferred mode has an amplification rate that is too low to be effectively utilized, using preferred mode excitation alone is not enough. Other

mechanisms have to be employed. This topic is discussed further in the next two sections.

In this section results of the spatial mode forcing studies are presented and discussed for mode 0, 1, ±1 and ±2 excitations.

Ideally, spatial modes can be generated continuously around the azimuthal direction. The waveforms of modes 0, 1 and ±1 generated in this manner are shown in Figure 3.3.9. The horizontal axes represent the time and azimuthal direction. The vertical axis represents the excitation amplitude, normalized by the maximum signal output. As shown, at any instant in time the excitation amplitude does not change along the azimuthal direction for m = 0 (Figure 3.3.9 a), while for the m=1 case (Figure 3.3.9 b), the amplitude of the generated signal changes in a sinusoidal fashion along both time and azimuthal directions.

Special attention should paid to mode ±1 excitation for the following reasons. First, this mode can generate an elliptic jet which has been considered to have the largest expansion rates, Gutmark and Ho (1982). Second, as will be shown later in the discussion of the dynamic mode control method, m= ±1 mode serves as the primary control mode.

Shown in Figure 3.3.9 c is the waveform for mode m=±1. As can be seen along the time axis, the waveform is sine shaped. Along the azimuthal direction, the waveform is rather complicated, however, several features can be noted.

1. This curve is symmetric with respect to the 180^0 azimuthal coordinate.
2. The excitation amplitude is zero alone the radial direction at 90^0 and 270^0.
3. At every time instance, the phase is always opposite at the azimuthal positions of 180^0 and the position of 0^0 or 360^0. Typically, at the time axis of 270^0, the amplitude at azimuthal position 180^0 is +1 while at 0^0 or 360^0 is -1.

The above features are very helpful in the analysis of the behavior of standing wave excitation. In practice, the waveforms are generated continuously along the time axis but discontinuously along the azimuthal direction. In the current experimental setup,

without phase offsetting, eight loudspeakers were spaced azimuthally separated by an angle of $\frac{\pi}{4}$ as shown in Figure 3.3.9 d. Under this arrangement, loudspeaker output signal at positions 0, 1 and 7 is always 180^0 out of phase with their counter part at positions 3, 4 and 5. This out of phase signal results in a piston like motion of forcing to the jet. Obviously, excitations like this would "push" the jet back and forth in the direction of actuation. It will be shown later that it is this kind of motion and not the amplification of the small perturbations that plays a major role in jet expansion. The discussion of mode $m = \pm 2$ is quite similar and will not be addressed here.

Phase speed

The phase speed was investigated in order to understand the development of flow structures and the possible interactions between different modes. The phase speed describes the translation velocity of vortical structures. Since only those vortices that have the same phase speed have the opportunity to interact, phase speed measurement is important for evaluating the possibility and mechanism of those interactions.

Shown in Figure 3.3.10 a, b and c are the phase speeds of modes 0, 1 and ±1 for various excitation frequencies.

As seen in Figure 3.3.10a for mode = 0 and z/D>2, excitation at a frequency of 160 Hz has a normalized phase speed close to 0.8. For frequencies between 315 to 550 Hz and locations 2<z/D<4 the eddies are convected downstream at a velocity of 0.65 to 0.7 U_j. This convection speed is higher than the numerical result of 0.5 to 0.65 U_j given by Peterson (1978), Bradshaw (1964) and Davies, Fisher and Barratt (1963). The discrepancies of the convection speed may due to a higher excitation level of the present experiment, about 2.5% compared with the numerical results of the above mentioned authors, which were less than 1%. The small amplitude excitation was difficult to carry out in the current experiment because of the quality of the loudspeakers chosen. Moreover, the 2.5% excitation level had been employed through this experiment and was

considered necessary for carrying out spatial mode control studies. Phase speed results acquired under this excitation level were, therefore, essential.

The normalized phase speeds for m = 1 are shown in Figure 3.3.10b. Noticeably is the normalize phase speed at 160 Hz that equals 0.78 at z/D = 4. This normalize phase speed matches the one for m = 0 at the same location. The identical phase speed are prerequisite conditions for resonant interactions to occur. In modes 0 and 1 cases, only the 160 Hz frequency excitation satisfies such conditions.

When two modes with identical mode number but opposite signs were excited simultaneously, both of the excited modes satisfy the resonant condition. Shown in Figure 3.3.10 c is the normalized phase speed of mode ±1 excitation. A distinctive feature of this figure is that for 160 Hz excitation the normalized phase speed decreases from 0.7 at z/D = 0.5 to about 0.3 at z/D = 4, while for other excitation frequencies the normalized phase speeds are all above 0.6. A decreasing phase speed at 160 Hz implies a corresponding slow down of the flow structure. This fact is thought to be very important for interactions among flow structures to occur and plays a major role in jet expansion in the far field. This mechanism will be discussed in more detail in the next section.

Based on the data shown in Figure 3.3.10, the wavelength of the excited frequency along the streamwise direction can be calculated, since wavelength equals phase velocity divided by frequency. For instance, mode ±1 excitation at 180 Hz has a normalized phase speed of 0.5 at z/D = 2, for which the wavelength at that location is about 2 diameters of the jet nozzle.

Mode spectra

The mode spectra were used for measuring the evolution of the large structures induced by forcing. Radial profiles of the modulus $|F_{mn}|$ along the streamwise direction, computed according to eqn. (3.1.3), are shown in Figure 3.3.11 for m=0, Figure 3.3.12 for m=1, and Figure 3.3.13 for m=±1 excitations. The radial axes are normalized by ($R_{0.9}$-$R_{0.2}$). The truncation points, based on the measured mean velocity profiles, are indicated

by the subscripts, e.g., at U/U_j=0.9 and 0.2. Such truncation is considered suitable for hot wire measurements. In each case the frequency of the fundamental mode is 180 Hz which is the forcing frequency.

Several observations can be made based on these figures:

1. The modulus decreases along the streamwise direction in all cases. However, for m=1 excitation, m=1 modulus, one may observe that there is an amplitude increase from 0.4 to 0.5 at $0.5<z/D<1.5$. After $z/D<1.5$ the amplitude dropped sharply - from 0.5 to 0.3 in a very short distance ($1.5<z/D<2.0$).
2. The amplitudes of $|F_{mn}|$ other than fundamental spatial mode are only secondary and in most cases are significantly smaller (cases m=1 and ±1).
3. The maximum $|F_{mn}|/U_j$ in each figure peaks at the range of $0<(r-R_{0.5})/(R_{0.9}-R_{0.2})<0.1$ - - the outer side of the shear layer. The maximum amplitude of mode ±1 is the highest with an amplitude of 0.75.
4. Towards the end of the potential core (z/D = 4) the amplitudes of all moduli are negligible and comparable to the background noise.

The existence of multiple modes in a single mode excitation is due to the imperfections of the experimental setup. For instance, instead of a continuous array of sound sources along the circumference, only eight loudspeakers were employed. The discrete sound source setup can result in velocity contour distortions. Moreover, even after careful calibration phase shifting cannot be completely eliminated. The phase shifting also generates undesirable modes.

Growth of amplification under excitation

The streamwise growth in amplitudes for m = 0, 1 and ±1 are shown in Figure 3.3.14 for excitation frequencies of 180, 235, 315, 400 and 550 Hz. As described in section 3.2.3, the derivative of the curves in this figure is proportional to the amplification rate.

The streamwise growth in amplitude for m=0 shown in Figure 3.3.14a has the lowest decrease in rate of amplification as compared to other modes. However, in the case of 235 Hz excitation, the amplitude has a slight increase in the range of $0.5<z/D<3$.

In Figure 3.3.14b for m = 1, the amplitude for all the excitation frequencies is declining.

In Figure 3.3.14c for m=±1, the amplitudes (except the case of 160 Hz) also decrease along the streamwise direction.

The decrease in growth of the amplitude has two implications: first, the excitation frequencies are going to lose their influence after a certain streamwise location; second, the control mechanisms that lead to good control of the jet (for instance the case of m=±1) are not dependent on the amplification resulting from the temporal perturbation.

3.3.3 Mean Iso-velocity Contours

As was mentioned in section 3.3.2, under $m = \pm 1$ excitation the generated waves are out of phase at the azimuthal displacement location numbered 0 and 4. As a result, the amplitude of the jet disturbance is more than doubled. The disturbance eventually results in non-linear expansion of the jet at a particular azimuthal direction, at locations down stream of the end of the potential core. The response of jet expansion to spatial mode excitation mechanism will be discussed later in this section after some of the issues affecting the spatial mode control are clarified

In this section, the issue of the resonant conditions for spatial mode forcing is examined first, 3-D views of the iso-velocity contours is given next, followed by an analysis of the effects of the excitation amplitude and ends with a discussion of jet expansion to spatial mode excitation.

Resonant conditions for spatial mode forcing

Cohen & Wygnanski (1987) showed through analysis that if two wavetrains are degenerate with spinning mode numbers +m and -m, the resonant condition can be expressed by the following interaction equation:

$$\hat{u}_3 = A_3(r,z)e^{-2\alpha_i x}\cos(2m\phi) \qquad 3.3.2$$

where $\hat{u}_3$ is the resulting perturbation and $|A_3(r,z)|$ the amplitude. Physically, the superposition of the two wavetrains produces a standing wave pattern. The resulting amplitude of the velocity varies azimuthally according to $\cos(2m\phi)$.

Guided by the above arguments, Figure 3.3.15 demonstrates the general behavior of the standing wave modes. The curve is calculated by eqn. 3.3.2 with an arbitrarily defined amplitude term. Figure 3.3.15 case (1) depict the shape of iso-velocity contours for spatial modes excitation: m=±0.5, ±1, ±1.5, ±2 for a constant excitation amplitude. The dashed line indicates the nozzle size. Most noticeable, compared with the nozzle geometry, are the protrusion at the corners (polygonal angles) which increase with increasing mode number. The number of protrusions equals the mode number divided by 0.5. In mode = ±0.5 case, the protrusion is on the right hand side while on the left hand side the shape of the velocity profile could be described as having an intrusion. For mode = ±1, there are two protrusions and the resulting profile is elliptic. Similarly for mode = ±1.5 the profile is triangular and for mode = ±2 nearly rectangular. Figure 3.3.15 case (2) shows the influence of excitation amplitude under m=±1 excitation. At an amplitude of 0.1 the velocity profile looks perfectly elliptical while for 0.2 it looks like a peanut. Further increase up to 0.8 lead to a velocity profile that is even more distorted.

Through the above discussion, it is clear that the controlling factors that determine the resulting velocity profile include not only the spatial mode number but also the excitation amplitude. For instance, it is incorrect to assume that the velocity profile of m = ±1 excitation is elliptic, since, as shown above, some other shapes result for different higher excitation amplitude.

Also, one should notice in Figure 3.3.15 that for m = ±1 the major axis of the velocity contour is aligned with the y axis. Adjusting the initial spatial phase angle may, therefore, result in reorienting the direction of the major axis while keeping its center position unchanged. The possibilities of utilizing this phenomenon were investigated and are described in section 3.4.

3-D view

Shown in Figure 3.3.16 a-c are the three dimensional, U/Uj = 0.5 iso-velocity contours of the excited jet for modes 0, 1 and ±1 respectively. The range of the measured streamwise location is $0.5 \leq z/D \leq 15$. Also given are the corresponding 2-D velocity contours at 4 streamwise locations z/D = 0.5, 4, 8, 15, where the contour outer boundaries are also U/Uj=0.5. The flow velocity was 20 m/s corresponding to a Reynolds number of 3.4×10^4 based on the nozzle diameter. The excitation frequency was 180 Hz, and the excitation amplitude was 2.5% of the nozzle exit velocity. The wavelength of the excited modes, as discussed earlier about phase speed in this section, ranged from about z/D = 2 to 3.5 depending on the mode excited. The measuring stations along the streamwise directions were about a quarter to half wavelength apart.

As seen from Figure 3.3.16 a, b for m = 0 and 1 excitation, the contours remain circular along the streamwise direction. This observation agrees with the prediction that single mode excitation does not alter the velocity contour (Cohen and Wygnanski (1987). The flow behaves quite differently when subject to m = ±1 excitation. Most noticeable is the fact that the excited flow iso-velocity contours do not exhibit an elliptic shape until after z/D = 4; the larger expansion actually happens after that station. Since the potential core ends at about z/D = 4 and the excited instability waves do not amplify at all after z/D = 4, the large expansion of jet after that location implies the existence of a new mechanism that controls the jet expansion. This new mechanism is elaborated upon later in the part: Jet expansion to spatial mode excitation of this section.

The large expansion after z/D = 4 is demonstrated in Figure 3.3.17 using the integrated volume flux Q. The integrations were truncated at $R_{0.1}$ and the volume flux was normalized by the flux at the exit of the nozzle - $(Q-Q_0)/Q_0$. As seen, the curve for f = 0, m = 0, m = 1 and m = ±1 are almost identical until z/D = 4, after which the m = 1 and m = ±1 deviate from the others and have a much larger increase in value. Particularly in the m = ±1 case, the entrainment ratio is about twice that of the unexcited case, while for m = 0, the entrainment ratio approaches that of the unexcited case in the far field (z/D>14).

Effects of excitation amplitude

The effects of excitation amplitude on the velocity contours were examined for m=±1 excitation. The excitation levels used were 1%, 2.5%, 5% and 10% of U_0. The iso-velocity contour lines of U/U_j = 0.5 are shown in Figure 3.3.18. Some interesting phenomena can be observed.

1. Under all excitation levels, the expansions of the velocity contour are larger than the unexcited case.
2. A comparison of all cases, at Z/D = 12, is shown in Figure 3.3.18. One can see that there is an excitation threshold at 2.5% excitation, above which the sizes of the velocity contours are almost the same. This may suggests the existence of a saturation excitation level.
3. The size of the velocity contour increases with excitation level under all conditions for streamwise Z/D<4. Beyond this location the differences are less obvious if the excitation level is above 2.5%.

Figure 3.3.19 shows the flow entrainment ratio plots corresponding to the data sets of Figure 3.3.18. As seen, the entrainment ratio does increase with increasing amplitude of excitation. Most noticeable is the sharp increase in entrainment ratio for 5% excitation after z/D = 4. The highest entrainment ratio is achieved for 5% excitation, which is about twice that of the unexcited case. However, contrary to the picture depicted

by the velocity contour in Figure 3.3.18 a further increase in the excitation amplitude to 10% causes the flow entrainment ratio to decrease.

By the above analysis it can be concluded that, there indeed exists a threshold of the excitation amplitude under which far field control is not effective. Based on velocity contours and entrainment rate this threshold is 2.5%.

Jet expansion to spatial mode excitation

It had been shown by Cohen and Wygnanski (1987) and was further proved in Chapter 2 that single integer mode excitations are independent of the azimuthal coordinate ϕ. Therefore, the azimuthal structure of the mean field of an axisymmetric jet remains axisymmetric when the jet is subjected to a single integer mode excitation. Also, by generating standing waves the resulting mean velocity contour varied according to $\cos(2m\phi)$. In the case of $m = \pm 1$ case it had an elliptic shape.

To further verify the above arguments, the experimental results of phase mean velocity data were analyzed using eqn. 3.2.3. Using this simple mathematical model the distortion of the mean flow can be qualified. The modulus $c_m = \left(a_m^2 + b_m^2\right)^{\frac{1}{2}}$ of each Fourier coefficient (m = 0, 1, 2, 3) were used to describe the distortion of the mean jet flow. For example, the c_2 coefficient had the largest value among the moduli for the interaction between mode +1 and -1, which corresponded to a $\cos(2\phi)$ distortion. Similarly for mode 1 excitation, c_1 had the largest value.

Figure 3.3.20 shows the mean flow of $u/U_j = 0.5$ contour distortion along the streamwise direction for m= 0, 1 and ±1 excitation. Each spectrum plot is normalized by $c_0 = \left(a_0^2 + b_0^2\right)^{\frac{1}{2}}$. The data sets are the same as for Figure 3.3.16. As seen, for m=0 excitation, Figure 3.3.20a, the modulus c_1/c_0 does not become predominant until after z/D = 7 where the potential core no longer exists and the helical mode prevails in the flow. For m=1 excitation in Figure 3.3.20b, the modulus c_1/c_0 of the excitation modes always

has the largest amplitude. Both figures indicate the predominant influence of the helical mode m = 1 downstream of the potential core. For the $m = \pm 1$ excitation, shown in Figure 3.3.20c, one notices the rapid rise of the c_2 coefficient in the axial range z/D < 7, followed by a leveling off. This means that the shape of the velocity contour is elliptic after that station. In contrast, before z/D < 2 c_2 has about the same amplitude as the other modes. This phenomenon indicates a circular shape of the velocity contour before z/D<2 since the distortion for modes larger than one are rather small. This is evidenced by the 2-D contour shown in Figure 3.3.16c where the contours are indeed circular in the near field and gradually become elliptic toward the far field.

The discussions of this chapter and Chapter 2 have shown that the standing wave excitation of m=±1 can achieve good flow entrainment and jet expansion. It has been argued by various authors (Cohen and Wygnanski (1987), Long and Perterson (1992), Corke and Kusek (1993) that the non-linear interactions of the instability waves play a major part in the jet distortion. While this is true in the near field, it may not fully explain the large expansion after the near field (z/D>4) as was observed in the $m = \pm 1$ case of this study. In order to further analyze the jet expansion mechanism, detailed measurements of phase mean velocity in the near and transitional flow field (0.5<z/D<8) were made using a fine data point grid in the streamwise direction (about 10% of the characteristic wavelength). Shown in Figures 3.3.21, 3.3.22, 3.3.23 and 3.3.24 are the phase mean velocity contours of U/U_j=0.5 for modes m= 0, 1, ±1 and ±2 excitations respectively. Each figure shows six different phases, 54^0 apart that animate the spatial growth of the phase mean velocity contour.

As seen, for the case of m=0, Figure 3.3.21, the growth of the perturbations in the streamwise direction is axisymmetric. The jet column does not have appreciable radial expansion with increasing streamwise distance. It is obvious that the symmetric pulsation of the jet column inhibits its growth. One can observe that as the jet develops with temporal phase angle, it contracts and expands reciprocally. Since the contraction part of

the jet constrains its expansion part from further expansion, the total jet column expansion is restrained.

In the case of m=1, Figure 3.3.22, it is interesting to note the twist-like distortions caused by the helical modes. The twist-like distortion is robust both in time and space. A three dimensional view of the jet structure looks like a spiral. Therefore, it may appear axisymmetric from one point of view and asymmetric from an orthogonal point of view (Yoda, 1992). However, a top view of the twist-like movement in the streamwise direction appears symmetric. Since the expansion is caused by the growth of the instability wave perturbations along the streamwise direction, a symmetric perturbation along the azimuthal direction constrains the jet expansion from any preferred direction so that the total expansion is restricted also.

The picture of $m = \pm 1$, Figure 3.3.23, looks quite different, (Video animation was able to convey this much better). Referring to Figure 3.3.9d and position number definition in section 3.3.2, one may see that the excitations of $m = \pm 1$ are symmetric from one side (parallel to location numbered 2 and 6, termed as "direction x") and asymmetric from the other side (that parallels the speakers numbered 0 to 4, termed as "direction y"). One may also notice the alternating appearance of bulges from either side of locations numbered 0 and 4 over direction y that are asymmetric if viewed from the top. The growth of bulges results in the swinging of the jet in the y direction. Particularly, one may notice that the bugles do not have much growth until after z/D = 4, where the potential core ends. After the potential core region the jet expands very rapidly while the bulges lose their identity. It is obvious that the potential core plays an important role in inhibiting the bulges on the both sides (over the direction y) from interacting with each other. The reader may also recall that the phase speed of the wave decreases rapidly after the potential core ends (Figure 3.3.10c). Therefore, the bulge that is located farther from the nozzle has a phase speed that is lower than the one that is closer to the nozzle. Evidently, in the near field the asymmetric structures are composed of bulges that are created alternately along the y direction. These bulges travel downstream with little

growth because the small amplification rate of the flow instability there. After the potential core ends the jet expands rapidly. It is considered that this rapid growth is the result of slowing down of the phase speed in that region. As each bulge reaches the end of the potential core and slows, it is pushed outward and later merges with the bulge following it. This causes very rapid outward jet expansion in a preferred direction (direction y in this example) that combines the non-linear interactions of both bulges during their coalescence.

Mode m=±2 is shown in Figure 3.3.24 to further verify the conclusions derived from $m = \pm 1$. A distinguishing feature of Figure 3.3.24 is the square shaped velocity contour that forms after the potential core ends - just as the theoretical analysis predicts (see Figure 3.3.15). Also seen in this figure are the bulges in the near filed that grow alternatively, similar to $m = \pm 1$, but in two directions (positions numbered 1 to 5 and 3 to 7) instead of one. In the near field, at any cross section, no two bulges coexist both in time and space. After the potential core, the bulges begin to merge with each other and lose their identity. The general observation that the jet expands more rapidly after the potential core and that the bulges grow parallel in streamwise direction in the near field, also applies to this case.

The general behavior observed from the $m = \pm 1$ case also applies to the case of $m = \pm 2$. Consequently, the conclusion can be drawn that the non-linear interactions generated by standing wave excitation actually happen after the potential core ends.

3.4 Dynamic Mode Control

The objective of this section is to introduce a new actuation scheme - The Dynamic Mode Control Method. This method is based on the results of static spatial modes. These results showed that the far field can be affected using proper mode excitation and that there are unique relationships between the mode excited and the velocity contour generated. This results had led to the dynamic mode proposal.

However, in order to introduce the concept of dynamic mode control another important observation has to be addressed first. This is discussed in next section.

3.4.1 Phase Offset Phenomenon

A distinguishing feature of the spatial mode m=±1 is its orientation maneuverability along the azimuthal direction by phase offset. This phenomenon has been observed by previous workers, Long and Peterson (1992). However, the phase offset phenomenon was introduced by them to avoid total cancellations in standing wave pattern at any particular speaker. For example, as shown in Figure 3.3.9d, when the relative phase offset of the loudspeakers is zero, the actuator numbered 2 and 6 would have zero output.

Long and Peterson (1992) have shown that varying the phase offset between actuators changes the polar orientation of the mean flow distortion. The change of orientation can be easily controlled and predicted. Using linear analysis it can be shown that the superposition of two spinning waves propagating along a non-dispersive mixing layer can be modeled as follows:

$$u=\frac{1}{2}A_{amp}e^{i(\alpha z+m\phi-\omega t-\psi_0)}+\frac{1}{2}A_{amp}e^{i(\alpha z-m\phi-\omega t)}+c.c.,$$

where ψ_0 is the phase offset. The longitudinal wave stress is

$$\overline{u^2}=\left|F_u^2\right|\left\{1+\cos\left[2m(\phi-\psi_0/2m\right]\right\}$$

The phase offset should result in a shift in the principal axis by the amount $\psi_0/2m$. This prediction was verified in this study as shown in Figure 3.4.1 for mode m=±1. When the phase offset ψ_0 is incremented in steps of $\frac{1}{2}\pi$ the principal axis will advance in steps of $\frac{1}{4}\pi$ as predicted.

3.4.2 The Proposal and Implementation of Dynamic Mode Control

The phase offsetting shown in the last section is controlled statically in time. However, since the phase offsetting can be well predicted it had prompted us to contemplate the possibility of controlling it dynamically. Three schemes are proposed in this section to examine this hypothesis.

A. Phase modulation

From Figure 3.4.1 it is seen that under proper excitation amplitude and zero phase offset, m=±1 excitation results in an elliptic shaped jet with the major axis aligned in the y direction of the figure. A change of phase offset will change the relative orientation of the jet while maintaining its elliptic shape. It is postulated that this kind of phenomenon (i.e., the shifting in orientation), would still exist when dynamically changing the phase offset. As a result the jet expansion angle in the far field may also change accordingly, since the phase offsetting in the near field and jet shape and expansion direction in the far field are uniquely related. As a consequence, improved far field control may be achieved.

Figure 3.4.2 shows a typical generated signal that controls the dynamic phase offsetting under $m = \pm 1$ excitation. One may notice the difference between this figure and Figure 3.3.9c ($m = \pm 1$ with zero phase offset). Along the time axis, the amplitude and phase of the wave form are modulated while in Figure 3.3.9c they are not. Also, the variations of the amplitude along the azimuthal direction are different in two respects. First, by phase-offsetting the amplitude does not completely cancel out at any particular azimuthal station. Second, the peak of the amplitude moves in the azimuthal direction as time evolves. As a result, although the physical positions of the actuators do not move, their spatial phase reference moves virtually in the clockwise direction. Consequently, the jet will experience a successive excitation that moves along the azimuthal direction.

Figure 3.4.3 shows the test results that had utilized the phase modulation method. The data was acquired at the z/D = 4 station, shown are the U/Uj=0.5 velocity contours. As seen, the jet does rotate in the azimuthal direction as the phase of the excited signal is

modulated in time. The velocity contours are, in general, still elliptic, although some distortions can be observed as in the case of temporal phase = 180^0. One can notice the hysteresis of the phase angle of the velocity contour caused by dynamic phase offsetting. For example, at phase zero the velocity contour shown in Figure 3.4.1 with static phase offset is aligned vertically, while in Figure 3.4.3 for the same phase there is roughly a 45^0 phase lag. Overall, the phase modulation performs as was postulated. The controlled input can manipulate the phase offset in the near field and make it complete the orientation shift in one phase modulation cycle. A key question, however, is whether the phase modulation mechanism affects the far field, an issue described in the following section.

Figure 3.4.4 shows the three-dimensional U/U_j=0.5 contours under controlled phase modulation. Shown are six pictures that depict different temporal phases 54^0 apart. As shown, the jet has a swirl-like motion. This motion is observable up to z/D = 12. The controllable region is considerably larger than for the static $m = \pm 1$ excitation shown in Figure 3.3.16 or 3.3.23, where the region is less than z/D = 4. The resulting velocity contour in the far field, where the phase between the excitation source and the flow decorrelates, becomes more circular instead of elliptic. Because of the rotation of the jet column in the near and transitional flow field, the area the jet covers in the far field is much larger. Using a different mechanism the extent of the controllable region to z/D>15 is examined, discussed next.

B. Switching modulation

The switching of axis is a typical phenomenon in non-circular jets, Ho & Gurmark (1987), Hussain & Husain (1989). A key disappointment of past studies was that although the application of spatial mode control to circular jet enabled the emulation of many characteristics of elliptic jets, including the major and minor axis ratio, it failed to produce the axes switching, a very important entrainment mechanism in non-circular jet.

A scheme was proposed in this study to create artificial axes switching. In this scheme the modes were dynamically changed from $m = \pm 1$ to m=0 with zero phase-offset and then back to $m = \pm 1$ with a 90^0 phase-offset.

Shown in Figure 3.4.5 are six images that depict different temporal phases, 54^0 apart. One can clearly see the axis switching. The jet expands alternatively on opposite orthogonal direction in the x-y plane. When the jet first expands in the near field (for instance the phase 108^0 picture) it grows very fast in one diagonal direction but almost none in the other, very similar to the behavior of static $m = \pm 1$. At about z/D=6 to 7 the jet starts to contract; at about z/D=8 it starts to expand again but in other diagonal direction. During the second expansion period, the jet expands rapidly in both orthogonal directions, creating a much larger jet cross sectional area at about z/D = 15. The distance required for expansion or contraction depends upon the time span that dynamic mode changes from $m = \pm 1$ to 0. With known phase speed, the switching position can be controlled. Therefore, one may control the length of either the expansion or the contraction part.

C. Spatial modes modulation

A third scheme for dynamic mode modulation was proposed making use of the unique properties of standing wave excitation. As discussed in section 3.2.4, standing wave excitation can generate velocity contours of different shapes, for example, m= ±1, elliptic; m= ±1.5, triangular and m= ±2, square. It is postulated that switching dynamically between standing wave modes will change the contour of the jet accordingly. For example, changing modes from m = ±1 to m = ±2 is postulated to result in a continuous change of the velocity contour from elliptic to square. This scheme was not tested during the course of the study, and will be examined at a later time.

3.4.3 Zone of Influence of the Spatial and Dynamic Spatial Mode Control

In this section an attempt is made to evaluate the zone of influence of spatial mode excitations. The organized fluctuation u" is defined as:

$$u'' / \overline{U}_m = \sqrt{\left(\overline{U}_p - \overline{U}_m\right)^2} / \overline{U}_m, \qquad (3.4.1)$$

where $\overline{U}_p$ is the phase mean velocity and $\overline{U}_m$ the time mean velocity. Physically, it describes the amount of fluctuations generated by a periodic excitation, and therefore, can be used to evaluate the region where the periodic excitation has an influence.

Shown in Figure 3.4.6 is the organized fluctuation contours for spatial mode excitations of 0, 1, ±1, ±2, and dynamic mode excitations using phase modulation, and switching modulation. As seen, the extent of the influenced region for dynamic mode excitations (Phase modulation and Switching modulation) is much larger than those of static spatial mode excitations. For example, the 20% fluctuation amplitude of the organized fluctuation u" is sustained up to z/D = 15 for switching modulation. This result shows that the phase of the excited jet is not decoralated to the excitation signal up to streamwise location of z/D = 15. However, the same amplitude for static spatial modulations is sustained only up to z/D < 3.5.

The results of measured organized fluctuation clearly show the advantages of using dynamic mode control method to control the far field of jet. The phenomenon of "phase decorralation", which is present in all excited jet to date, can be solved by the dynamic mode control method. Dynamic mode control exhibits mechanisms that enhance mixing typically found only in passive control and non-circular jet. The non circular jet can enhance mixing through both large and small scale structures. By simulating these passive control mechanisms with the dynamic mode control method, control over how and where the mixing occurs can be achieved. One can say that the dynamic control method is more flexible when compared to any former methods, using frequency and "static" spatial modes excitation. By proper manipulation, the dynamic control method can handle the global as well as the local mixing and expansion rates.

3.5 Discussion and Summary of Results

This chapter an investigation of the response of a circular jet to excitation has been presented. Specific topics covered are listed below. Those topics are:

1. An in-depth examination of the behavior of a circular jet with initial top hat velocity profile excited by spatial modes.

2. An analysis of the basic mechanism that governs far field control.

3. An evaluation of a new actuation scheme -- the dynamic mode control method.

It was found that static spatial mode control method could effectively be applied to a top hat circular jet. Large jet expansion, increased entrainment ratio and control over the far field were achieved.

The basic mechanism that produce large jet expansion in the far field is considered to be the non-linear interaction of the asymmetric structures that are generated in the near flow field. This observation agrees with conclusions of former investigators, but with a new understanding that the non-linear interaction mechanism does not become effective until after the potential core. The direction of the expansion can be easily predicted and the extent of the expansion controlled.

These results led to a new method for controlling the far field of jet -- the dynamic mode control method.

The dynamic mode control method includes three schemes: (1) Phase Modulation; (2) Switching Modulation; and (3) Spatial Mode Modulation. During the course of the study only the first two were implemented. The most important feature of this type of excitation is the enhanced control of the jet far field it offers compared with any other control methods. It is considered as a unique actuation scheme in jet control.

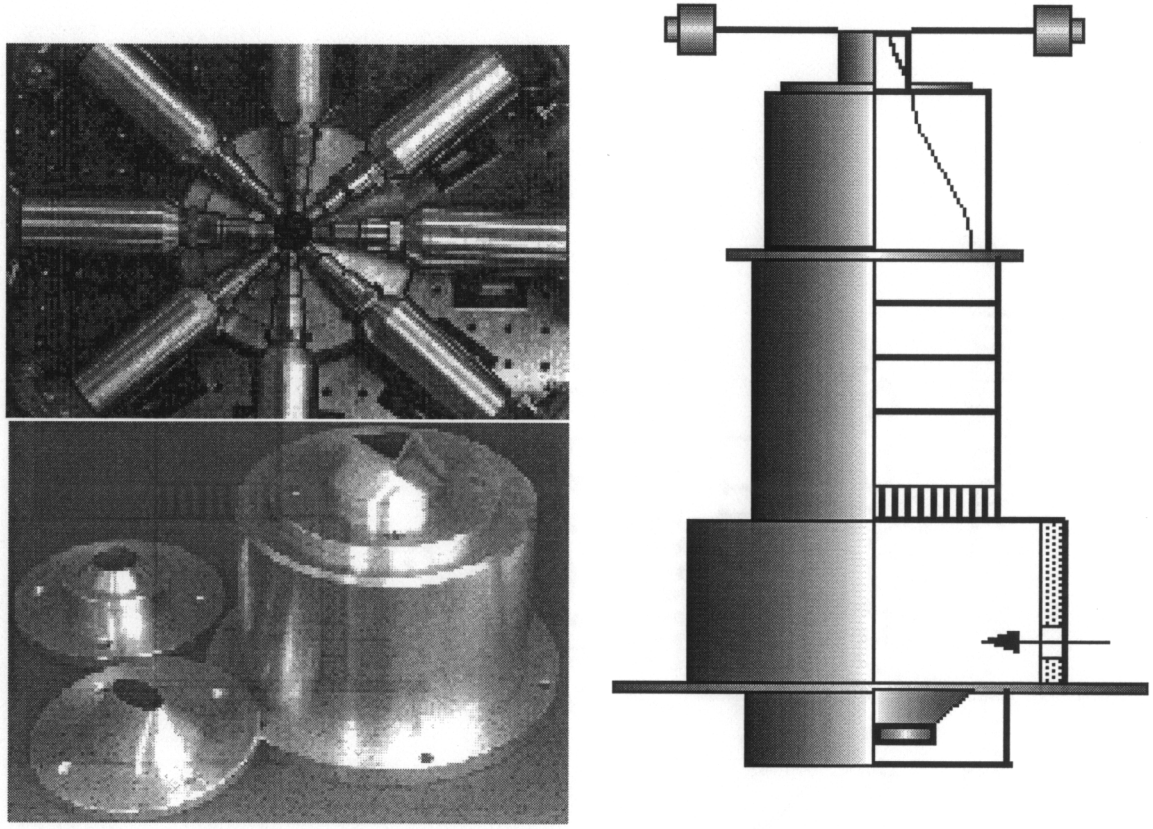

Figure 3.2.1 Schematic View of Jet Facility

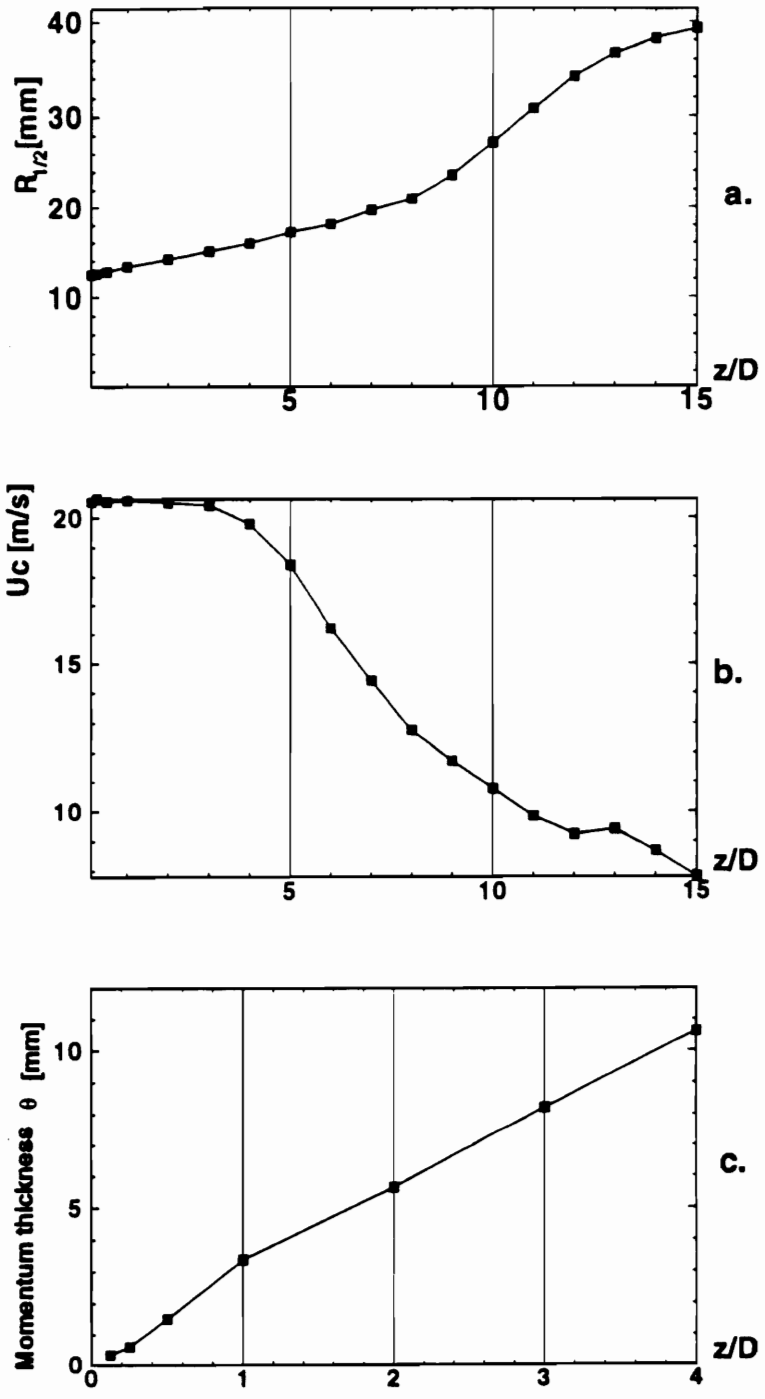

Figure 3.3.1 Streamwise variation of length and velocity scales: a. Jet radius (U=0.5 U_0); b. Centerline mean velocity; c. Momentum thickness

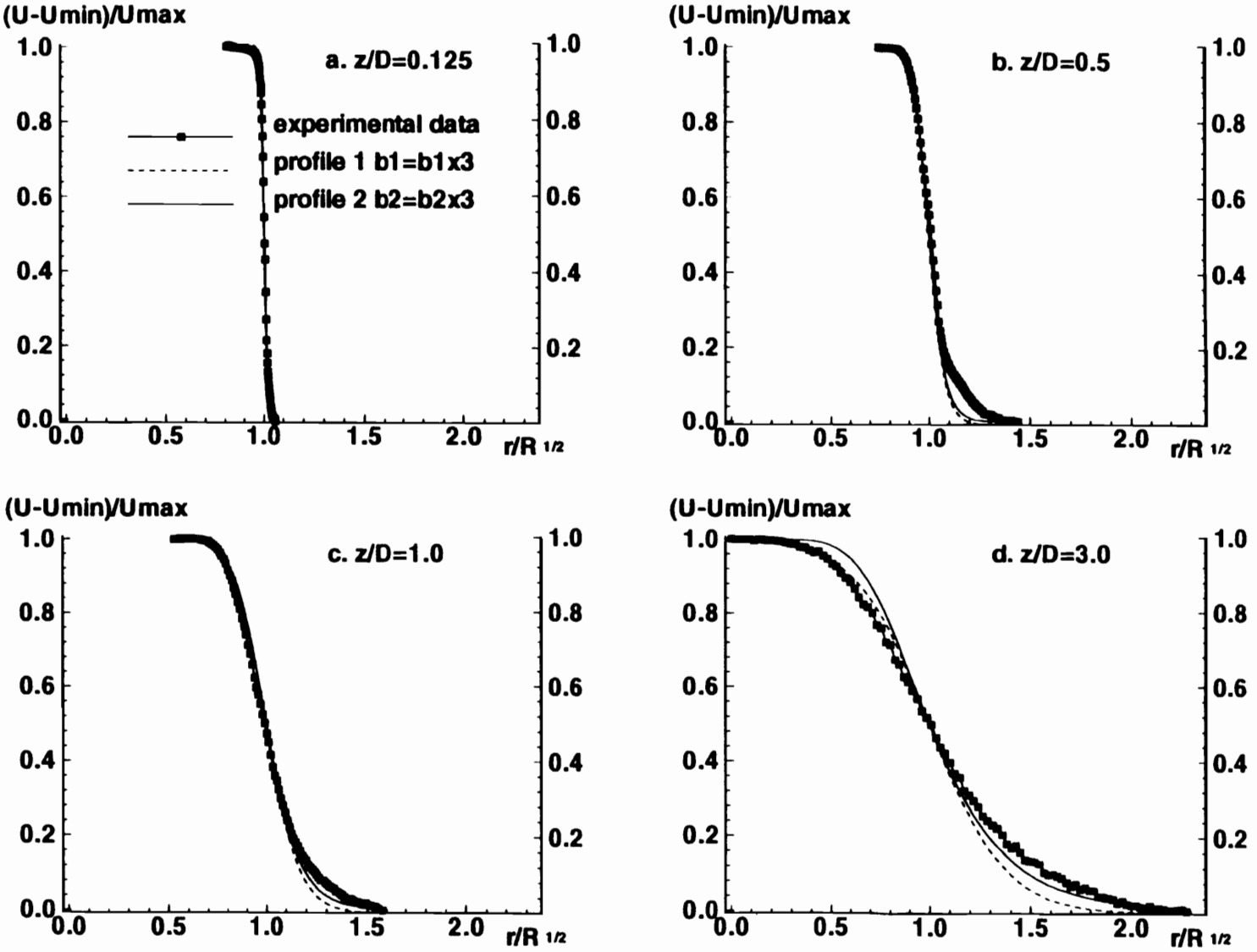

Figure 3.3.2 Mean velocity profiles along four different streamwise locations

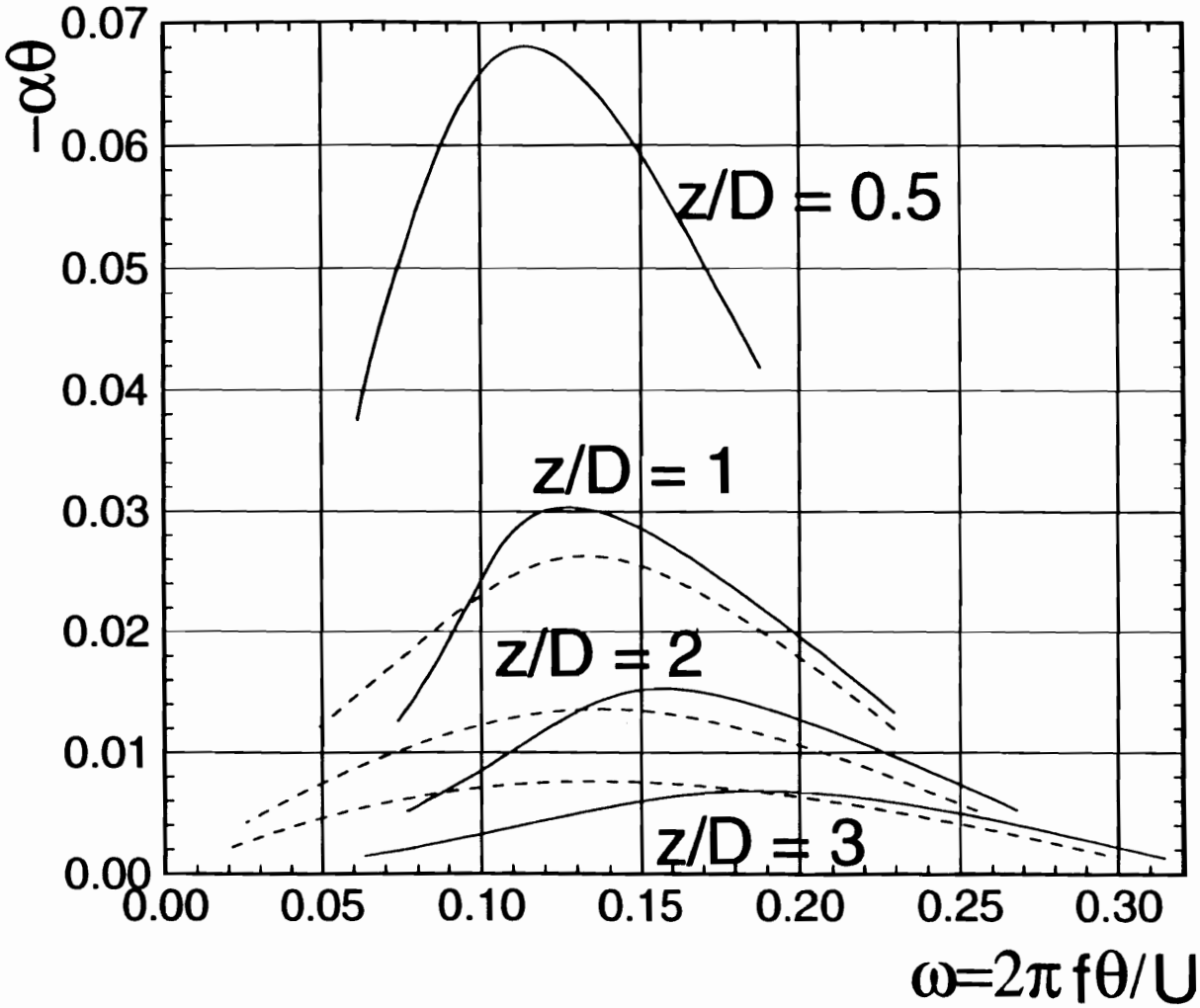

Figure 3.3.3 Growth rate for mode 0 and 1 (solid line for 0, dashed line for 1)

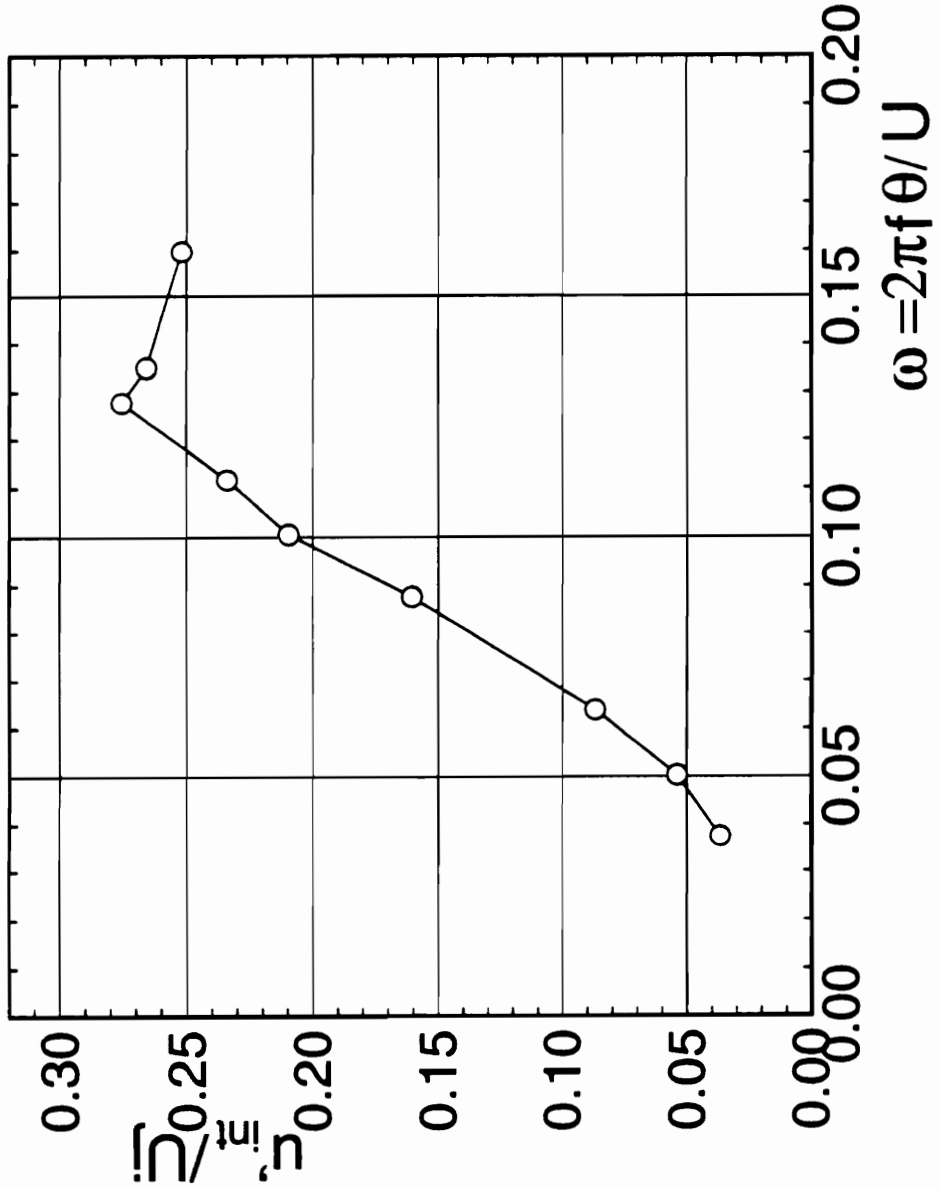

Figure 3.3.4 Growth of the fundamental amplitude

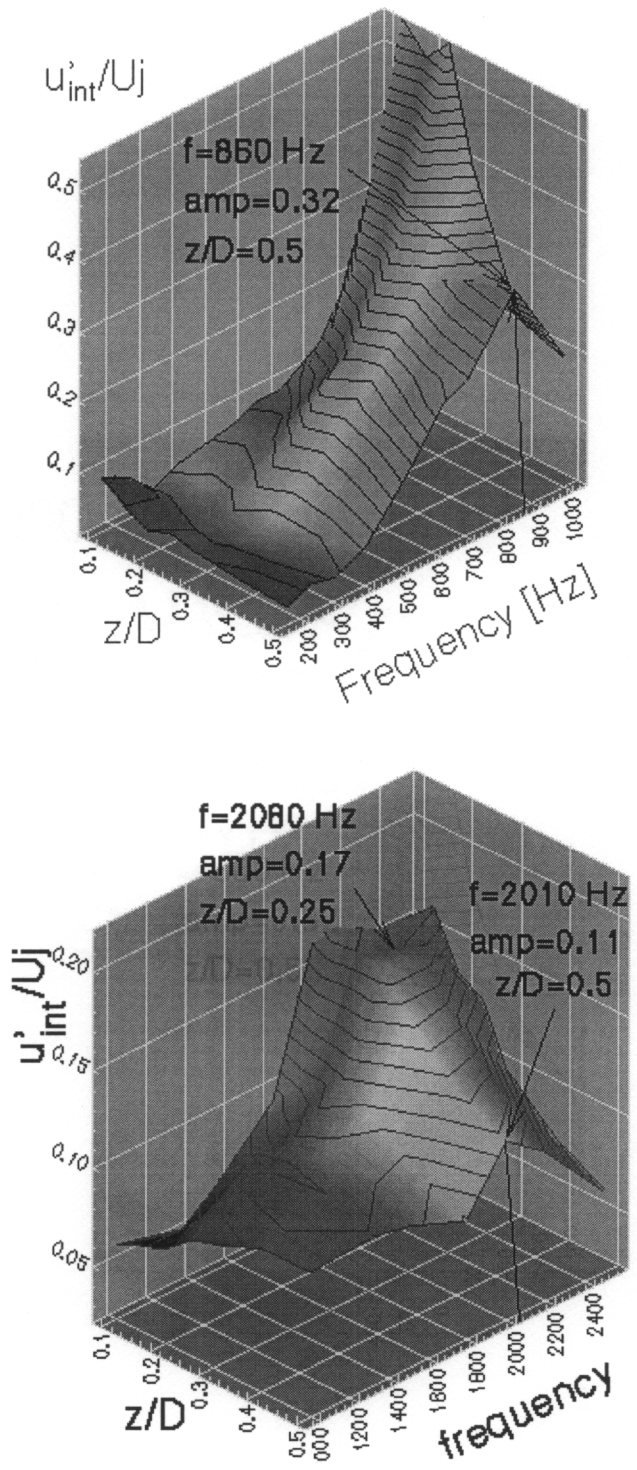

Figure 3.3.5 3-D view of the amplification of the excited fundamental amplitude (0<z/D<0.5)

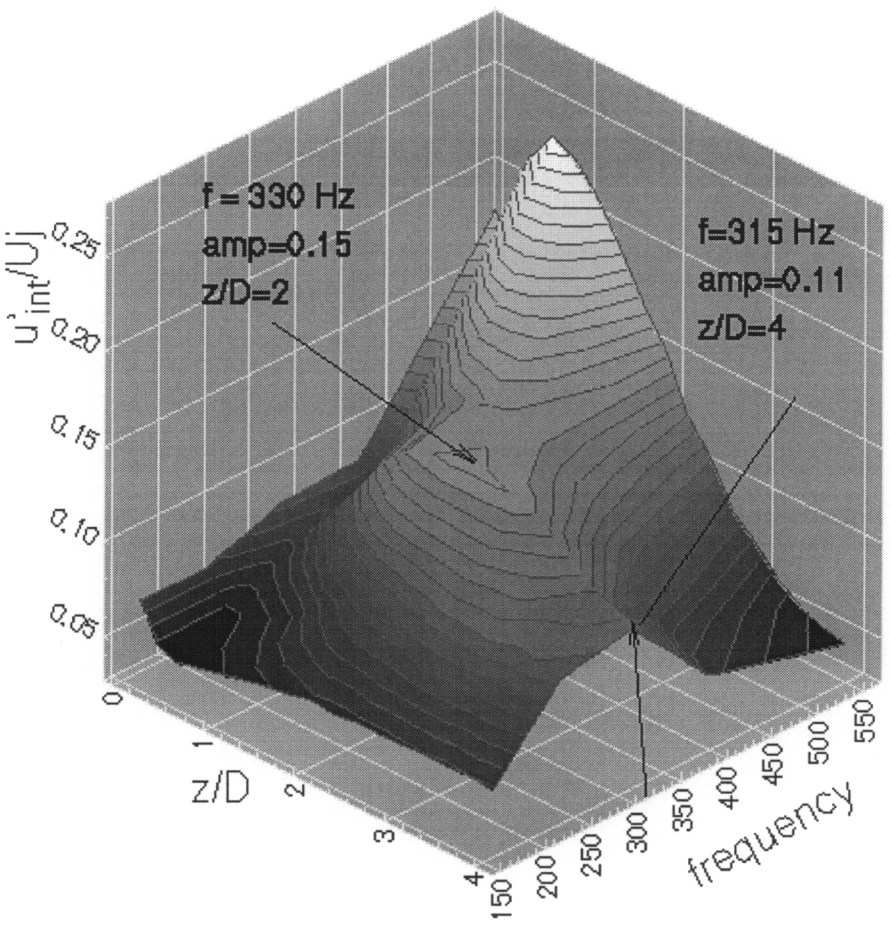

Figure 3.3.6 3-D view of the amplification of the excited fundamental amplitude (0<z/D<4)

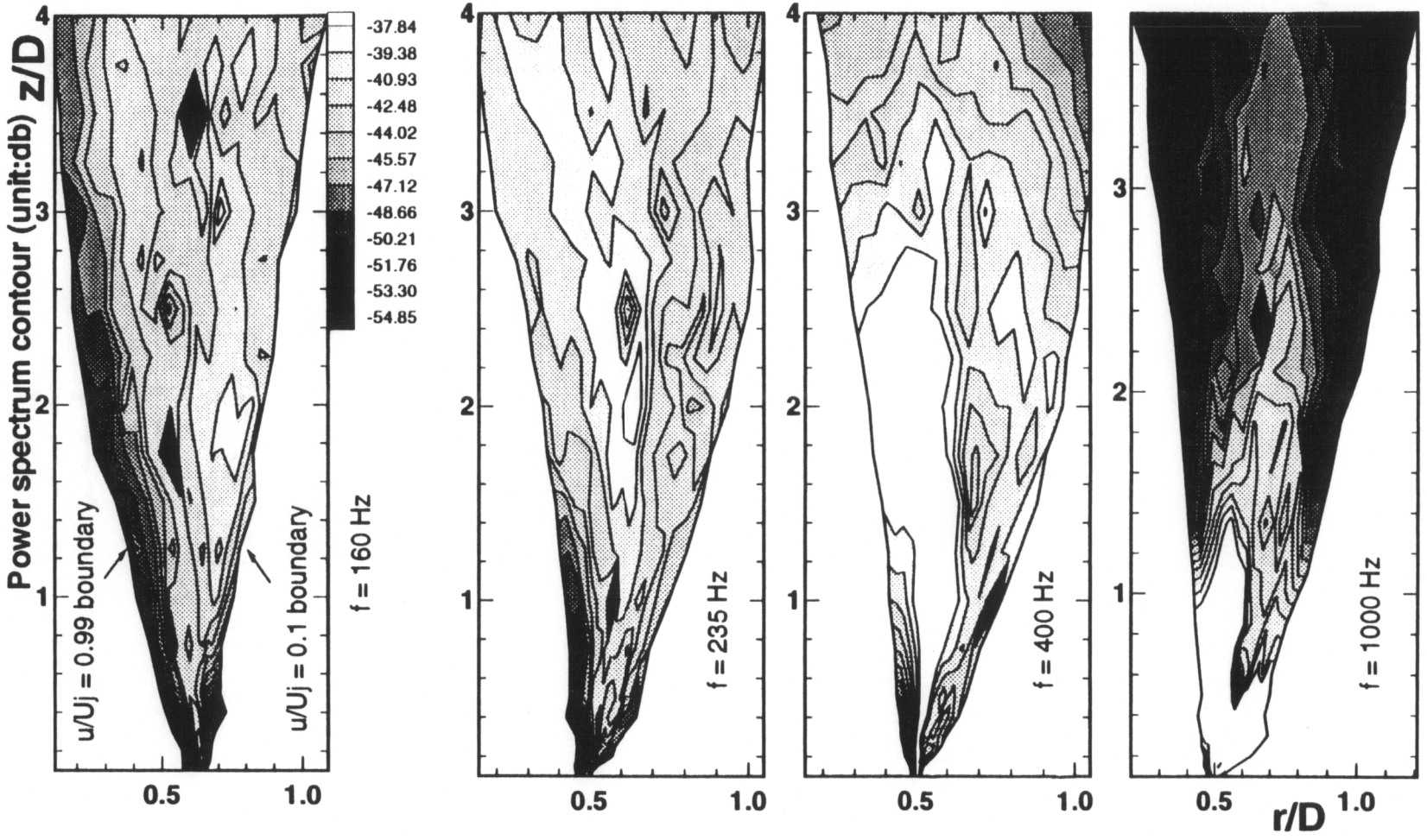

Figure 3.3.7 Power spectra of the development of amplitude of the excited fundamental frequency

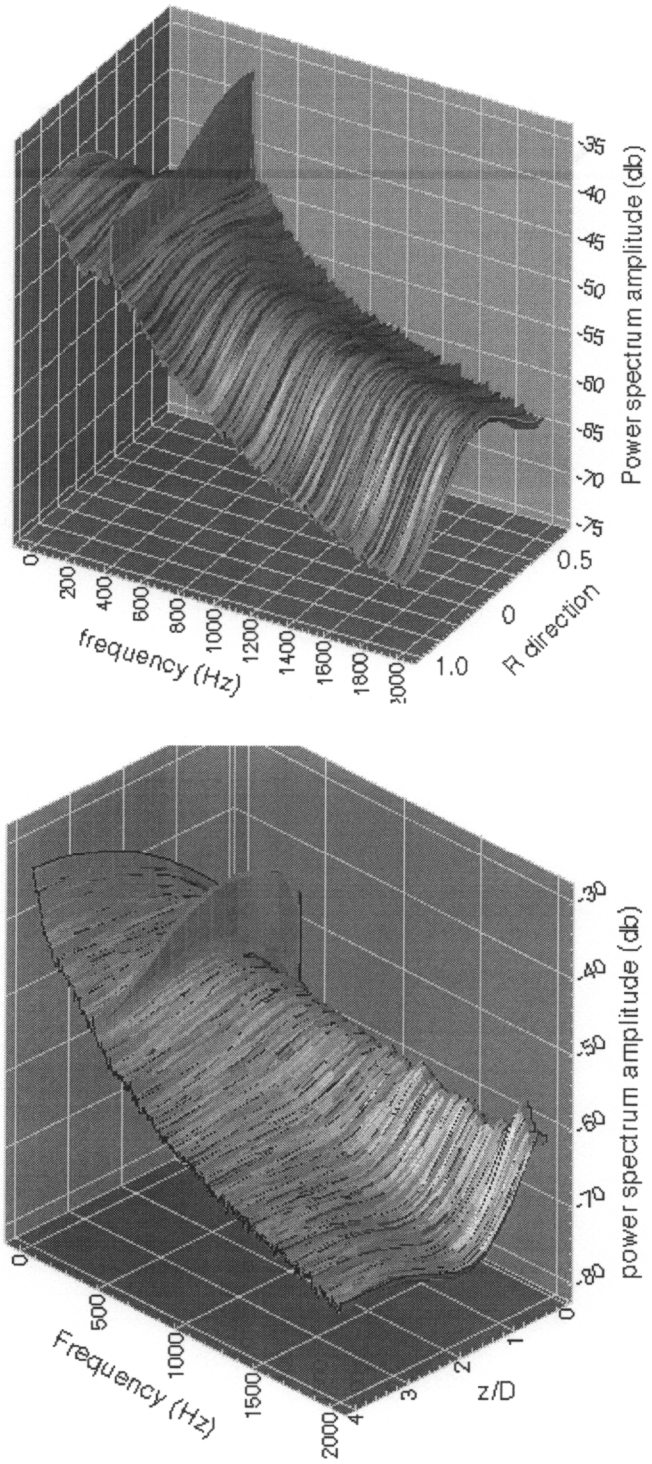

Figure 3.3.8 Distribution of power spectra across shear layer and along streamwise direction, f = 200 Hz. a. Across shear layer, z/D = 2.0; b. Along streamwise direction

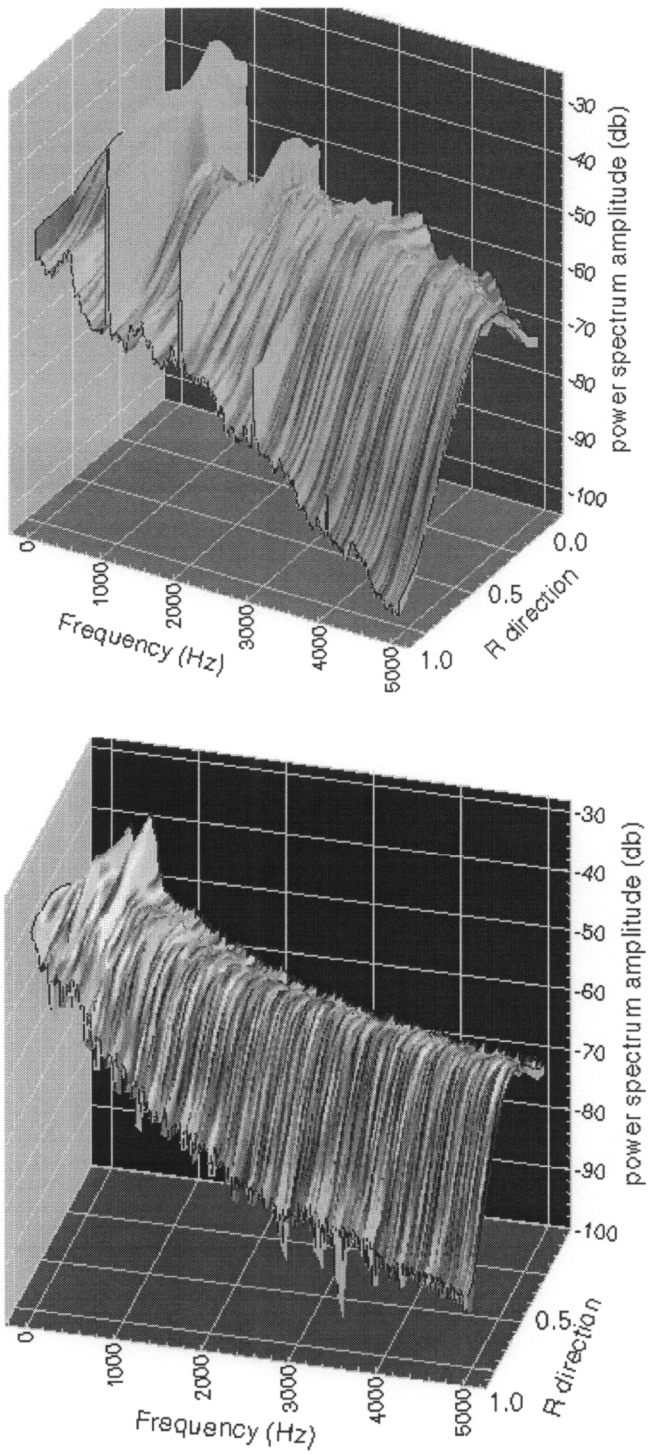

Figure 3.3.8 Distribution of power spectra across shear layer and along streamwise direction, f = 200 Hz. c. Across shear layer, z/D = 2.0; d. Along streamwise direction

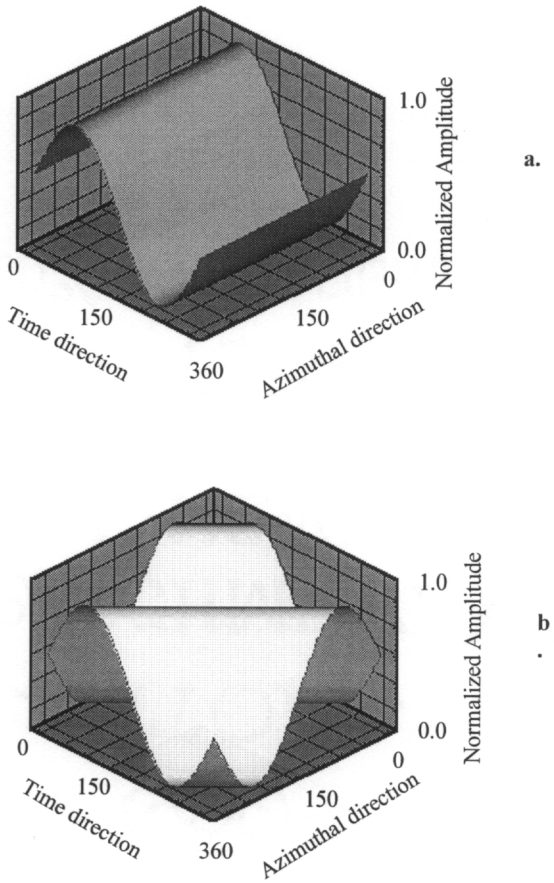

Figure 3.3.9 Time and azimuthal variation of the control signal for single mode excitations, a. m = 0; b. m = 1; where the normalized amplitude equals the signal output at any instant divided by its maximum output

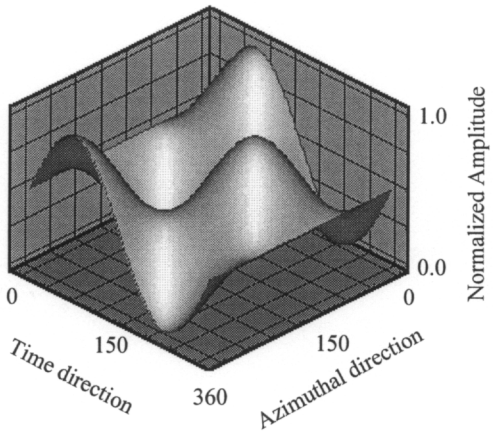

c.

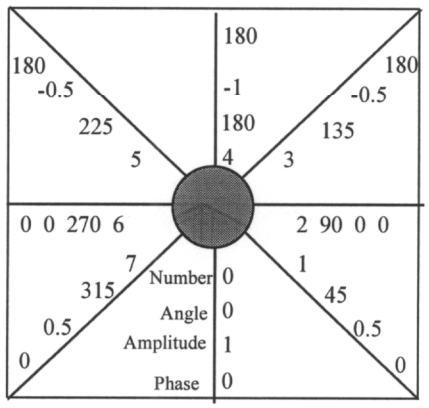

d.

Figure 3.3.9 Time and azimuthal variation of the control signal for single mode excitations, c. m = ± 1, where the normalized amplitude equals the signal output at any instant divided by its maximum output; d. Schematic view of m = ± 1 setup (continued)

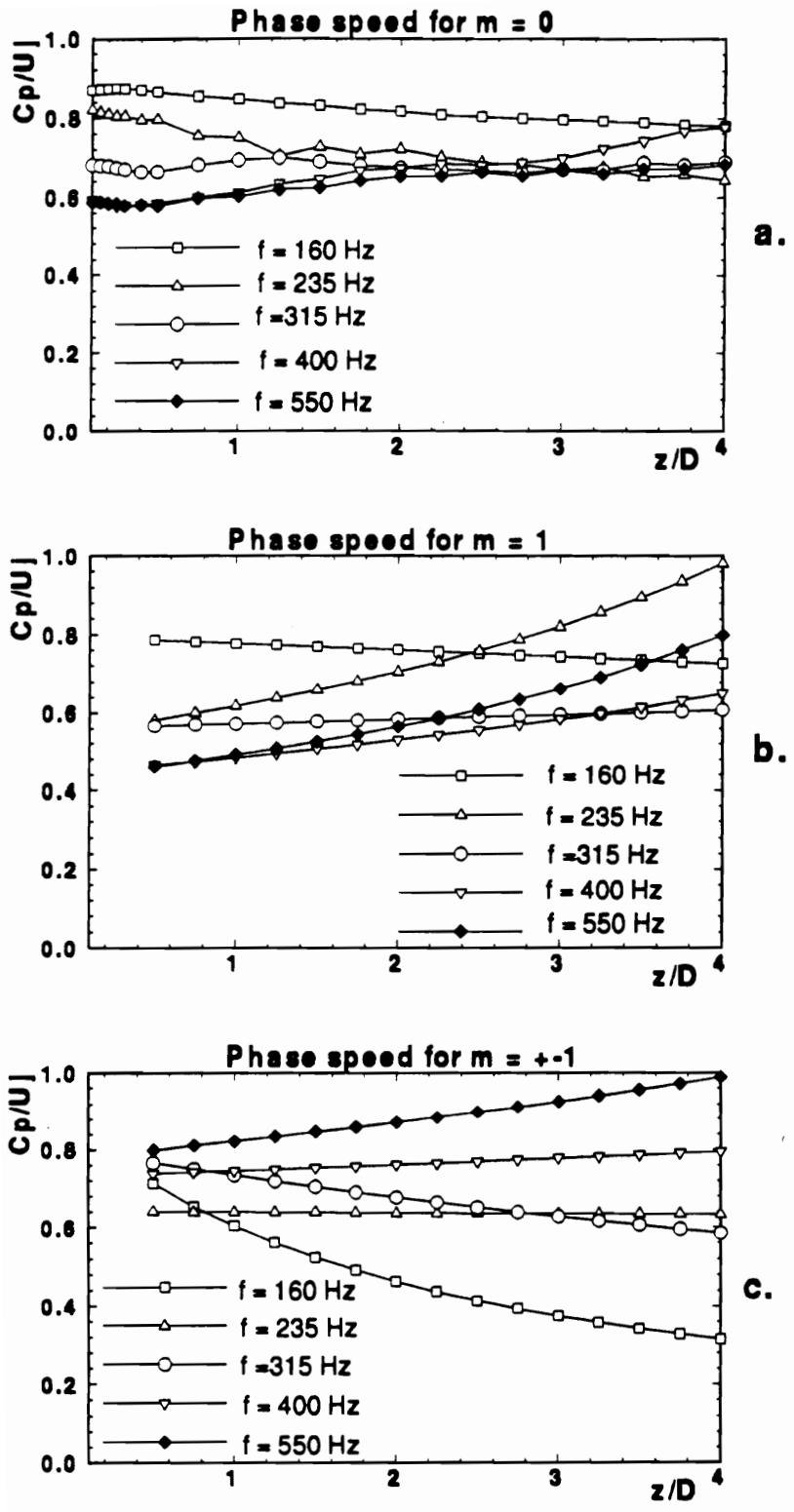

Figure 3.3.10 Phase speed of different spatial modes

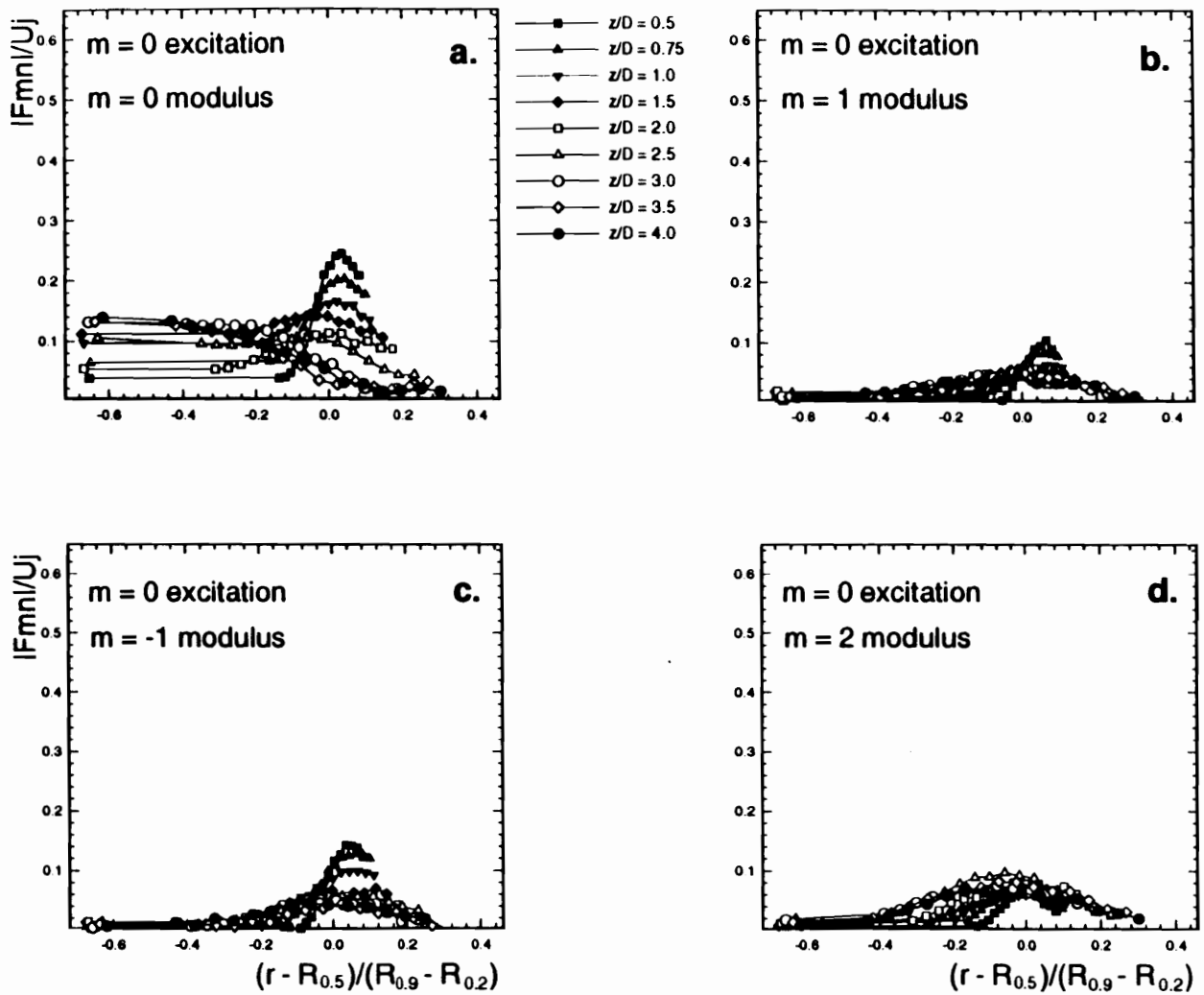

Figure 3.3.11 Streamwise development of phase averaged modulus under m=0 excitation

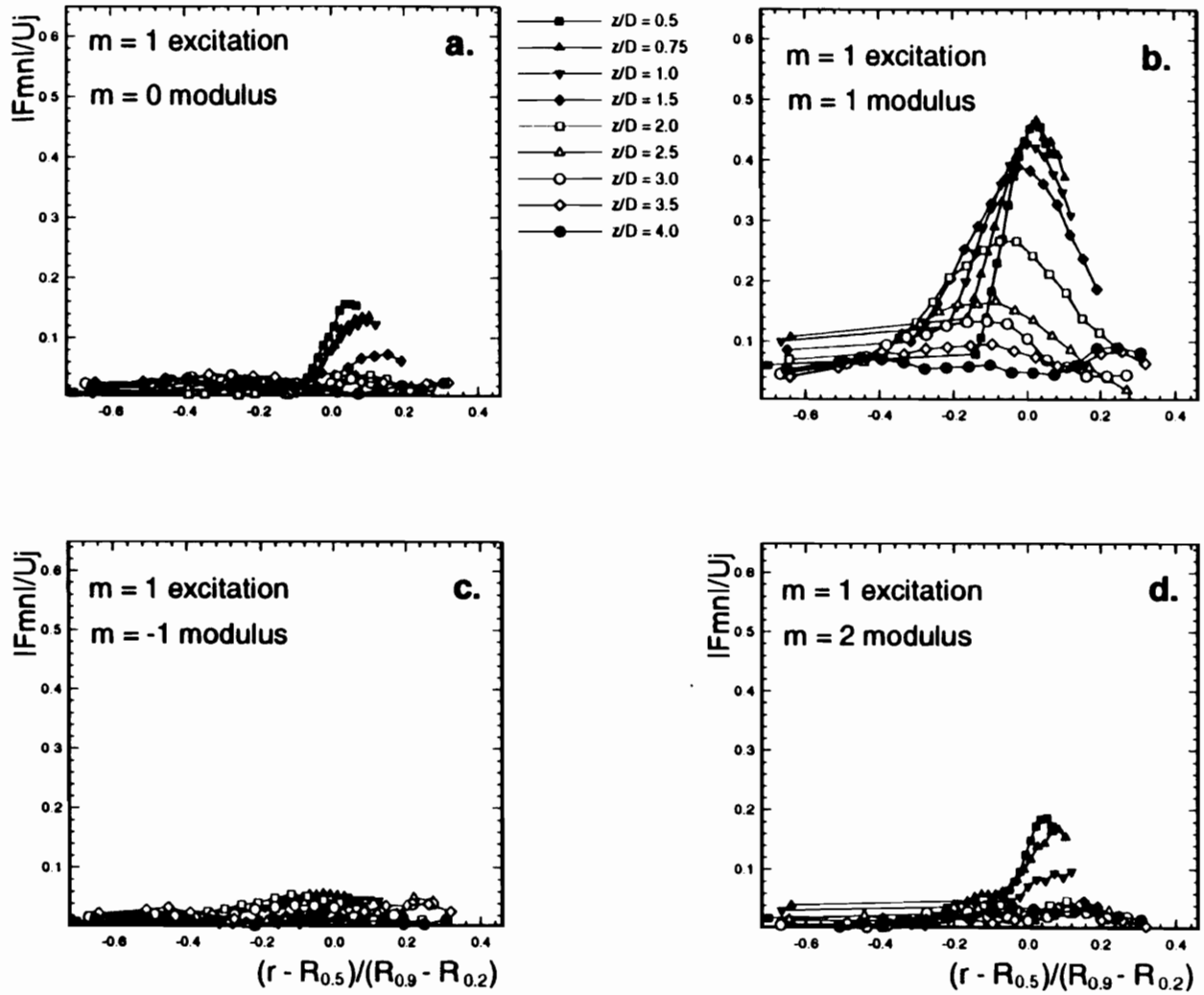

Figure 3.3.12 Streamwise development of phase averaged modulus under m=1 excitation

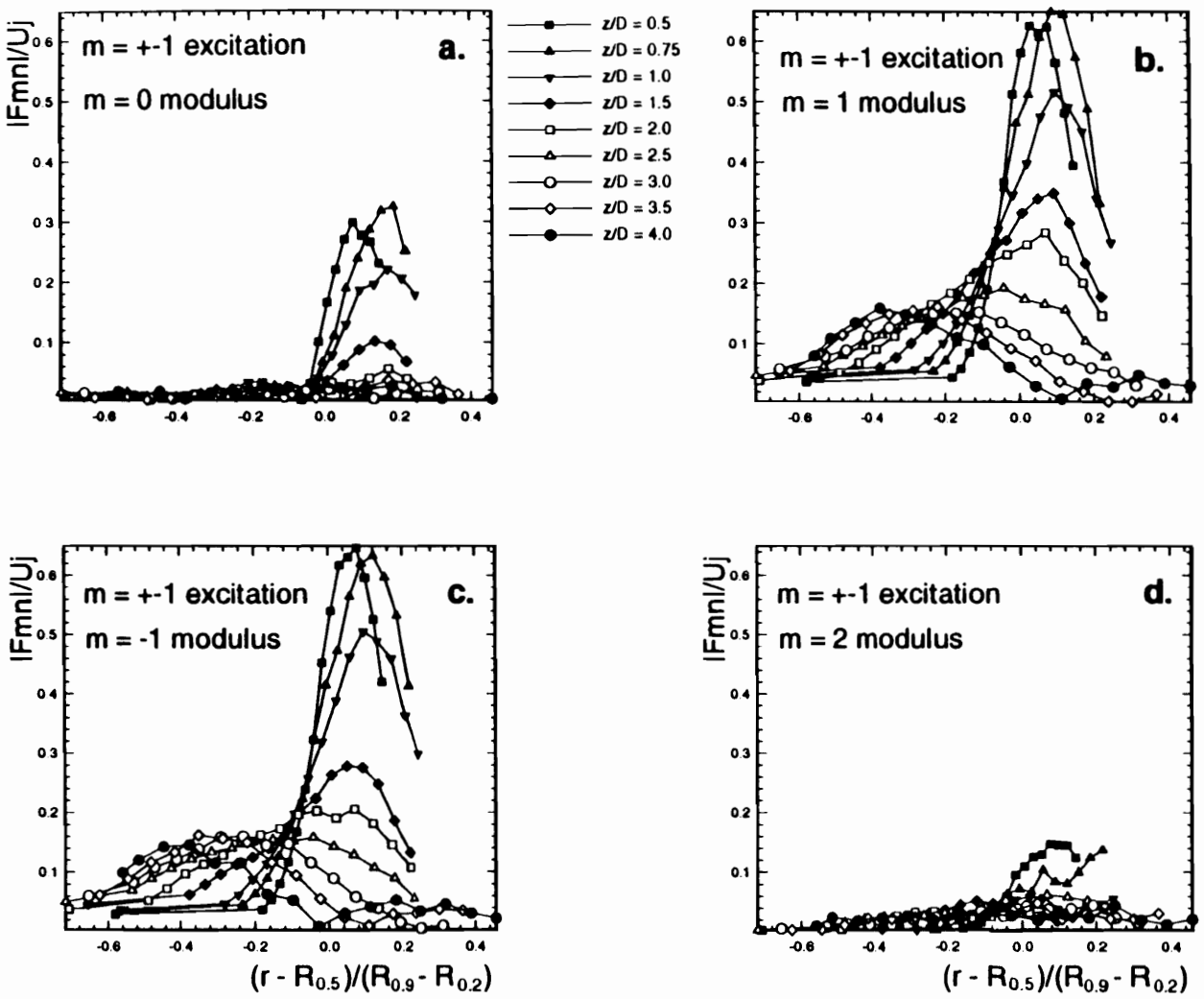

Figure 3.3.13 Streamwise development of phase averaged modulus under $m = \pm 1$ excitation

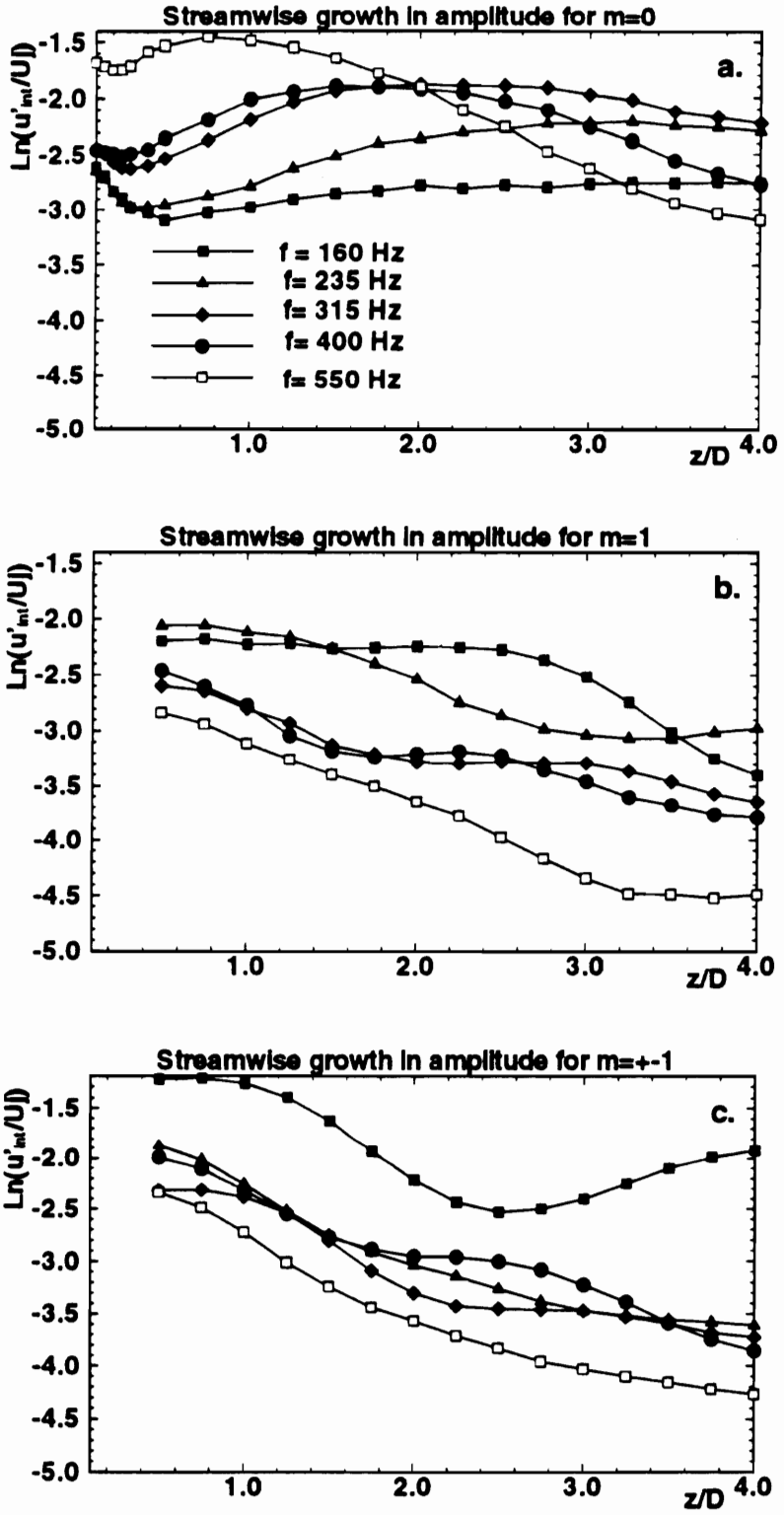

Figure 3.3.14 Streamwise growth in amplitude for different spatial mode excitation and excitation frequencies

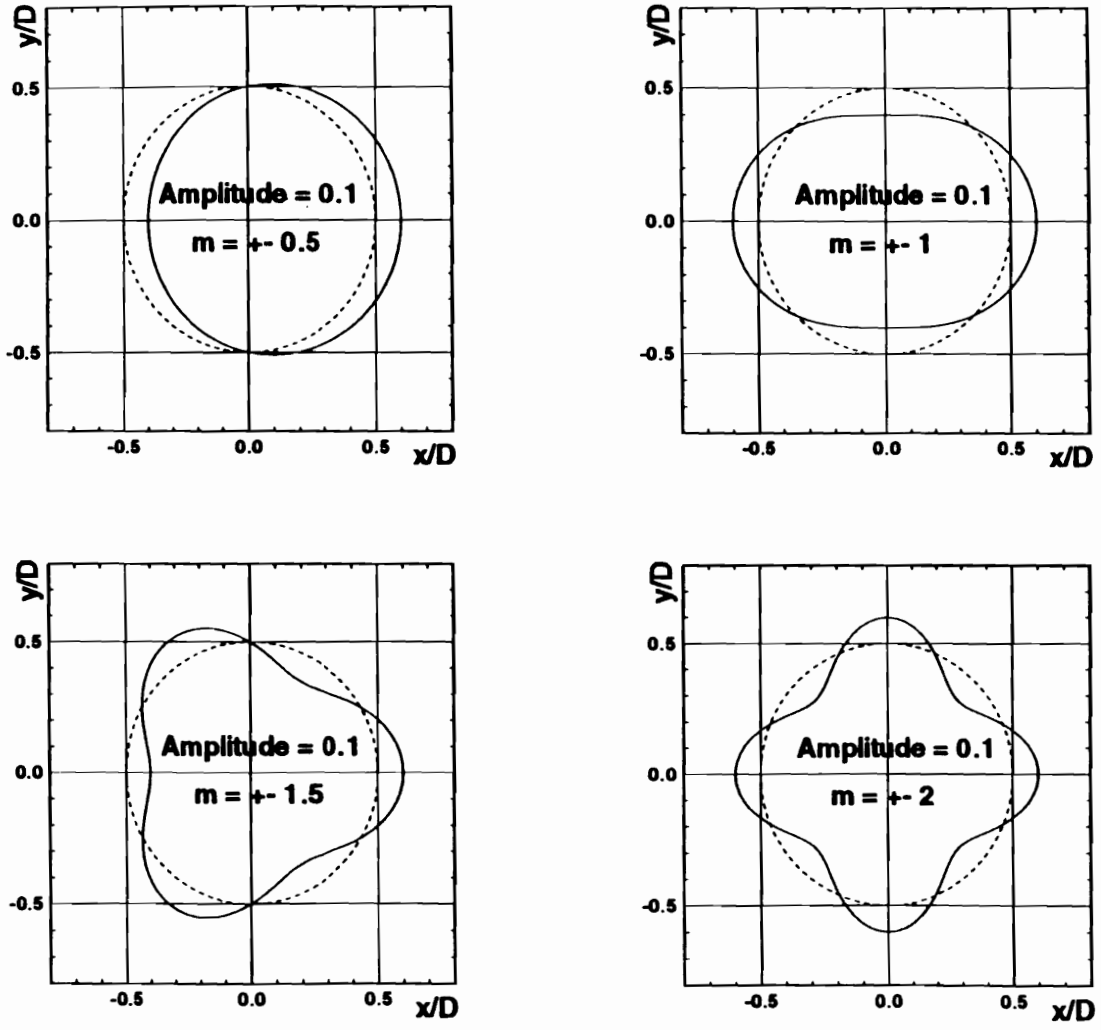

Figure 3.3.15 Velocity contour simulation under standing wave manipulation, case 1) Change of modes

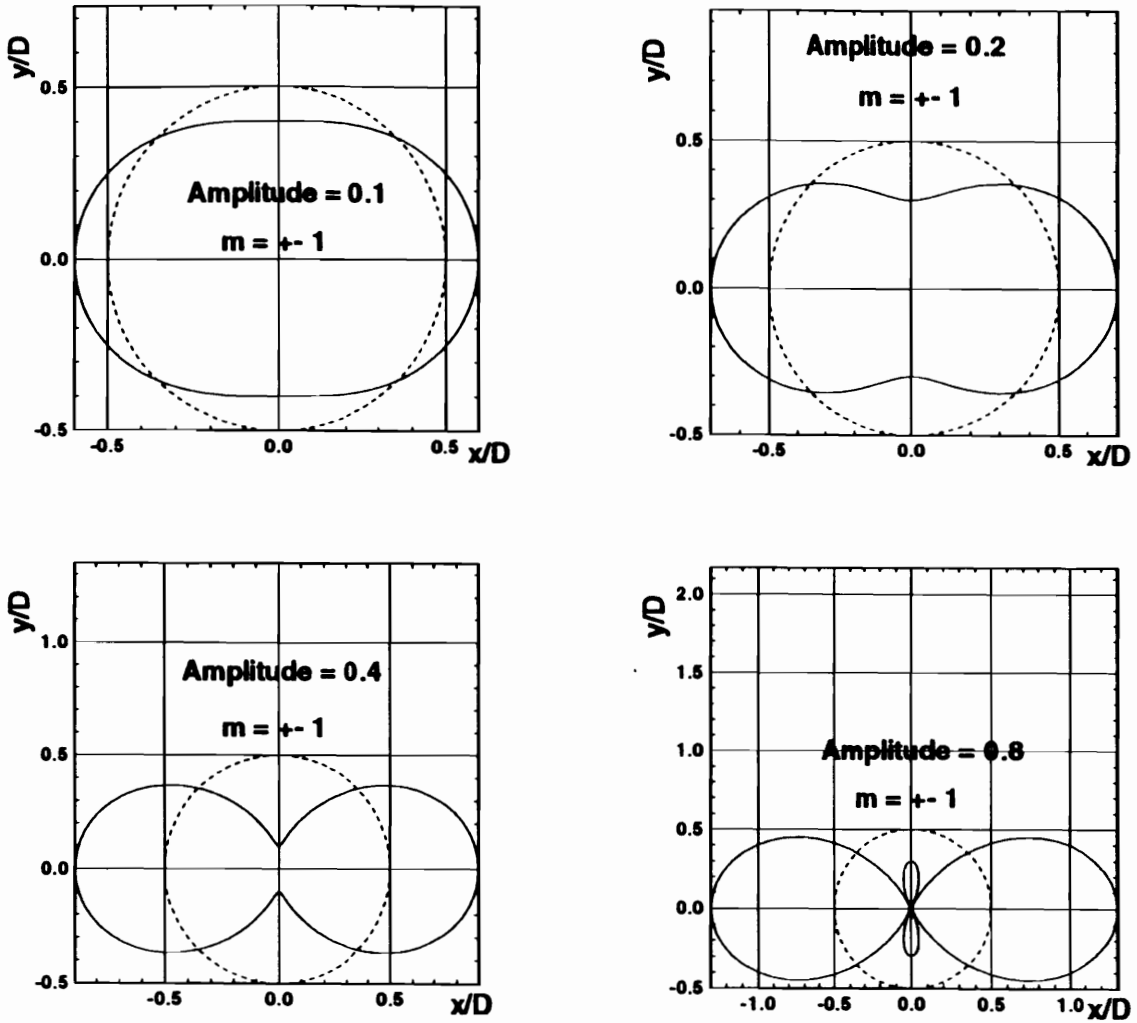

Figure 3.3.15 Velocity contour simulation under standing wave manipulation, case 2) Change of amplitudes

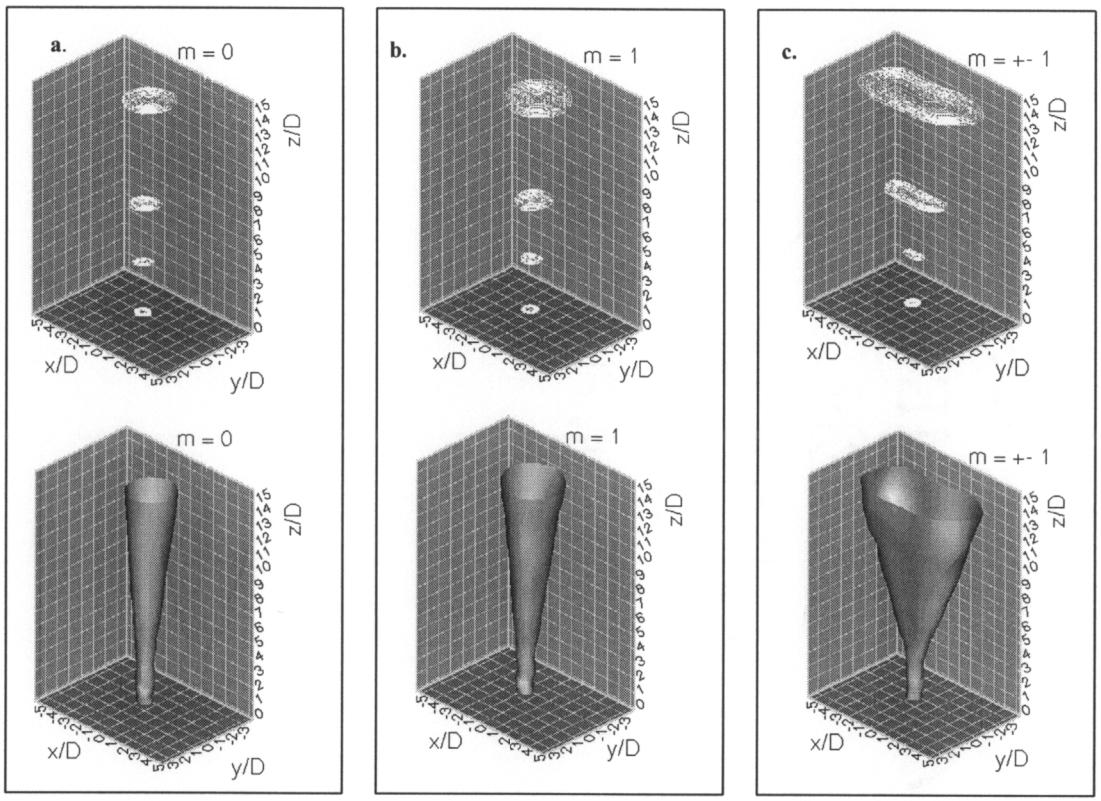

Figure 3.3.16 Iso-velocity contours of excited jets, 3-D surface for U/U_j=0.5, 2-D outer limit also is U/U_j=0.5, z/D=0.5 to 15, excitation frequency: 180 Hz, spatial modes: a. m=0, b. m = 1 and c. m = ±1

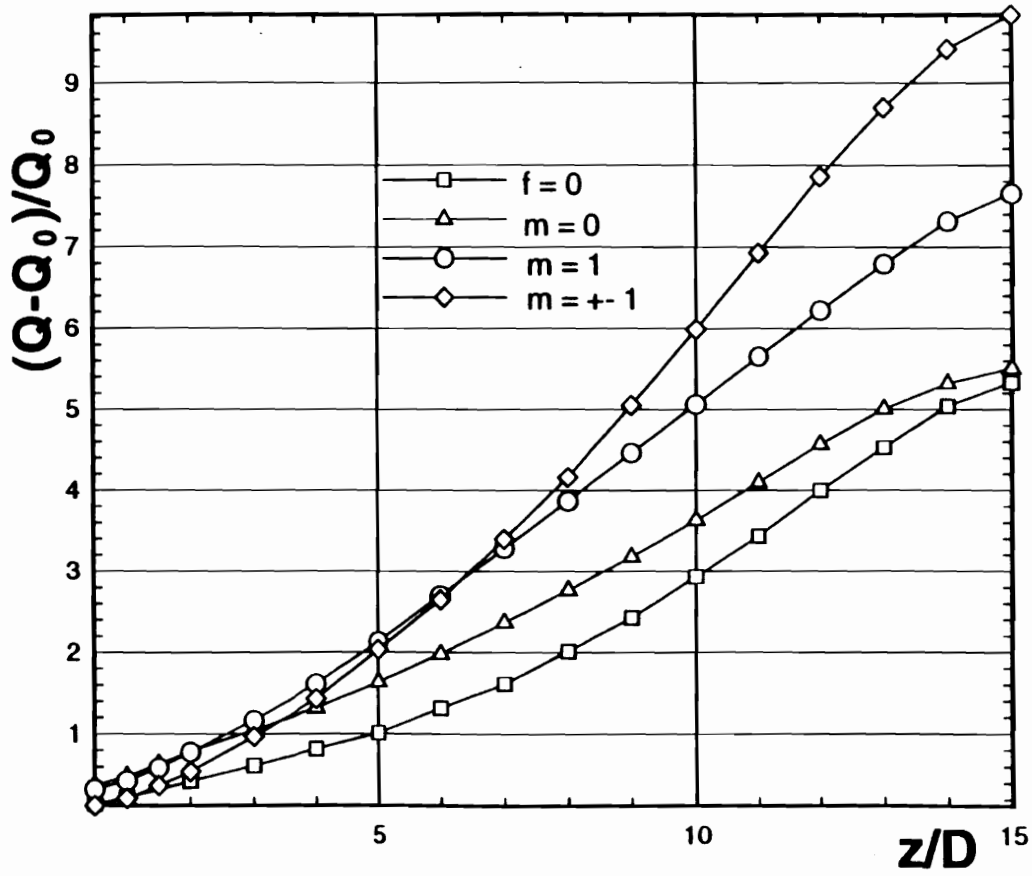

Figure 3.3.17 Entrainment ratio for unexcited and excited jet f_e = 180Hz, m=0, 1 and ±1

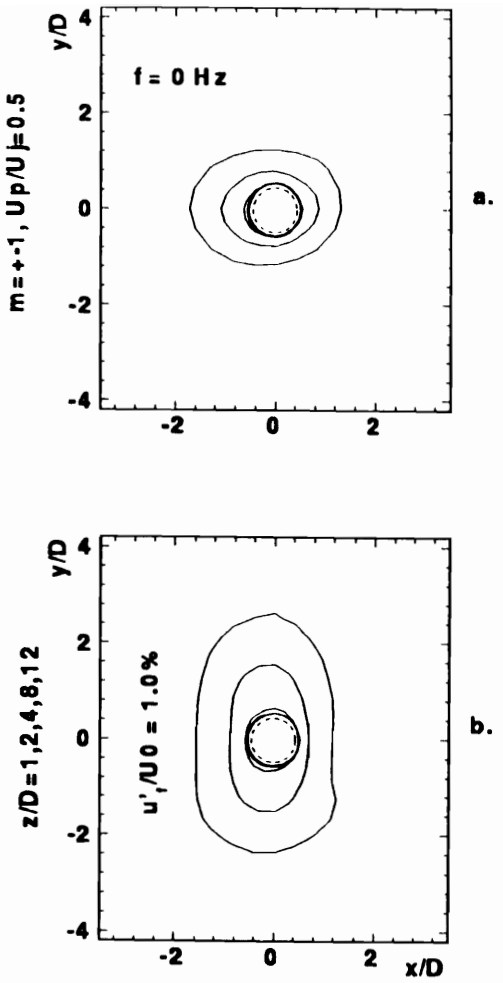

Figure 3.3.18 Effects of excitation amplitude to the expansion of the velocity contour

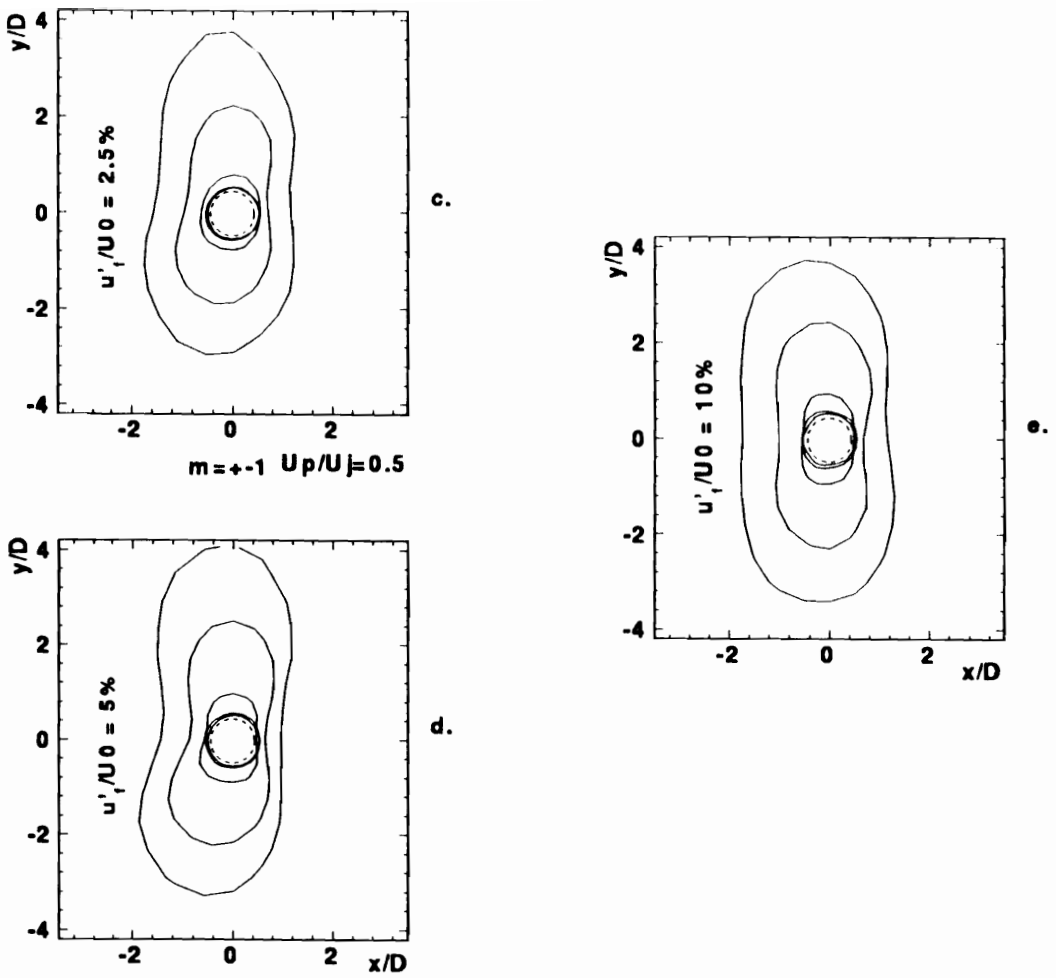

Figure 3.3.18 Effects of excitation amplitude to the expansion of the velocity contour (continued)

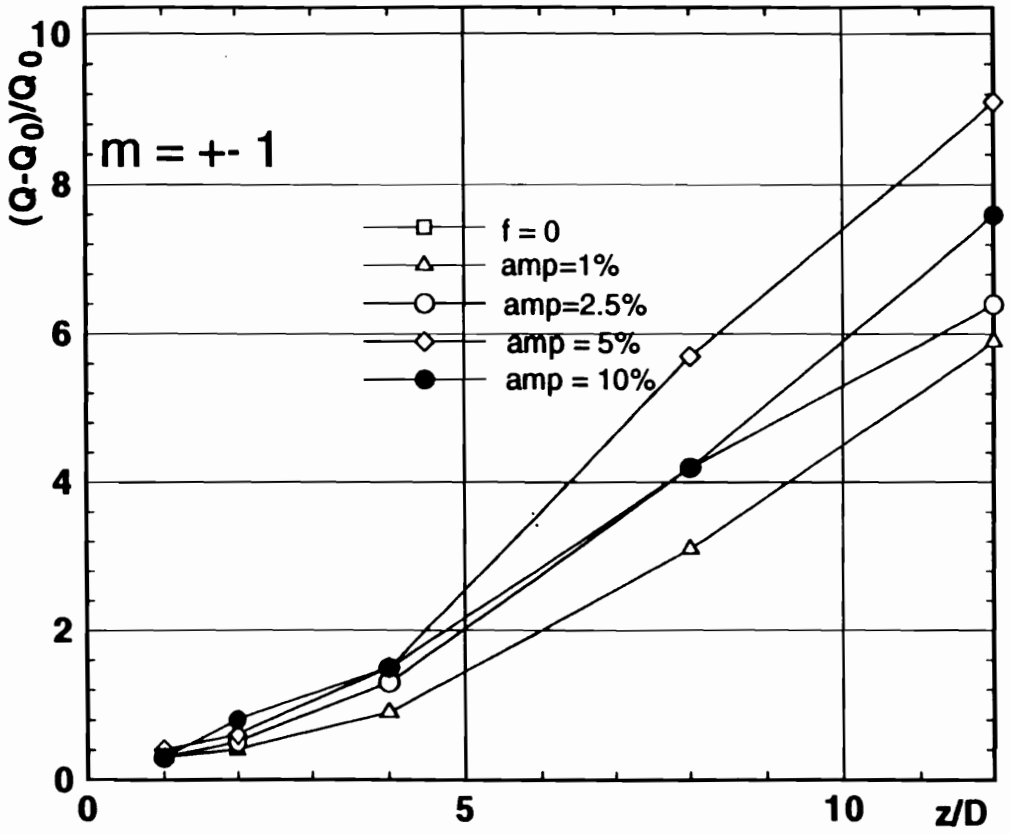

Figure 3.3.19 Entrainment ratio of the jet under different excitation amplitude

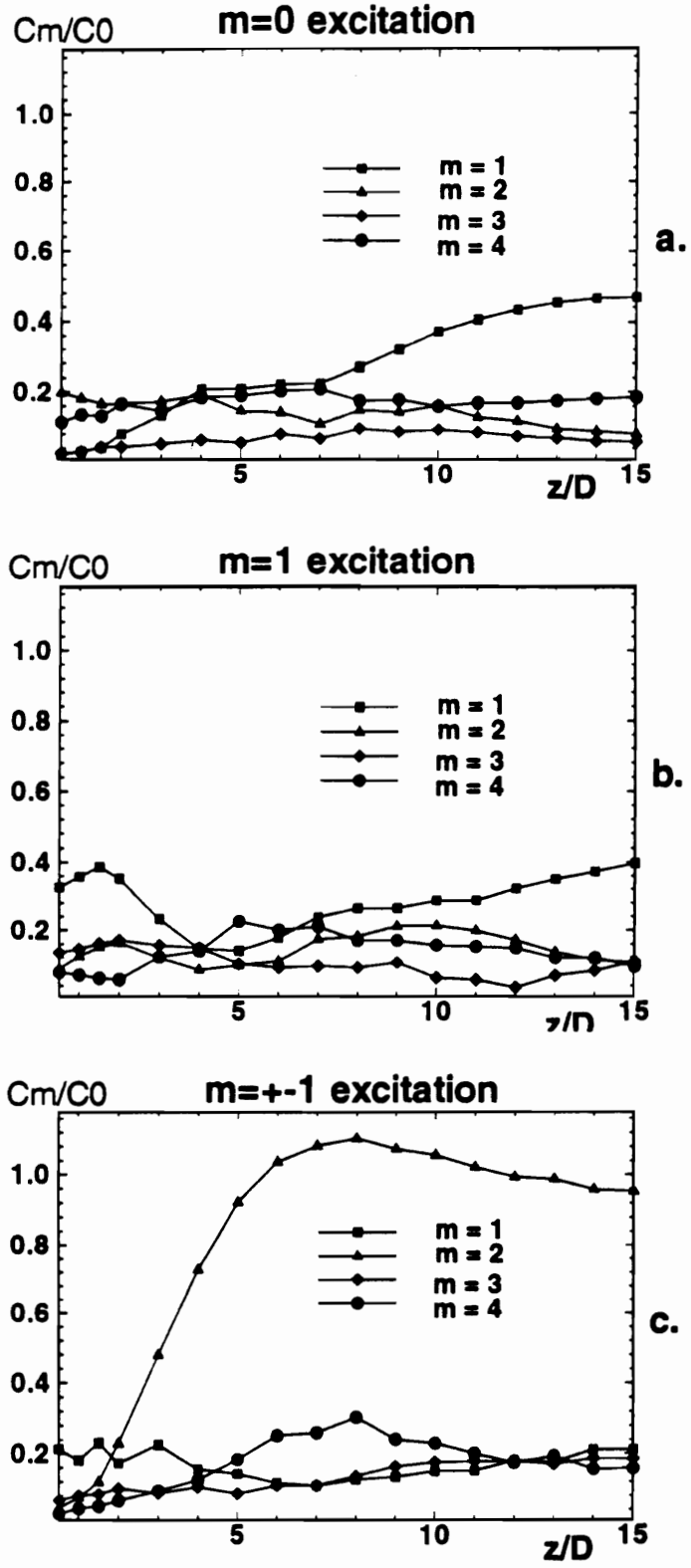

Figure 3.3.20 Mean flow of $U/U_j = 0.5$ distortion along the streamwise direction for excitation modes =0, 1 and ±1

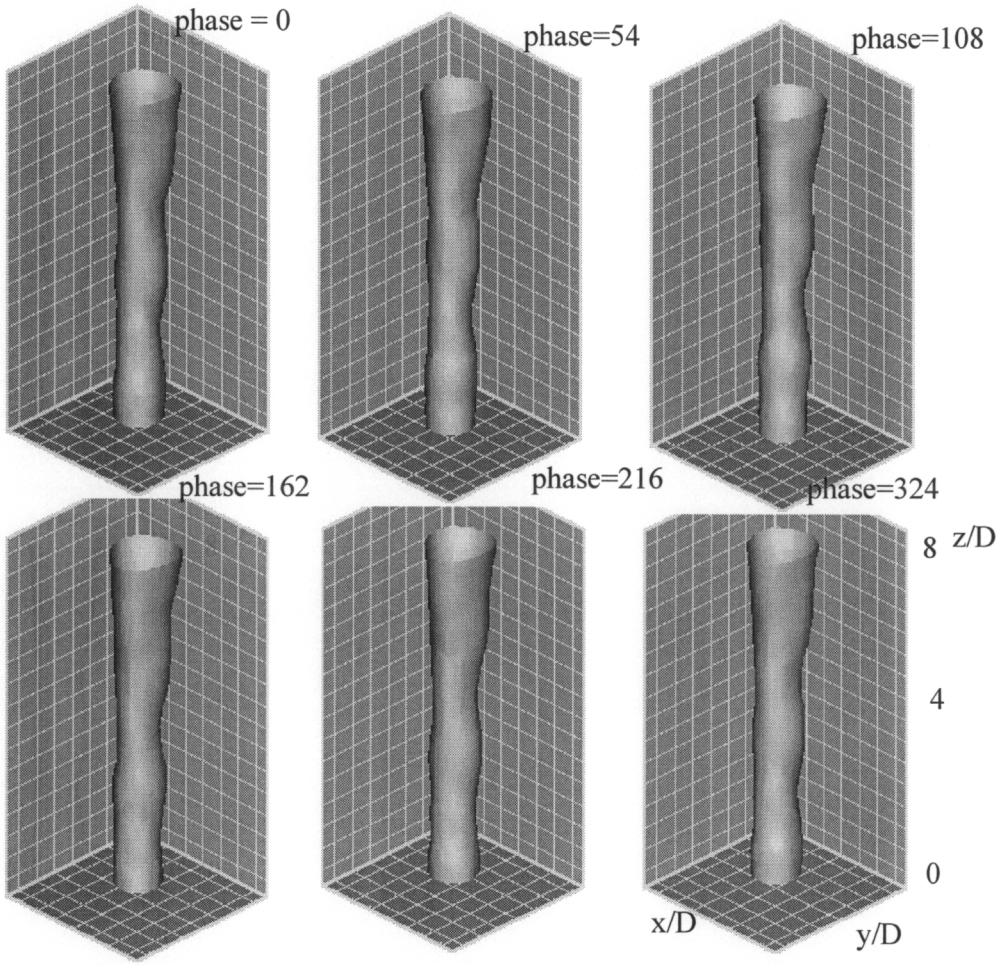

Figure 3.3.21 3-D view of phase mean velocity contour of $U/U_j = 0.5$, m=0 excitation, $f_e = 180$ Hz

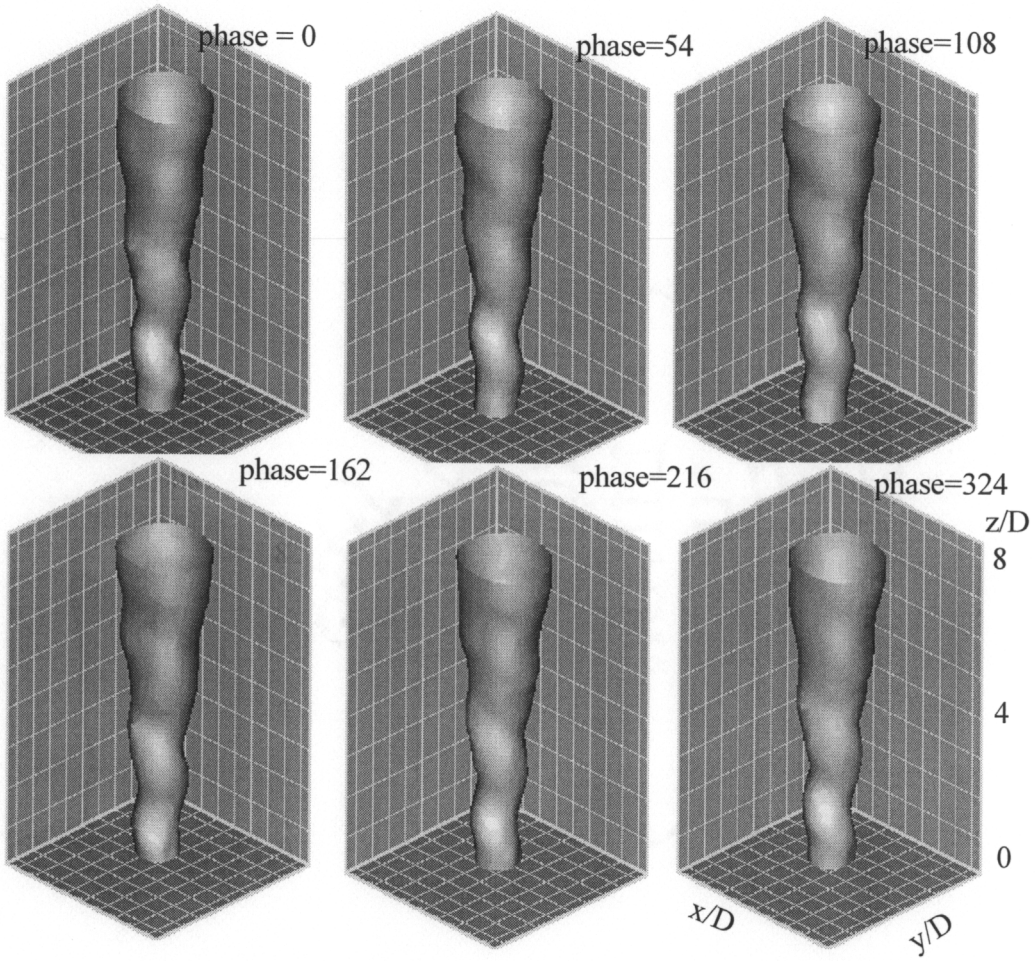

Figure 3.3.22 3-D view of phase mean velocity contour of U/Uj = 0.5, m=1 excitation, f_e = 180 Hz

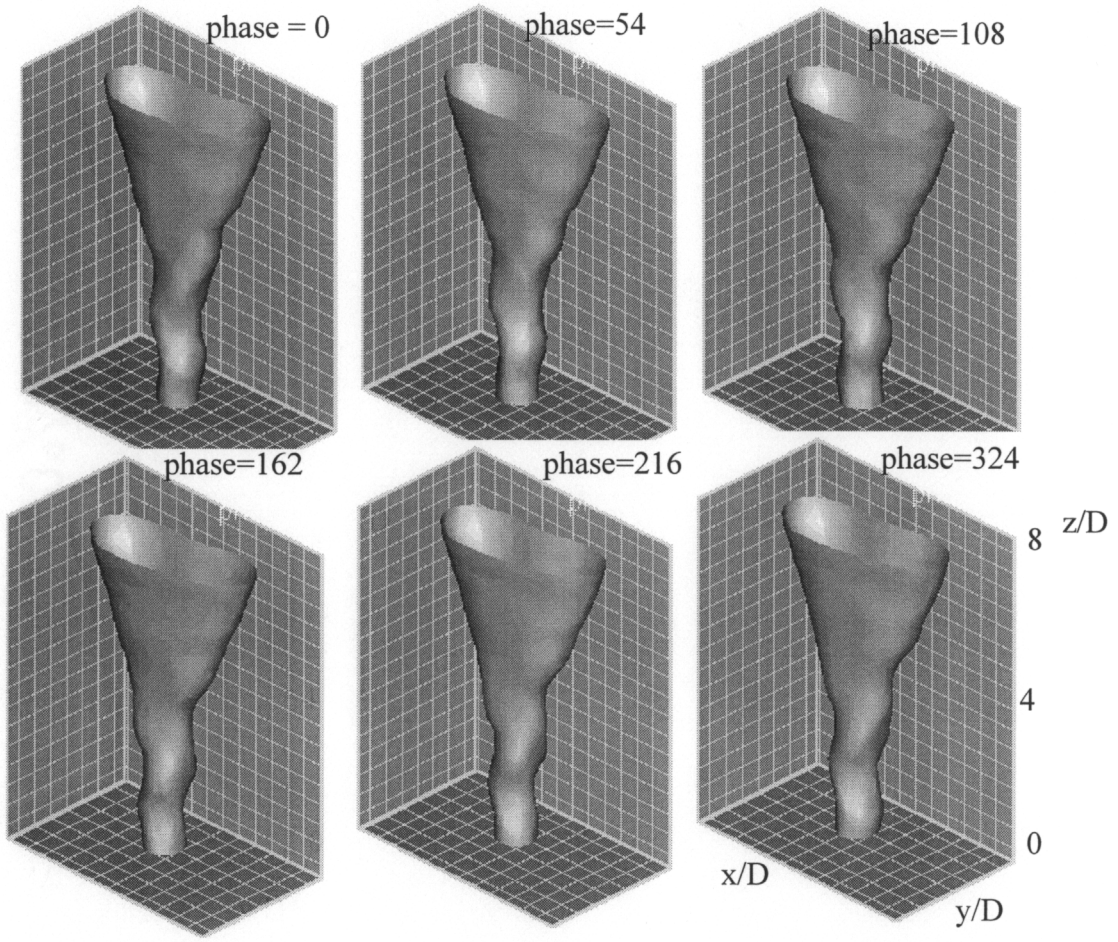

Figure 3.3.23 3-D view of phase mean velocity contour of U/Uj = 0.5, m=±1 excitation, f_e = 180 Hz

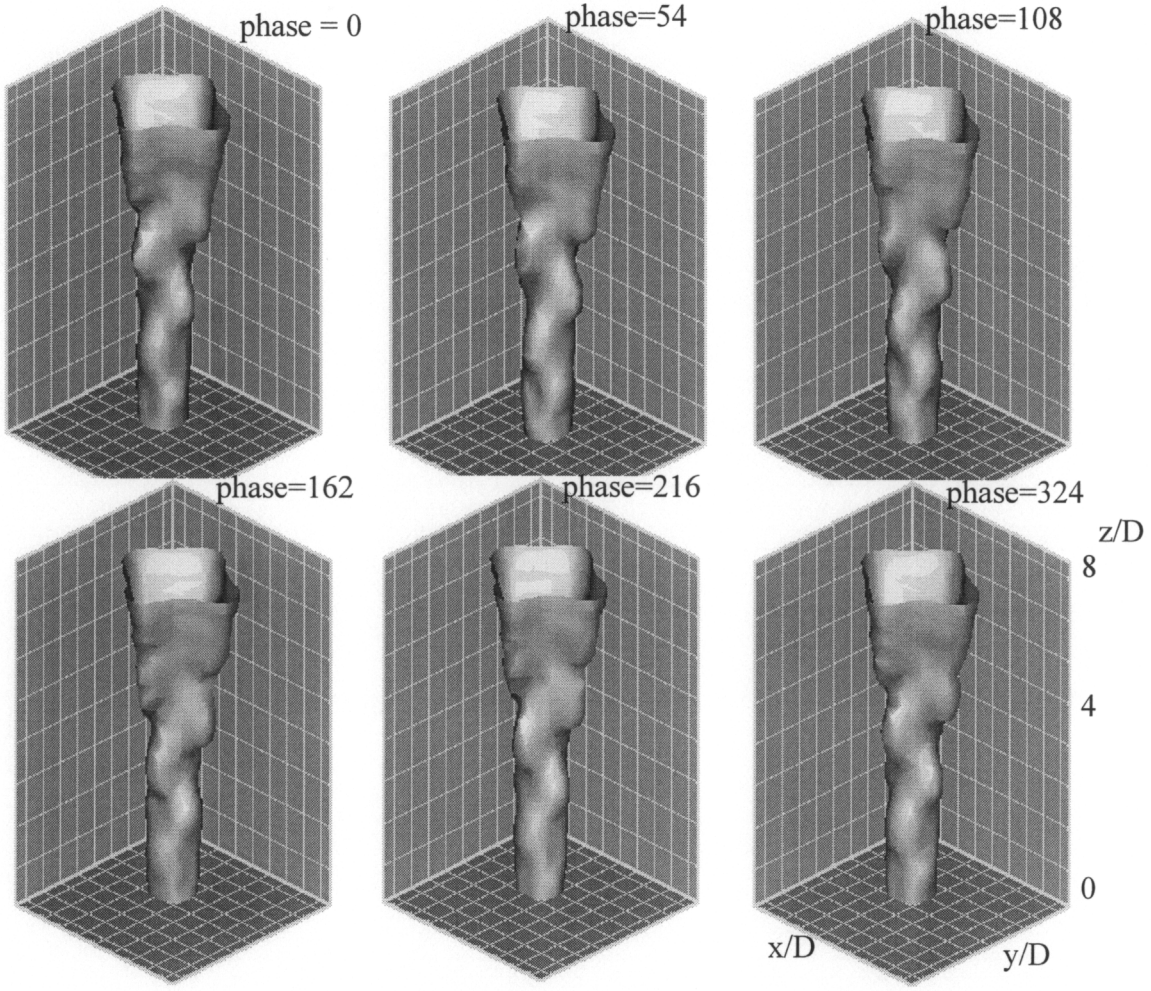

Figure 3.3.24 3-D view of phase mean velocity contour of U/Uj = 0.5 m=±2 excitation, f_e = 180 Hz

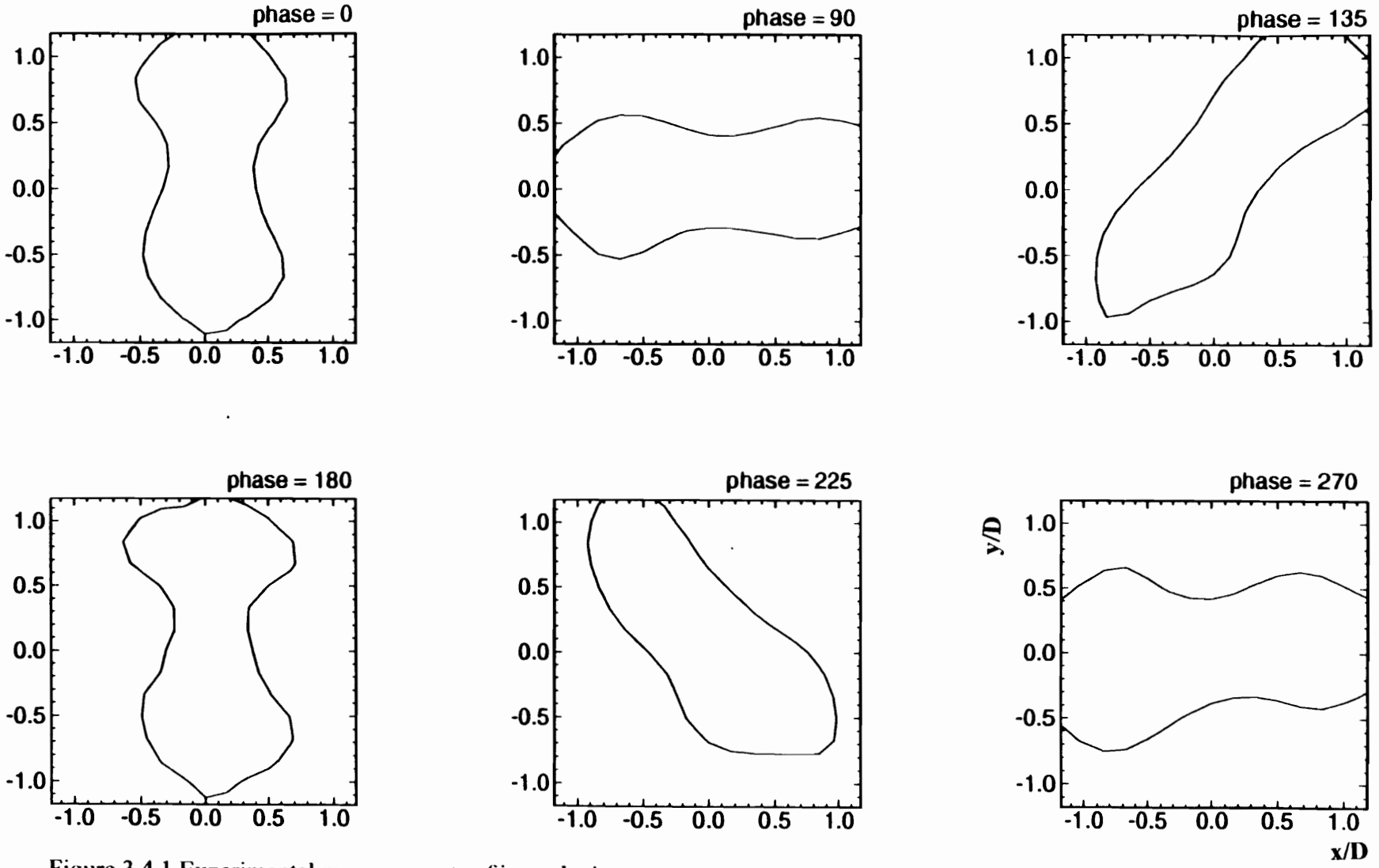

Figure 3.4.1 Experimental measurements of iso-velocity contours reflecting the effects of static phase-offsetting, $m = \pm 1$ excitation

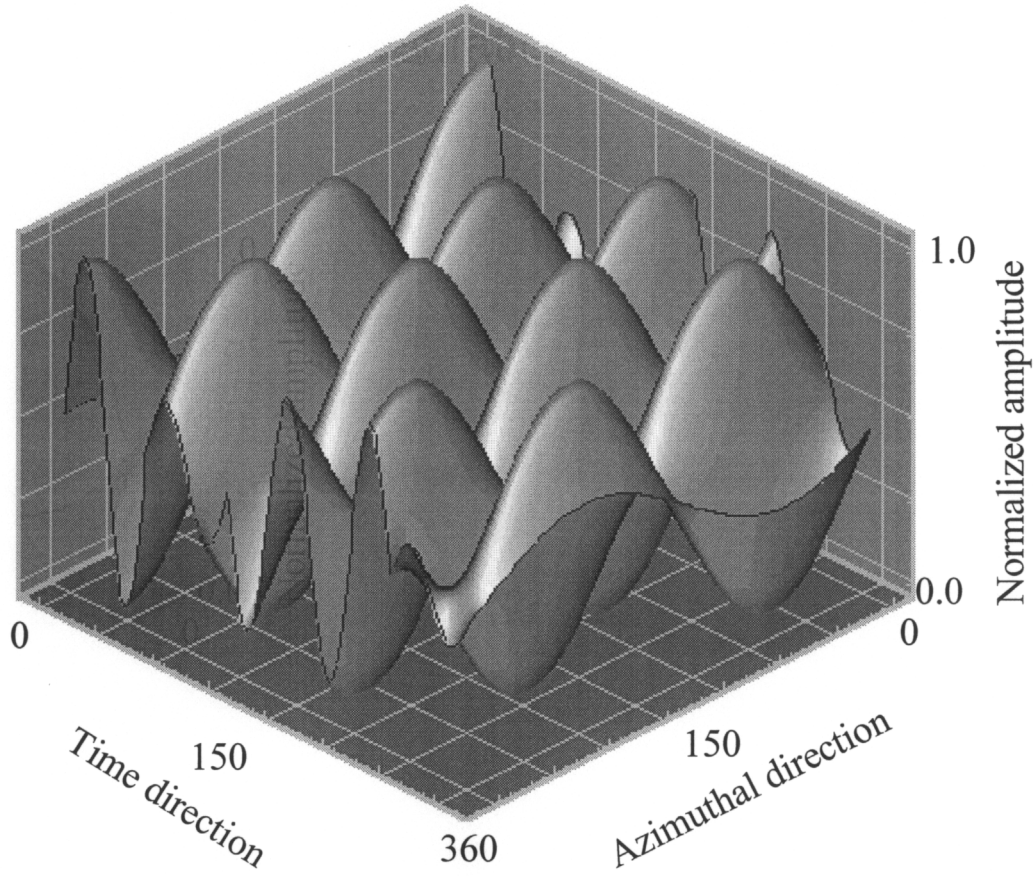

Figure 3.4.2 Time and azimuthal variation of the control signal for phase modulation, where the normalized amplitude equals the signal output at any instant divided by its maximum output

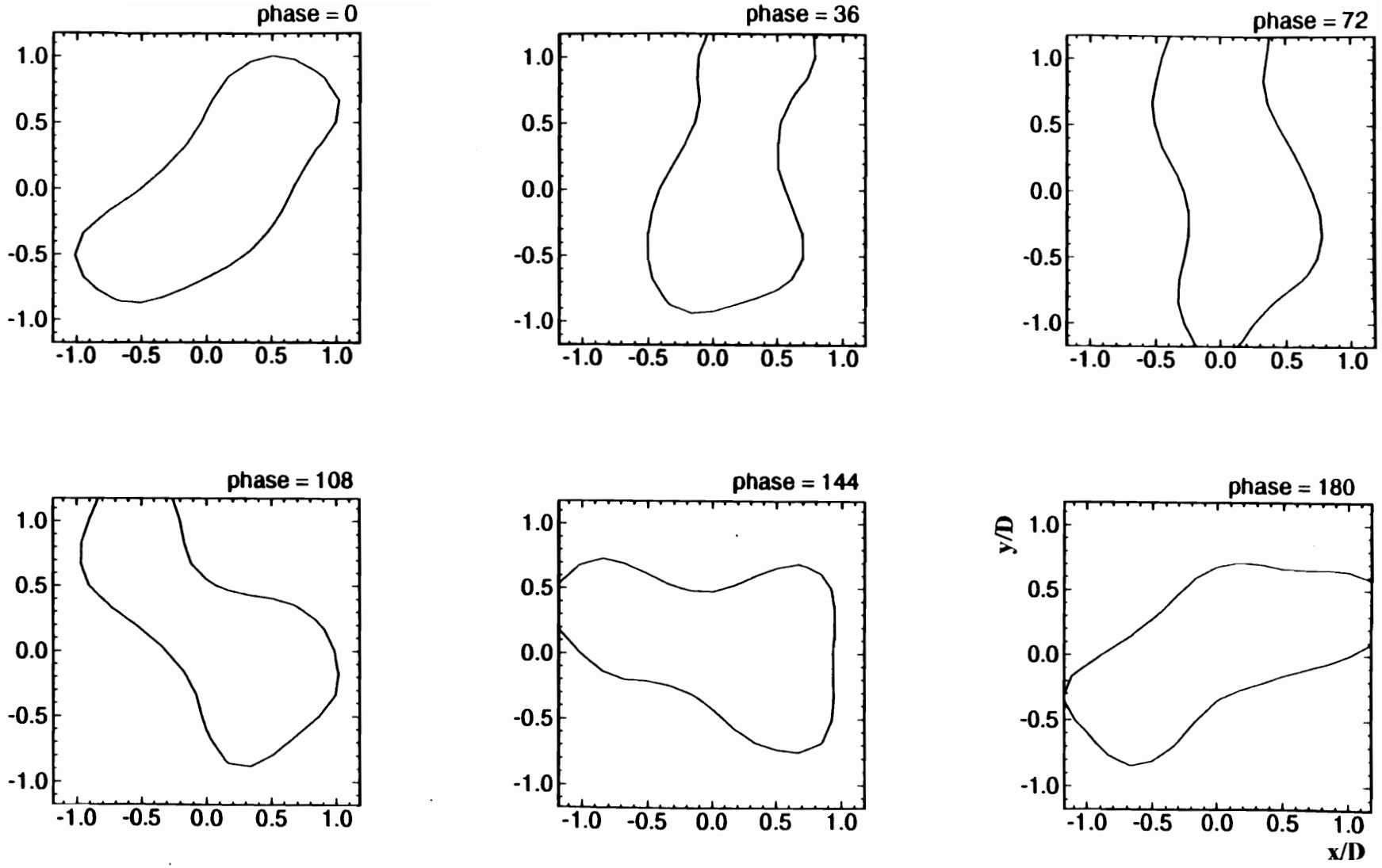

Figure 3.4.3 Experimental measurements of iso-velocity contours reflecting the effects of dynamic phase-offsetting under $m = \pm 1$ excitation

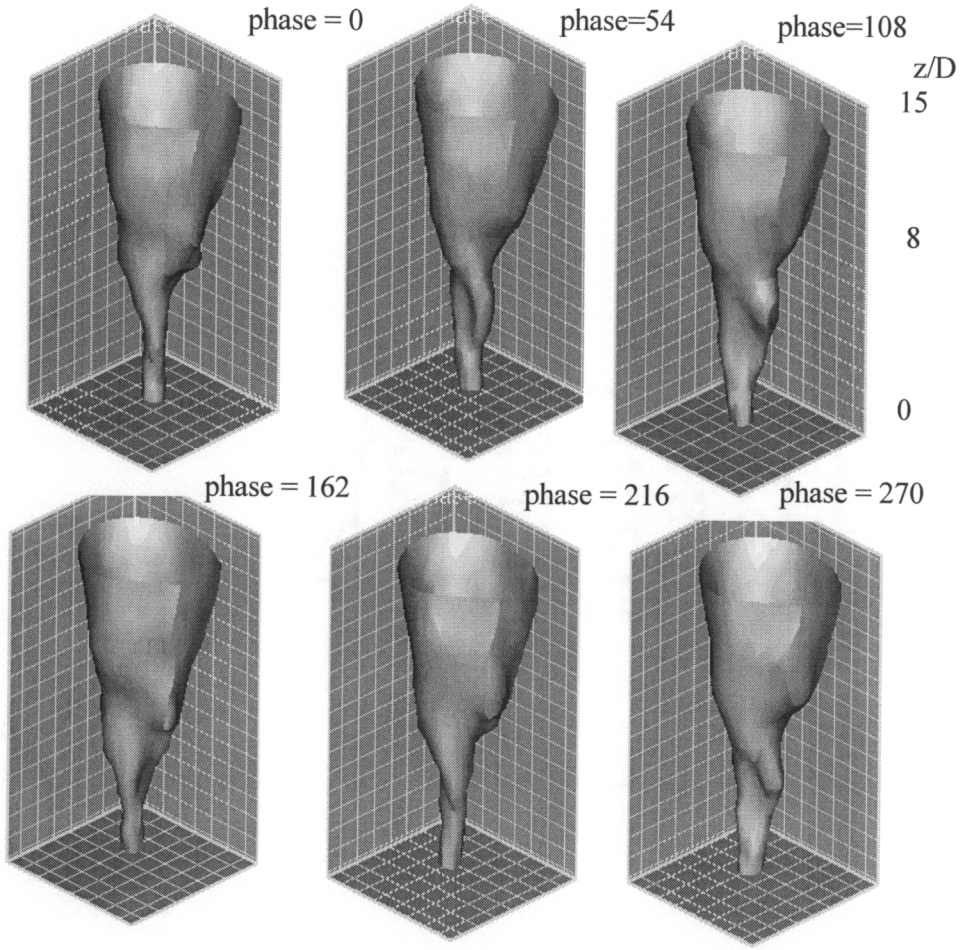

Figure 3.4.4 3-D view of phase mean velocity contour of U/Uj = 0.5 under phase modulation, f_e = 180 Hz

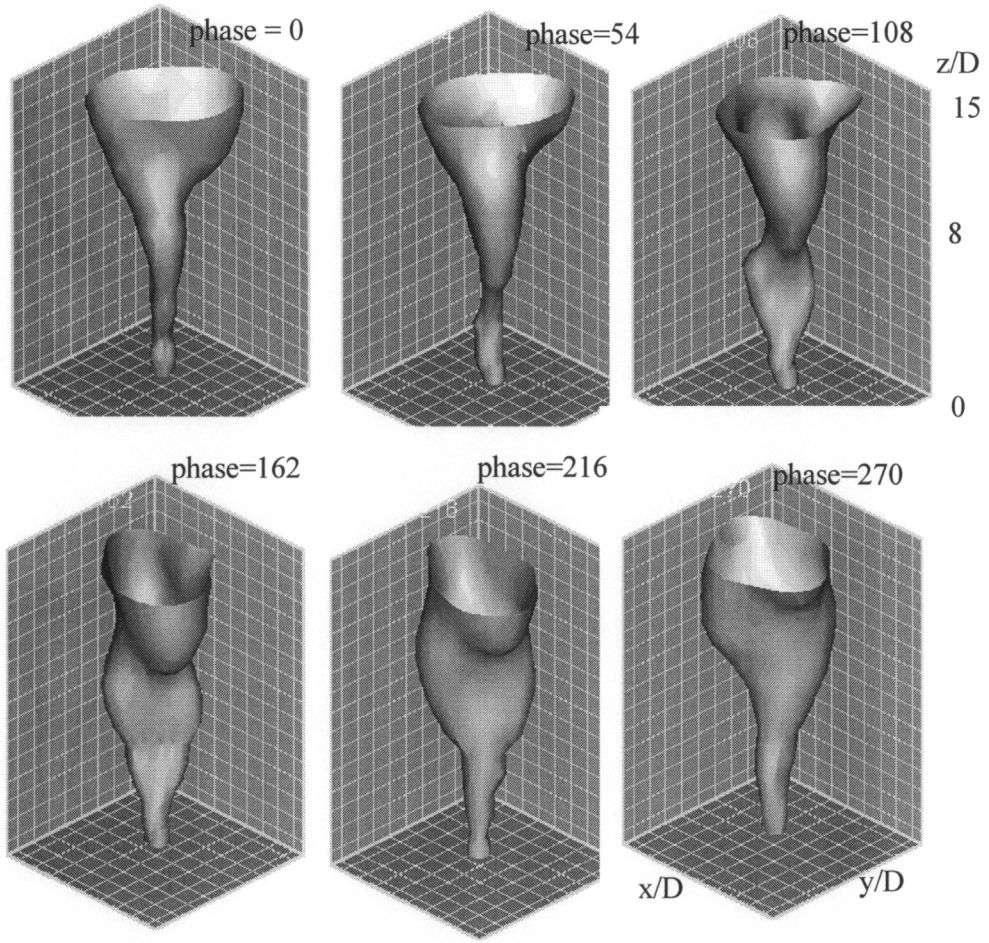

Figure 3.4.5 3-D view of phase mean velocity contour of U/Uj = 0.5 under switching modulation, f_e = 180 Hz

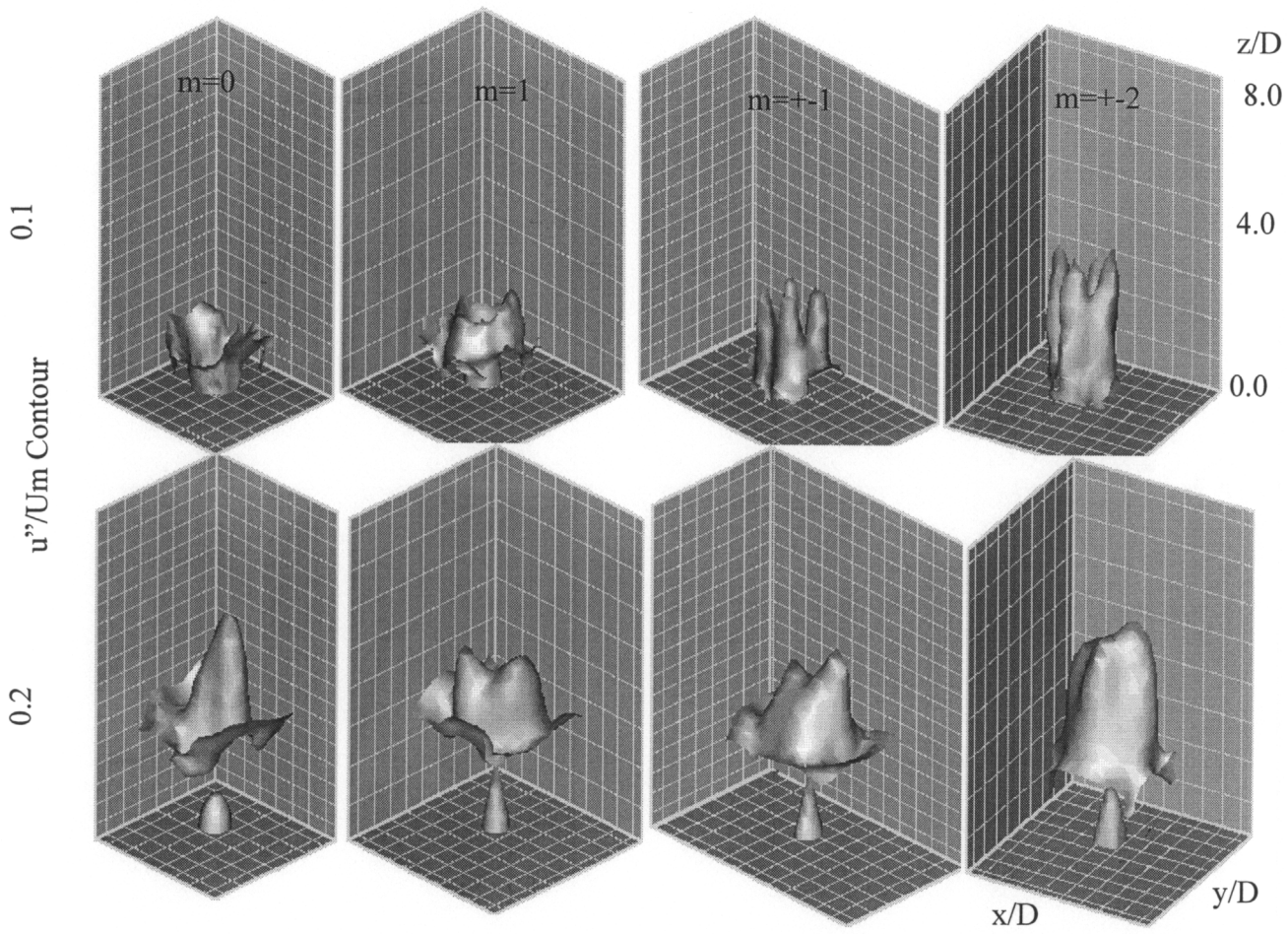

Figure 3.4.6a. 3-D view of organized turbulence level contours for cases of m= 0, 1 ±1 and ±2

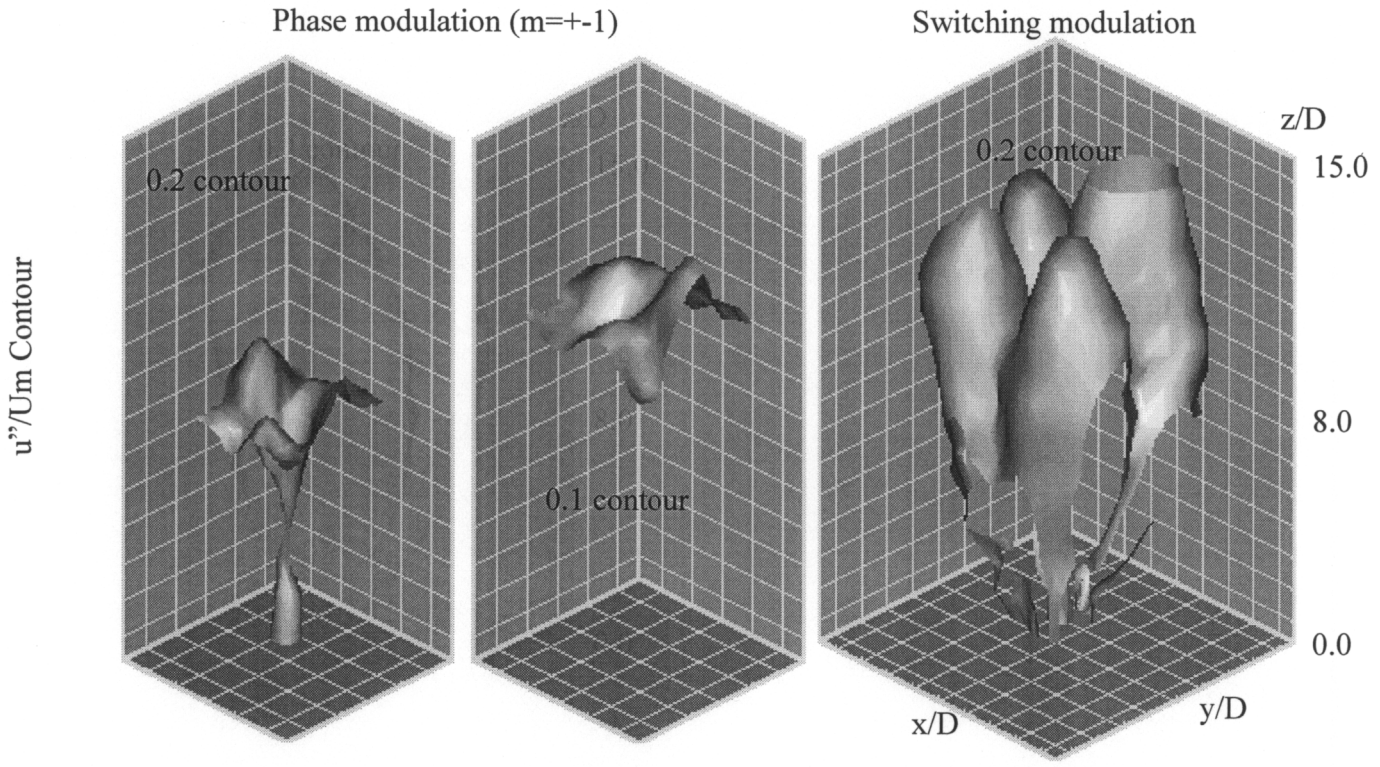

Figure 3.4.6b. 3-D view of organized turbulence level contours for cases of phase modulation and switching modulation

Chapter 4 Triangular Jet with Top Hat Velocity Profile

4.1 Introduction

In Chapter 2, spatial mode control was successfully applied to a triangular jet with a fully sheared exit velocity profile. In this Chapter, an examination of a triangular jet with an initial top-hat velocity profile is presented.

A top hat jet has a thinner shear layer near the nozzle, one might deduce that it is easier to control than a bell shaped jet. The reason for this assumption seems obvious that a thinner shear layer has a higher velocity gradient and therefore, is more admissible to outside disturbances, Huang and Ho (1982). While this is true, one may also recall the fact that the preferred mode has an amplitude that is almost an order of lower than the amplitude of the most amplified frequency in the near field. The preferred mode is taken as the most amplified frequency at the end of the potential core where the local velocity profile is almost bell shaped. Therefore, as a result of the fast deterioration of the most amplified frequency, the instabilities in the axisymmetric mixing layer is unable to influence the far field. Consequently, the existence of a thin shear layer in the near field is considered to have little effect over the far field when only frequency excitation is employed. It was pointed out in Chapter 3 that the large jet expansion in the far field was a result of interactions of large structures at the end of the potential core. Obviously, the shear layer near the nozzle has to be thick enough for the excited structures embedded in it to interact. The jet with bell shaped velocity profile satisfies this condition immediately. However, in this case the excited structures may not be able to grow large enough to interact unless the excitation level is sufficiently high. The top hat velocity profile helps the growth of the structure, but requires a longer distance for the axisymmetric shear layer to merge.

To address this question, this chapter contains the results of an investigation of a triangular jet with a top hat exit velocity profile; and the response of this kind of jet to spatial mode excitation. Other issues, such as dynamically control of the triangular jet, will also be briefly addressed.

The material presented includes unexcited and excited jet characteristics as deduced from the physical (velocity) and spectral spaces. First, the general behavior of the time mean flow without excitation is described. Second, an extended examination of the frequency domain characteristics (including determination of the preferred mode) is discussed. This is followed by a two dimensional mode spectra analysis in which the role of the multiple spatial modes is emphasized. Third, the growth of the amplification in the near field and the velocity contours which depict the jet expansion under different spatial mode excitation is explored. Fourth, a brief introduction of the dynamic spatial mode control using phase modulation is given. Finally, a discussion is presented to stress the role that the initial velocity profile and the nozzle geometry have on jet expansion and flow entrainment.

4.2 Characterization of the Unexcited Flow

In this section the initial flow conditions are defined. The jet facilities and experimental techniques used in this investigation were described in Chapter 3. The flow conditions used in this experiment were the same as those in Chapter 3. The jet speed was 20 m/s which resulted in a Reynolds number of 3.4×10^4 based on the momentum equivalent nozzle diameter of 2.54 cm. The free-stream turbulence level was less than 0.1%. The length scale D had been used extensively in this experiment because it was a more relevant factor than the length scale θ/R in describing the development of jet in the far field. The actuators used in this experiment were three loudspeakers positioned on the flat sides of the nozzle. This arrangement, similar to the setup in Chapter 2, helped to compare the results between triangular jets with different velocity profiles. It has to be

noted that other setups could also be used. For example, six actuators could be mounted on both the flat sides and the sharp corners. This kind of setup is, however, not presented in this dissertation.

Shown in Figure 4.1 is the velocity and turbulent level distribution at z/D = 0.125. This equilateral triangular nozzle is symmetric about each of the three lines (we may call it the center line) that cross the centroid and the apex. Therefore, the distributions along only one line are shown. As seen, the mean velocities are flat except at both the flat side and sharp corner (vertex) where the thin shear layers exist. The turbulent level at the sharp corner is slightly higher than on the flat side (11.5% vs. 9.5%). This difference is not as pronounced when compared to the result of Chapter 2 and the case reported by Gutmark et al. (1987). The fact that the differences between the turbulent levels of the flat side and the sharp corner are small may affect the performance of the jet and will be examined later.

Figure 4.2 shows the momentum thickness distributions measured along the flat side and the vertex. As seen, the momentum thickness over the flat side is thicker than the apex.

The velocity profile along the streamwise direction measured at the centroid is shown in Figure 4.3 using the equivalent momentum diameter for non-dimensional scaling. Similar to the circular jet discussed in Chapter 3, the center line velocity is approximately constant for $z/D < 4$, followed by a rapid decrease after the end of the potential core. The agreement between this result and that of Chapter 3 that the potential core ends at z/D=4 demonstrates the validity of equivalent momentum flux assumption.

4.3 The Preferred Mode

For a better understanding of near field behavior of the instabilities, the study of the preferred mode is necessary. However, this type of study is a non-trivial work since to determine the preferred mode the frequency domain information has to be acquired

through velocity measurements that are 3-D in space and 1-D in time. As mentioned in Chapter 3, Hussain's method (1989) was adopted in this study to determine the preferred mode. In this method, artificial excitation with excitation levels higher than the background noise was used to excite instabilities of the jet so that the most unstable mode can be determined.

Extensive frequency measurements were made in the near region of the triangular jet (z/D < 0.5) on both the flat side and the sharp corner using the bottom loudspeaker as the excitation source (equivalent to m=0 excitation). While keeping the excitation level constant ($u_f' / U_0 = 1\%$ at z/D=0 and r/D = 0), the range of excitation frequency was scanned between 160 Hz and 3000 Hz. Similar to the results of the circular nozzle addressed in Chapter 3, the most amplified frequencies on both the flat side and the sharp corner peaked at 2000 Hz for z/D < 0.125. This result was not unexpected because the momentum thickness at the outlet of both nozzles was roughly equivalent. However, similar to the argument discussed in Chapter 3, the most amplified frequency was not the most important factor that governed the development of the jet in the far field, and hence, was of less of concern. Next, the region beyond z/D = 0.5 is explored in greater detail.

Shown in Figure 4.4 is a 3-D view of the measurements in frequency domain for the flat side. As mentioned in Chapter 3, u_{int}' / U_0 represents the growth of amplification and its slope the amplification rate. Two distinguishing features can be observed. First, the amplitude of amplification decreases rapidly along the streamwise direction. The higher the frequency the quicker it decreases, typically at f = 1000 Hz the amplitude decreases from 0.7 at z/D = 0.125 to 0.01 at z/D=4. Second, there are two peaks below 1000 Hz, one for f=400 Hz (amplitude = 0.14, at z/D=1.8) and the other for f=315 Hz (amplitude = 0.08, at z/D=4). Similar observations can be made for the sharp corner as shown in Figure 4.5. In this case the higher peak is at f=550 Hz (amplitude = 0.2 at z/D=1.5) and the lower peak is at 300 Hz (amplitude = 0.07, at z/D=4). In both cases, the flat side and the sharp corner, one can observe the frequency shifting from higher to lower values. The continuous frequency shifting reflects the appearance of a new kind of

instability that is related to the jet column instability as opposed to the mixing layer instability close to the nozzle, a point that will be elaborated on later. The frequency that peaks at the end of the potential core is defined as the preferred mode, Hussain (1989). The preferred modes at both the flat side and the sharp corner are about the same (315 Hz vs. 300 Hz). Also, at the location where the preferred mode is defined (z/D=4) the amplification rate is much lower than the most amplified frequency close to the nozzle.

Power spectra contours for the flat side are shown in Figure 4.6. These figures depict the development of disturbances in the frequency domain along the radial and streamwise direction. Shown are the cases of f=160 Hz, 315 Hz, 550 Hz, and 1000Hz excitations that cover the frequency range of interest. Several observations can be made:

1. The growth of the shear layers along the streamwise direction are about the same for all cases. This result partly indicates the insensitivity of the jet to single mode excitation. The same observation was made for the circular nozzle.
2. The center of the peak values (above -40 db) of the power spectrum for f < 550 Hz are at the range of 0<z/D<2. For the case of f=1000 Hz the peak value is below z/D=1.
3. The peaks of the power spectra are not necessary centered along r = 0.5 line. They actually spread outwards downstream. For instance, at f=1000 Hz excitation, the peak of the power spectrum is at r/D = 0.45 for z/D = 0.125, and at r/D=0.5 for z/D = 0.8.

The power spectrum contours for the sharp corner are shown in Figure 4.7. The contours are only slightly different from that for the flat sides. For example, the peak value of the power spectrum are centered closer to the r/D=0.5 line. And in the case of 315 Hz, there are two peak amplitude regions with one below z/D = 0.5 and the other in the range of 1 <z/D < 3.

The power spectrum distributions along the radial direction at z/D = 2 for excitation frequencies of f=160 Hz, 315 Hz, 550 Hz, and 1000 Hz are shown in Figure 4.8 for the flat side. As can be seen, unlike in the case of the fully sheared jet discussed in Chapter 2, the jet responds and equals the excitation frequency for all cases. The

excited fundamental frequency attains its maximum closer to the r/D=0.5 along the radial direction. Except for f=1000 Hz excitation, no harmonics are observed. The results on the sharp corner shown in Figure 4.9 are very similar.

The power spectrum distribution along the streamwise direction for the flat side is shown in Figure 4.10. At every streamwise station, there are 16 power spectra data set along the radial direction. Among the data sets the one that has the maximum amplitude at the excitation frequency was chosen and plotted. As seen, except for the case of f= 160 Hz excitation, all of the amplitudes of excitation frequency decrease along the streamwise direction. In the f=1000 Hz case one can see the existence of harmonics and subharmonics. While it is true that higher excitation frequency (f >550 Hz) results in a higher amplitude, it also results in a faster drop of the amplitude. The f=160 Hz case has a noticeable increase in amplitude of the excitation frequency for z/D<2.

The power spectra along the streamwise direction for the sharp corner are shown in Figure 4.11. Similar to Figure 4.10, in the f = 1000 Hz case, there exists both harmonics and subharmonics. Noticeable difference to Figure 4.10 is that for f < 550 Hz, the frequency amplitude close to the nozzle is higher.

Generally speaking, the similarities that exist in the frequency domain between the flat side and the sharp corner are robust. This by no means indicates that the characteristics of the shear layers on both sides are the same. It only serves as a reminder to the reader of the fact that power spectra cannot be used as the only way to identify the state of the shear layer that develops from the flat side and the sharp corner of the triangular nozzle. One of the differences between the flat side and the sharp corner is, as pointed out by Hussain *el al.* (1989), that the sharp corner can generate intense self-induction resulting in cross-linking and fine-scale mixing while the flat side can not. It is obvious then, like the conclusions drawn from Chapter 3, that to control the jet solely by frequency excitation is impossible. Spatial mode control has to be incorporated. This will be discussed next.

4.4 Spatial Mode Control

When the flow is under one type of spatial mode forcing, many modes could be excited. In such occurrence, it is necessary to understand which mode is dominant in the excited flow and which mode has the fastest growth rate. The following two sections, "Mode spectra" and "Growth of spatial mode", examine these questions. After that, in the section "An overview of standing wave excitation" the behaviors of the standing wave excitation are explored using a very simple mathematical model based on equation 3.3.2,

$$U_m = A \times \cos(2m\phi + \psi_0)$$

where m is the standing wave mode number, ϕ the azimuthal position and ψ_0 the initial phase angle. The use of this equation is based on the reasoning that the shape of the velocity contour of the excited jet follows a $\cos(2m\phi)$ curve. As one can see, the resulting velocity curve is a function of excitation amplitude, the mode number and the initial phase angle. Aided by the useful information derived from the above mentioned sections, the most important part of this chapter -- the 3-D structures of the excited jet are investigated in the section "3-D view of the velocity contour" and important conclusions about the effects of initial conditions drawn. Finally, the control of the triangular jet using dynamic modulation is also examined in the section "Phase modulation".

Mode spectra

When the spatial mode excitation method was applied to a non-circular nozzle, the generated modes could become quite complicated. It is the goal of this section to investigate the possible combining influences of a non-circular geometry and spatial-mode manipulation.

Figure 4.12 shows the results of measured mode spectra as they develop along the streamwise direction. The maximum amplitude mode spectrum line along the radial direction is shown at each streamwise station.

The results of m=0 excitation are shown in Figure 4.12a. The generated modes 0 and 1 are about the same amplitude (about 0.08, non-dimensionalized by the center line velocity). The amplitudes of mode m= -1 and 2 are lower, both about 0.025. The mode amplitude for 0 and 1 decreases rapidly along the streamwise direction and reaches the same amplitude as modes -1 and 2 at a streamwise location of z/D=1.5. The fact that m=0 excites both the m=0 and m=1 modes is noteworthy.

The picture for m=1 excitation is different as shown in Figure 4.12b. Here, m=1 is the dominant mode. At z/D=0.5 the amplitude of m=1 is 0.14, twice that of the m=0 excitation. While always dominant, the amplitude of mode=1 decreases along the streamwise direction in the same manner as other modes. It is not clear, from the current study, why m=0 excitation excited multiple modes (m=0 and 1) while m=1 excitation excited only a single mode (m=1). However, the resulting flow field represented by velocity contours demonstrated dramatic differences. These differences will be discussed later.

Figure 4.12c shows m = ±1 excitation. In the near field (z/D=0.5), the amplitudes of m=1, -1 and 0 are comparable. Further downstream between $0.5 < z/D < 2$, m=1 has a higher amplitude. Contrary to the case of the fully-sheared triangular jet and the top hat circular jet, where both m=1 and -1 had a comparable amplitude, the amplitude of m= -1 in this case is comparable to the non-excited mode, i.e. m= 0, while m=2 had a much larger amplitude. One may be tempted to conclude that the smaller amplitude of m= 1 and -1 is a combined result of initial velocity profile and geometry. However, it was difficult to investigate its detailed mechanism using the available technique.

Growth of spatial mode

The growth of amplitudes for both the flat side and the sharp corner is shown in Figure 4.13. The spatial modes shown are m=0, 1, 0.75, ±1 and ±0.5. The trend in both cases are similar. The growth of amplitude decreases for almost all cases along the

streamwise direction. However, for the case of $m = \pm 0.5$ on the sharp corner there is a slight increase at z/D < 2.25. One can see that the slope for the flat side is steeper. This means a more rapid decay of the excited disturbance. Also one can observed that the amplitudes of the spatial modes of the flat side in the region of z/D<2 are higher than those of the sharp corner.

The decrease of amplitude along the streamwise direction shows that the jet expansion mechanism in the far field can not be explained by the near field instability mechanism. This conclusion is the same as of the circular nozzle examined in Chapter 3.

An overview of standing wave excitation

Using the same method discussed in section 3.2.3, one can study the possible jet shapes that could be generated by standing wave excitation. Figure 4.14 demonstrates the general behavior of standing wave modes. Figure 4.14a depicts the velocity contour of m=±0.5, ±1, ±1.5, ±2 excitation for the same amplitude. The dashed line indicates the nozzle size. One can observe from the figures that there are leaf-like protrusions in the profile. The leaf-like protrusion pattern follows the rule found in section 3.2.3. The rule states that the protrusion corners (polygonal angles) increase with increasing mode number (increments by 0.5). The number of protrusions equals the mode number divided by 0.5. However, there are differences as compared to the circular jet discussed in chapter 3. For instance, for m = ±1 case, at the junction of two "leaves" there is a wedge-like smaller sharp corner. The sharp corner shape exists in all cases, and all of them point to the direction of the geometrical sharp corner of the triangular nozzle. This behavior indicates the importance of the influence of the geometry. In mode = ±0.5 case, the leaf-like contour aligns somewhat with one side of the triangular nozzle. While for mode = ±1, the formation of the two "leaves", aligns with the horizontal line. One can observe such directional formation of the leaves in measured data introduced later.

The effect of excitation amplitude is shown in Figure 4.14b for m = ±1 excitation.. As seen, when amplitude increases, the center of the profile becomes narrower and the leaves tend to break away and expand outward.

The effect of phase-offset is shown in Figure 4.14c. As seen, the phase-offset can indeed re-orient the direction of the profile. For example, 0^0 phase-offsetting aligns along the horizontal direction and 90^0 vertical. However, the shape of the predicted profile changes as well. This examination can help to predict and explain the results of the phase modulation control discussed later in this chapter.

3-D view of the velocity contour

A three dimensional depiction of the velocity contour of the unexcited jet is shown in Figure 4.15. In this figure, three views are shown: a top view (top left hand corner), a zoomed 3-D view (bottom left hand corner, $0<z/D<0.5$) and a 3-D view (right hand side, $0<z/D<15$).

One of the distinguishing features of this figure is the existence of a switching phenomenon that was not observed in the same kind of figure (Figure 2.9 in Chapter 2). The switching phenomenon can be better observed from the zoomed view. As seen, the apex at the bottom of the triangular shaped velocity contour is opposite in its protruding direction to the one at the top. Since all other conditions are the same, it is obvious then that the initial velocity profile plays a decisive role in the existence of the axes switching. The triangular nozzle studied in Chapter 2 has a fully-sheared initial velocity profile while the current nozzle has a top-hat profile. A top hat velocity profile implies the existence of a very thin shear layer near the nozzle exit which helps the generation of vortex rings. The mechanism of vortex ring generation is similar to the one that was explained by Hussain and Husain (1989) in an elliptic jet. Because of the strong self-inducement of the vortex ring at the sharp corner, the ring rolls up faster there. It then folds in the direction of the opposite flat side. As a result, the induced velocity on the flat

side is directed outward and increases. Consequently, the vortex again takes a triangular shape, but the axis has been switched. While in the near field the view is different from that of the fully sheared triangular nozzle, in the far field the view is similar (the jet contour becomes circular). This is a natural transition after the jet becomes fully merged and the potential core disappears.

Shown in Figure 4.16 are velocity contours for several spatial mode excitations. The excitation frequency is 180 Hz in all cases. Shown are excitation modes m=0, 1, 0.75, ±0.5 and ±1 at 0^0 phase in the excitation cycle. On the left is the top view, the middle the side on the direction of the largest expansion, and on the right the 3-D view.

Shown in Figure 4.16a is the m=0 case. Surprisingly, no trace of switching can be observed. There, also, is no appreciable jet expansion as compared to the unexcited case. It seems that m=0 excitation inhibits both axes switching (a very important flow entrainment mechanism) and jet expansion. Although the initial velocity profile and the geometry are quite different, the triangular nozzle with a fully-sheared velocity profile, the circular nozzle with a top-hat velocity profile and, in this case, the triangular nozzle with a top hat velocity profile exhibit a very similar picture if viewed in a 3-D view. The observation is that the m=0 excitation results a small jet expansion. This similarity in behavior confirms the observations that axisymmetric excitation is ineffective in jet control.

Contrary to the case of m=0, m=1 excitation reveals both large jet expansion and axis switching behavior as seen in Figure 4.16b. Some observation can be made:

1. Before the end of the potential core (at about 3<z/D<4) the jet exhibits little expansion. However, jet undulations can be observed from the side view. This observation agrees with the mechanism suggested in Chapter 3, where it was argued that non-linear jet expansion happens only after the potential core ends as a result of interactions between opposite structures.
2. After the potential core ends (z/D=4), the jet demonstrates axis switching (see the 3D view) and a large expansion along the switched axis direction. This expansion is like

an overshooting that spreads outward along the formerly flat side. Along the formerly sharp corner there is less expansion. After z/D>10 the expansion is about equal from all azimuthal directions.

3. The cross sectional velocity contour in the resulting far field is still triangular as seen from the top view. This phenomenon indicates that m=1 excitation is able to maintain the original jet geometry, while at the same time achieves large expansion.

Figure 4.16c shows the jet for m=0.75 excitation. The shape of velocity contour in the far field is shaped rather like a triangle than an ellipse. Switching can still be observed and large jet expansion is achieved in the far field. If observed from the top view, one may see the similar behavior as shown in Figure 3.11c of the same mode excitation but for a fully-sheared initial velocity profile. Again, similar to the results of other configurations, the jet expands only after the potential core ends. One can also notice that the size of the area enclosed by the U/U_0=0.5 contour is smaller than the m=1 case. This is contrary to the fully sheared jet discussed in Chapter 2.

Standing wave excitation for $m = \pm 1$ and $m = \pm 0.5$ are shown in Figures 4.16d and 4.16e respectively. Compared to Figure 4.14a of the predicted velocity contour, one can see that the orientation of the measured velocity contour is indeed as predicted. For example, for $m = \pm 0.5$ excitation the predicted tilting angle is about 45^0. This agrees with the measured data shown in Figure 4.16e (top view). Similarly, in the $m = \pm 1$ case the predicted and the measured contours all align with the horizontal direction. However, the measured cross sectional shape of the velocity contour fails to match the predicted one. The former is more elliptically shaped. The amount of jet expansion in both cases is satisfactory and is of the same order. In both cases the resulting contours in the far field are shaped in an elliptical pattern and axis switching can be observed.

Dynamic mode control -- Phase modulation

In this section dynamic spatial mode control method is examined using only the phase modulation method. During the discussion of Figure 4.14c, it was argued that the direction of the expansion angle can be easily determined and modulated for m = ±1 excitation. To verify this prediction, Figure 4.17 shows six frames of iso-velocity contours of U/U_0=0.5 sampled 30^0 apart. As seen, compared to the spatial mode excitation, the flow has a better response to excitation, since the flow structure extends farther downstream. However, the iso-velocity contour does not respond to phase-offsetting -- there is no rotation of the iso-velocity contour. This is contrary to the prediction by Figure 4.14c that as the phase offset dynamically the iso-velocity contour can rotate along the azimuth. The simple algorithm employed in depicting phase offset in Figure 4.14c, although proved to be able to predict the phase modulation characteristic of a circular jet, failed in this case. This fact shows that the flow structure of a non-circular jet is more complex than a circular jet.

4.5 Discussion and Summary

The most noteworthy result derived from this chapter is that the initial velocity profile plays a very important role in determining the development of jet expansion in the far field. The result can be summarized as follows:

1. It has been a recognized phenomenon that non-circular jets exhibited axis switching. However, it was found in this study that this observation was valid only in a jet with an non-symmetrically shaped nozzle and an initial top-hat velocity profile. Axis switching would result only when these two conditions were satisfied. An initially fully-sheared jet cannot generate a vortex ring -- the necessary condition for axis switching. It is obvious then that there would be no axis switching in such a jet, even though the nozzle geometry is non-circular.

2. The most interesting comparison was made with m=1 excitation. It may be difficult to explain precisely why m=1 excitation succeeded in achieving large jet expansion in a jet described in this chapter while failed to do so in a jet described in Chapter 2. However, it is evident that the initial velocity profile had played an important role. The jet discussed in Chapter 2 was fully sheared at the nozzle exit, while the jet discussed in this chapter had a top-hat velocity profile at the nozzle exit. Because of this, both axis switching and a large jet expansion was achieved using m=1 excitation. It is postulated that an initial top-hat velocity helps the formation of vortex ring. The coexistence of a vortex ring and non-uniform geometry helps to generate the axis switching. The m=0 excitation destroys the self inducement mechanism of the vortex ring by pumping the flow at the same time on all three sides of the jet. As a result, any jet expansion at one period is prevented by the jet contraction at the following period. The m=1 excitation avoids such side effects by exciting the triangular jets azimuthally in a sequential manner. In such a way, the jet expansion develops successively along the azimuth.

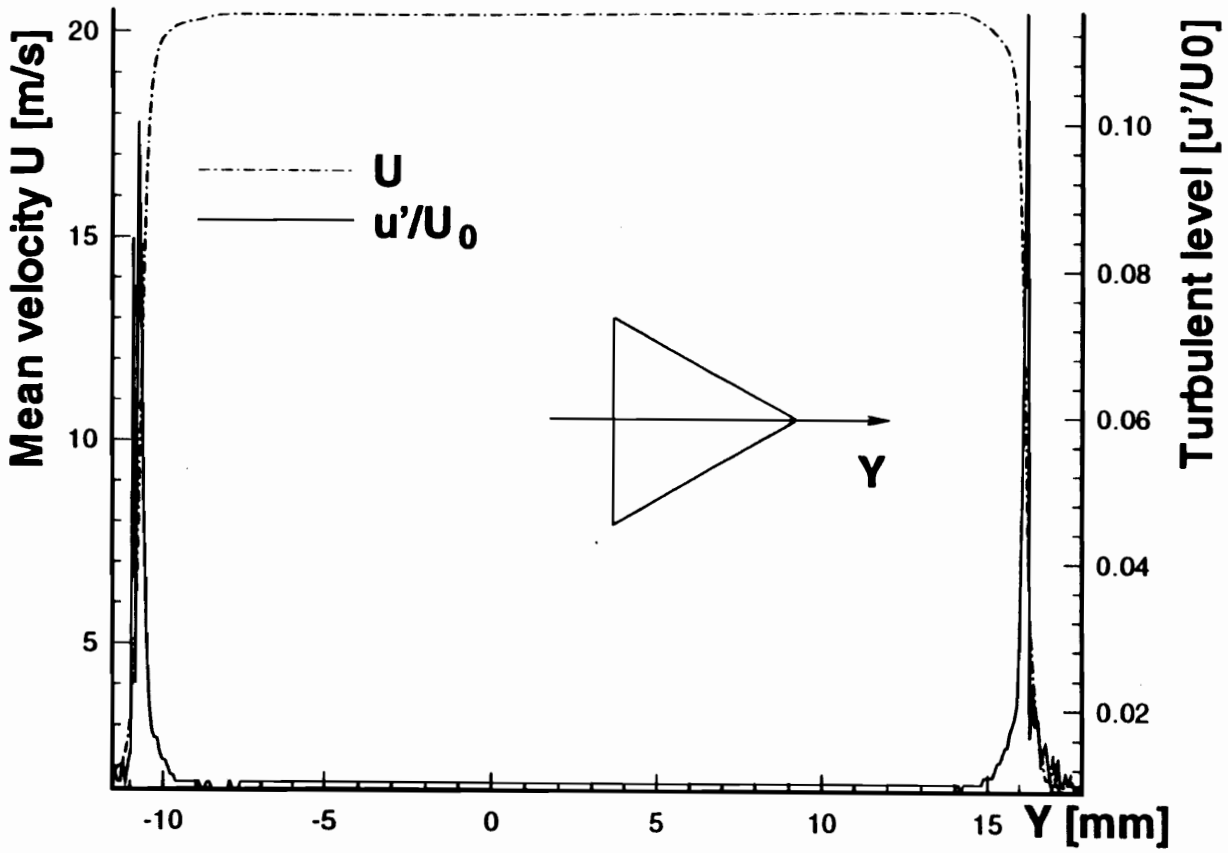

Figure 4.1 Mean jet velocity and turbulence intensity profile (flat side to vertex cross section)

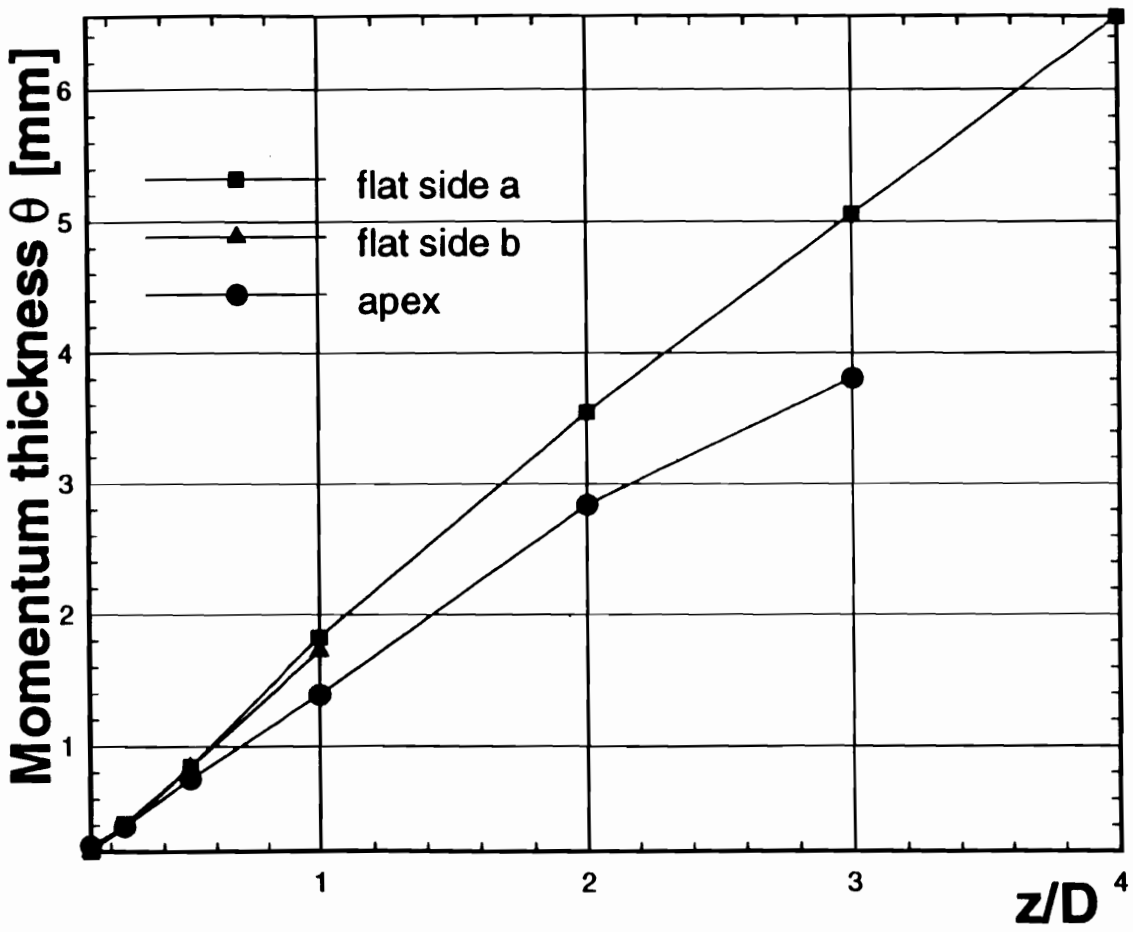

Figure 4.2 Momentum thickness on flat side and sharp corner along the streamwise direction

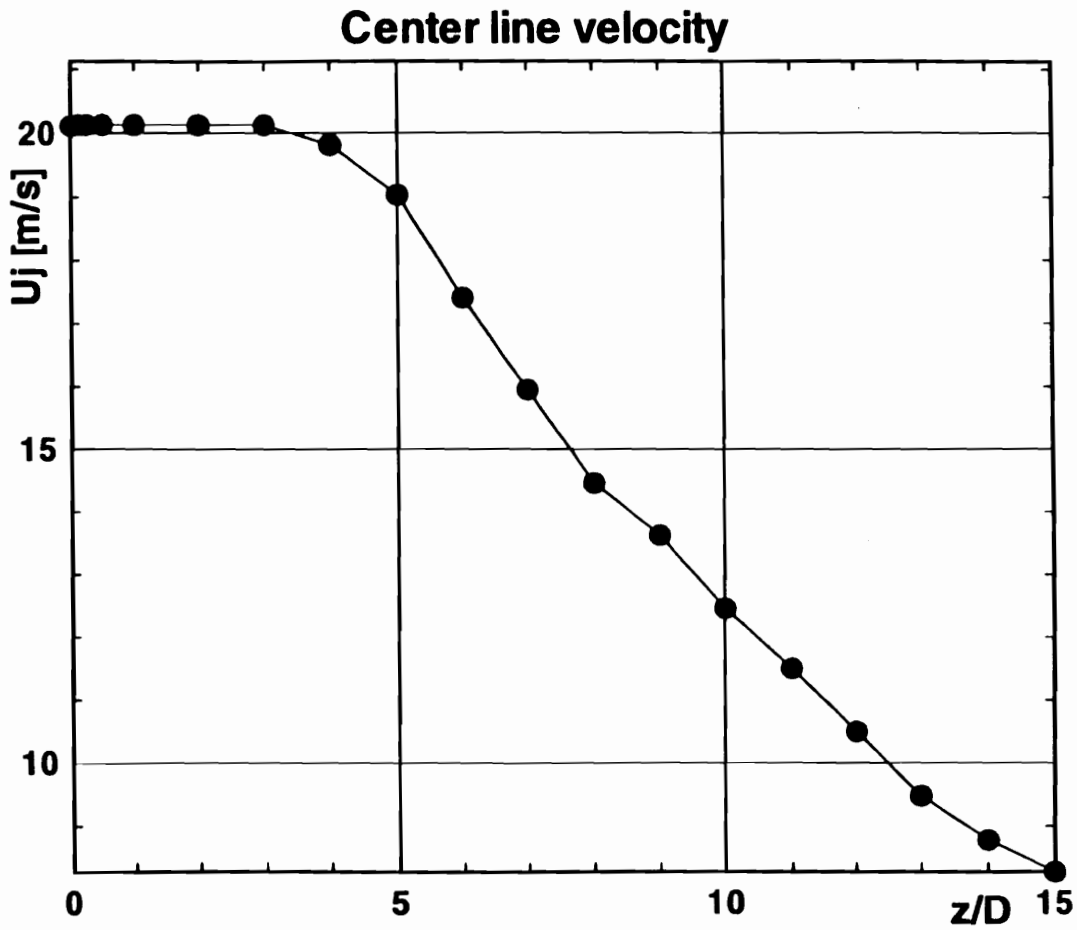

Figure 4.3 Center line velocity along streamwise direction

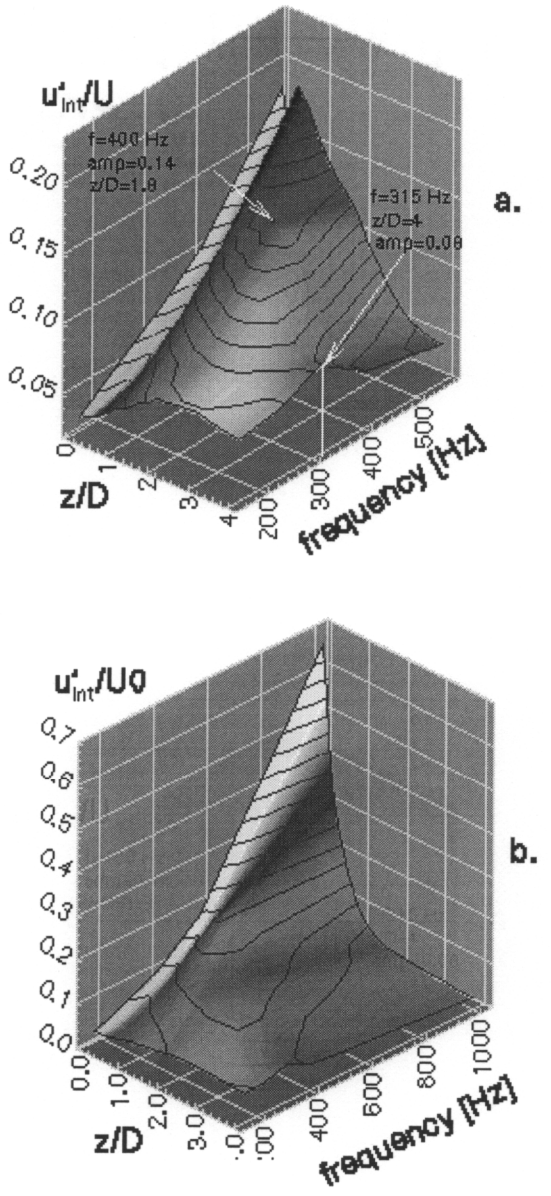

Figure 4.4 Three dimensional view of the amplification of the excited fundamental amplitude on flat side, a: 0<z/D<4; b: 0<z/D<0.5

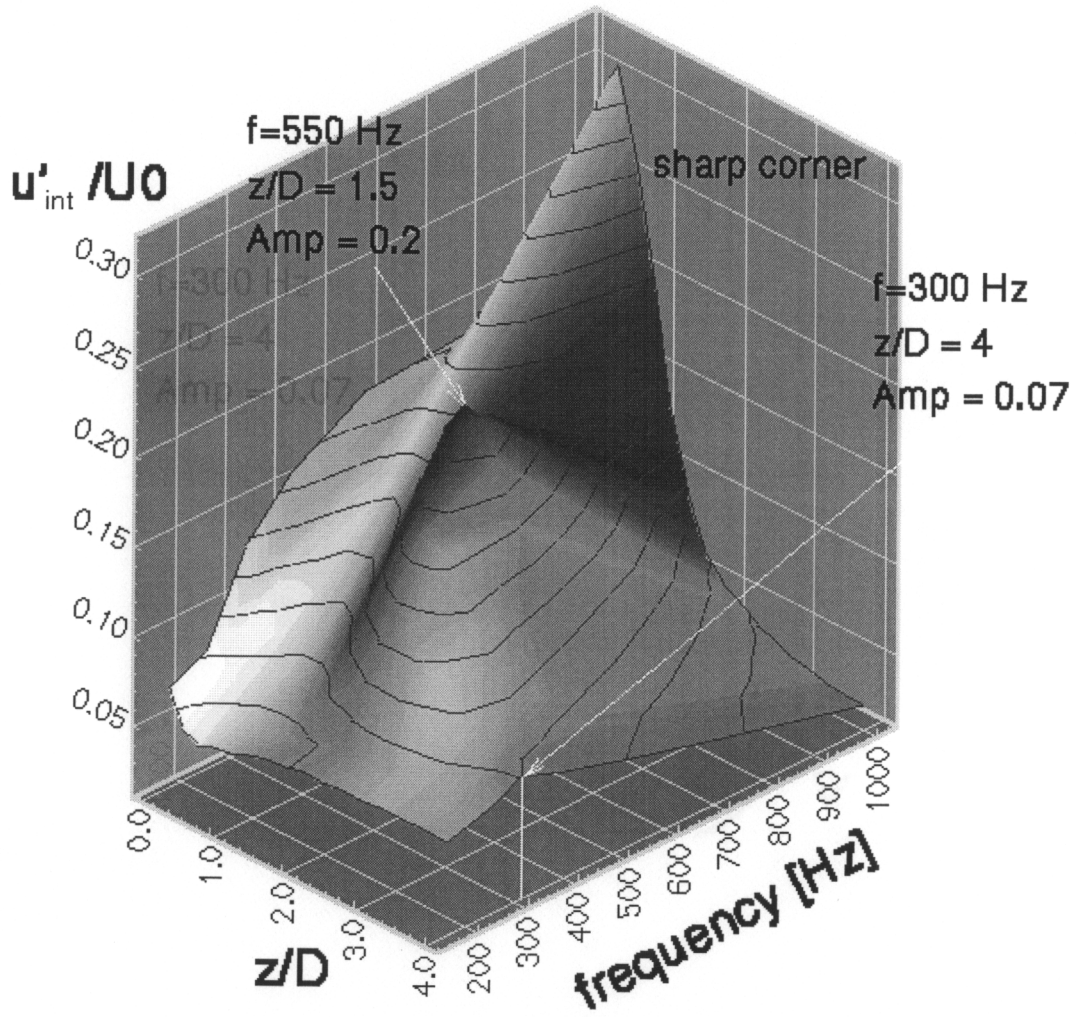

Figure 4.5 Three dimensional view of the amplification of the excited fundamental amplitude at the sharp corner, 0<z/D<4

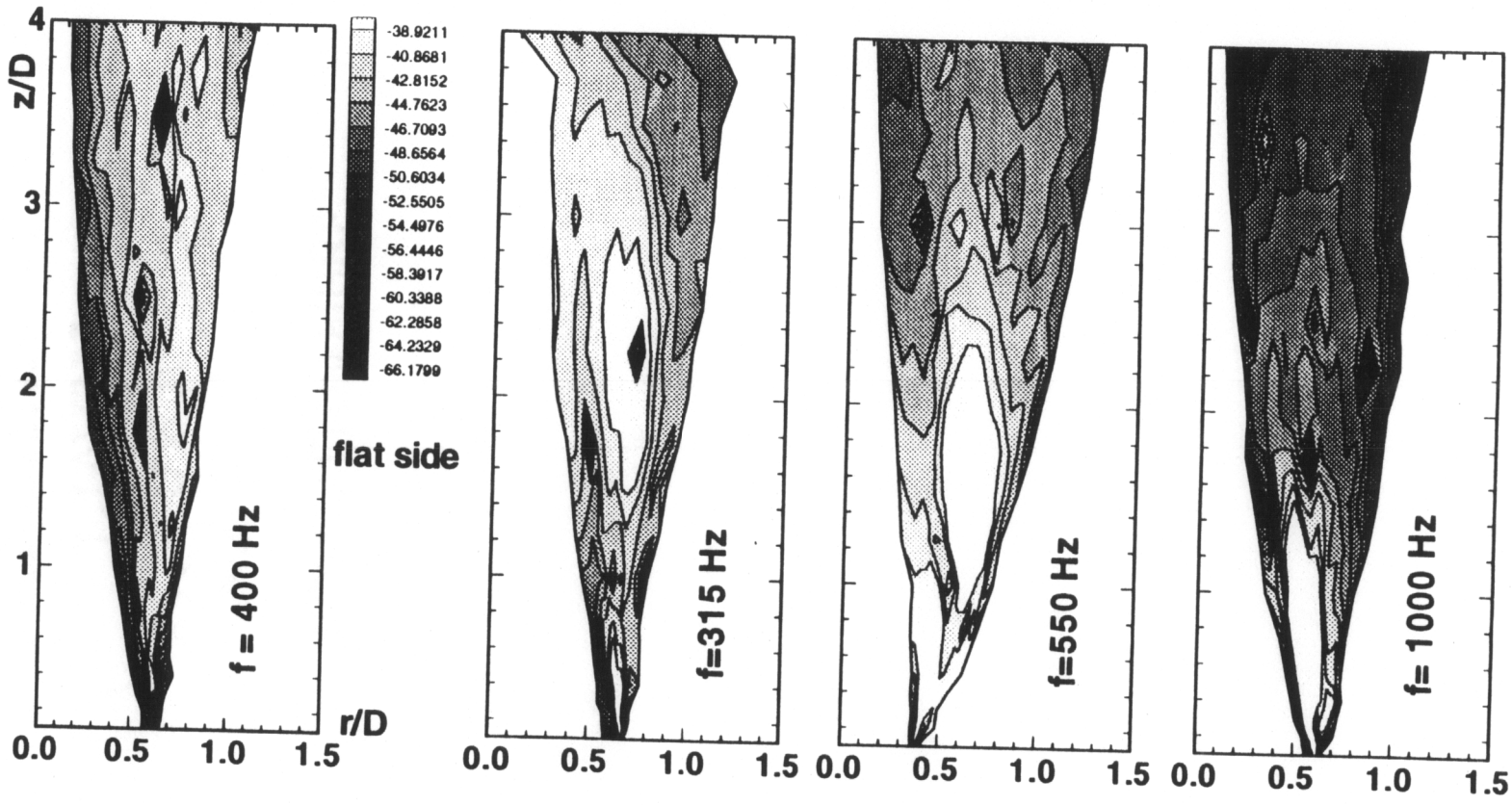

Figure 4.6 Power spectra of the development of the disturbance amplitudes at the excited fundamental frequency on flat side

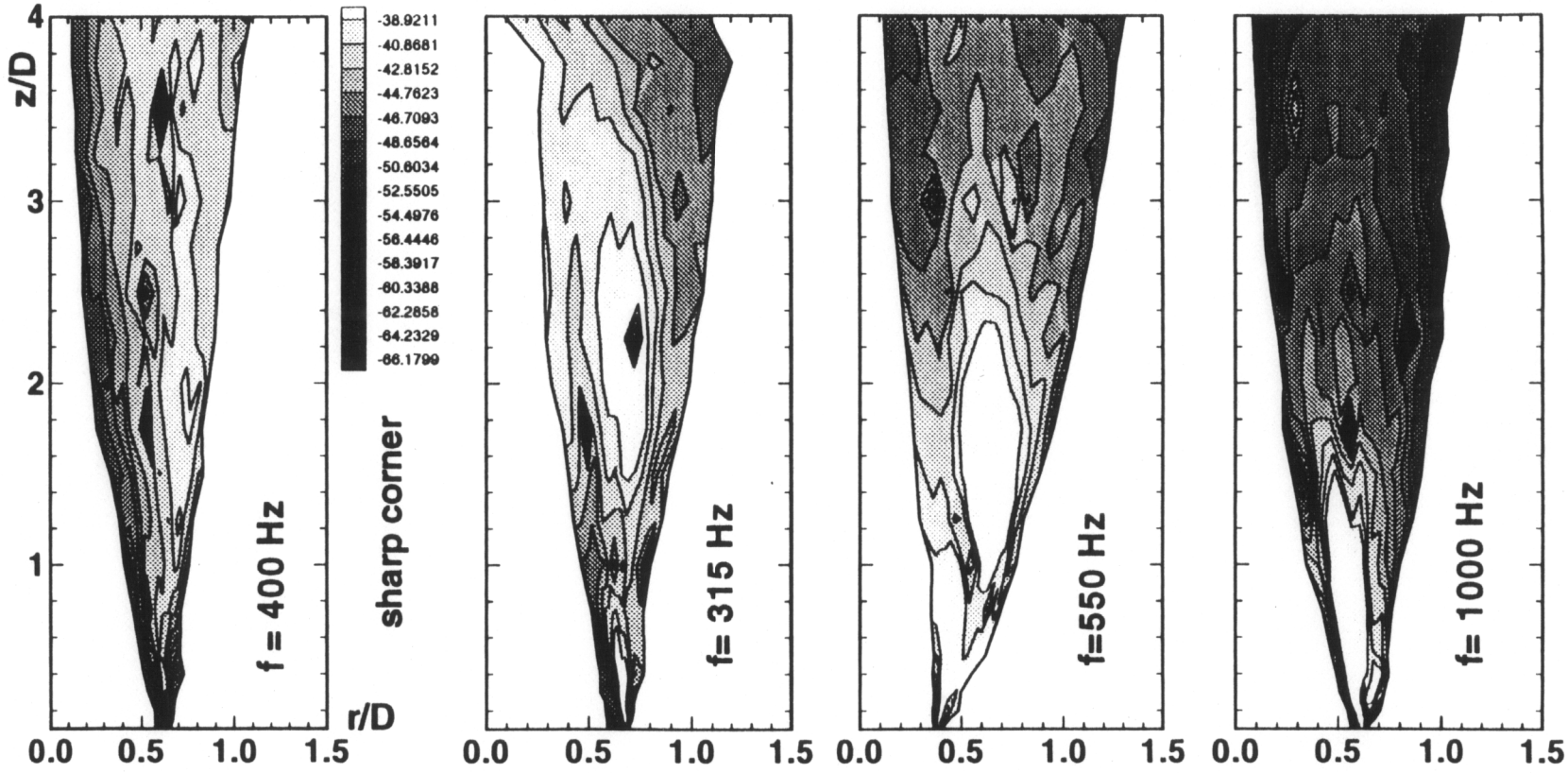

Figure 4.7 Power spectra of the development of the disturbance amplitudes at the excited fundamental frequency at a sharp corner

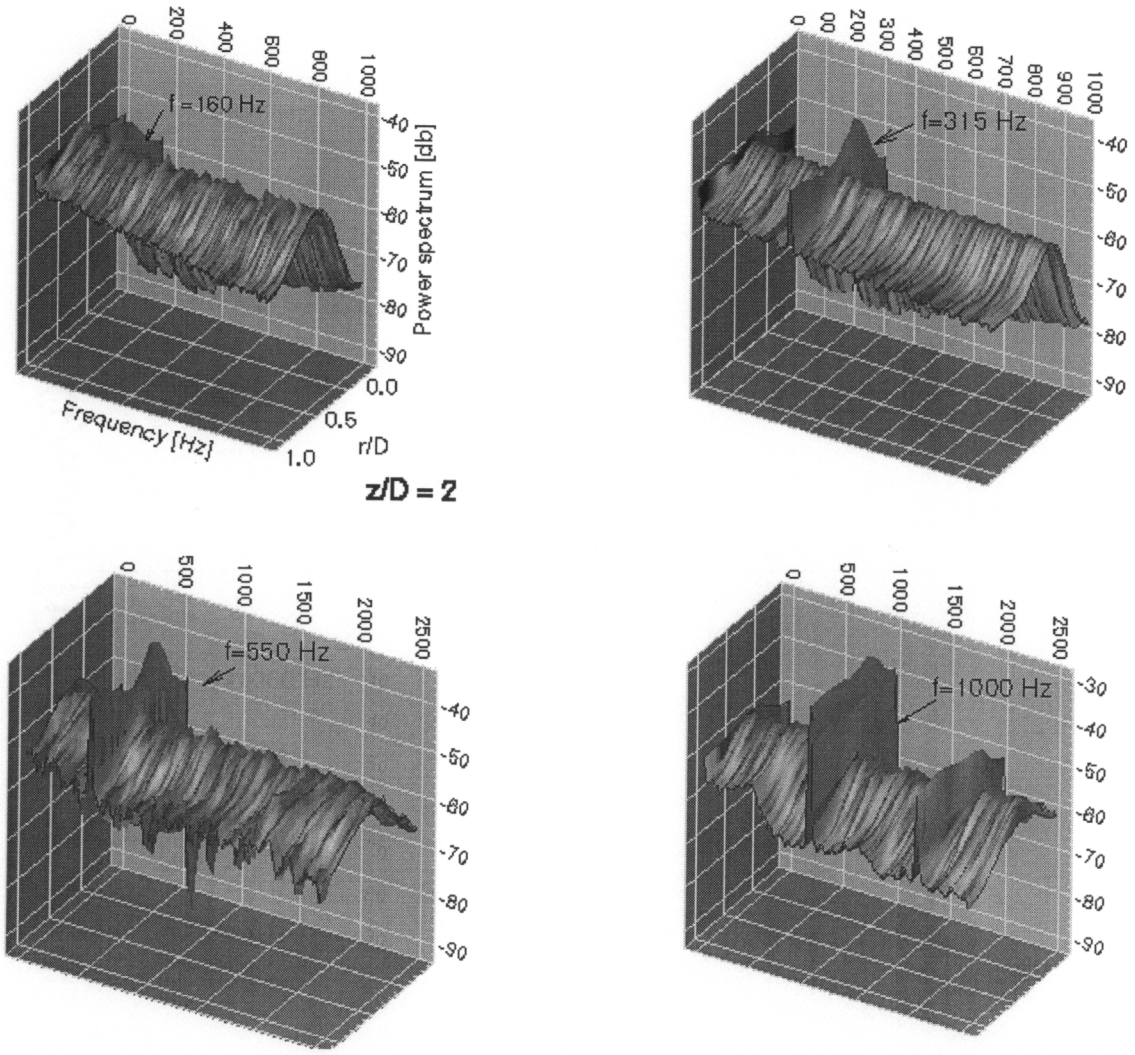

Figure 4.8 Distribution of power spectra across shear layer for flat side at streamwise location, z/D=2.

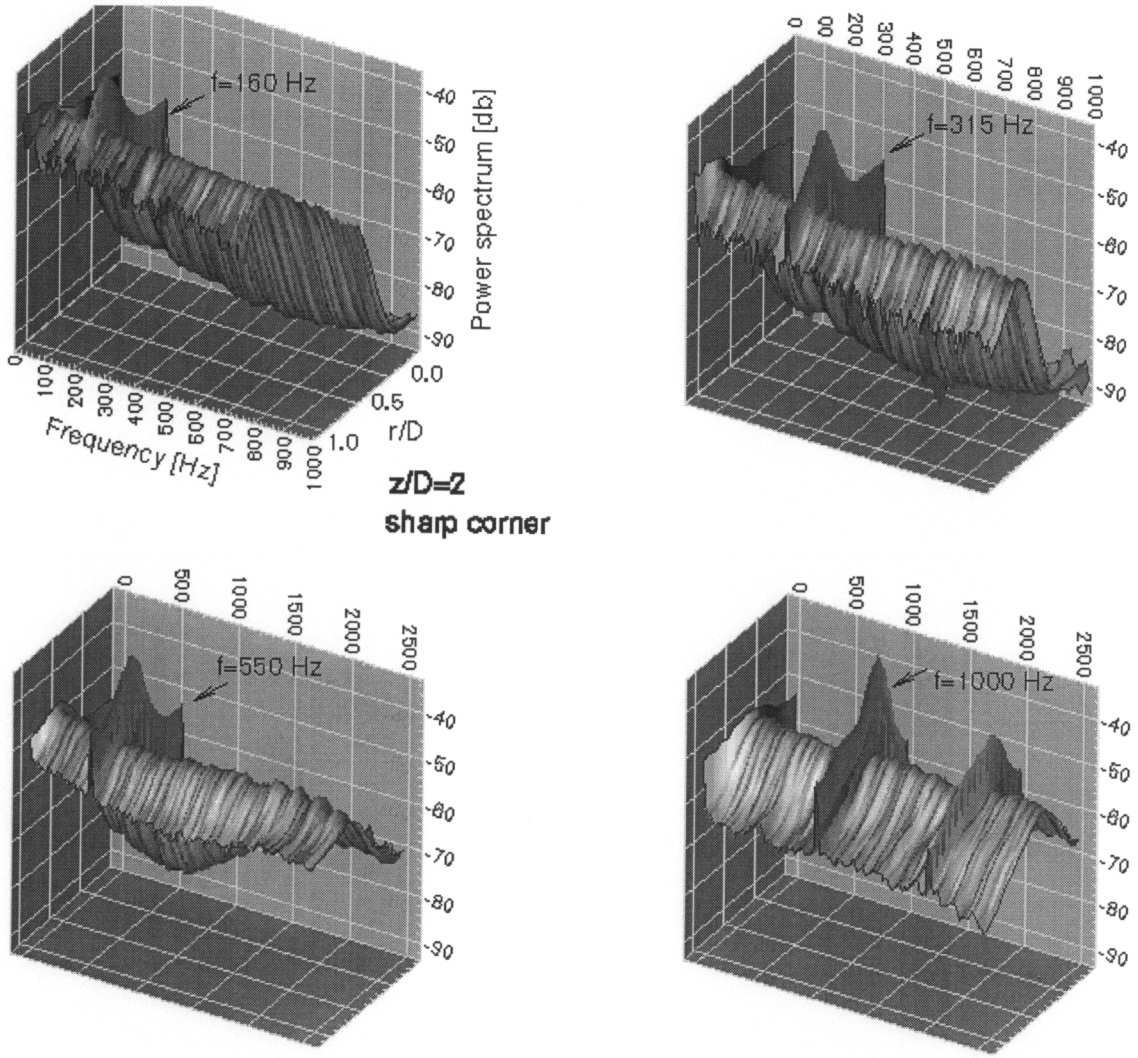

Figure 4.9 Distribution of power spectra across shear layer for sharp corner at streamwise location, z/D=2.

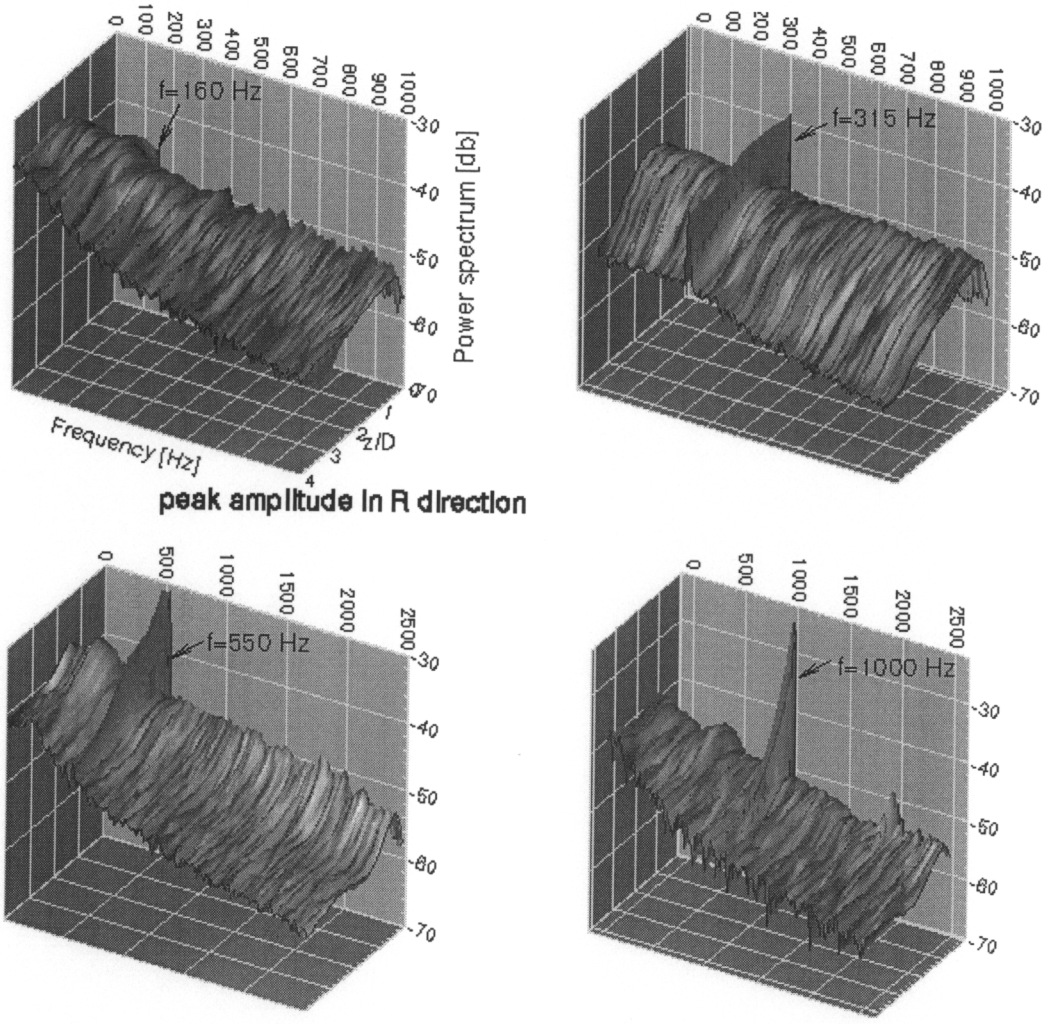

Figure 4.10 Distribution of power spectra across shear layer for flat side along the streamwise location

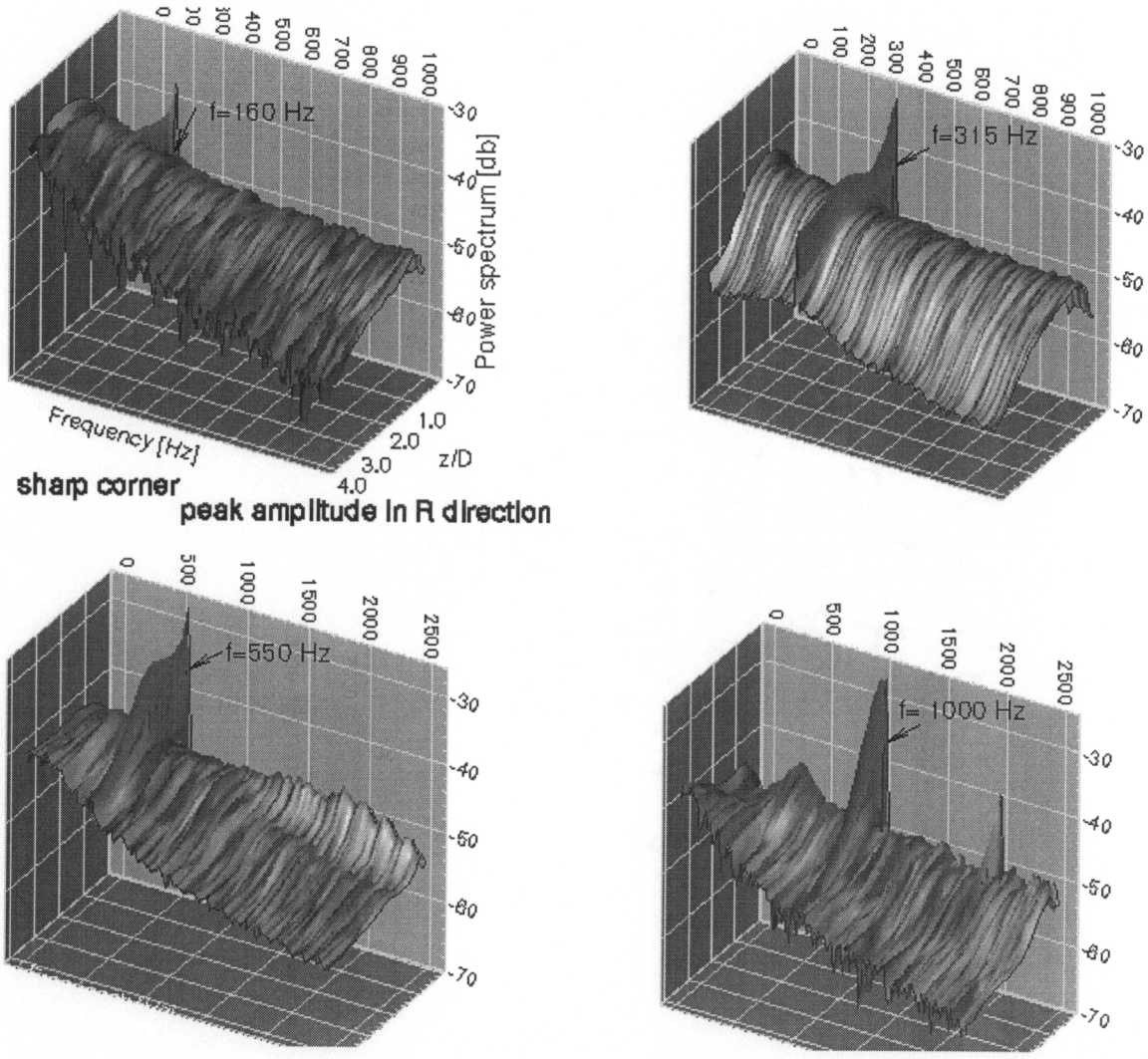

Figure 4.11 Distribution of power spectra across shear layer for sharp corner along the streamwise location

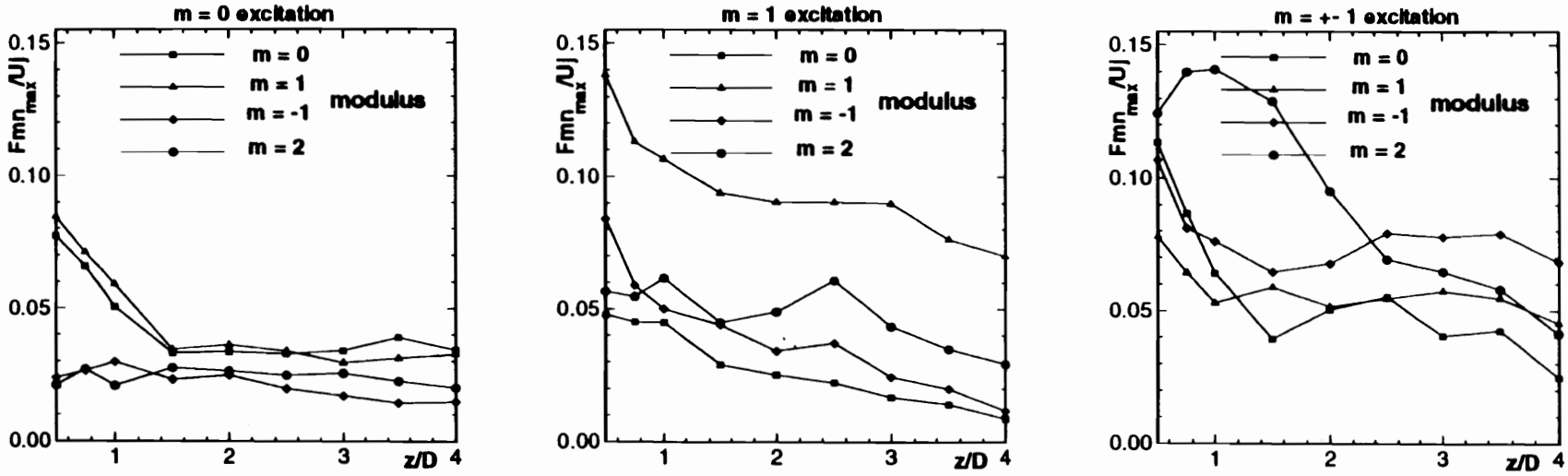

Figure 4.12 Streamwise development of phase averaged modulus under m=0, 1, 0.75, ±1 and ±0.5 excitation

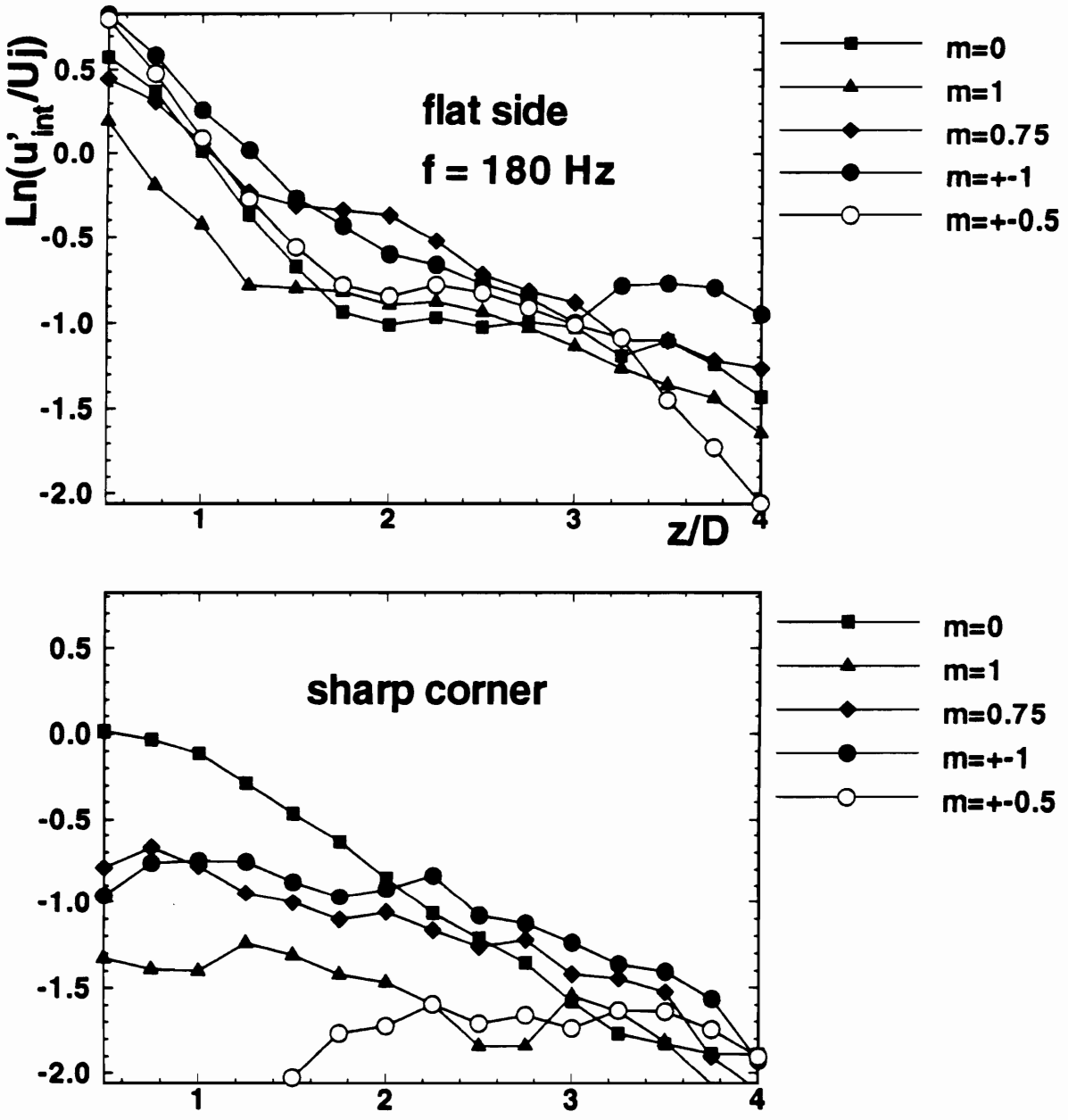

Figure 4.13 Streamwise growth in amplitude for different spatial mode excitations, a: flat side; b: sharp corner

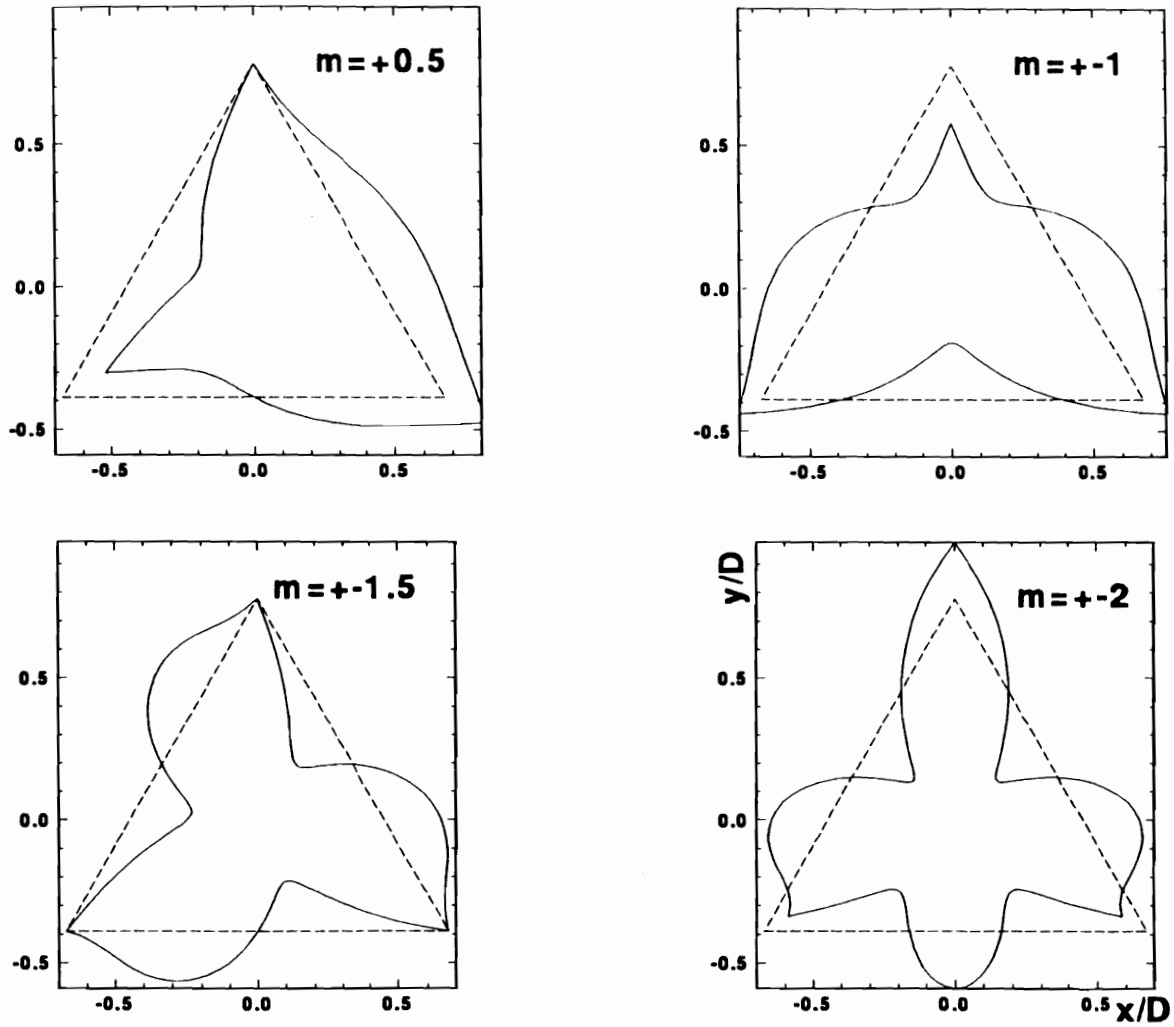

Figure 4.14a Velocity contour simulation under standing wave excitation for different excitation modes

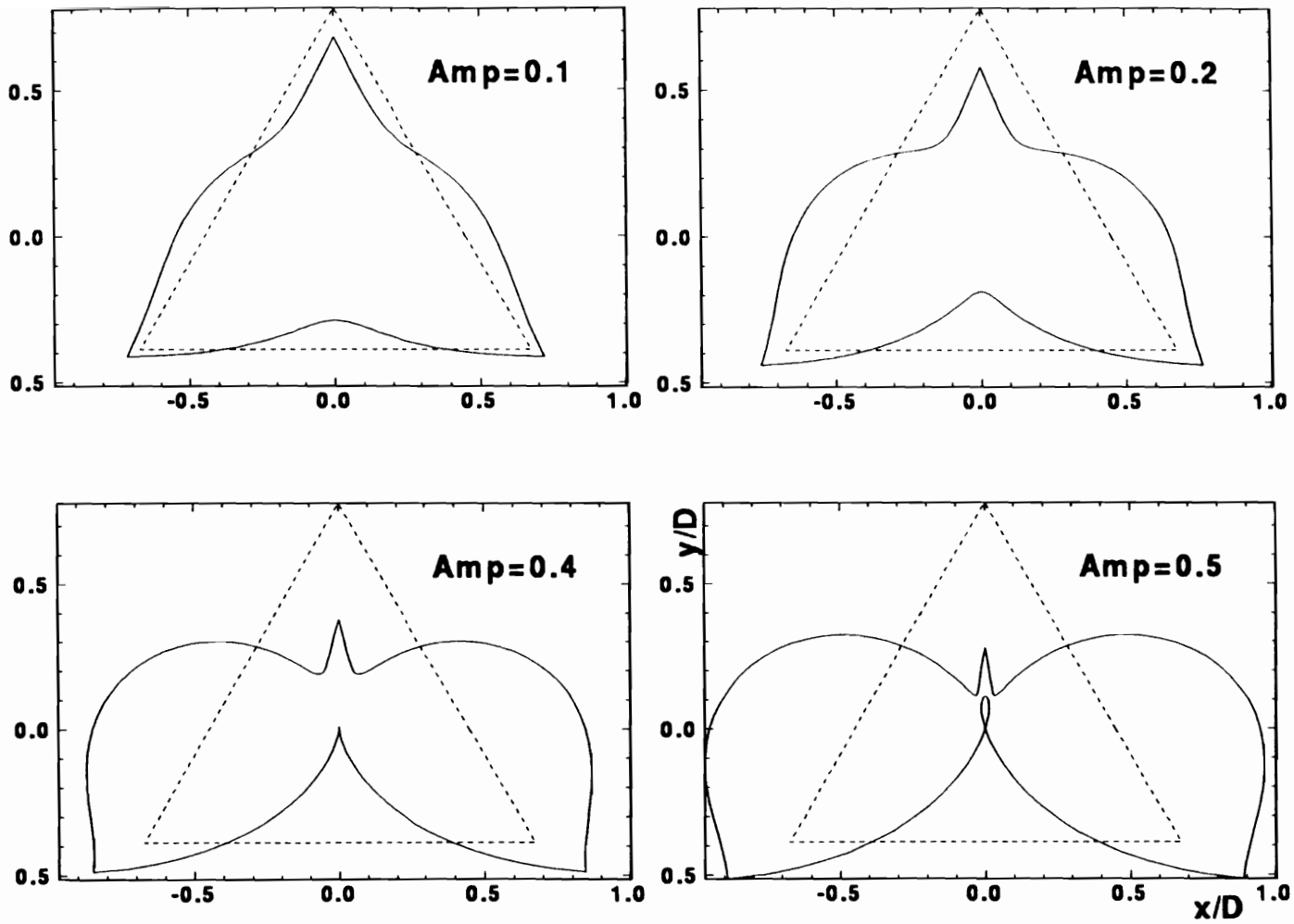

Figure 4.14b Velocity contour simulation under standing wave excitation for m=±1, effect of excitation amplitude

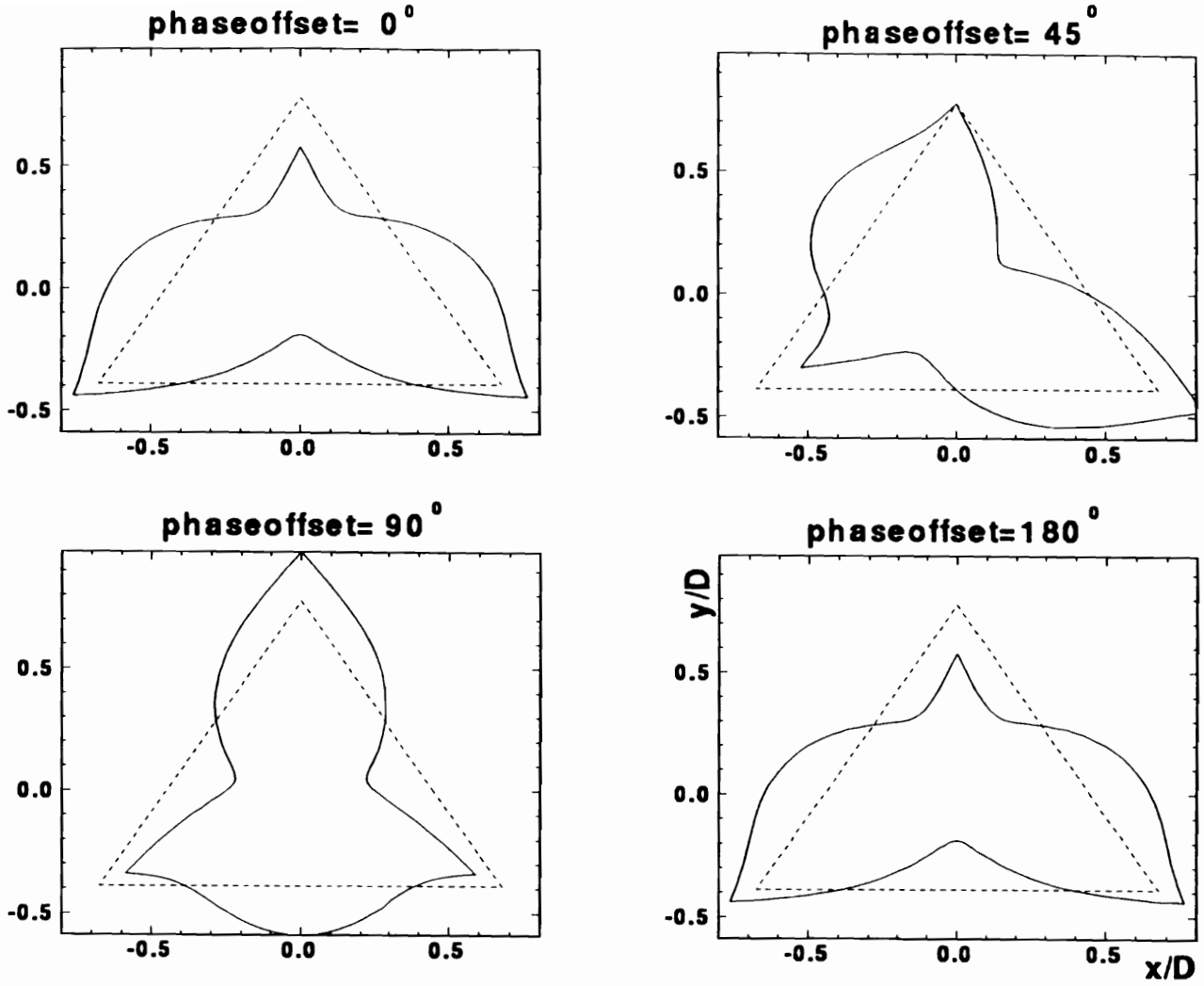

Figure 4.14c Velocity contour simulation under standing wave excitation for m=±1, effect of phaseoffsetting

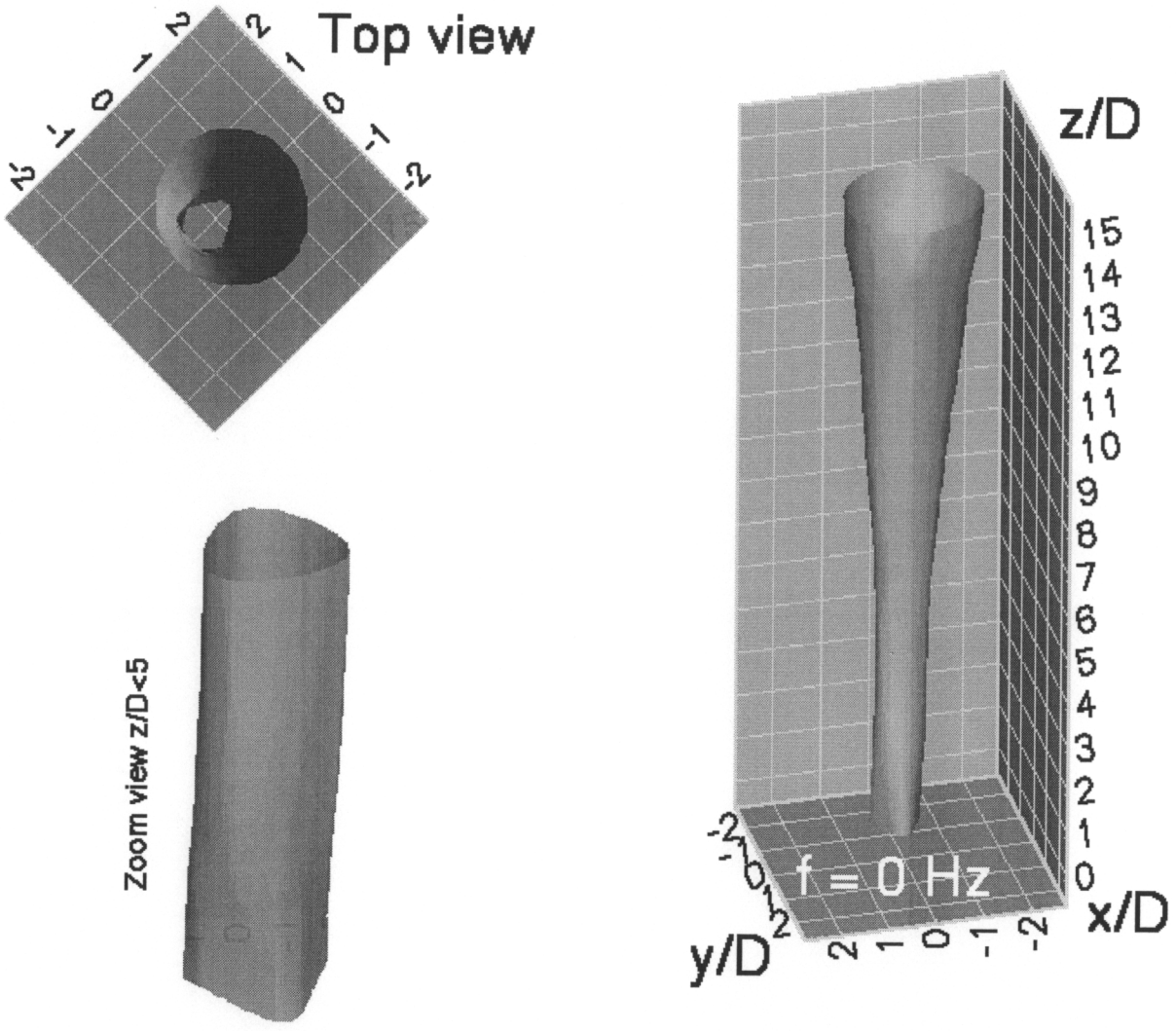

Figure 4.15 Three-dimensional view of veloity contour of the unexcited jet, (U/Uj=0.5)

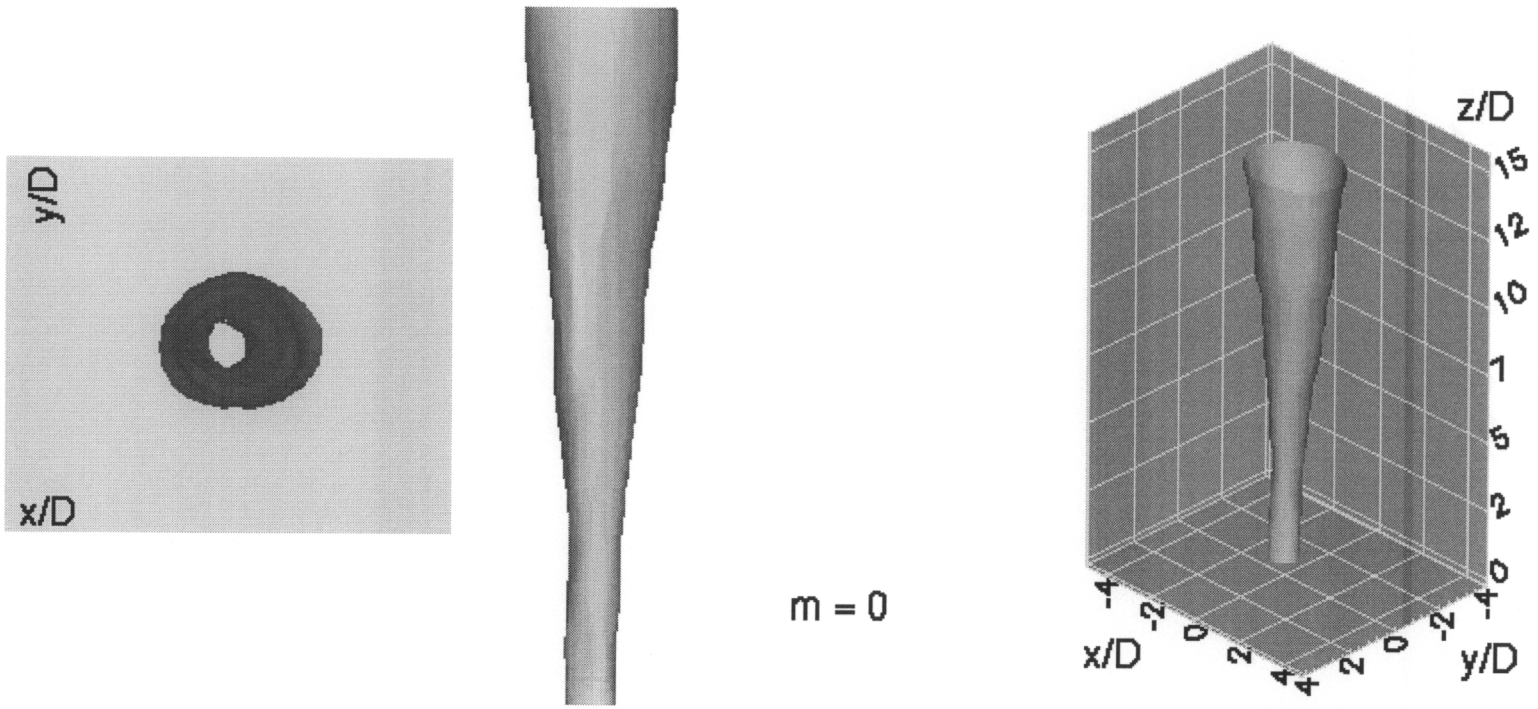

Figure 4.16a Three-dimensional views of the "top hat" triangular jet subject to m=0, fe =180 Hz, excitation (U/U_j=0.5)

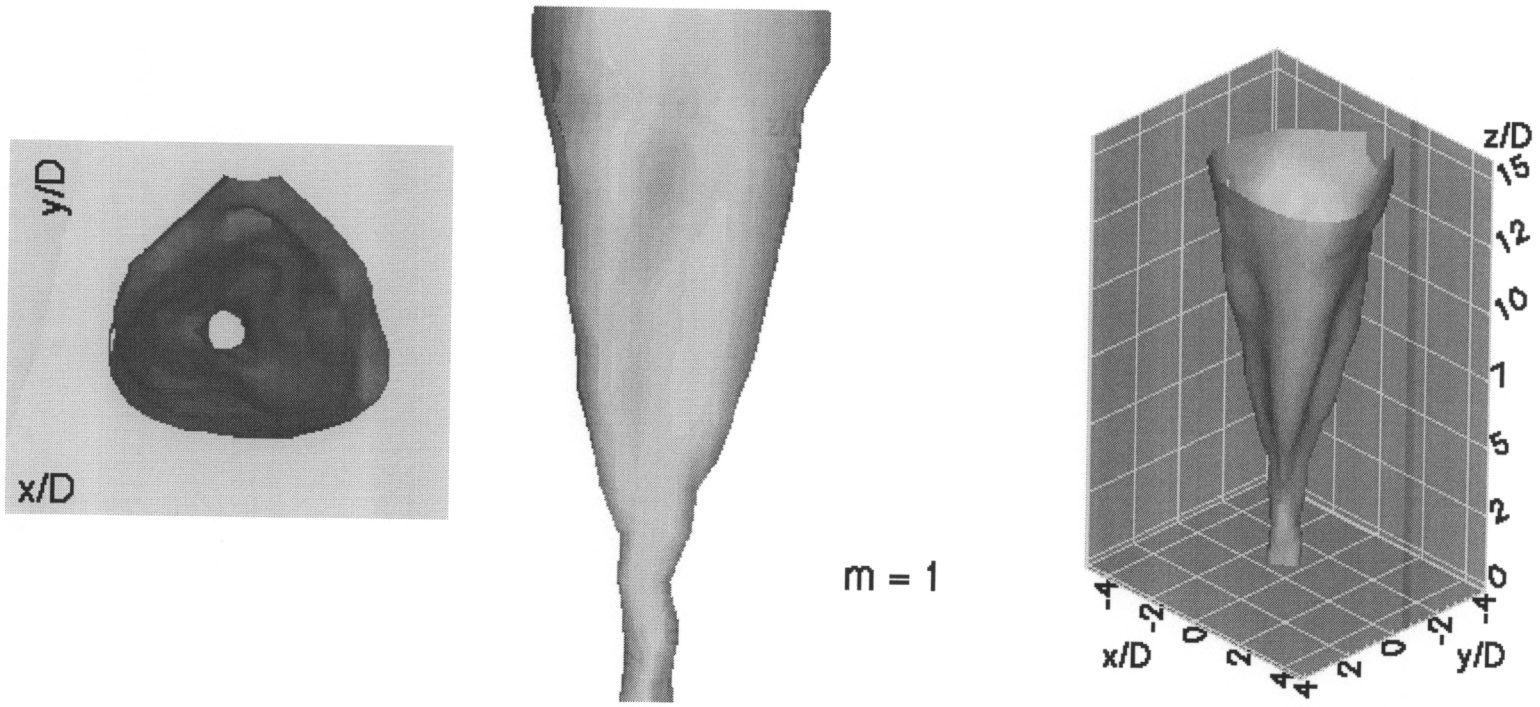

Figure 4.16b Three-dimensional views of the "top hat" triangular jet subject to m=1, *f*e =180 Hz, excitation (U/U_j=0.5)

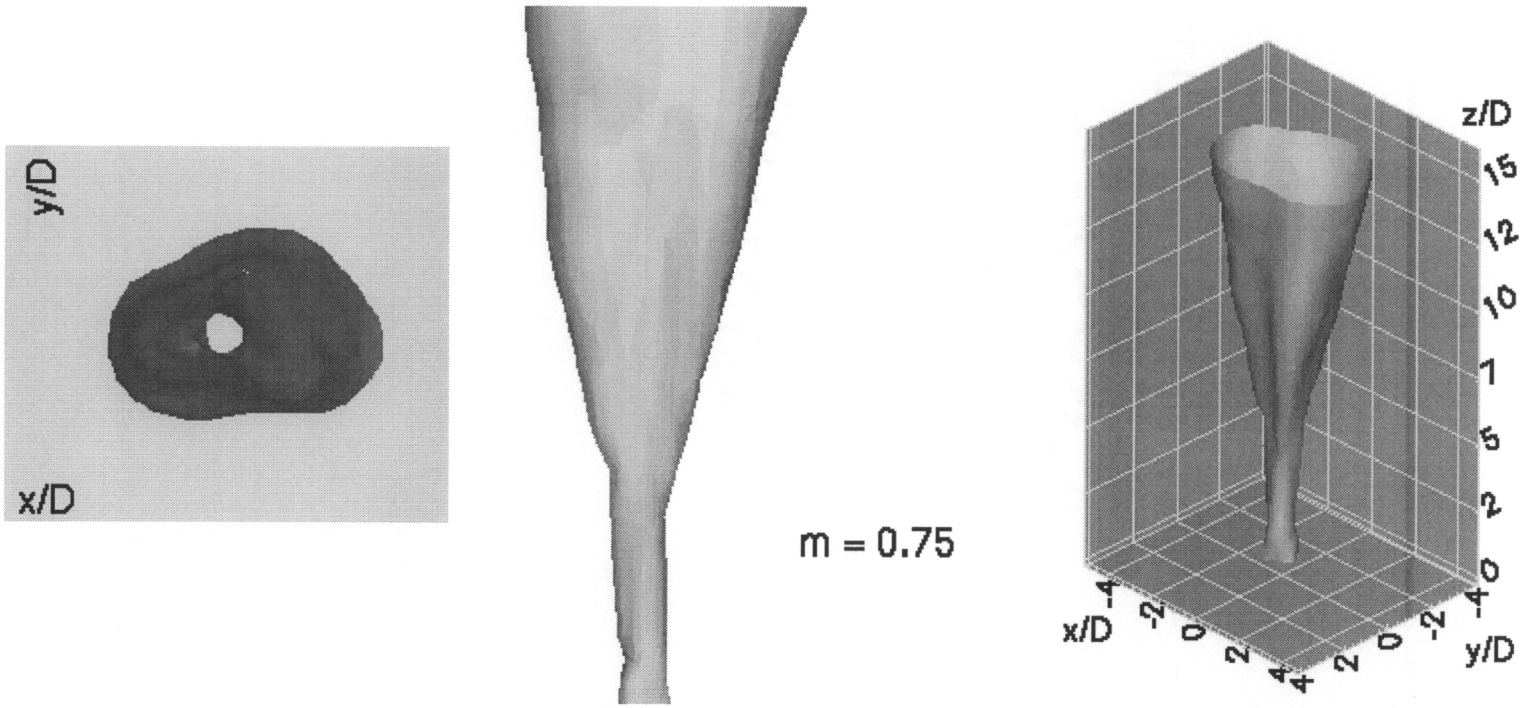

Figure 4.16c Three-dimensional views of the "top hat" triangular jet subject to m=0.75, *f*e =180 Hz, excitation (U/U_j=0.5)

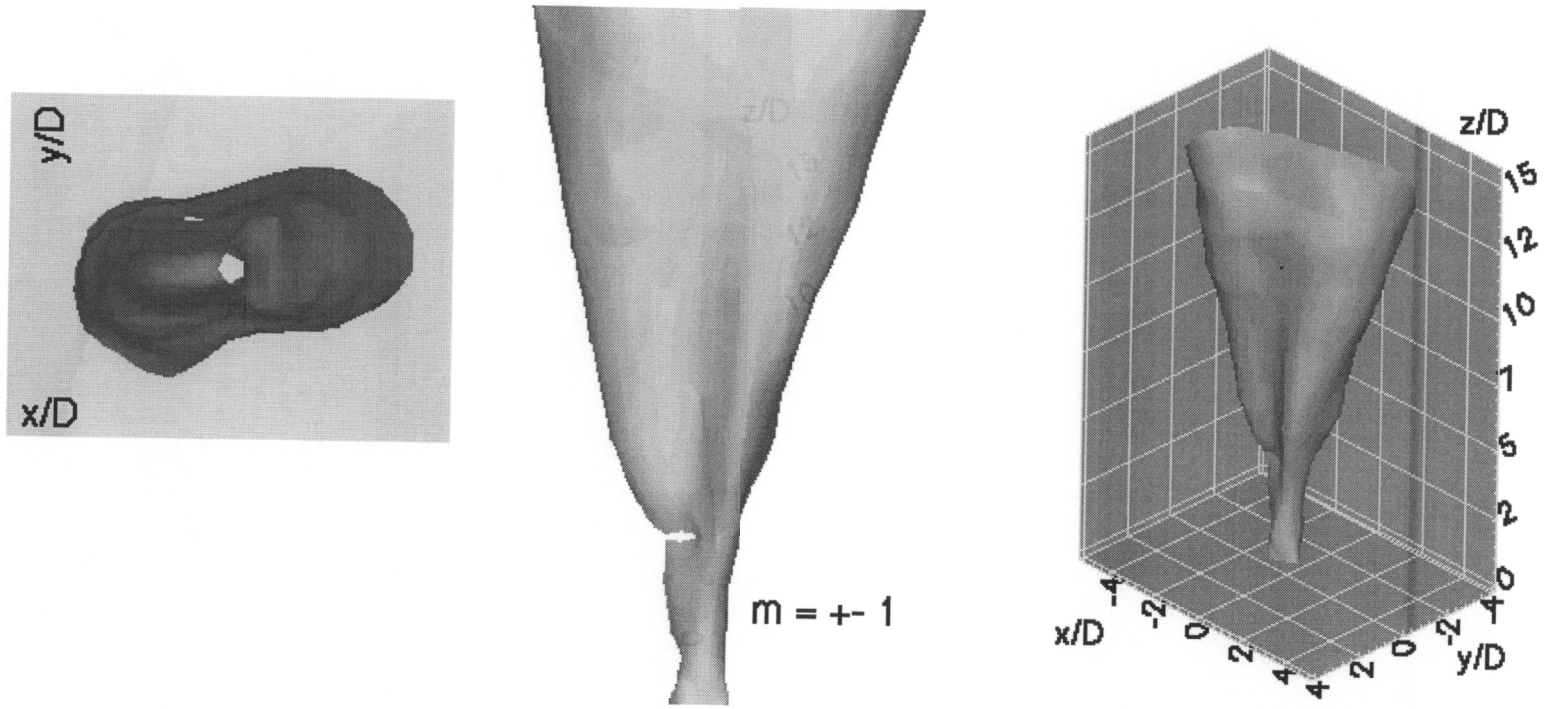

Figure 4.16d Three-dimensional views of the "top hat" triangular jet subject to m=±1, fe =180 Hz, excitation (U/U_j=0.5)

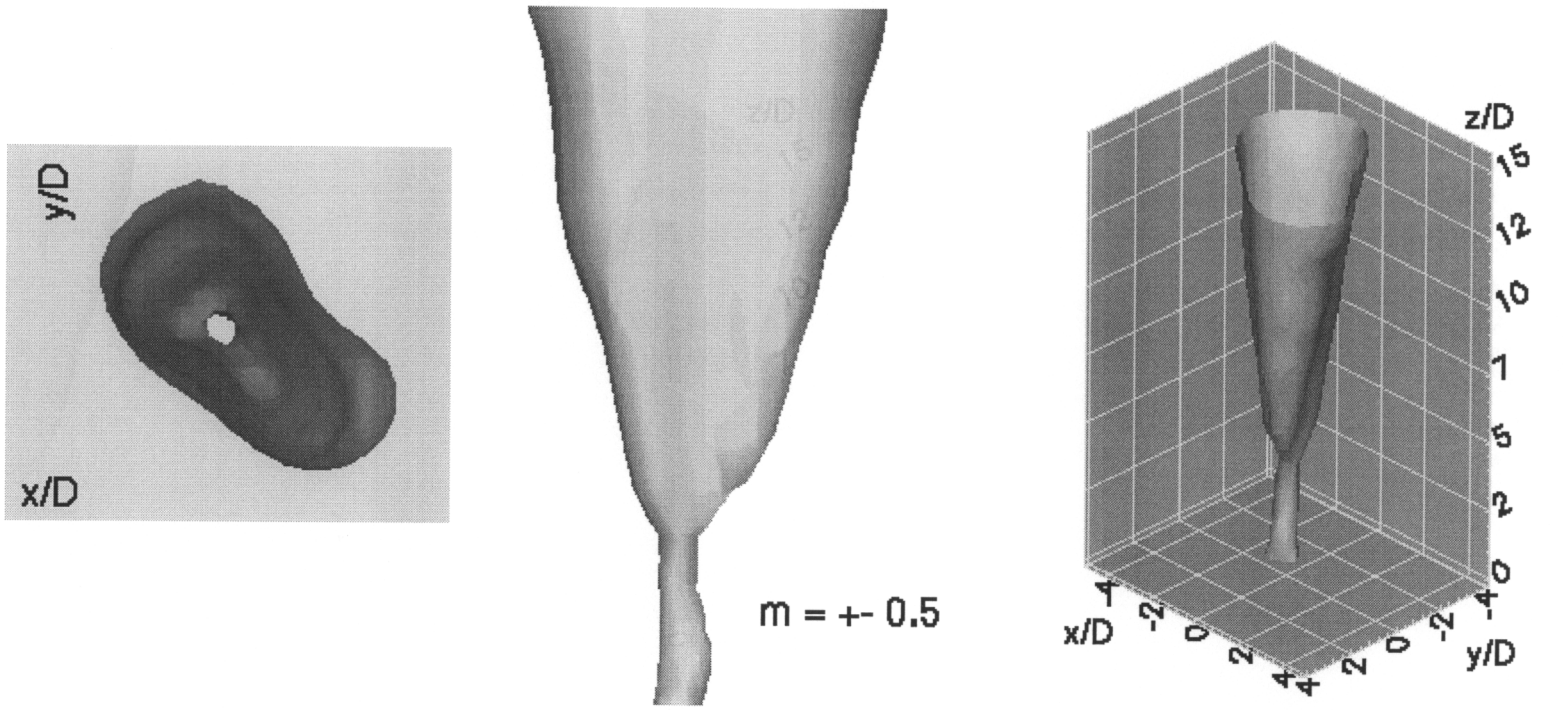

Figure 4.16e Three-dimensional views of the "top hat" triangular jet subject to m=±0.5, *f*e =180 Hz, excitation (U/U_j=0.5)

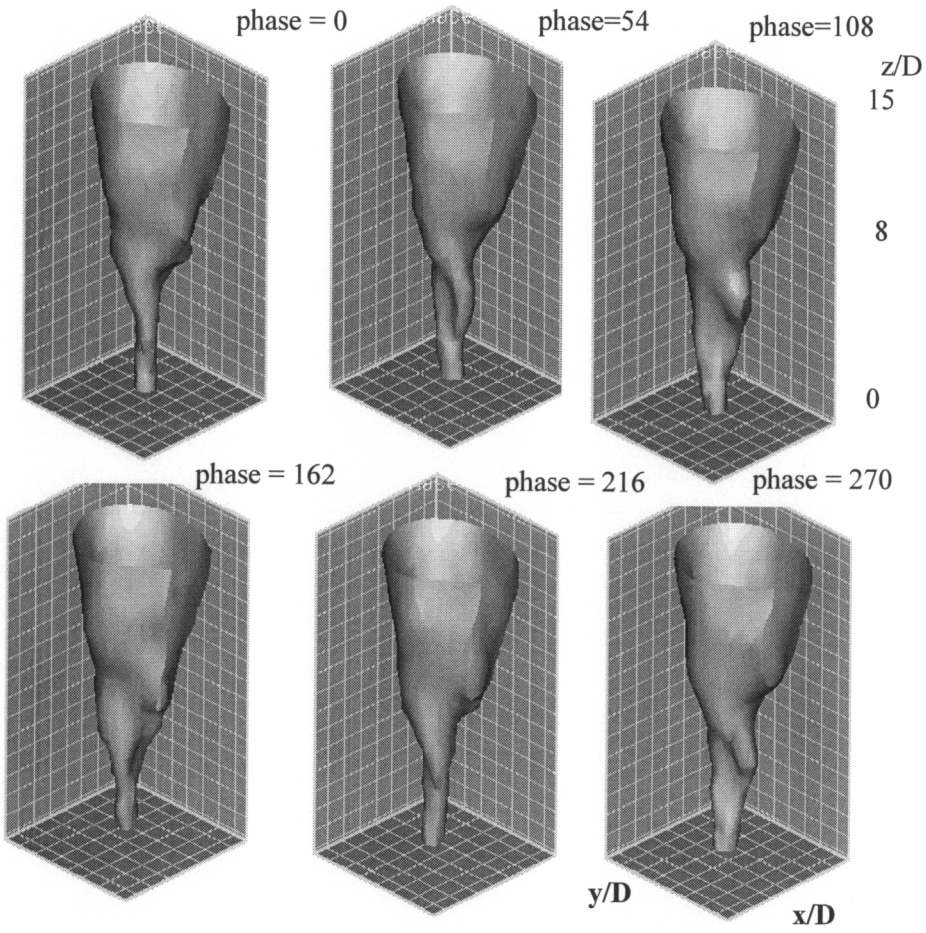

Figure 4.17 Three-dimensional view of phase mean velocity contour under phase modulation, U/Uj=0.5, *f*e=180 Hz

Chapter 5 Summary, Major Conclusions and Open Points

The objective of this dissertation was to determine effective and beneficial actuation methodologies for free shear flow control. This included two aspects: large-impact actuation using spatial and dynamic mode control and low energy actuators.

The topic of this dissertation (covered in chapters 2, 3 and 4) has been the examination of the controllability of jet flows both in the near field, and more importantly the far field. In this topic, the effects of initial flow conditions of different nozzle geometry, the mechanisms of spatial mode control, and the enhancement of jet controllability using new control schemes were the major issues.

The possibility of controlling the evolution of a turbulent triangular jet in the far field was investigated in chapter 2. The purpose of this study was to put the spatial mode control methodology under the toughest test in a combined high background noise and non-circular geometry environment. It served to validate the advantages and limitations of the spatial mode control method and pointed to a direction that subsequent investigations (topics in chapter 3 and 4) should pursue. The study was performed on an equilateral triangular jet with fully sheared exit flow. Piezoelectric actuators were mounted on the flat sides of the nozzle. Excitation based on frequency modulation was found to be ineffective for the purpose of achieving control over the jet evolution into the far field. In contrast, excitation of certain azimuthal modes was shown to enable the desired control. Specifically, excitation of non-integer modes and standing wave modes resulted in asymmetric evolution of the jet. Even though the far field was still completely decorrelated from the excitation signal, the expansion rate and the directional spreading of isovelocity contours in the far field could be controlled by azimuthal mode manipulation. Entrainment ratios in the far flow field (z/D=30), about three times larger than the unexcited case, were achieved.

The mechanism of spatial mode control was investigated in more detail in chapter

3. With a clear understanding of the basic control mechanism, a new control method -- the dynamic spatial mode control was proposed. Experiments were conducted on a circular jet with an initial top-hat velocity profile. Eight loudspeaker drivers were equally distributed around the azimuth to excite two dimensional disturbances, both in time and space.

It was confirmed that control of the far field using spatial mode control method could be effectively applied to a top-hat circular jet. Large jet expansion, increased entrainment ratio and control over the far field were achieved.

Spatial mode control was demonstrated to be most effective under standing-wave excitation. The basic mechanism that governs the far field control was thought to be the non-linear interaction of the asymmetric structures that were generated in the near field. This observation agrees with conclusions of former investigators (Cohen and Wygnanski (1987), Perterson & Samet (1990), Corke & Kusek (1993)) but with a new understanding that the non-linear interaction mechanism of the large structures do not become effective until after the potential core, where the flow is fully sheared. Typically, the asymmetric structures are composed of bulges that are created on alternate sides in the near field. These bulges travel downstream with little growth because of the small amplification rate of the flow instability there. The data reveals that, after the potential core ends, the jet expands rapidly. It is postulated that this rapid growth is a result of slowing down of the phase speed in that region. As each bulge reaches the end of the potential core and slows, it is pushed outward and later merges with the faster bulge that following it. This kind of interaction causes very rapid outward jet expansion in a preferred direction that combines the non-linear interactions of both bulges during their coalescence. The direction of the expansion can be easily predicted and the extent of the expansion controlled due to the unique relationship between the actuation and the jet response.

The mechanism that governs the excited triangular jet (discussed in chapter 2) also applies to the preceding description except that there is no potential core at the

nozzle exit. Therefore, a higher excitation level is required. As a result, the large structures will interact with each other right after the nozzle exit.

The unique relationship between the spatial mode excited in the near field and the directional jet expansion in the far field has guided the studies to propose a new control method. This method, termed as the dynamic mode control method, was designed mainly to control the far field of jets.

Three schemes of the dynamic mode control method were proposed: 1) "phase modulation", 2) "switching modulation" and 3) "spatial mode modulation". The former two were implemented.

By phase modulation, the spatial phase of the actuators was offset dynamically. Since the controlled directional jet expansion was uniquely determined by the original phase offset, dynamically varying the phase offset resulted in a dynamic rotation of the jet. There were two advantages in this type of control. First, the direction of the jet expansion (both in the near and far field) was controlled. Second, as a result of jet rotation, the dynamically controlled jet expansion was able to cover a much larger area as compared with the non-rotated, spatial mode controlled jet.

By switching modulation, both the phase and modes of the actuators was controlled dynamically. This type of control, as indicated by its name, was able to simulate the switching of the major and minor axis of an unexcited jet. This type of algorithm was impossible to implement when using conventional spatial mode control method. In addition, the controlled switching could extend well into the far field and the location of the switching could also be controlled.

The most important feature of this type of control is its enhanced controllability of the far field, compared with any former control method. The so called "phase decorrelation" issue, which exists in all other methods, can be readily solved with this method. Dynamic mode control combines mechanisms that enhance mixing typically found only in passive control (non-circular jet with axis switching) while yielding control over the mixing characteristics in three dimensions. By simulating mechanisms typical of

passive devices with the dynamic mode control method, control over how and where the mixing occurs can be achieved. One can say that the dynamic control method is more flexible when compared with any former method which controls only the frequency and "static" spatial modes. By proper manipulation, the dynamic control method can handle the global as well as the local mixing and expansion rates. Therefore, it is considered to be a unique actuation scheme in jet control.

It was shown in this dissertation that the jets studied had very similar control mechanisms -- the non-linear structure interactions were activated at the fully sheared region of the jets under proper spatial modes control. The differences in nozzle geometry (triangular vs. circular), especially in initial velocity profiles (fully sheared vs. top hat), seemed to have little effects to the conclusions drawn to the controllability of the far field. While it was true that the control mechanisms were the same, it was also true that the different type of jets responded to initial conditions differently. This observation was substantiated by the fact that the axis-switching phenomenon, which has been known to exist in non-circular jets, Gutmark and Ho, (1983), Hussain, (1989), was not observed in the current triangular jet study (discussed in chapter 2). However, by examining the experiments done by previous researchers, it was found that the initial velocity profile of the non-circular jets studied were invariantly not fully sheared. The axis switching could, therefore, be a combined result of non-circular geometry and a non fully-sheared initial velocity profile. This postulate was tested (discussed in chapter 5) employing a triangular jet that had a top hat velocity profile at the nozzle exit.

The study showed that in order to create axis switching, the jet employed had to be non-circular and to have a top hat velocity profile at the nozzle exit. It was reasoned that an initially fully-sheared jet could not generate a vortex ring, the necessary condition for axis switching, with the consequence that there would be no axis switching occurred in such a jet, regardless whether it was circular or non-circular.

It was also found in this study that m=1 excitation, contrary to the corresponding fully-sheared triangular jet case (discussed in chapter 2) and the top-hat circular jet case

(discussed in chapter 3), succeeded in achieving both large jet expansion and axis switching, while m=0 excitation failed in all three cases. It was postulated that an initial top-hat velocity profile helped the formation of vortex rings. The coexistence of vortex rings and non-uniform geometry helped to generate the axis switching. The m=0 excitation destroyed the self inducement mechanism of vortex ring by pumping the flow at the same time on all three sides of the jet. As a result, any vortex ring stretching at one period was prevented by the corresponding contracting at the following period. The m=1 excitation avoided such side effects by exciting the triangular jets azimuthally in a sequential manner. In such a way the strength of axis switching was augmented that in turn enhanced the jet expansion.

There are some recommendations for future work of this study.

In terms of experiments, it is suggested that the following experiments are needed:

1. Quantification of the dynamic mode control method, which typically include: 1) the amount of enhancement in jet expansion rate as compared with other control methods, and 2) measurement of the scope of the controllable region for the switching modulation.
2. Implementation of the third dynamic mode scheme -- the spatial mode modulation.
3. Study more instances of initial velocity profiles and nozzle geometries so that the conclusions drawn about the effect of initial flow conditions can be strengthened.
4. Development of new schemes based on the idea of the dynamic mode control method.

In terms of technology, it is suggested that the 3-D hot wire probe (miniature type preferable) with the combined hardware and software for 3-D vector velocity and vorticity measurements schemes should be implemented. This technique is simple and suitable for 3-D free jet measurements. Only through true 3-D measurements can it be possible to understand the intricate nature of 3-D jet flow.

In terms of computation, the direct numerical simulation method is considered the best tool to describe the phase locked 3-D jet flow. This method can provide additional

insight into the mechanisms of the flow structure, which would be impossible to observe from experimental results alone.

BIBLIOGRAPHY

Batchelor, G. K. and Gill, A. E., 1961, "Analysis of the stability of axisymmetric jets," ***JFM***, vol 14, pp529-551.

Bradshaw, P. Rerriss, D. H. and Johnson, S., 1964, "Turbulence in the noise producing region of a circular jet," ***JFM*** vol 19, pp591-610.

Chan, Y. Y., 1977, "Wavelike eddies in a turbulent jet," ***J. of AIAA***, vol.15, NO.7.

Crow, S. C. and Champagne, F. H., 1971, "Orderly structure in jet turbulence. ***JFM***, Vol 48, pp 547-591.

Cohen, J. and Wygnanski, I., 1987, "The evolution of instabilities in the axisymmetric jet. Part 1. The linear growth of disturbances near the nozzle," ***JFM***, vol. 176, pp. 191-219.

Cohen, J. and Wygnanski, I., 1987, "The evolution of instabilities in the axisymmetric jet. Part 2. The flow resulting from the interaction between two waves,", ***JFM***, vol 176, pp 221-235.

Corke, T. C. and Kusek, S. M., 1993, "Resonance in axiymmetric jets with controlled helical-mode input,", ***JFM***, vol. 249, pp. 307-336.

Crighton, D. G. & Gaster, M., 1976, "Stability of slowly diverging jet flow," ***JFM*** vol. 77 pp. 397-4131.

Dimotakis, P. E., 1991, "Turbulent Free Shear Layer Mixing and Combustion," ***Progress in Astronautics and Aeronautics***, Vol. 137, pp. 265-340.

Ding Chen and Uri Vandsburger, 1992, "A self-excited wire method for control of the evolution of a turbulent mixing layer," ***31st Aero. Sciences Meeting, AIAA-93-0433*** (also published in ***J. of AIAA*** April 1995 issue).

Ding Chen and Zhang ShiYing, 1989, "Control of separation in diffusers using forced unsteadiness," ***AIAA 2nd Shear Flow Conf. AIAA-89-1015***.

Ding Chen and Uri Vandsburger, "The spatial modulation of a forced triangular jet. "2nd Conf. on Recent Advances in Active Control of Sound and Vibrations, April 1993,

Blacksburg, VA, USA, also published by ***Journal of Exp. in Fluids***, Vol 18 (1995) pp239-248.

DuPlessis, M. P., Wang, R. L. & Kahawita, R,. 1974, "Investigation of the near-region of a square jet," ***Trans. ASME I: J. Fluids Engng*** vol 906, pp. 246-251.

Fieddler, H. E. and Mensing, P., 1985, "The Plane Turbulent Shear Layer with Periodic Excitation," ***JFM***, Vol. 150, pp. 281-309.

Freymuth, P., 1966, "On transition in a separated laminar boundary layer," ***JFM***, vol 25, pp 683-700.

Gaster, M., Kit, E. & Wygnanski I., 1985, "Large scale structures in a forced turbulent mixing layer," ***JFM*** vol 150, pp23-54.

Glezer, A., Katz, Y. and Wygnanski, I., 1989 "On the vbreakdown of the wave packet trailing a turbulent spot in a laminar b oundary layer," ***JFM***, vol 198, pp 1-26.

Gutmark, E., Schadow, K. C., Parr, D. M., Harris, C. K., Wilson, K. J., 1985, "The mean and turbulent structure of noncircular jet," ***AIAA shear flow control conference***, ***AIAA 85-0546***, Boulder/Co, USA.

Gutmark, E. and Ho, C. M., 1983, "Preferred modes and the spreading rates of jets" ***Phys. Fluids***, vol. 26, No. 10, pp2932-2938.

Gutmark, E., Shcadow, K. C., Parr, T. P., Hanson-Parr, D. M. and Wilson, K. J., 1989, "Noncircular Jets in combustion systems," ***Experiments in Fluids***, vol 7 pp248-258.

Helmholtz, see also Drazin, 1982, "Hydrodynamic stability", ***Cambridge University Press***.

Ho, C. M., and Huang, L. S., 1982, "Subharmonics and Vortex Merging in mixing layers," ***JFM***, Vol. 119, pp. 443-432.

Ho, C. M. and Hurre, P., 1984, "Perturbed free shear layers." ***Annual Review of Fluid Mechanics***, Vol. 16, pp. 365-424.

Ho, C.-M & Gurmark E. 1987, "Vortex induction and mass entrainment in a small-aspect-ratio elliptic jet," ***JFM***, vol. 179, pp. 383-405.

Ho, C. M., Y., Zohar, Y., Foss, J. K. and Buell, J. C., 1991, "Phase decorrelation of coherent structures in a free shear layer," ***JFM***, vol 230, pp. 319-337.

Hasan, M. A. and Hussain, A. K. M. F., 1982, "The self-excited axisymmetric jet," ***JFM***, vol. 115, pp. 59-89.

Hussain, F. & Husain, H., 1989, "Elliptic jets. Part 1. Characteristics of unexcited and excited jets," ***JFM*** vol. 208. pp. 257-320

Hussain, F. & Husain, H., 1991, "Elliptic jets. Part 2. Dynamics of coherent structures: pairing," ***JFM*** vol. 233. pp. 439-482

Janjua, S. I. and Mclaughlin, D. D. (1982), "Turbulence measurements in a confined jet using a six-orientation hot wire probe technique", ***AIAA-82-1262***.

Kelvin - see Drazin, 1982, "Hydrodynamic stability", ***Cambridge University Press***.

Leconte, J., 1858, "On the influence of musical sounds on the flame of a jet of coal - gas," ***Phil. Mag***., Vol 15, 235-239.

Long, T. A., and Petersen, R. A., 1992, "Controlled interactions in a forced axisymmetric jet. Part 1. The distortion of the mean flow," ***JFM***, vol 235, pp. 37-55.

Long, T. A., and Petersen, R. A., 1992, "Controlled interactions in a forced axisymmetric jet. Part 2. The modulation of broadband turbulence," ***JFM***, vol 235, pp. 57-72.

Mattingly, G. E. and Chang, C. C., 1974, "Unstable waves on an axisymmetric jet column," ***JFM*** vol. 65 pp. 541.

Michalke A., 1965, "On spatially growing disturbances in an inviscid shear layer," ***JFM*** vol. 65, pp. 521-544.

Michalke, A. 1984, "Survey on jet instability theory," ***Prog. Aerospace Sci***. Vol. 21, pp. 159-199.

Parker, R. 1966, "Resonance effects in wake shedding from parallel plates; some experimental observations," ***J. Sound Vib.*** vol. 4, pp.62-80.

Parker, R. 1967, "Resonance effects in wake shedding from parallel plates: calculation of resonant frequencies," ***J. Sound Vib.*** vol. 5, pp. 330-341.

Perterson, R. A. and Samet, M. M., 1988, "On the preferred mode of jet instability," ***JFM*** vol. 194. pp. 153-173.

Plaschko, P., 1979, "Helical instabilities of slowly divergent jets," ***JFM*** vol. 92, pp. 209-215.

Quinn, W. R. & Militzer, J., 1988, "Experimental and numerical study of a turbulent free square jets," ***Phys. Fluids***. vol. 31, pp. 1017-1025.

Rayleigh, Lord, 1879, "On the instability of jets," ***Proc. London Math. Soc.,*** Vol 10, 4-13.

Schubauer G. B. and H. Skramstad, 1947, "Laminar boundary layer oscillations and transition on a flat plate," ***J. Res. Nat. Bur. Standards***, vol. 38, pp. 251-292 [see also NACA Report 909, (1948)].

Sforza, P. M., Steiger, M. H. & Trentacoste, N., 1966, "Studies on three-dimensional viscous jets," ***AIAA J.*** vole 4, pp. 800-806.

Sun, F.P. and Mitchell, L. D. 1991, "Two-dimensional velocity data smoothing and structureal angular velocity extraction using a DFT-IDFT technique", ***DE-Vol. 38, Modal analysis, Modeling, Diagnostics, and Control - Analytical and Experimental, ASME***.

Trentacoste, N. & Sforza, P. M., 1967, "Further experimental results for three-dimensional free jets," ***AIAA J.*** vol. 5, pp. 885-891.

Tso, J. & Hussain, F., 1989, "Organized motions in a fully developed turbulent axisymmetric jet," ***JFM*** vol.203, pp. 425.

Reynolds, A. J., 1962, ***JFM***, Vol 14, pp 552.

Reynolds, O.,1883, [see Drazin, 1982, "Hydrodynamic stability", ***Cambridge University Press***].

Strange, P. J. R., 1983, "Spinning modes on axisymmetric jets. Part 1," ***JFM*** vol. 134, pp. 231-245.

Vandsburger U. and Ding, C, "The spatial modulation of a forced triangular jet," ***Journal of Exp. in Fluids,*** Vol 18 (1995) pp239-248.

Yoda, M., 1992, "The instantaneous concentration field in the self-similar region of a high Schmidt number round jet," ***Ph. D. Dissertation, Department of Aeronautics and Astronautics, Standford University***.

Yu, M. H. and Monkewitz, P. A., 1993, "Oscillations in the near field of a heated two-dimensional jet," ***JFM*** vol 255, pp. 323-347.

Wiltse J. M. and Glezer, A., 1993, "Manipulation of free shear flows using piezoelectric actuators," ***JFM***, vol 249, pp. 261-285.

Wygnanski, I., Champagne, F, and Marasli, B., 1986, "On the Large Coherent Structure in Two-dimensional Small-deficit Turbulent Wakes", ***JFM***, Vol. 168, pp.31-71.

Wygnanski, I. J. & Petersen, R. A., 1987, "Coherent motion motion in excited free shear flows," ***AIAA J.***, Vol. 25, NO. 2., pp 201-213.

Zaman K. B. M. Q. & Hussain, A. K. M. F., 1977, ***Turb. Shear Flows***, pp.11-23, ***Pennsylvania State University***.

Zaman K. B. M. Q. & Hussain, A. K. M. F., 1980. "Vortex pairing in a circular jet under controlled excitation. Part 1. General jet response," ***JFM,*** vol. 101, pp.449-491.

Appendix A Self-Excited Wire as a Shear Flow Control Device

A.1 Introduction

This chapter includes a description of an investigate on excitation scheme that is characterized by simplicity, low-energy consumption and "best-coupling between the flow and the actuator. The method uses a music wire as the actuator to excite a two-stream, turbulent, planar mixing layer. The resulting effects on the structure and evolution of the flow field were also explored.

Although the mechanisms involved in active control of the planar mixing layer have been well understood, the methods of control, which include actuation methods, practical actuator design and implementation are far from satisfactory. Usually to achieve a desired increase in mixing rate, previously proposed methods either require too much energy or are impractical because of the complexities in installing the actuator. Both problems negate the advantages of active flow control compared to passive control methods. Hence, there is an urgent need to develop new actuation methods for control.

The fundamental physics underlying the development of planar shear layers, natural and excited, have been the subject of much research during the last two decades. A wealth of information can be found in the works of Ho and Huang (1982) and Ho and Huerre (1984). Results for turbulent shear layers were reported among others by Wygnanski and Petersen (1987), Fiedler and Mensing (1985) and compiled lately by Dimotakis (1991).

Analysis of the locally excited, turbulent, planar mixing layer reported here is based on concepts and measures advanced by previous researchers like Ho and Huerre (1982, 1984), Dimotakis (1991) and Wygnanski and Peterson (1987). Examples are shear layer growth rate, forcing characteristics, receptivity, most amplified and sub harmonic frequencies, vortex merging, and entrainment rate ratio.

The experimental facilities and techniques are introduced first. The major findings are reported next. A discussion of the governing mechanisms follows, with some recommendations for possible applications made at the closure.

A.2 Facilities and Methodology

The study was performed in a small scale wind tunnel, Figure A.1a. Mufflers were installed between the blowers of the two streams and the diffuser in order to dampen a periodic component in the flow caused by the blower vane passage frequency. The test section is connected to the two plenum chambers through a 16:1 contraction and each stream exits through a cross section 63 mm (2.5") high and 102 mm (4.0") wide. Achievable velocities are 10-40 m/s on the high speed side and 4-15 m/s on the low speed side, with a turbulence level of 0.5%. The separation of the two streams is terminated in the test section using a splitter plate with a 3" sharp edge. The test section used was 300 mm (12") long, and made of plexiglass. The experiment employed a velocity ratio of 0.67.

The planar shear layer was excited by a (music) wire strung across the test section through holes in the side walls and placed in the region near the trailing edge (x=0), at several y coordinates, see Figure A.1b for setup and coordinates. Several types of music wire (piano and guitar) were used with diameters in the range of 0.15-0.76 mm (0.006-0.03"). The wire length was 6-8 times the width of the test section to ensure uniform spanwise excitation. The wire self-vibration frequency, 85-400 Hz in this study, was varied by changing the wire diameter (moment of inertia), material (modulus of elasticity) and tension. The amplitude of the wire vibrations was 6 mm in all cases.

The flow field structure was surveyed using a hot wire anemometer and some smoke wire flow visualization. The hot wire probe (TSI type 1210 T1.5) was mounted on a traverse with three degrees of freedom. Data acquisition and probe location control were performed by a PC computer via a DT 2801-A A/D 12 bit board using DMA.

Sampling rates of 27 KHz could be reached. Velocity signals collected by the wire and passed through a IFA-100 anemometer were used to obtain maps of mean velocity and turbulent kinetic energy. Spectral analysis of the signals was done mostly on the PC using a dedicated Zonic PC2000 FFT board. During later experiments, a Tektronix 2630 FFT system was used. Graphical analysis and presentation of the data were done using Techplot and Image Pro-Plus on the PC-486 and AVS4 on a Silicon Graphics Workstation.

The DT 2801-A A/D board was calibrated by 343A DC Voltage Calibrator (made by John Fluke Co., USA) with a resolution of 10^{-6} Volts. The gain used for hot wire data sampling was 0 - +2.5 Volts. With 12 bit A/D board resolution, the sampled analog to digital signal could reach a final resolution of 6.1^{-4} Volts.

The hot wire was calibrated in the exit of a calibration nozzle exit against a standard Pitot tube at 20 different velocities. The pressure gauge used as the reference had a resolution of 1.0^{-5} meters of water. At standard atmospheric condition this gave a maximum velocity error of 0.0652 m/s. With the velocity field considered (0-40 m/s) the hot wire output range was 1.0 Volts. Fourth order polynomial interpolation method was incorporated to map the measured analog voltage input with the calibrated curve points. The estimated error was $0.56\Delta H\varepsilon^4$, where ε<0.00254 m and ΔH is the dynamic pressure head. In this experiment the estimated error is less than 0.1 m/s.

The statistical estimations of the measured errors of the flow are listed in Table I each using 40 samples for the quantity of mean velocity of the upper and lower sides of the mixing layer and turbulence level at y = 0 and x = 10 mm. With σ^2 unknown the confidence interval is $(\bar{x} \pm t_{\alpha/2} \frac{s}{\sqrt{n}})$:

Velocity quantity	$\bar{x}$	s	95% confidence interval
U_L	7	0.00023	$\bar{x} \pm 7.3\times10^5$
U_H	37	0.00017	$\bar{x} \pm 5.4\times10^5$
u'/U	0.017	0.01	$\bar{x} \pm 0.0032$

It should be mentioned that the error analysis of the data sampled by hot wire discussed in the following Chapters follow the same algorithm as that of in this Chapter. The mean velocity and turbulence level have about same order of error as in this Chapter. Therefor, this kind of analysis will not be repeated.

Two types of data were collected: time series and phase locked. The time series data was used to obtain time-mean information of the flow field. Naturally, this data washes out detailed (frequency specific) information about the shear flow. Phase locked information was obtained with the help of a phase-reference (laser-detector) system, shown in Figure A.1b. The self-excited wire passed through the beam of a He-Ne laser which was targeted on a photodetector. The signal outputs from the detector were too weak to be used as the triggering signal (about 100 mv). Thereby, a circuit was built to amplify the weak signal. A more detailed schematic view of the circuit is shown in figure A.1.c. As shown, the sensor used was a high speed light type. Since the signal output of the sensor was negative and small, a Lm324 chip was connected after it to amplify the signal to minus five volts. This was followed by a flip flop chip 7473 to change the signal to plus five volts -- acceptable to DT 2801 series triggering input. Since the wire interrupts twice of the laser light in one excitation cycle, another role of the 7473 Chip was to cancel the odd (or even) number pulses. This circuit has two functionalities: 1) it furnishes as an accurate measure of the excitation frequency; 2) it serves as a trigger source for the phase-locked sampling.

A schematic drawing of the smoke wire system is shown in figure A.1d. The wire, coated with the toy automotive smoke oil, was heated by a pulse generator which was synchronized by a trigger signal with the camera. A time delay circuit was located between the pulsed generator and the camera. By proper adjustment of the time delay the camera could capture the image of the smoke when it propagated downstream, thus the image of the flow structure. Due to the turbulent dissipation of the smoke, the highest

velocity that could be reached in this experiment was about 10 m/s on the high speed side of the mixing layer.

A.3 Characterization of the Flow

A.3.1 Mean Flow and Frequency Domain Analysis

Addressed in this chapter are the effects of local excitation on the evolution of a planar mixing layer with free stream velocities of $U_L = 7.0 \ \ m/s$ on the low speed side and $U_H = 36 \ \ m/s$ on the high speed side. This corresponds to a velocity ratio of: $R = (U_H - U_L)/(U_H + U_L) = 0.67$, and a momentum thickness Reynolds number of 1380, based on a momentum thickness of 3.0 mm at an axial distance of 40 mm where the flow became unstable. The boundary layer on both sides of the splitter plate were intentionally kept turbulent. Both streams consisted of air, and thus the density ratio was unity.

The characteristics of the natural, turbulent, shear flow was examined first. Auto power spectra were obtained at various stations in the axial direction near the outer boundaries of the shear layer. Very near the trailing edge the spectra constituted of broad band noise with no particular vortex shedding frequency discernible, typical of turbulent flow. At an axial location of 40 mm from the trailing edge a broad peak between 200 to 1000 Hz with a maximum about 550 Hz was observable and shown Figure A.2a. This station corresponds to an axial position of about one wavelength of the most unstable waves. Figure A.2a also reveals that the turbulent case is characterized by a band of frequencies (based on the average velocity 21.5 m/s and the characteristic frequency 550 Hz), unlike in the laminar case where a single most amplified frequency and its harmonics exist. This band moves to lower frequencies as the flow progresses downstream, as seen in Figure A.2b. Both of these characteristics were reported earlier by Wygnanski and Peterson (1987) and Wygnanski, Champagne and Marasli (1986).

The unexcited mean flow velocity profiles, for several axial locations, are plotted in Figure A.3 using similarity variables according to Gaster et al. (1985), where the

similarity variable $\eta=y/\theta$. The experimental data collapsed well. One should notice that profile 2, which is a modification of 'tanh' profile shown as profile 1, provides a better fit. Therefor, profile 2 will be used as the reference velocity profile to calculate the amplification rate in the next section.

Although the mean flow profile do not exists in a turbulent flow, the instability mechanism of the turbulent mixing layer can still be determined based on the mean velocity profile, Gaster,m., Kit, E. Wygnanski, I. (1985). The mixing layer will evolve in the far field according to its most unstable mode, despite the fact that many other modes can be excited in the near field. Thus, in the case of the turbulent mixing layer, the most amplified frequency and its sub harmonics can still be determined from instability analysis of the mean velocity profiles in the near field.

For the work reported herein the excitation frequencies ranged from 85 Hz to 400 Hz, which included frequencies well below to frequencies near the most amplified frequency. The range of frequencies chosen was restricted by the physical properties of the available wires, the free stream velocities, and the difference between the velocities of the two streams. As an example; a 0.15 mm (0.006") piano wire could only be excited with a free steam velocity above 10 m/s and a velocity ratio R>0.3. In all cases the wire had to be placed near the trailing edge in the mixing layer to be excited and as mentioned before in the velocity gradient region.

A.3.2 Linear Instability Analysis of the Mixing Layer

As an estimate and evaluation of the liner instability theory, Michalke's (1965) spatial instability theory is employed. According to his work the flow of an inviscid fluid is governed in the two-dimensional case by the Helmholz vorticity equation

$$\frac{d\Omega}{dt}=\frac{\partial\Omega}{\partial t}+u\frac{\partial\Omega}{\partial\zeta}+v\frac{\partial\Omega}{\partial\eta}=0 \qquad \text{(A.1)}$$

Here $u(\zeta,\eta,t)$ and $v(\zeta,\eta,t)$ denote the x- and y-components of the velocity and

$$\Omega=\partial v/\partial x-\partial u/\partial y \qquad \text{(A.2)}$$

Assume that a unidirectional steady basic flow is given by its velocity profile U(y) and its vorticity distribution

$$\Omega_0(\eta) = -U' \tag{A.3}$$

where the prime denotes differentiation with respect to y. Further, as a common procedure in linear instability analysis, a small disturbance $\varepsilon u_1(x,y,t), \varepsilon v_1(x,y,t)$ and $\varepsilon\Omega_1(x,y,t)$ is impose upon this basic flow. The instantaneous velocity and vorticity are given by

$$\begin{aligned} u(\varsigma,\eta,t) &= U(\eta) + \varepsilon u_1(\varsigma,\eta,t) \\ v(\varsigma,\eta,t) &= \varepsilon v_1(\varsigma,\eta,t) \\ \Omega(\varsigma,\eta,t) &= \Omega_0(\eta) + \varepsilon\Omega_1(\varsigma,\eta,t) \end{aligned} \tag{A.4}$$

Introducing a stream function $\psi_1(x,y,t)$ where

$$u_1 = \partial\psi_1/\partial\eta, \quad v_1 = -\partial\psi_1/\partial\varsigma, \tag{A.5}$$

and can be expressed as wave disturbances

$$\begin{aligned} \psi_1(\varsigma,\eta,t) &= \Re\left\{\phi(\eta)e^{i(\alpha\varsigma-\beta t)}\right\} \\ \Omega_1(\varsigma,\eta,t) &= \Re\left\{\omega(\eta)e^{i(\alpha\varsigma-\beta t)}\right\} \end{aligned} \tag{A.6}$$

where α and β are complex number, α_i is the spatial growth rates and $\beta_r=2\pi fU_0/\theta$ is the cyclic frequency. Further if one assumes that

$$\phi = \exp[\int \Phi(\eta)d\eta] \tag{A.7}$$

a Riccati equation in $\Phi(y)$ for equation (A.1)

$$\Phi' = \alpha^2 - \Phi^2 + U''/(U-\beta/\alpha) \tag{A.8}$$

with the boundary conditions

$$\Phi(+\infty) = -\alpha; \quad \Phi(-\infty) = +\alpha \tag{A.9}$$

is obtained.

The basic flow velocity was found to be described better by the following equation

$$U(\eta) = \frac{U-U_L}{U_H-U_L} = 0.5[1+\tanh(4.0\,\eta)] \text{ and } \eta = \frac{y-y_{0.5}}{\theta} \tag{A.10}$$

which is termed as profile 2 in the present document compared with the commonly used tanh profile

$$U(\eta) = 0.5[1 + \tanh(\eta)]. \tag{A.11}$$

Introduction of a new independent variable

$$z = \tanh(4.0\,\eta) \tag{A.12}$$

into equation (A.8). And use of

$$U'' = -16\tanh(4.0\,\eta)\sec h^2 y = -z(1-z^2)$$

one can obtain the eqn.

$$\frac{d\Omega}{dz} = \frac{\alpha^2 - \Phi^2}{1-z^2} - \frac{2z}{1+z-2\beta/\alpha} \tag{A.13}$$

and from (A.9) with $z_b = \pm 1$

$$\Phi(z_b) = -z_b\alpha \tag{A.14}$$

Equation (A.13) can be integrated numerically using the Runge-Kutta-Gill procedure. Figure A.4 shows the spatial growth rates as compared to the measured data in figure A.2a. As seen, the numerical results fall lower than the experimental results. The most amplified frequency calculated from profile 2 is 500 Hz, which is very close to the experimental result of 550 Hz.

A.4 The Effects of Wire Excitation

The effects of wire excitation are reported in this section. First, time-mean data is presented followed by phase-locked information. The wire was placed close to the trailing edge of the splitter plate at several y coordinate locations, see Figure 1b. The amplitude of vibration was always about 6 mm, of the same order of local mixing layer thickness. The effect of the wire excitation, using time-mean data, will first be evaluated in terms of spatial evolution (growth) of the mixing layer. A commonly used measure for the extent of the mixing layer is its momentum thickness. Figure A.5 shows the growth of the mixing layer momentum thickness as a function of downstream distance from the splitter plate, for unexcited flow and excitation at 85, 200, and 400 Hz; wire positioned at y=0mm, x=5mm.

Several observations are made. The natural mixing layer spreads almost linearly. All excited cases exhibit increased growth. Excitation at frequencies equal or less than 200 Hz results in a significant shear layer spread, localized around x=120 mm, as will be shown later this corresponds to the location where vortices begin to merge, followed by a second linear region with the same growth rate as in the initial region. The effect of excitation frequency on mixing layer growth has been examined and is shown in Figure A.6. It can be seen, indeed, that there is an optimum frequency around 160-240 Hz, in the range of subharmonics of the most amplified frequency for the unexcited mixing layer.

Examination of the spectral evolution of the mixing layer is shown in Figures A.7, A.8 and A.9 for excitations at 200 Hz and 400 Hz and 85 Hz respectively. One can see that the flow strongly locked to the excitation frequency both in the near and far flow fields. Notice, that for 200 Hz excitation, at x=40 mm, the first harmonic contains more energy at y=0.0mm, (Figure A.7a), while at y=-8.5 mm (Figure A.7b) the fundamental contains more energy. In contrast, in the case of 400 Hz excitation (Figure A.8a and A.8b) the first harmonic always has the highest energy. It is the authors view that Figure 7a and 7b might indicate different coherent structures which co-exist at the same location, a point that will be elaborated further in the following text. In both cases mentioned above, the decreasing in power spectra amplitude is very small along the streamwise direction. Similar phenomenon can also be observed for the case of 85 Hz shown in Figure A.9. The combination of strong phase locking in the far flow field and the low frequency excitation indicates that the so called "collective interaction", Huang and Ho (1982), might exist in these case which is a global resonant phenomenon and is expected to be able to achieve better effects than the subharmonic excitation.

Another way to examine the effect of excitation on the mixing layer development is to plot its boundaries as a function of axial distance downstream. Using a measure of turbulent kinetic energy, $\left(u'/U\right)^2$, time-mean contour maps have been drawn and are shown in Figure A.10. Part (a) is for the unexcited mixing layer; in parts (b) and (c) the

wire was excited at 200 Hz, and placed at a lateral coordinate of y=0 and y=3.0 mm respectively. Images are for the mid plane location in the transverse direction. It is clear from the images that the excitation increased the spreading of the mixing layer, the region of turbulent fluid, and therefore the region of mixed fluid, which is related but not identical with the region displayed here, Dimotakis (1991). In both cases (a) and (b) the shear layer spreads more into the low velocity side, consistent with existing knowledge, Dimotakis (1991). This situation can be changed by moving the exciting wire in the y direction. Figure A.10c shows a case where the wire was placed at y=3.0mm, and self excited at 200 Hz. Here the mixing-layer spreads more symmetrically. In this case an increased amount of fluid is entrained into the mixing layer from the high speed flow, compared with the symmetrical wire location of Figure A.10b. As a consequence, the proportions of fluid from the two streams contained in the mixing layer can be varied through small adjustments in the lateral location of the wire relative to the splitter plate; a point of importance to chemically reacting shear layers.

After the simplicity and effectiveness of the self-excited wire method has been demonstrated, more information on the flow field structure and evolution was sought. For that purpose, phase-locked data was collected, analyzed, and presented in the x-y-t, space-time domain. Ensemble averages of phase-specific data for the mixing layer mid-plane were calculated. Turbulent kinetic energy maps (x-y planes) for six instances during an excitation cycle, for 200 Hz excitation are shown in Figure A.11. Examination of the near field of the flow reveals that the flow contains multiple coherent structures, of different sizes. One may see that at 0^0 phase. there exist two large structures between the streamwise locations of 50 - 100 mm. The structure on the high speed side is ahead of the one on the low speed side. These structures develop as the phase increases. Due to the differences in local phase speed the structure on the lower speed side is retarded during the progress while the one on the high speed side catches up and merges with the much larger structure ahead of it that resulted a much larger increase in mixing layer thickness. The same maps are shown in Figure A.12 for an excitation frequency of 400

Hz. In this case, however, only a single large scale structure is evident. No merging process is observed. This can easily be explained since the flow is excited at about the fundamental of the most amplified frequency. There seems therefore to be a fundamental difference in the response of the mixing layer to excitation below versus above the subharmonic range (e.g. 200 Hz) of the most amplified frequency.

Conditions of 85 Hz and 300 Hz of excitations are shown in figure A.13 and A.14. Again, the lower end subharmonic excitation of 85 Hz does show multiple-structures. For example, observing two instances at phase 72^0, and 144^0, the structure at the location of x=35mm on the high velocity side (in the first instance) moves to x = 75 mm in the second instance in which there appears another structure on the low speed side at x = 50 mm. The 300 Hz excitation case, shown in figure A.14, although substantially lower than the most amplified frequency (about 550 Hz), exhibits only a single structure at any time and spatial location. This shows that for multiple structures to occur the excitation frequency has to be equal or lower than the subharmonic of the most amplified frequency.

Other evidence of the existence of large structures under excitation is shown by fluid visualization using smoke wire in figure A.15 where comparisons is made over the unexcited case and the excited case of f = 200 Hz. One may see clearly the growth of the structure as it propagates downstream when the flow is under excitation while for the unexcited case the structures are much smaller and less organized.

Enhanced entrainment is a more relevant measure to evaluate the improvement of mixing. Figure A.16 shows the comparisons of flow entrainment under different conditions. As seen the 200 Hz excitations has the highest flow entrainment ratio which for case a) is close to twice of the unexcited case at streamwise location of 250 mm. As expected 400 Hz excitation has lesser effect on the entrainment ratio (7.0 as compared to the over 8.0 for the case of 200 Hz excitation. Also one may notice that the adjustment of wire location along the lateral directions does have some effect on the overall flow entrainment, for instance, at x = 250 mm, flow entrainment ratio for case a) is 9.0 while

for case b) is 8.0. In summary, one can say that excitations other than subharmonic have lesser effect on the entrainment ratio. This may in part attributed to the lack of vortex merging as in the case of f = 400 and 300 Hz excitation.

The effect of the excitation on the flow field structure in terms of propagation of coherent structures was examined using three dimensional views of phase-mean velocity surfaces. Shown in Figure A.17 a, b, c and d are four surfaces $(u-U_L)/(U_H-U_L)=0.5$ for 200, 400, 85 and 300Hz excitations respectively. Clearly, the 200 Hz excitation exhibits a stronger effect on the flow field structure. This is most noticeable in the near-field where the "zigzag" shaped waveform is an indication of interaction between multiple structures. A similar picture can be seen in the case of 85 Hz excitation. However, in the cases of 300 Hz and 400 Hz excitation, one can see the more organized waves that propagate downstream. The well-organized wave form is an indication that there are no interactions between the structures.

A.5 Discussion

The self-excited wire method has proven very simple, rather effective, and does not require external energy input. It has been observed that the wire will not vibrate in either free stream of the mixing layer. It was also observed that the path of the wire is elliptical in the x-y plane, with the major axis in the y direction typically 6 mm long, and the minor axis in the x direction; axis ratio 2-3:1. After an initial transient the wire will always follow an elliptical path which moves it from the low speed side to the high speed side of the shear layer and back (near the trailing edge of the splitter plate). The wire is traveling between the low and the high speed streams experiencing a time varying drag force, which is counteracted by the elastic (spring) reaction of the wire. The balance of these forces results in a limit cycle for the wire trajectory. The amplitude of the wire (self) vibration in the cross stream (y) direction can be controlled, and in order to be effective should be of the same order of the local mixing layer thickness.

Despite the fact that the excitation amplitude was kept constant best results were achieved for the subharmonic excitation. Examination of the space-time, x-y-t domain revealed that existence of multiple coherent structures in the near field for excitation frequency equal to or below the subharmonic, but not for higher excitation frequencies. In contrast, in the far field the flow always locked on to the excitation frequency, i.e., far from the excitation point the response frequency of the flow always equaled the excitation frequency. This reveals the strong influence the music wire excitation can exert upon the flow.

Even though the near field spectra of the unexcited mixing layer show a peak around 550 Hz, the most effective excitation frequency was found to be around 200 Hz. This is no contradiction, since the effectiveness is judged here in terms of mixing layer spread. As was reported already, for excitation frequencies of 200 Hz or lower the near field contained multiple structures, which paired while traveling downstream. This pairing led to a dramatic increase in mixing layer thickness, at x=120 mm, see Figure A.5. This pairing-like event can be seen in Figure A.11, occurring somewhere between the axial position of 100 and 150 mm. The spectra of the 200 Hz excitation case, shown in Figure A.7, also supports this picture.

The response of the mixing layer to the wire excitation demonstrates the importance of efficient coupling of the perturbation energy into the flow. The coupling efficiency depends on three parameters: location of perturbation, frequency, and amplitude of the perturbation. The wire was placed near the trailing edge of the splitter plate due to the known high receptivity of the shear layer in this region. The frequency of excitation should be close to the subharmonics of the natural flow, though with large enough amplitude the flow will lock to almost any frequency. Whether the flow perturbation caused by the actuator can be considered small depends on the amplitude and location of excitation. In contrast to vibrating plate arrangements, which perturb the whole boundary layer leaving the splitter plate, the vibrating wire does not interfere with the incoming flow. As such, this type of excitation is more local compared with other

methods reported in the past. The only requirement related to the excitation amplitude, using the wire, is that it be of the same order as the local shear layer thickness (near the trailing edge). This requirement is set by the physical characteristics of the wire, i.e., for it to reach a self sustaining limit cycle, and not by minimum energy required to excite the flow.

Before discussing some potential applications, one has to note that in the work reported here the wire vibrated in its fundamental mode, resulting in uniform excitation along the splitter plate. As a consequence the excited structures are two dimensional. Additional improvement in the mixing between the two fluids can be achieved through three dimensional mixing layer evolution. Using a vibrating wire this may be realized by causing it to vibrate in higher modes (was demonstrated in the author's laboratory).

Potential applications are proposed in two areas. In the area of aerodynamics a vibrating (self-excited) wire can be placed in front of the airfoils to change their stall characteristics by decreasing the size of the separation bubble. Variation in the wire frequency of vibration can be achieved mechanically or thermally. Such an application has been demonstrated (unpublished) for the shortening of a separation bubble formed by a forward facing step by about 2/3. One should, though, keep in mind the drag on the wire when considering airborne applications. An application even more natural is in the area of mixing of two separate fluids. This could be particularly useful in reacting flows like many step stabilized combustors, though, it has to be noted that the effectiveness of the wire method in flows with heat release has yet to be determined. When compared with alternatives such as acoustic bulk modulation, thermal modulation and mechanical trailing edge actuation, the self-excited wire method is attractive due to its simplicity and zero energy input requirement.

A.6 Summary

Perturbation and control of the evolution of a two stream turbulent, planar, mixing-layer was achieved through the use of a flow-excited wire mounted in front of the trailing edge of the splitter plate. Excitation of the mixing layer at frequencies between 85 and 400 Hz was attained. In all cases the wire vibration amplitude was about 6 mm. For all excitation frequencies, the response frequency of the flow in the far field was equal to the excitation frequency, i.e., complete locking of the flow was observed. In the near field the response of the flow depended on the excitation frequency. For excitation frequencies below the subharmonics of the natural flow, multiple structures were observed, while for frequencies excited close to the fundamental only single structures existed. The effect of the excitation was to increase the mixing layer momentum thickness in all cases. However, it was found that the most increase, greater than a factor of two, was attained for frequencies around 200 Hz. This marked increase in momentum thickness is attributed to interaction (pairing) between several structures in the near field.

Using the wire excitation it was also possible to control the directional evolution of the mixing layer. Unexcited and excitation with a symmetrically placed wire the mixing layers spread more into the low speed side (bottom flow). By displacing the wire slightly in the vertical direction off the symmetrical location, this situation could be arbitrarily altered. Small displacements in the wire (actuator) location offer, therefore, a method for control over the entrainment ratio of the two fluids; of crucial importance to mixing and reacting flows.

In conclusion the vibrating wire actuator offers an interesting alternative for shear flows actuation. It virtues, compared with the standard techniques are: 1) being self-excited, requires no external energy input, 2) couples into flow field locally, thus not creating a bulk disturbance, and 3) enables control over the mixing ratio between the two streams.

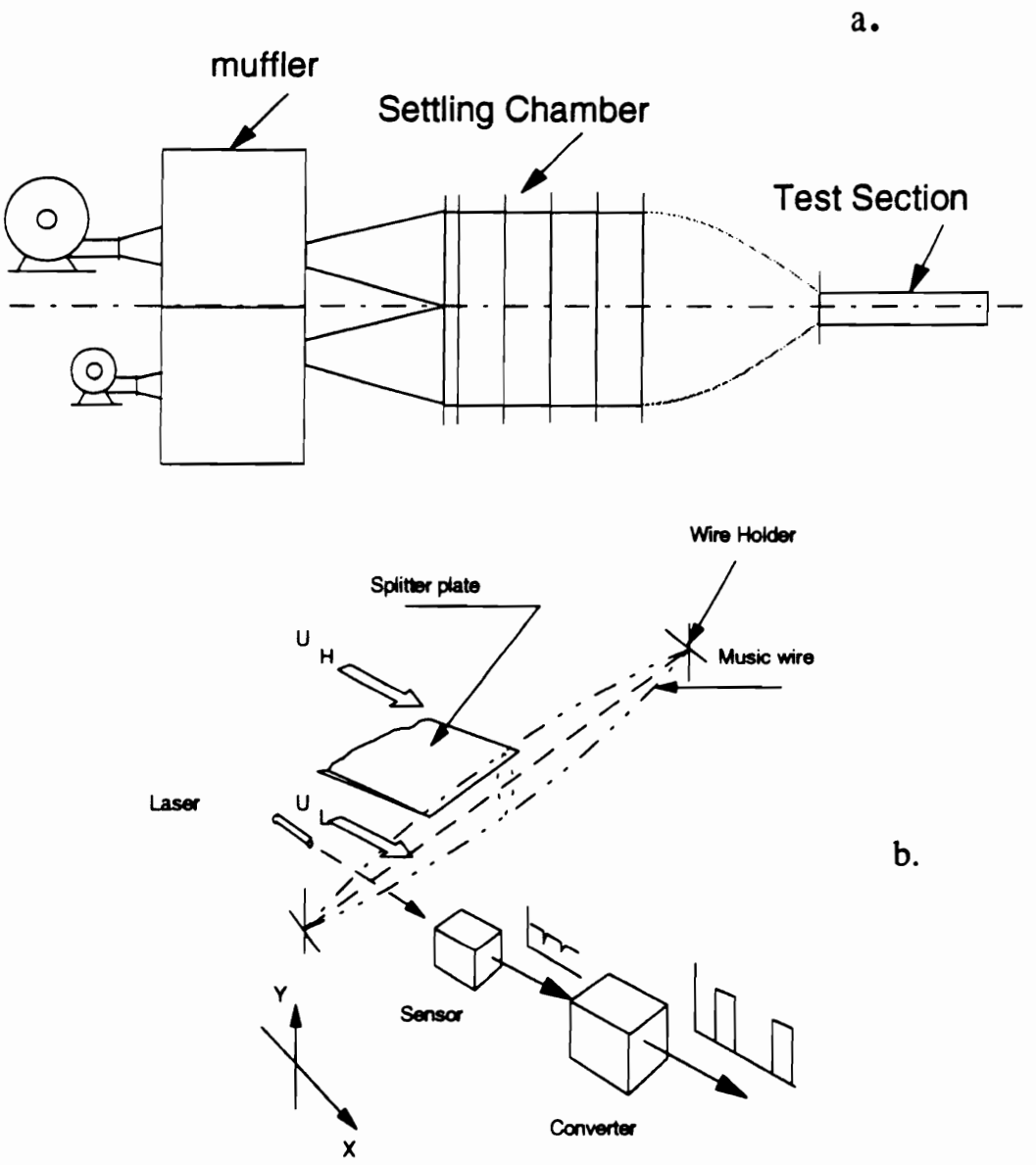

Figure A.1 a). Schematic view of the wind tunnel; b). Schematic view of the wire setup

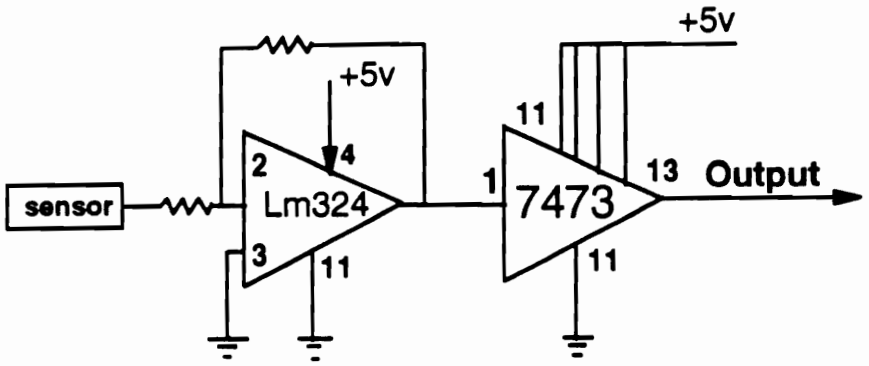

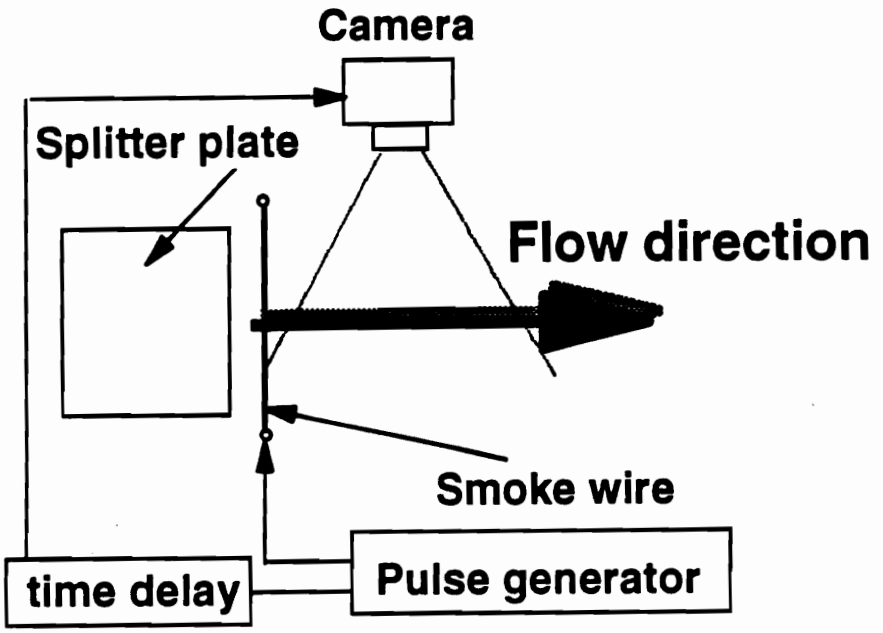

Figure A.1 c). Schematic view of the signal synchronization circuit; d). Schematic view of the smoke wire visualization setup

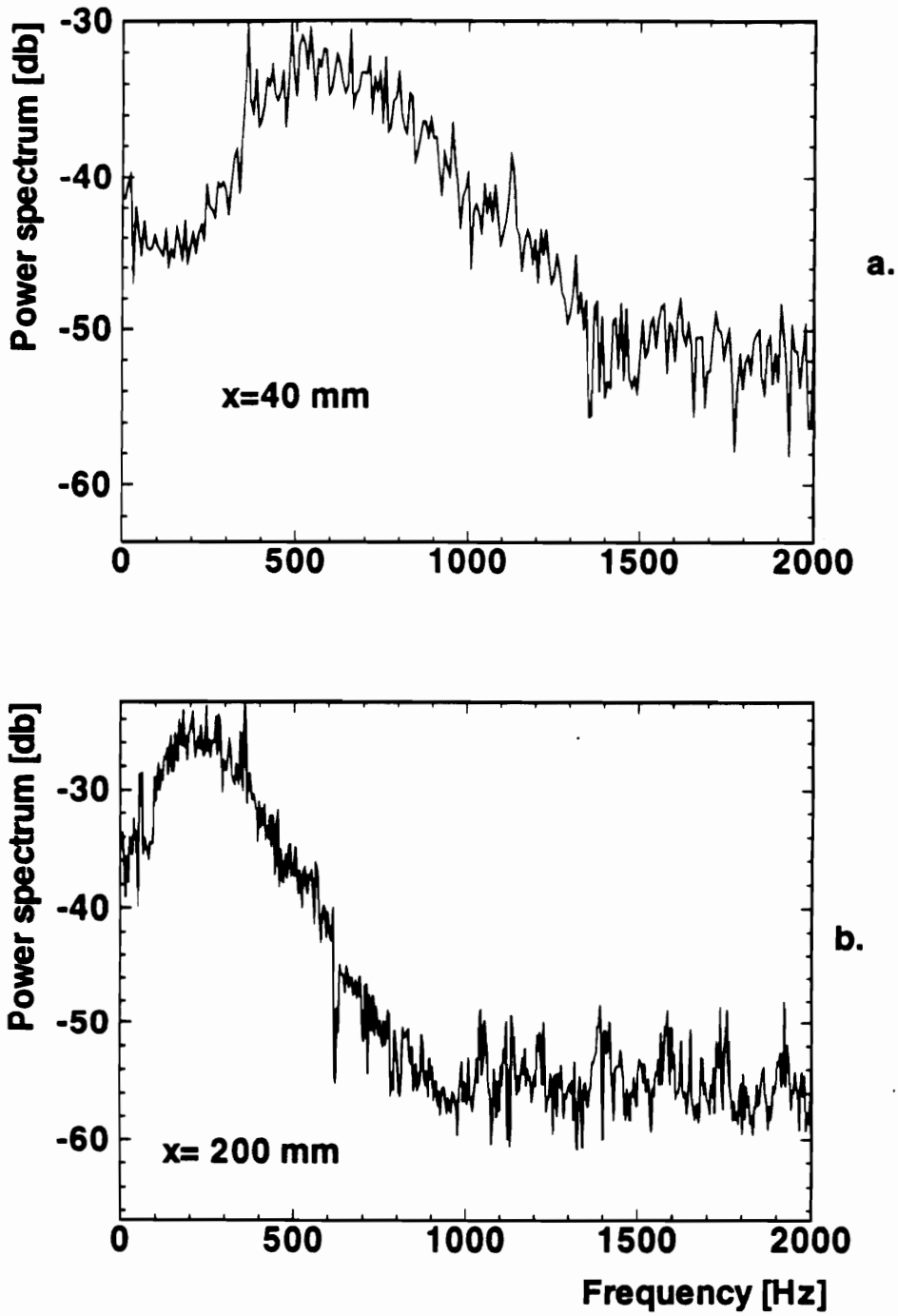

Figure A.2 Power spectra of the unexcited flow. a). x = 40mm; b). x = 200 mm

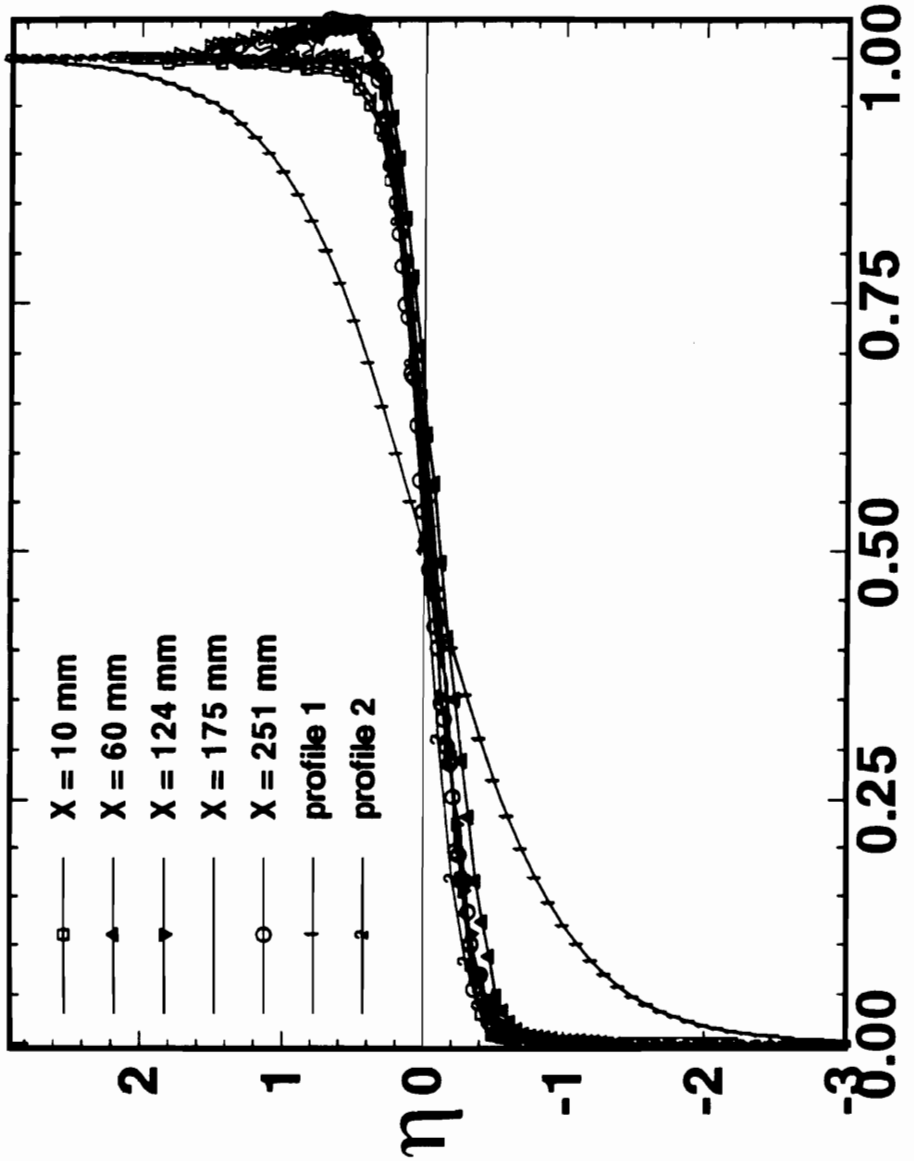

Figure A.3 Normalized velocity profiles across mixing layer

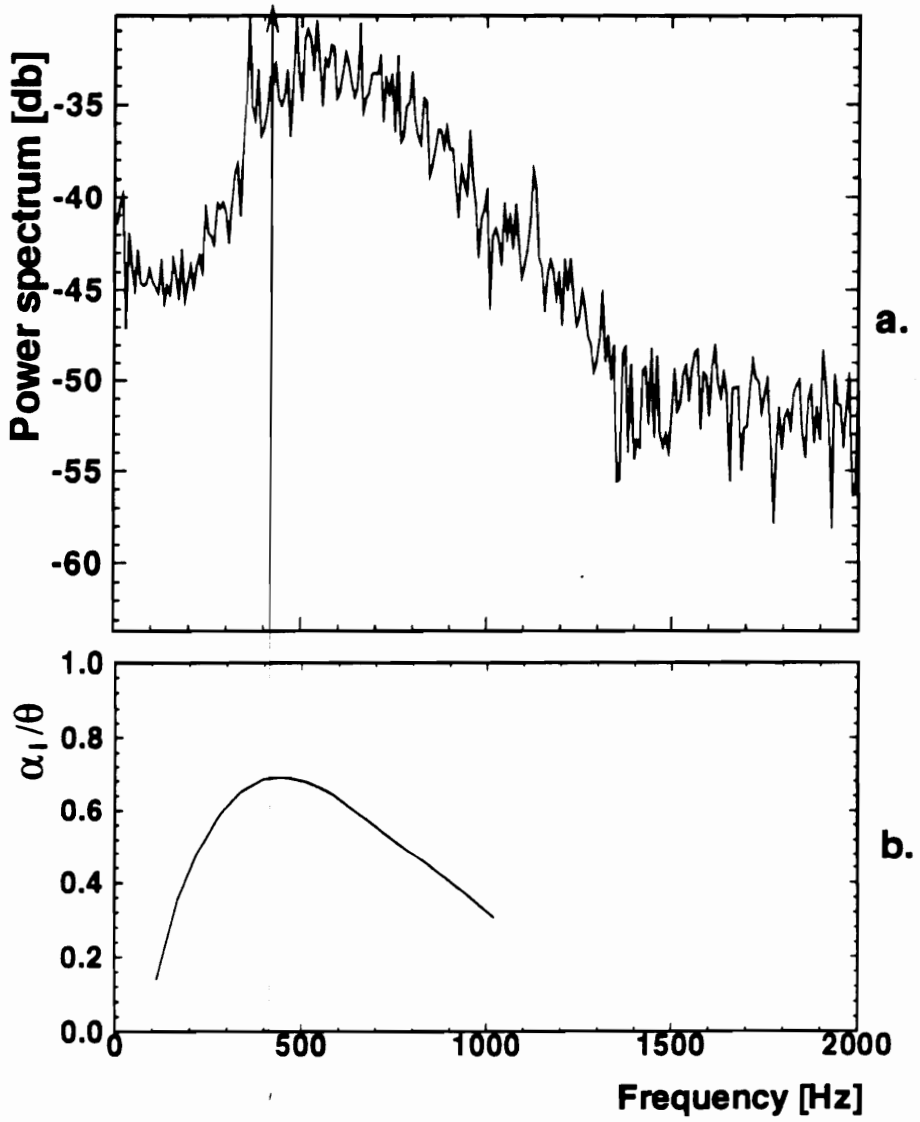

Figure A.4 (a) Power spectra of the measured streamwise velocity ; (b) calculated spatial growth rate as a function of the dimensional frequency

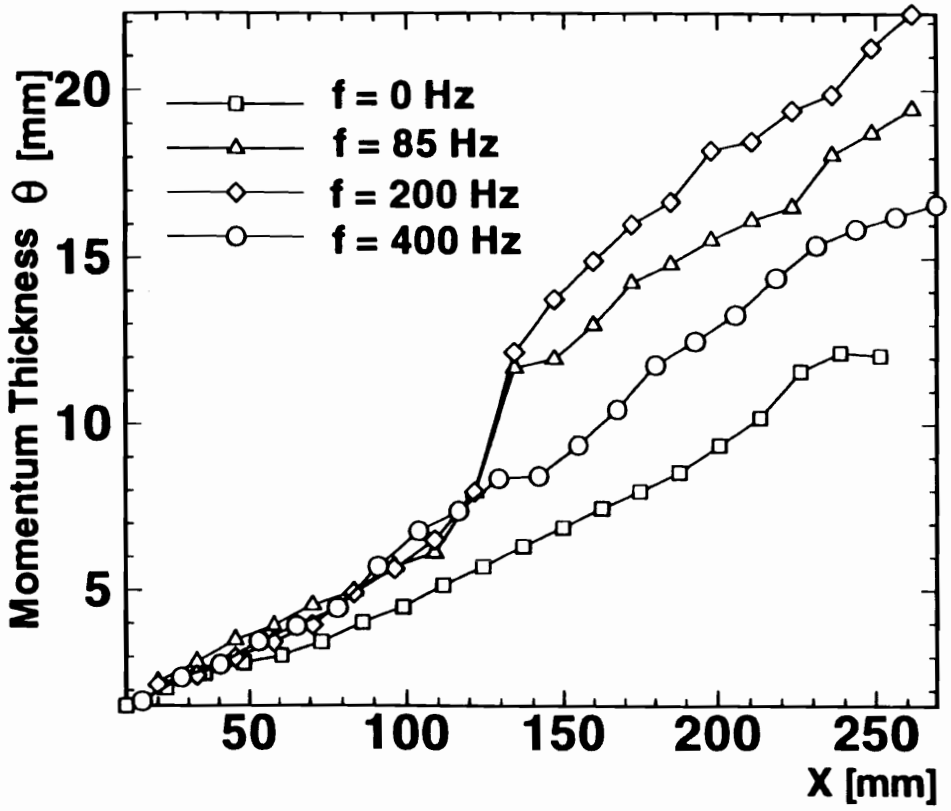

Figure A.5 Momentum thickness of mixing layer for different excitation frequencies

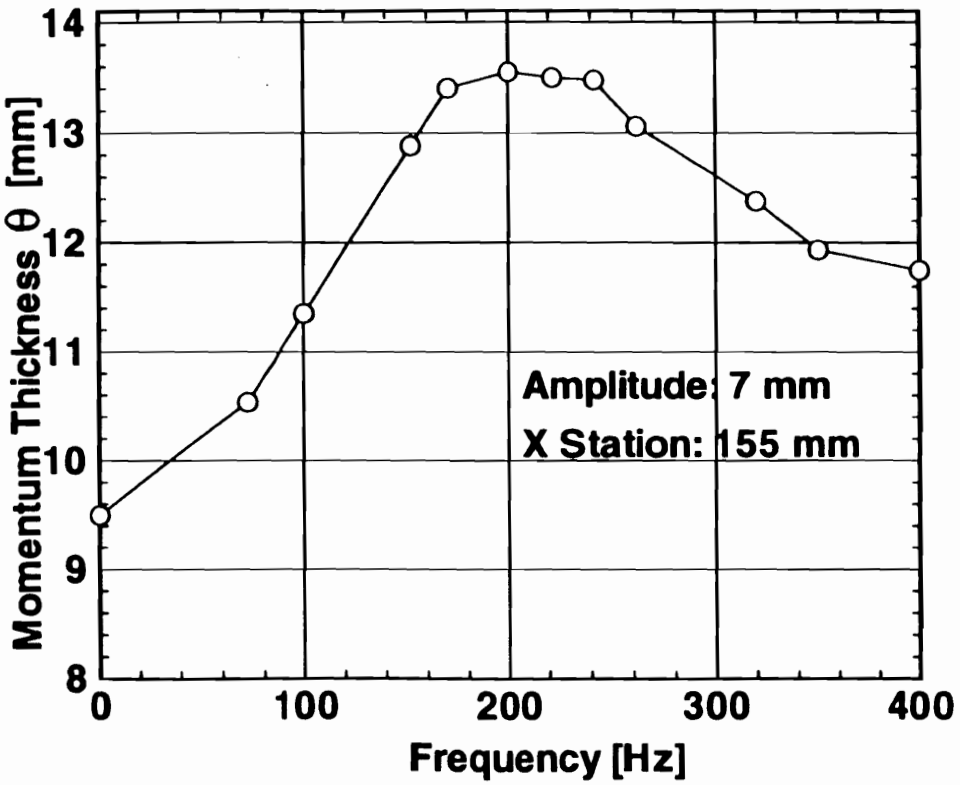

Figure A.6 Momentum thickness dependence on excitation frequency

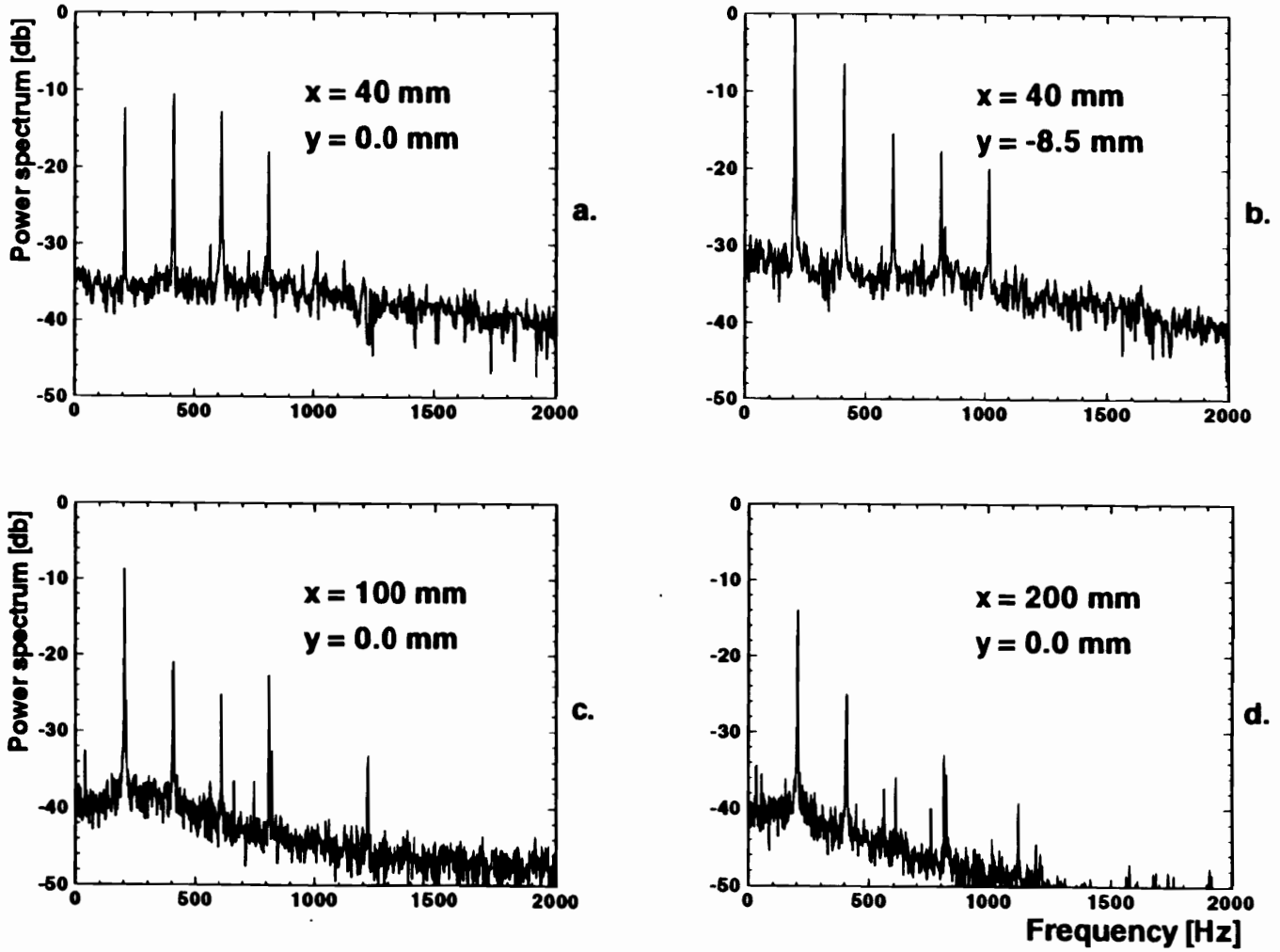

Figure A.7 Spectral analysis of mixing layer excited at 200 Hz

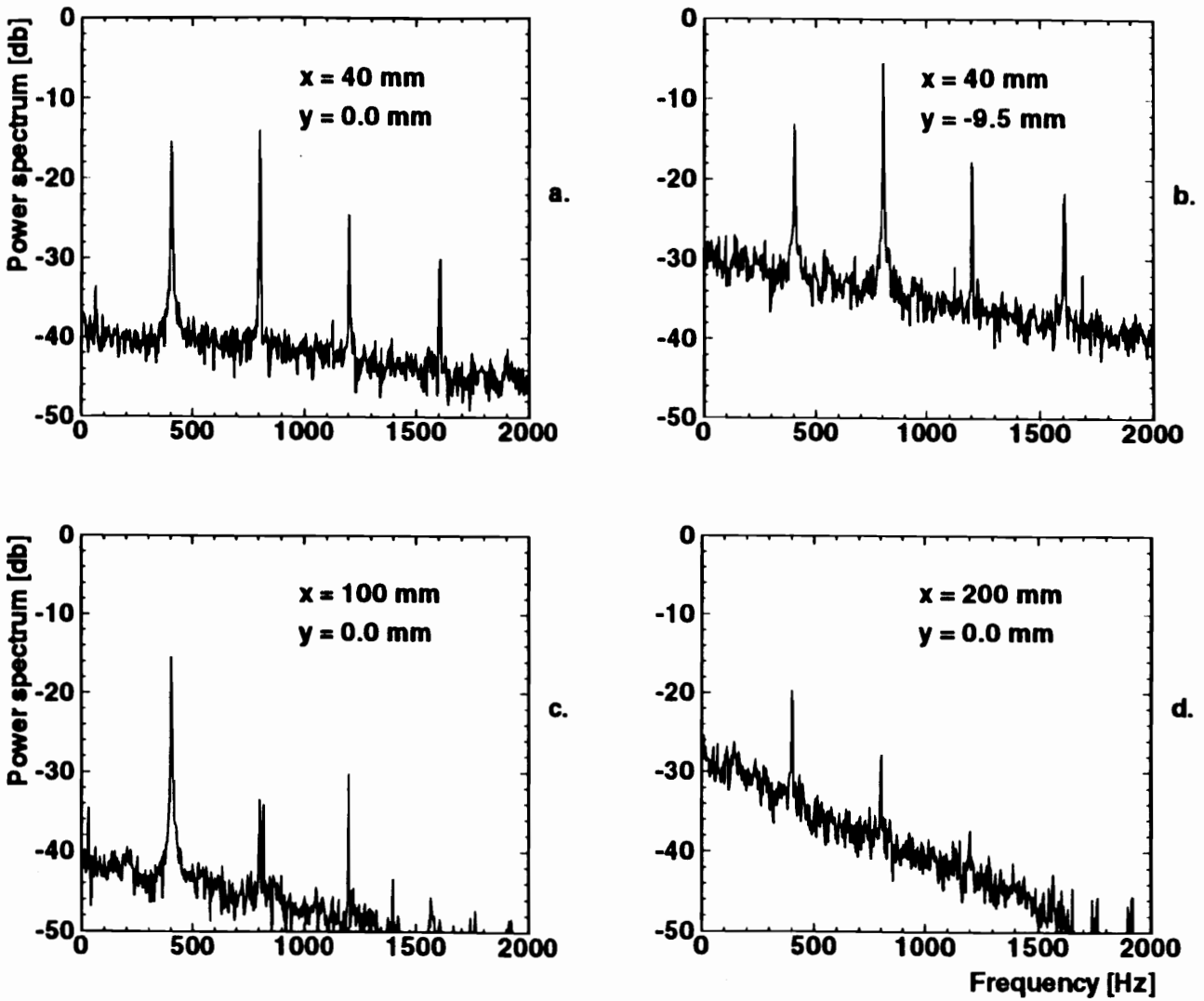

Figure A.8 Spectral analysis of mixing layer excited at 400 Hz

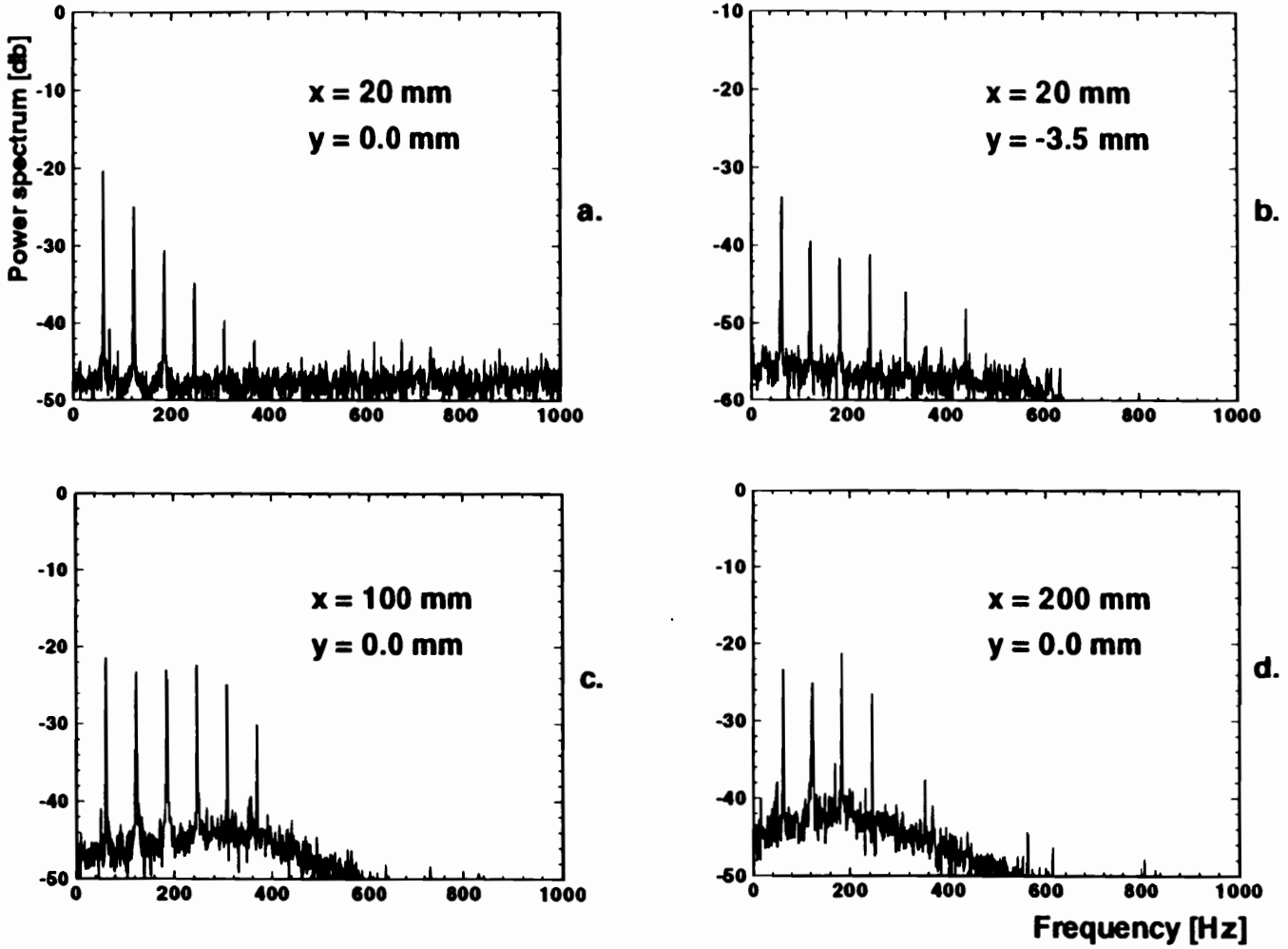

Figure A.9 Spectral analysis of mixing layer excited at 85 Hz

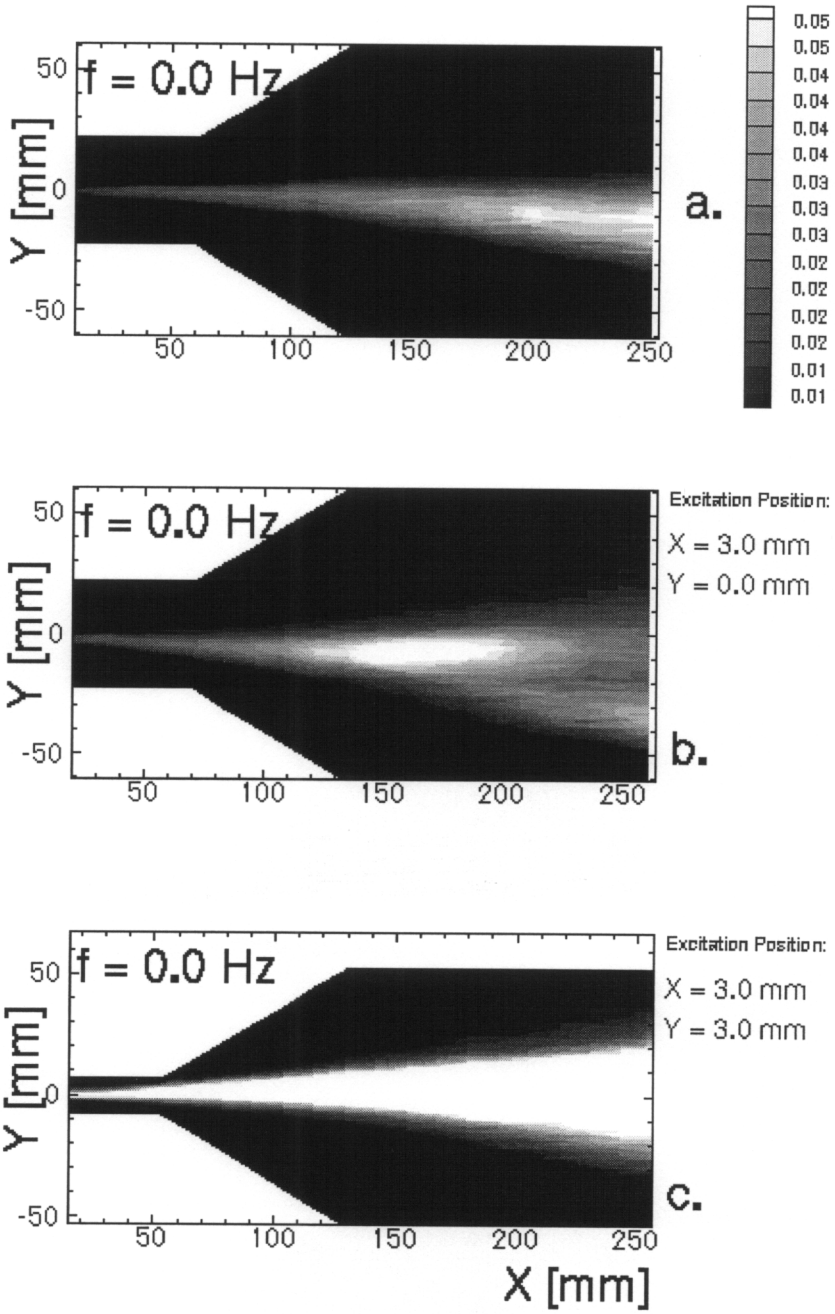

Figure A.10 Turbulent kinetic energy. a). unexcited; b). f_e = 200 Hz, symmetric wire; c). f_e = 400 Hz, asymmetric wire

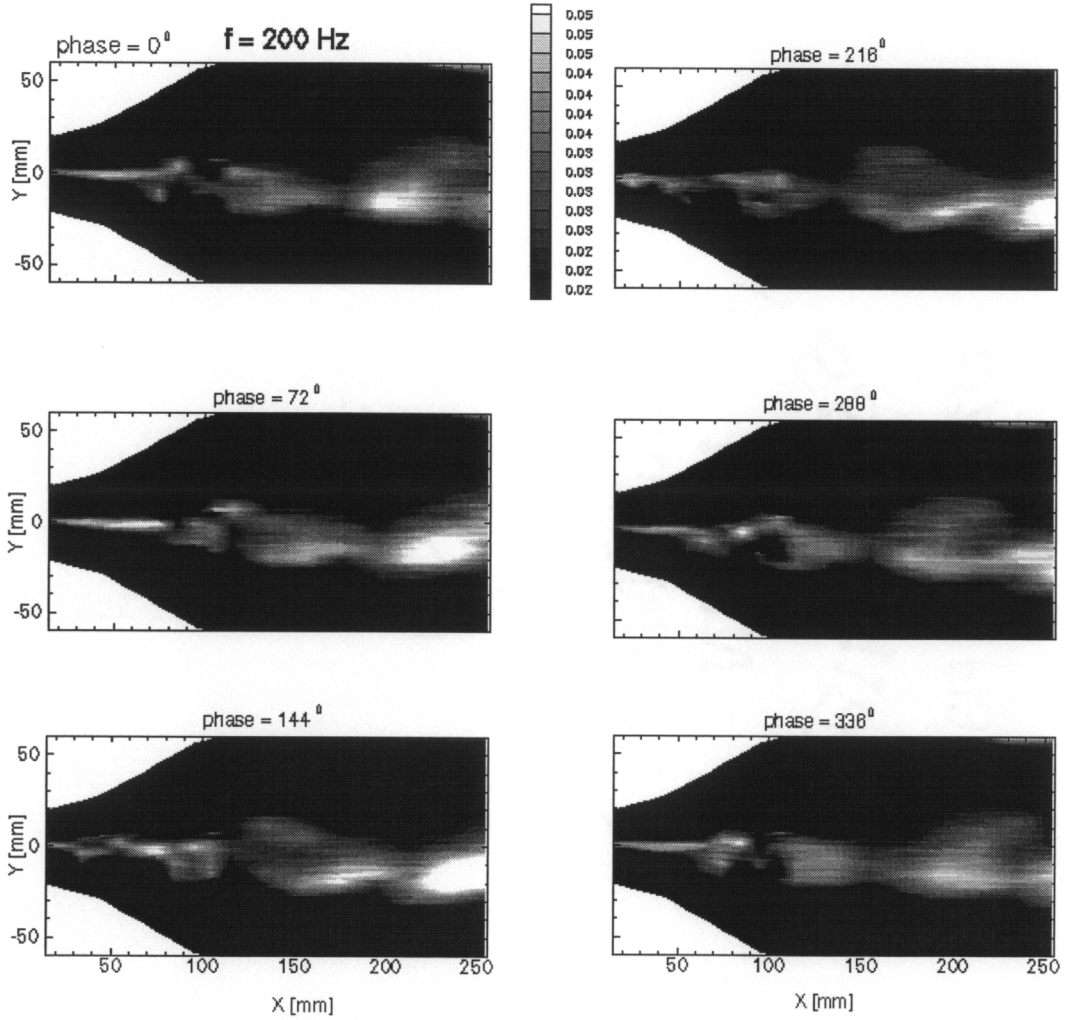

Figure A.11 Turbulent kinetic energy maps at six times during an excitation cycle for f_e = 200 Hz

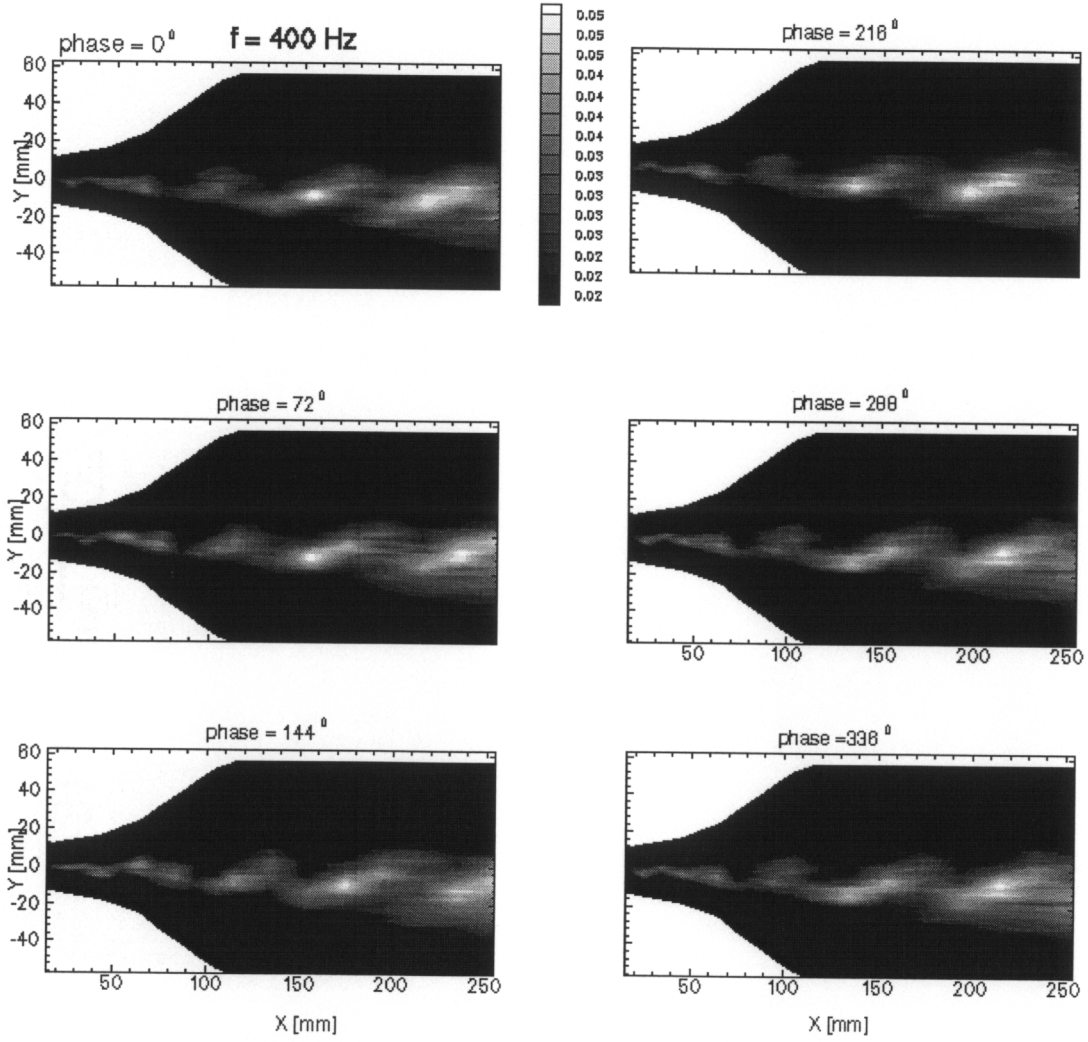

Figure A.12 Turbulent kinetic energy maps at six times during an excitation cycle for $f_e = 400$ Hz

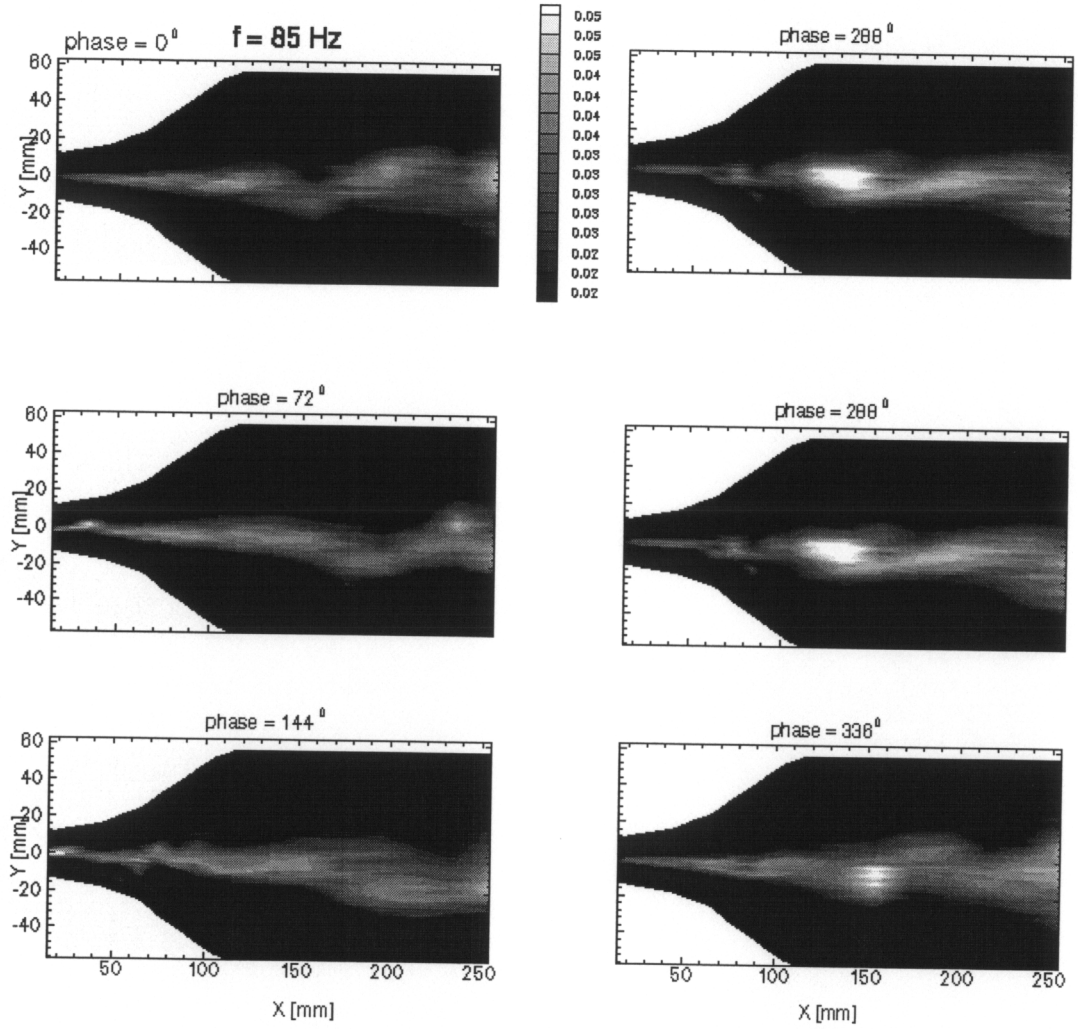

Figure A.13 Turbulent kinetic energy maps at six times during an excitation cycle for $f_e = 85$ Hz

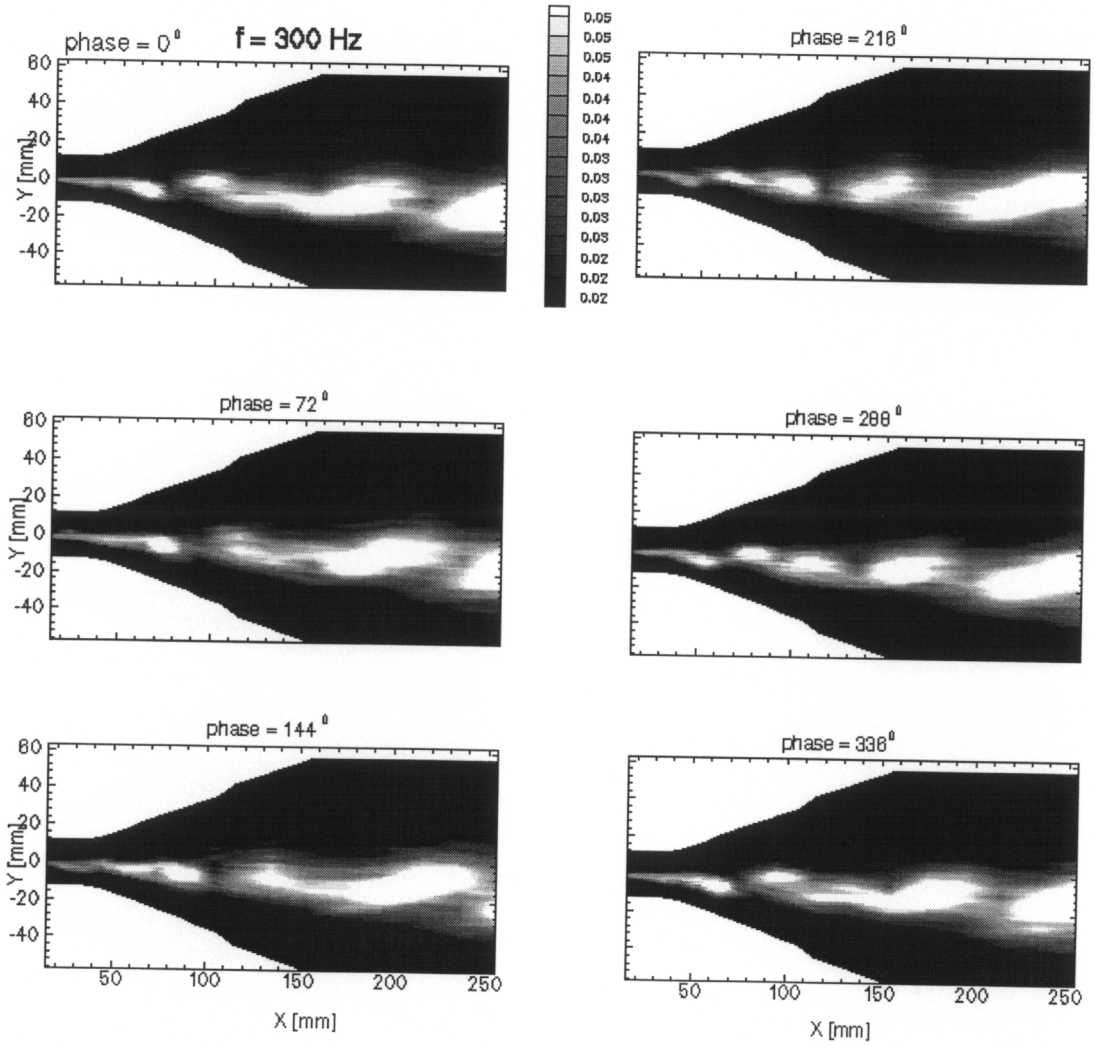

Figure A.14 Turbulent kinetic energy maps at six times during an excitation cycle for $f_e = 300$ Hz

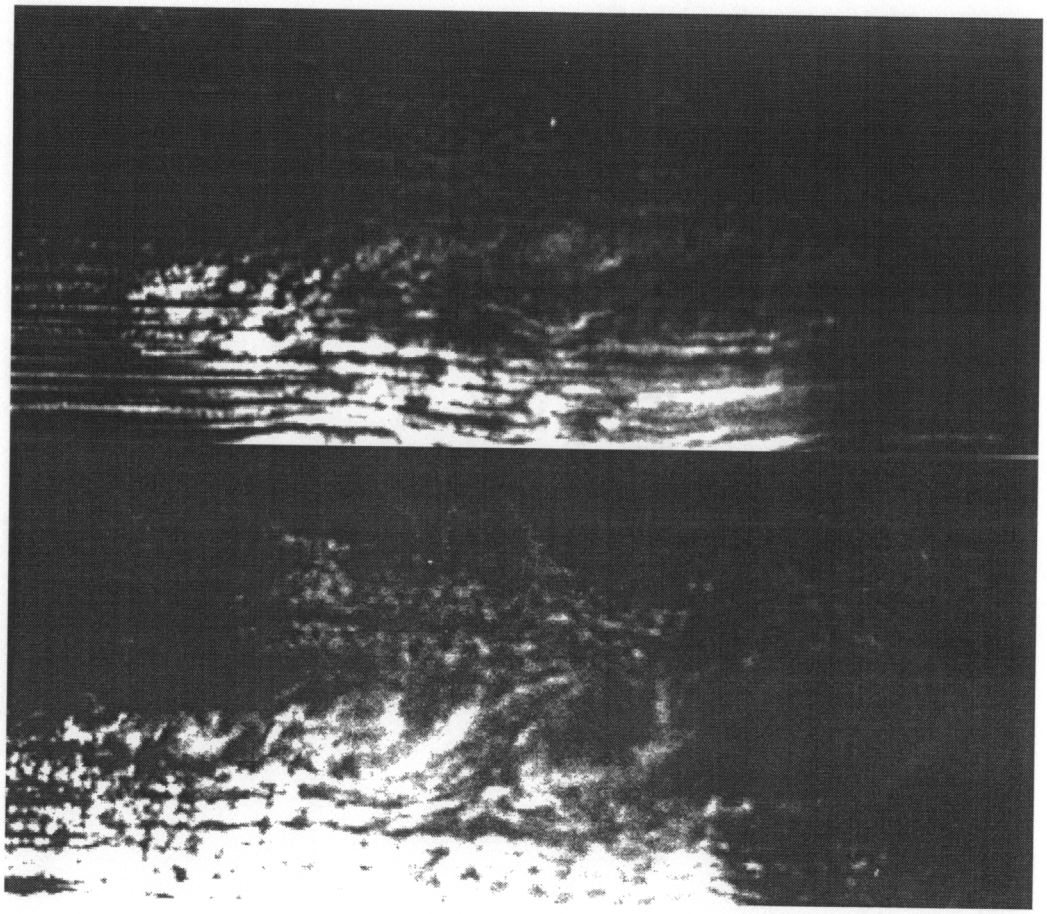

Figure A.15 Smoke wire visualization: (a). unexcited; (b) excited at 200 Hz

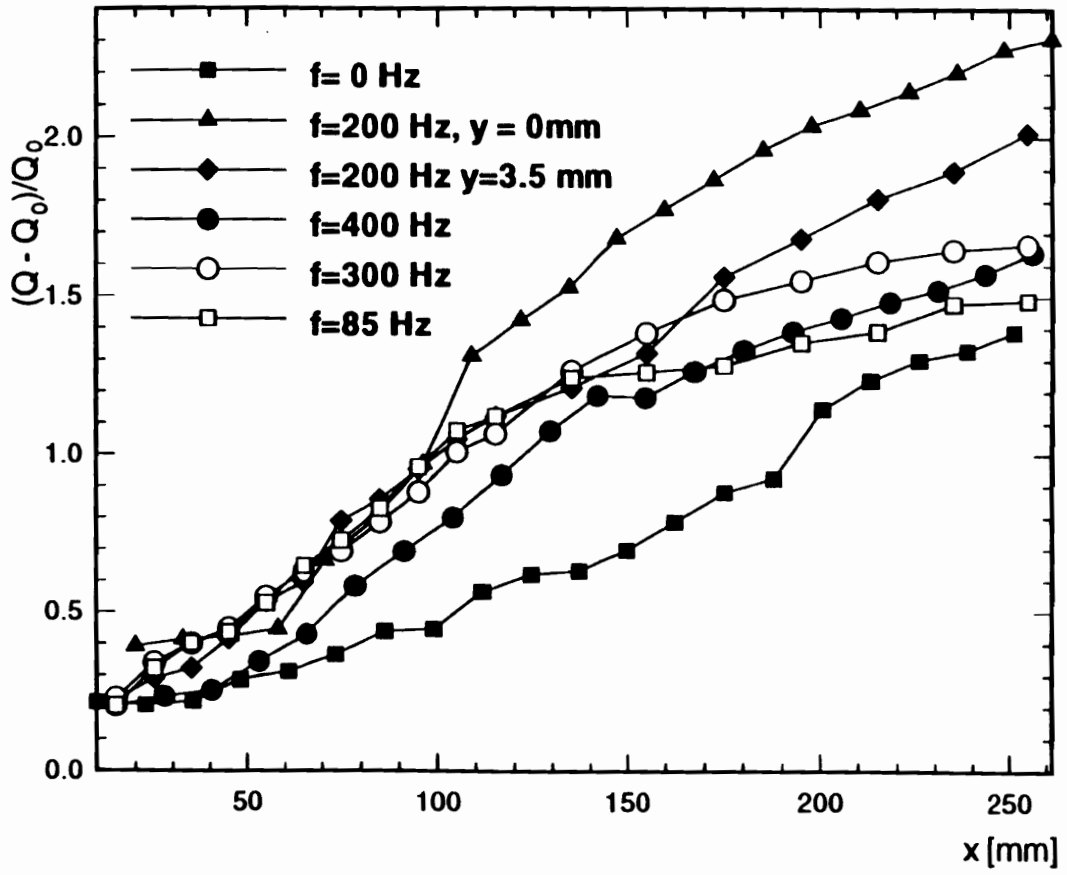

Figure A.16 Flow entrainment ratio under different excitation frequency, x=3.0 mm.

Case a: excitation position; y = 0.0 mm; case b: y= 3.0 mm

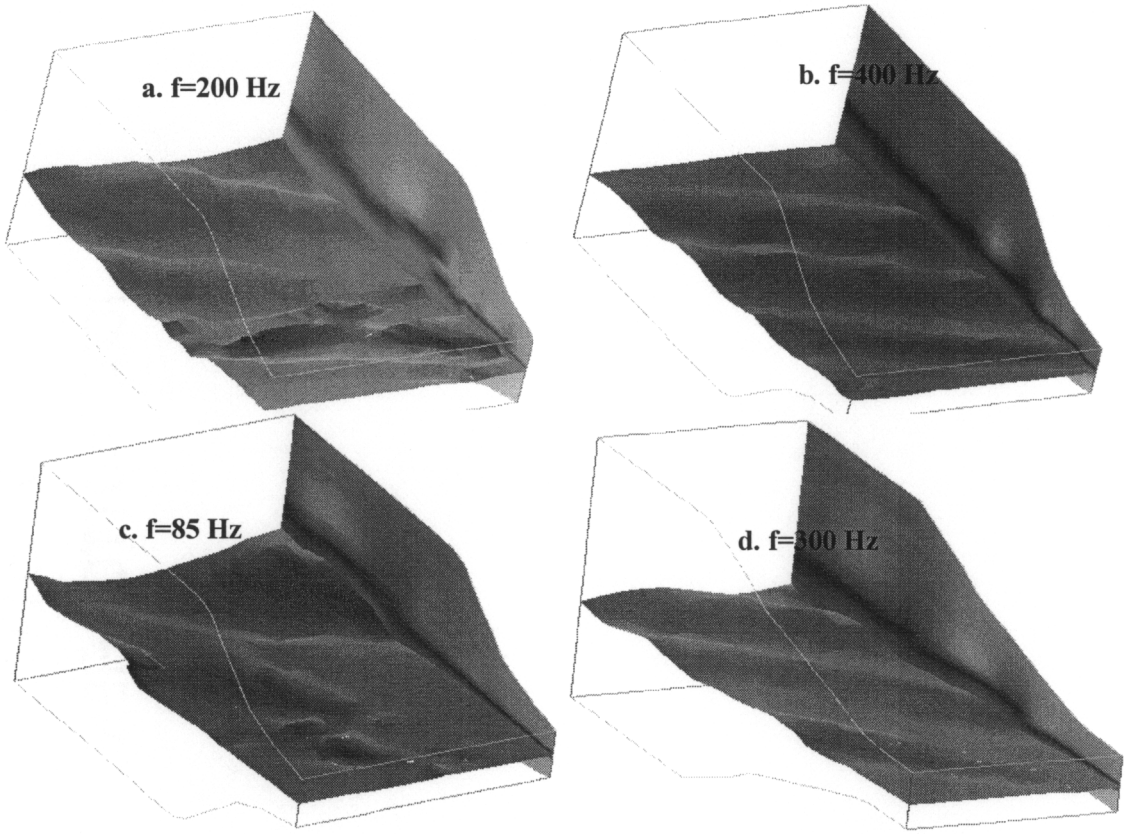

Figure A.17 Phase mean iso-velocity surface, $(U - U_L)/(U_H - U_L) = 0.5$ in the x - y - t space. a). f_e = 200 Hz, b). f_e = 400 Hz, . c). f_e = 85 Hz, d). f_e = 300 Hz

Appendix B Hardware Control, Data Acquisition and Reduction System

B.1 System Equipment

The computer facilities used in the studies contributing to this dissertation have been developed over the past few years into a small network of PC computers and signal processing instrumentation utilized in various aspects of wind tunnel control and automation, data acquisition, interactive real-time processing and computer-based-intensive data post-processing.

Three major types instrumentations, other than the computers, have been employed in the studies:

1) Data Translation DT-2801 series A/D boards which have been mainly used for data acquisition and for automation process control. The board has 8 differential A/D channels, two D/A channels and two 8 bit I/O ports, with on board clock up to 37kHz and accept external clock. It also has DMA (direct memory access) capabilities which is essential for real time data acquisitions. The board have many accompanying software's packages ranging from the high level window software to low level function calls. Only the low level function calls, which constituted PC LAB Library, were employed in this study because of their flexibility and easy adaptation to this studies' special requirements.
2) An AT-AO-10 D/A board which was designed for applications such as automation and process control. It has 10 D/A channels double-buffered, multiplying, 12-bit DACs, unipolar and bipolar voltage output, 4 to 20 mA current output, with sample and hold capabilities, internal and external signal update capability for waveform generation, an on board 1k-word FIFO buffer,

transfer rates up to 200 K samples/sec per channel, onboard analog output auto calibration circuitry, eight digital I/O lines able to sink up to 24 mA of current; timer-generated and externally generated interrupts, a high-performance RTSI bus interface, analog output auto-initialization at startup, and full PC I/O channel DMA capability with analog output.

3) A Tectronics 2600 FFT analyzer. This frequency analyzer has a frequency response up to 100 KHz deemed adequate for the present study. The Instrument Program runs on the host computer and handles the displays, menus, and data storage. The analyzer does all of the time critical and computation-intensive work. It can either run manually using window menus or automatically by direct function calls. Unfortunately the library was written in Borland turbo Pascal which is not compatible to Microsoft C or Fortran which was used software written. The present experiments to solve this problem is to generate the executable file that satisfies the post-data reduction requirement and then call those .exe files using program written in Microsoft C or Fortran.

The current research effort has mostly used a two PC computer systems in the following manner. The hard ware is shown in figure A.1. The D/A AO-AT-10 board, attached to Compute I, has 10 channels, out of which 8 channels were used to generate the simultaneous signal outputs. These output signals amplified by the amplifier were used to control the actuators. The remaining 2 channel were used to trigger Computer II (one channel used for triggering the other for the external clock). In this way both computers could be synchronized for data sampling and control. Computer II was used to control the automated multi-dimensional stages through I/O port and sample the data by hot wire through the A/D board and the FFT analyzer. The reason for using the hard wire FFT analyzer was to relieve the burden from the computer and increase the pre-processing data speed.

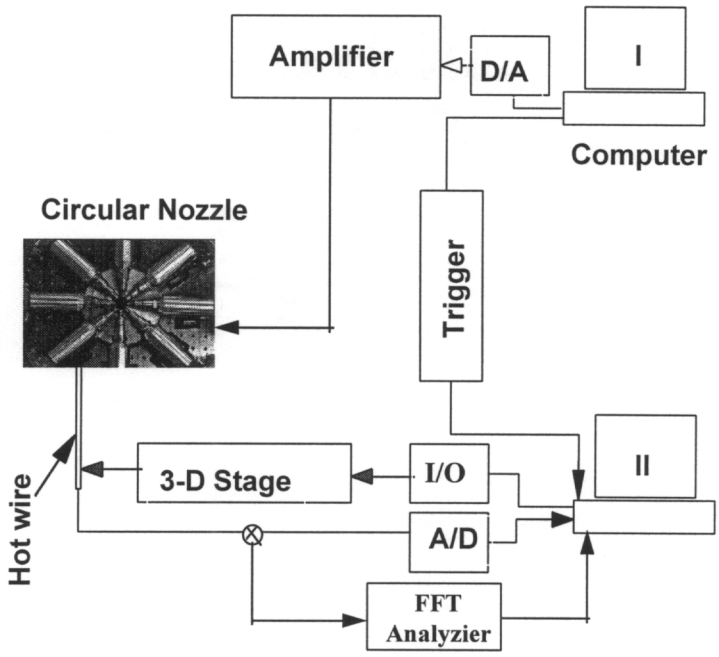

Figure B.1 Schematic view of the control and data acquisition systems

The automated data acquisition software were divided into two separate programs. These two programs were designed to execute simultaneously because of the multitasking nature of the conditional data sampling technique. There are two levels of programming available to handle computer interfacing. The high level one uses the function calls which are usually provided by the vendors in C, Pascal, Fortran or Basic languages. The better the product the more powerful and easier to use those function calls are. The lower level programming talks directly to the address of the interfaces. This method can increase the data handling speed. However, unless the user is very familiar with the hard ware of the interfacing board, it is not the recommended method.

B.2 Data Sampling and Control Program

The program was designed to control the stages and data sampling. The flow of data sampling is like this: The 3-D translation stage moves the sensor to the desired spatial station and pauses for the A/D board to sample the data, it then moves again to another location and so on.

a) Translation stage control

The stages was driven by stepper-motors. Stepper-motor requires 24 volts inputs to actuate. However, the I/O output voltage from the computer is only 5 volts. A special designed amplifier, powered by a DC power supply was placed between the computer and the stage and provided the specified power required for the stepper-motor. The stepper-motor also requires four logical signal inputs to implement the stage motion control:

1. A pulsed signal that varies between logical zero to one. For each pulse, the step motor rotates 7.5^0.
2. A directional signal that commands the step motor to rotate either clockwise (logical zero) or counter clockwise (logical 1).
3. A signal to power (logical one) or disable (logical zero) the amplifier.
4. A signal for ground reference.

These signals can be provided by the I/O port of the computer, usually either D/A or A/D boards carrying I/O ports. If those ports were unavailable, the parallel board for printers could be used instead. The parallel board is comprised of three I/O ports: one for control, one for output, and the third for input. The address of these ports can be found from the manual or in the computer system boot up menu. In the current study two I/O port on the DT2801-A board were employed. Each port had 8 bits output. Therefore the DT2801-A board could control a total number of four stepper motors. Function calls in either C or Fortran were provided by the associated PC-LAB software. The stepper motor used had a current requirement of 4.7 A, while the power supply could only supply

5 A at its maximum. Therefore, only one motor could be driven at a time and the motors had to be turned off alternatively.

To implement the stepper motor control, two consecutive commands are required to move the stepper motor one step. The command the computer sends to the first byte of the I/O port that controls two stepper motors is shown in the following table:

i) First motor actuated and rotates in clockwise direction

Commands to the I/O Port I

1	0	0	0	0	0	0	0
1	0	0	0	0	0	1	0

The two rows shown above represent the two consecutive command sends to the port. In this command, the first four bits (counted from right to left) controls the first stepper motor and the second four bits controls the second stepper motor. In each of the four bits, bit 0 is used for direction, bit 1 for pulse, bit 2 for ground and bit 3 for power control. Seen in this example, the power for the first motor is on while the second motor is off. The pulse bit changes from 1 to zero thus completes one pulse.

ii) Similarly, second motor actuated and rotates in clockwise direction:

Commands to the I/O Port II

0	0	0	0	1	0	0	0
0	0	1	0	1	0	0	0

An example program written in Fortran is given below using PC-LAB function calls. In this program, the binary representation of logical number was translated into decimal. For example, the binary 10000000 = decimal 128 and binary 10000010 = decimal 130, etc. The virtual argument STEP represents the number of pulses required to move the translation stage to the desired position. For example, 200 pulses is required for the current employed stepper motor to rotate one complete circle, for each circle the stage

moves 1/16". The argument NB represents the moving direction of the stage, NC, the translation stage used (total of four) and FN power enabling or disabling.

```
SUBROUTINE SM(STEP,NB,NC,FN)
      INTEGER*2 STATUS,STARTC,ENDCHA,GAIN,TIMING,SAMPLE,COUNT
      INTEGER*2 XEFO,XODV
      INTEGER*4 ISTEP
      EXTERNAL XEFO,XODV
       DIMENSION N(2,4)
C      NOTE: EACH TURN REQUIRES 200 PULSES
      ISTEP=INT(STEP)/10
C     Port acutated -1 = non
      STATUS=XEFO(-1)
C      Now using port 0
      IO=0
C      If NC equals 2 using Port 1
      IF (NC.EQ.2) IO=1
C      Actuating the port
      STATUS=XEFO(IO)
C      The assignment of the command
C      First or third (depending on IO chosed ) motor, clock wise direction
      N(1,1)=128
      N(1,2)=130
C      Second or fouth motor, clockwise direction
      N(1,3)=132
      N(1,4)=134
C      First or third (depending on IO chosed ) motor, counter clock wise direction
      N(2,1)=8
      N(2,2)=40
C      Second or fouth motor, counter clockwise direction
      N(2,3)=72
      N(2,4)=104
      I1=ISTEP
      IF(NC.EQ.0) GOTO 1
      IF(NC.EQ.2) GOTO 1
      I1=ISTEP
1      CONTINUE
      IC=1
      II=2
      IF (NC.NE.1) goto 111
      IC=2
      II=4
111     J1=N(IC,1)
      J2=N(IC,2)
      J3=N(IC,3)
      J4=N(IC,4)
      IF(NB.NE.0) GOTO 120
C      CW DIRECTION
      DO 30 J=1,I1
      DO 10 I=1,II
```

```
10    STATUS=XODV(IO,255,J2)
      DO 20 I=1,II
20    STATUS=XODV(IO,255,J1)
30    CONTINUE
      goto 140
120   CONTINUE
C
C     CCW DIRECTION
C
      DO 60 J=1,I1
      DO 40 I=1,II
40    STATUS=XODV(IO,255,J4)
      DO 50 I=1,II
50    STATUS=XODV(IO,255,J3)
60    CONTINUE
140   CONTINUE
      DO 11 JJJ=1,10000
      DO 11 JJ1=1,10
11    CONTINUE
      IF(IO.EQ.0) STATUS=XODV(1,255,136)
      IF(IO.EQ.1) STATUS=XODV(0,255,136)
      IF (FN.NE.0.0) GOTO 150
      STATUS=XODV(IO,255,136)
150   CONTINUE
      RETURN
      END
```

b) Data Sampling Control

The data sampling program used in this experiment was capable of direct memory accessing, accepting external as well as internal triggers. It is, therefore, suitable for phase locked data sampling. The program's functionality is represented in the following subroutine.

In this subroutine, the first argument NCK represents the time interval required for data sampling. The on board clock has a pulse interval of 1.25 msec, however, the minimum time interval that can be used is 30×1.25 msec. The argument NN represents the number of points sampled. The data sampling can be actuated with trigger or without trigger. With triggering, the data can be acquired at the desired time and time interval.

This program accepts four data sampling conditions depending on the value of the argument, TIMING:

1) TIMING=0: no trigger

2) TIMING=1: internal clock, internal trigger

3) TIMING=2: internal clock, external trigger

4) TIMING=3: external clock, external trigger

```
      SUBROUTINE ADS(NCK,NN,TIMING)
      COMMON /A2/XR(1024),XI(1024)
      INTEGER*2 STATUS,STARTC,ENDCHA,GAIN,TIMING,SAMPLE,COUNT
      INTEGER*2 XINIT,XTERM,XSB,XST,XSCD,DATPTS,ANALOG(1024)
      INTEGER*2 XDLY,XSTB,XWD,XSC,XGC,XCEV,XREV,XGF,CHANLS
      INTEGER*2 XAV,XAOT,XSA,XAS,XBAD,XCAD,XTAD,XWAD,XSAD
      INTEGER*2 XDV,XDOT,XSD,XDS,XBDD,XCDD,XTDD,XWDD,XSDD
      INTEGER*2 XEFO,XEFI,XODV,XODOT,XIDV,XIDOT,XIXR,XIXW
      INTEGER*2 XSECW,XGDE,XRD,XFDL,XESC,XDSC,PLOTS,PLTPNT
      INTEGER*4 CLOCKD
      EXTERNAL XINIT,XTERM,XSAD,XSDD,XWD,XSC,XCEV,XESC,XDSC
C
C  end of PCLAB subroutines definition
C
      STATUS=0
      DATPTS=NN
      CLOCKD=NCK
C      DEFINITION OF 'TIMING' SEE PAGE 6-8
C      EACH CLOCK TICK = .00000125 SEC., MINIMUM CLOCK TICKS = 30
C
      STARTC=0
      ENDCHA=0
C     Gain = 4 means the range is 0-2.5 volts for unipolar
C     The polarity can be set by changing the jumper on the board, please refer to the mannual for detail
      GAIN=4
      CHANLS=(ENDCHA+1)-STARTC
      SAMPLE=CHANLS*DATPTS
      ANALOG(1)=SAMPLE
      STATUS=XDSC
      STATUS=XRD
      STATUS=XINIT
      STATUS=XSCD(CLOCKD)
      STATUS=XSA(TIMING, STARTC, ENDCHA, GAIN)
      STATUS=XDSC
      STATUS=XBAD(SAMPLE, ANALOG(1))
      STATUS=XTAD(COUNT)
      STATUS=XWAD(ANALOG(NN))
C     The resolution of the board is 12 bit.  Henceforth, the gain range can be divided into
```

```
C     2^12 = 4096.  For 2.5 volts range the value in volts in shown below represented by XR(I)
      DO 10 I=1,NN
10    XR(I)=(FLOAT(ANALOG(I))*2.5/4096.0)
      RETURN
      END
```

B.3 Control Program with GUI Interfacing under Windows 3.X Environment

The hardware used to generate the control signal for actuator control was AT-AO-10 described in section B.1. The platform used to develop the relevant software was Microsoft Windows 3.1 SDK (Software Development Kit).

There are many advantages the Windows has over the MS-DOS environment:

- A graphical user interface featuring windows, menus, dialog boxes, and controls for applications
- Queued input
- Device-independent graphics
- Multitasking capabilities
- Data interchange between applications

In a Windows application, all inputs from the keyboard, mouse, and timer are intercepted by Windows, which places the input in the appropriate application's message queue. When the application is ready to retrieve the input, it simply reads the next input message from its message queue. Unlike the standard C program the application itself (in this case, the signal control program) does not have a main() routine. A Windows application, must share the resources with all other applications that are running at the same time. For this reason, Windows controls the resources and requires Windows applications to use a program interface that guarantees that Windows maintains control of those resources.

Every Windows application comprises a WinMain function, a Message loop and Windows procedures (in which the control code can be embedded). In the Windows SDK environment a Windows application can be constructed by implementing the following steps.

1. Create a C-language source file that contains the WinMain function, Message loop, and the application code (Window procedure).
2. Use the resource editors (Image Editor and Font Editor) to create any cursor, icon, bitmap, and font resources the application will require.
3. Create a resource-definition (.RC) file that defines the application's resources. The file lists and names the resources you created in the preceding step. It also defines menus, dialog boxes, and other resources.
4. Create the module-definition (.DEF) file, which defines the attributes of the application modules, such as segment attributes, stack size, and heap size.
5. Compile and link all C-language source files
6. Use RC to compile the resource-definition file and add it to the executable file.

The application code or Windows procedure in this study is the control program that controls the ten channel signal output in which eight channels were used to control the actuators, one channel for external clock and one channel for triggering. The requirement of this are as follows:

1) The waveform output of the ten channels should independent of one another and, at the same time, can be synchronized.
2) The program can be interrupted at any time.
3) The program must have the real multitasking capabilities. This requirement requires that this program must guarantee the seamless signal output at 1 Mhz speed while other applications are running at the same time.

The relevant control flow Chart is shown in figure B.2. The function calls defined in the rectangular frame are the accompanied NI_DAQ Software that comes with the AT-AO-10 board.

The generated Window for spatial mode control is shown in figure B.3. As shown, this software can be used to control either single or standing-wave modes. It can also be used to control any number of channels less than eight (the remaining two channels are used for triggering and external clocking for synchronization purposes).

Each channel can be adjusted individually in phase shifting, output amplitude and phase offset.

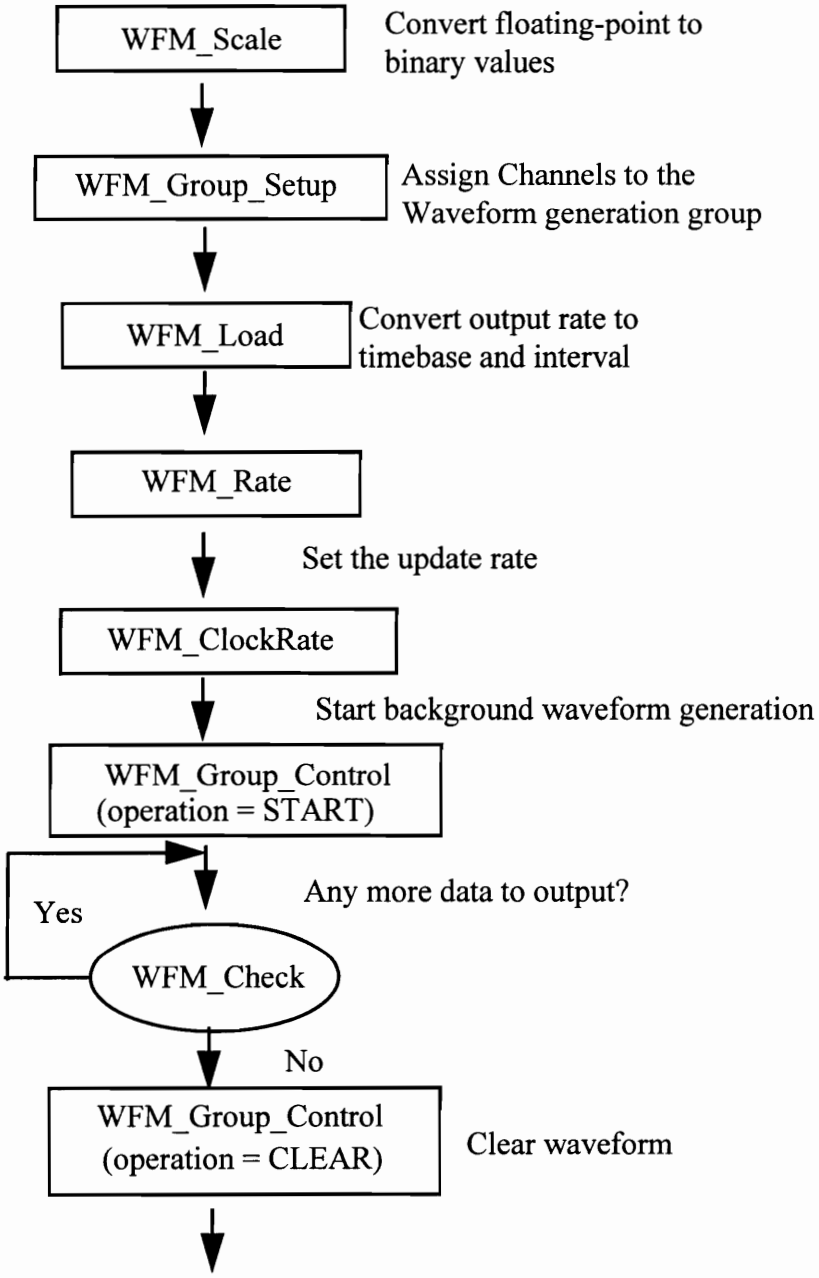

Figure B.2 Flow Chart of the signal control subroutine

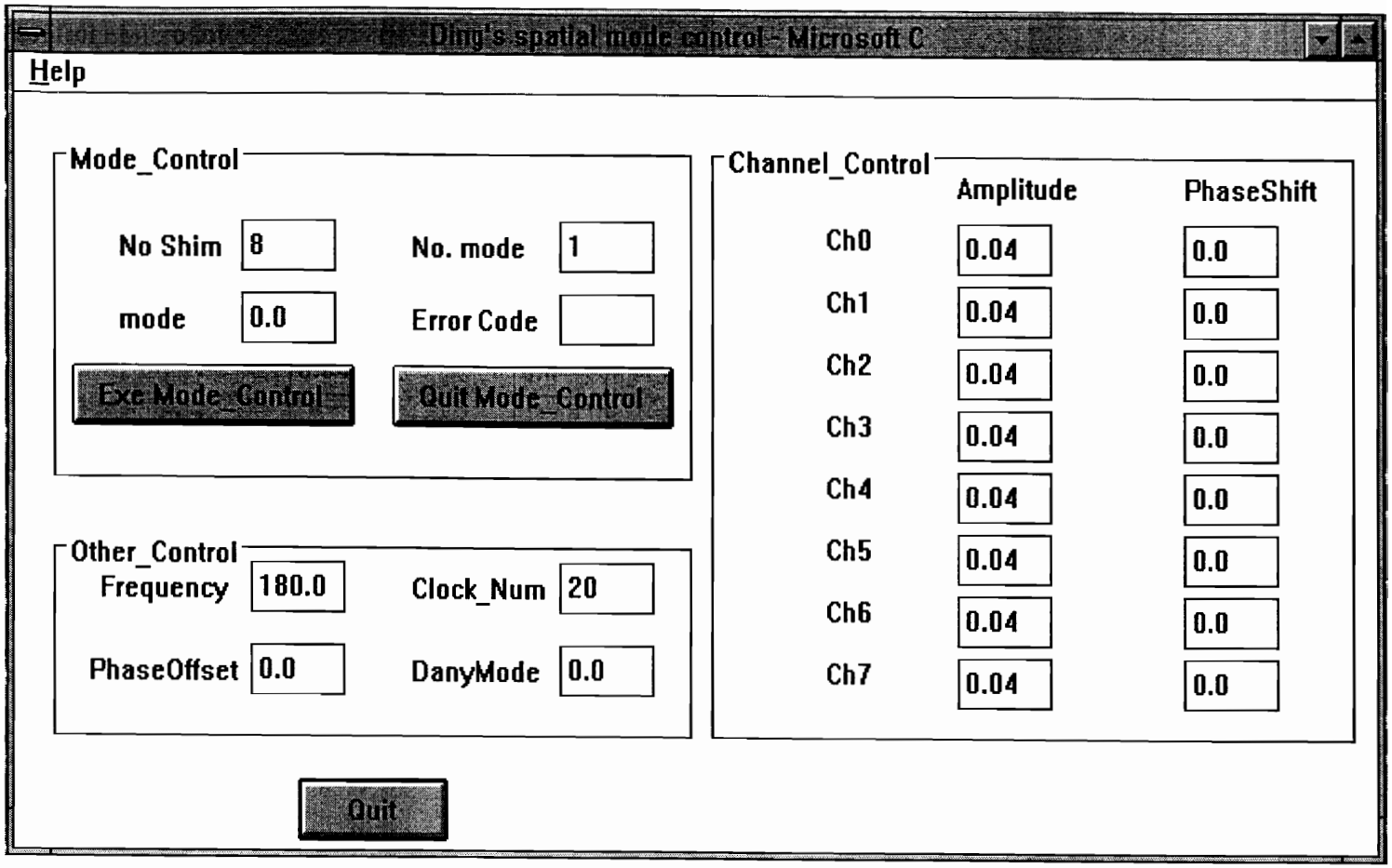

Figure B.3 Control program for Window application

The C-language source (.C)file, the header (.H)file, the resource-definition (.DEF) file and the Makefile for the control software are listed below.

1. C source file

```
/************************************************************************
 *    Program designed by Chen Ding of the VT ME Dept. used for Windows *
 *    Dynamic-Link Library (DLL) with Microsoft C and the Windows SDK  *
 *                                                                      *
 *  -- This program allows the user interactively using windows    *
 *    to control 10 channel D/A board to produce different wave forms  *
 ************************************************************************/

/************************************************************************
  INCLUDE FILES
 ************************************************************************/

#include <windows.h>
#include <math.h>
#include "wdaq_c.h"
#include "ding_c.h"

/************************************************************************
  GLOBAL VARIABLES
 ************************************************************************/

HANDLE hInst;          /* current instance */
HWND   hEbShim,        /* Shim number edit box */
     hEbNo_Mode,      /* Single mode (= 1) or counter rotating mode
                          (= 2)*/
     hEbFreq;        /* sin wave frequency */
     hEbAmp;         /* sin wave amplitude */
     hEbMode ,       /* such as mode = 1, 0.75, 0.5 etc */
     hEbErrCode1,    /* error code output box */
     hQuitButton;    /* quit application button */

/************************************************************************
   WinMain(HANDLE, HANDLE, LPSTR, int)
   -- calls initialization function, processes message loop
************************************************************************/

int PASCAL WinMain(hInstance, hPrevInstance, lpCmdLine, nCmdShow)
  HANDLE hInstance;          /* current instance  */
  HANDLE hPrevInstance;      /* previous instance */
  LPSTR lpCmdLine;           /* command line      */
  int nCmdShow;              /* show-window type (open/icon) */
{
```

```
  MSG msg;                /* message */

  /* if other instances running, initialize shared things */
  if (!hPrevInstance)
    if (!InitApplication(hInstance))
          return (FALSE);

  /* Perform initializations that apply to a specific instance */
  if (!InitInstance(hInstance, nCmdShow))
    return (FALSE);

  /* Acquire and dispatch messages until a WM_QUIT message is received. */
  while (GetMessage(&msg,NULL,NULL,NULL))
    {
    TranslateMessage(&msg);    /* Translates virtual key codes */
    DispatchMessage(&msg);     /* Dispatches message to window */
    }
  return (msg.wParam);     /* Returns the value from PostQuitMessage */
}

/*************************************************************************
   InitApplication(HANDLE)
   -- Initializes window data and registers window class
*************************************************************************/

BOOL InitApplication(hInstance)
  HANDLE hInstance;            /* current instance */
{
  WNDCLASS  wc;

  /* fill in window class structure */
  wc.style = NULL;               /* Class style(s).              */
  wc.lpfnWndProc = MainWndProc;      /* Function to retrieve messages for */
                                     /* windows of this class.         */
  wc.cbClsExtra = 0;             /* No per-class extra data.        */
  wc.cbWndExtra = 0;               /* No per-window extra data.       */
  wc.hInstance = hInstance;          /* Application that owns the class.  */
  wc.hIcon = LoadIcon(hInstance, "ding");
  wc.hCursor = LoadCursor(NULL, IDC_ARROW);
  wc.hbrBackground = GetStockObject(WHITE_BRUSH);
  wc.lpszMenuName =  "Ding'sModeControlMenu";
  wc.lpszClassName = "MainWndClass";  /* Name used in call to CreateWindow */
 /* Register the window class and return success/failure code. */
  return (RegisterClass(&wc));
}
/*************************************************************************
   InitInstance(HANDLE, int)
   -- Saves instance handle and creates main window
*************************************************************************/

BOOL InitInstance(hInstance, nCmdShow)
```

```
  HANDLE        hInstance;        /* Current instance identifier.      */
  int           nCmdShow;         /* Param for first ShowWindow() call. */
{
  HWND hWnd,              /* Main window handle.               */
       hTemp;

  /* Save the instance handle in static variable, which will be used in  */
  /* many subsequence calls from this application to Windows.          */
  hInst = hInstance;

  /* Create a main window for this application instance.  */
  if (!(hWnd = CreateWindow("MainWndClass",
         "Ding's spatial mode control - Microsoft C",
         WS_OVERLAPPEDWINDOW,CW_USEDEFAULT,CW_USEDEFAULT,420,410,
         NULL,NULL,hInstance,NULL)))
    return (FALSE);

  /* Draw controls for AO_VWrite group */
  if (!(hTemp = CreateWindow("Button","Mode_Control",BS_GROUPBOX | WS_CHILD |
         WS_VISIBLE,20,20,340,165,hWnd,-1,hInstance,NULL)))
    return(FALSE);
    if (!(hTemp = CreateWindow("Button","Other_Control",BS_GROUPBOX | WS_CHILD |
         WS_VISIBLE,20,210,340,100,hWnd,-1,hInstance,NULL)))
    return(FALSE);

   if (!(hEbShim = CreateWindow("Edit","8",ES_LEFT | WS_CHILD | WS_VISIBLE |
         WS_BORDER,120,60,50,25,hWnd,-1,hInstance,NULL)))
    return(FALSE);
  if (!(hEbNo_Mode = CreateWindow("Edit","1",ES_LEFT | WS_CHILD | WS_VISIBLE |
         WS_BORDER,290,60,50,25,hWnd,-1,hInstance,NULL)))
    return(FALSE);
  if (!(hEbMode = CreateWindow("Edit","0.0",ES_LEFT | WS_CHILD | WS_VISIBLE |
         WS_BORDER,120,95,50,25,hWnd,-1,hInstance,NULL)))
    return(FALSE);
   if (!(hEbFreq = CreateWindow("Edit","80.0",ES_LEFT | WS_CHILD | WS_VISIBLE |
         WS_BORDER,120,250,50,25,hWnd,-1,hInstance,NULL)))
    return(FALSE);
   if (!(hEbAmp = CreateWindow("Edit","0.5",ES_LEFT | WS_CHILD | WS_VISIBLE |
         WS_BORDER,290,250,50,25,hWnd,-1,hInstance,NULL)))
    return(FALSE);
   if (!(hEbErrCode1 = CreateWindow("Static","",ES_LEFT | WS_CHILD | WS_VISIBLE |
         WS_BORDER,290,95,50,25,hWnd,-1,hInstance,NULL)))
    return(FALSE);
  if (!(hTemp = CreateWindow("Button","Exe Mode_Control",BS_PUSHBUTTON |
         WS_CHILD | WS_VISIBLE,30,130,150,30,hWnd,PB_WRITE,hInstance,NULL)))
    return(FALSE);

   if (!(hTemp = CreateWindow("Button","Quit Mode_Control",BS_PUSHBUTTON |
         WS_CHILD | WS_VISIBLE,200,130,150,30,hWnd,PB_END,hInstance,NULL)))
    return(FALSE);
```

```
  /* Draw quit application button */
  if (!(hQuitButton = CreateWindow("Button","Quit",BS_DEFPUSHBUTTON |
          WS_CHILD | WS_VISIBLE,150,330,80,30,hWnd,PB_QUIT,hInstance,NULL)))
    return(FALSE);

  /* Make the window visible; update its client area; and return "success" */
  ShowWindow(hWnd, nCmdShow);  /* Show the window                    */
  UpdateWindow(hWnd);          /* Sends WM_PAINT message             */
  return (TRUE);               /* Returns the value from PostQuitMessage */
}

/*************************************************************************
  DrawScreen(HWND)
  -- writes textual labels for each group
 *************************************************************************/

void DrawScreen(hWnd)
  HWND hWnd;
{
  HDC  hDC;          /* display context for main window */
  PAINTSTRUCT ps;

  hDC = BeginPaint(hWnd,&ps);
  TextOut(hDC,55,65,"No Shim",7);      /* label AO_VWrite group */
  TextOut(hDC,210,65,"No. mode",8);
  TextOut(hDC,55,100,"mode",4);
  TextOut(hDC,210,100,"Error Code",10);
  TextOut(hDC,45,255,"Frequency",9);
  TextOut(hDC,210,255,"Amplitude",9);

  EndPaint(hWnd,&ps);

  return;
}

/*************************************************************************
  Execute_AO_VWrite(HWND)
  -- This function calls the NI-DAQ function call AO_VWrite, which
    writess a voltage to a board as given by the input parameters
 *************************************************************************/

void Execute_AO_VWrite(hWnd)
  HWND hWnd;    /* window handle */
{
  HCURSOR hNewCur,           /* new (hourglass) cursor */
          hOldCur;           /* old (arrow) cursor */
  int    No_Shim,            /* board number */
         No_Mode,            /* channel number */
         err;          /* return error code */
  double  volt;              /* voltage */
```

```
char   sz[MAXSTRINGLENGTH];  /* temporary string variable */
HANDLE  hMem;

int  WF_Buffer[1024];          /* very large waveform buffer that will */
                              /* probably have a page boundary in it  */
int  WF_Buffer_1[10][102];

int  huge  *lpMem=WF_Buffer;

int board,  chanVect[10], WF_timebase;
int numChans,chan, cyclepoints, halfReady, wfmStopped;
int dbMode, oldDataStop, partialTransferStop;
unsigned numPts, i, j, k, l, alignIndex, iterations, WF_interval, numPts_half;
unsigned long bufferSize, pointsDone, itersDone, count;
double pi, step_size, phase,Freq,Amp, Mode, phase7;
char cr;

BOOL    bSuccessful;

/* change the cursor to the hourglass */
hNewCur = LoadCursor(NULL,IDC_WAIT);
hOldCur = SetCursor(hNewCur);

/* read input parameters from edit boxes */
GetWindowText(hEbShim,sz,MAXSTRINGLENGTH);
No_Shim = atoi(sz);
GetWindowText(hEbNo_Mode,sz,MAXSTRINGLENGTH);
No_Mode = atoi(sz);
GetWindowText(hEbMode,sz,MAXSTRINGLENGTH);
Mode = atof(sz);
GetWindowText(hEbFreq,sz,MAXSTRINGLENGTH);
Freq = atof(sz);
GetWindowText(hEbAmp,sz,MAXSTRINGLENGTH);
Amp = atof(sz);
/* call DLL function */

numChans = 10;
numPts =1000;
cyclepoints =100;
bufferSize = 2000;
pi = 3.141592654 ;
step_size =2.0*pi / (double) cyclepoints ;
phase = Mode*2.0*pi / (double)No_Shim;
phase7 = Amp*2*pi/360.0;
Amp=0.5;

        for (i=0; i<numChans; i++)
                {
           chanVect[i]=i;
                }
```

```
  iterations = 0 ;
/*-------------------------------------------------------------------------*/
/* A 1MHz timebase with an interval of 10 (10 microsecs) is selected*/
/*-------------------------------------------------------------------------*/
  WF_timebase = 1  ;
  WF_interval = (double)1000000/(double)100/Freq;
  board = 1;
  chan = 1;

          switch (No_Mode)
          {
             case 1:
          for (i=0; i<numChans; i++)
          {
           for (j=0; j<=cyclepoints; j++)
 {

   WF_Buffer_1[i][j] = (int)(Amp*sin( step_size * (double)j+(double)i*phase) * (double)2047 ) ;
 }
          }
           for (j=0; j<=cyclepoints; j++)
 {

   WF_Buffer_1[7][j] = (int)(Amp*sin( step_size * (double)j+(double)i*phase7) * (double)2047 ) ;
 }

          break;
           case 2:   /* this is for the counter rotating mode */

                     l = 0;
                     for (i=0; i<numChans; i=i+2)
          {
           for (j=0; j<=cyclepoints; j++)
 {

   WF_Buffer_1[i][j] = (int)(Amp*sin( step_size * (double)j+phase*(double)l) * (double)2047 ) ;

   WF_Buffer_1[i+1][j] = (int)(Amp*sin( step_size * (double)j-phase*(double)l) * (double)2047 ) ;
 }
          l = l+1;
          }
    }

          for (i=8; i<=9; i++)
          {
           for (j=0; j<=cyclepoints; j++)
 {
   WF_Buffer_1[i][j] = 0;
 }
          }
           WF_Buffer_1[9][cyclepoints-4]=Amp*(double)2047;
```

```
            WF_Buffer_1[8][cyclepoints-2]=Amp*(double)2047;

                        for (j=0; j<=cyclepoints; j=j+5)
  {
    WF_Buffer_1[8][j] = Amp*(double)2047;
  }

          k=0;
            for (j=0; j <= cyclepoints; j++)
          {
            for (i=0; i<numChans; i++)
                  {
            WF_Buffer[k+i] = WF_Buffer_1[i][j];
                  }
            k=k+10;

           }

          err = WFM_Group_Setup (board, numChans, chanVect, 1);

 /* display output variables to edit boxes */
  sprintf(sz,"%d",err);
  SetWindowText(hEbErrCode1,sz);

  /* change the cursor back to the previous value */
  SetCursor(hOldCur);


  if((hMem=(HANDLE)GlobalAlloc(GMEM_FIXED,20480)) !=NULL)
  {
  if(*lpMem = (int huge *)GlobalLock(hMem) != 0)
              {

          err = WFM_Load (board, numChans, chanVect, WF_Buffer, (unsigned long) numPts, (unsigned
long) iterations,1);

 /* display output variables to edit boxes */
  sprintf(sz,"%d",err);
  SetWindowText(hEbErrCode1,sz);

  /* change the cursor back to the previous value */
  SetCursor(hOldCur);


          err = WFM_ClockRate(board, 1, 0, WF_timebase, (unsigned long) WF_interval, 0);


  /* display output variables to edit boxes */
  sprintf(sz,"%d",err);
  SetWindowText(hEbErrCode1,sz);
```

```
   /* change the cursor back to the previous value */
   SetCursor(hOldCur);

            err = WFM_Group_Control (board, 1, 1);

   /* display output variables to edit boxes */
   sprintf(sz,"%d",err);
   SetWindowText(hEbErrCode1,sz);

   /* change the cursor back to the previous value */
   SetCursor(hOldCur);


            GlobalUnlock(hMem);
               }
               }
            GlobalFree(hMem);
            hMem=0;
}

 /************************************************************************
   Stop_mode_control(HWND)
   -- This function calls the NI-DAQ function call AO_VWrite, which
     writess a voltage to a board as given by the input parameters
 ************************************************************************/

void Execute_AO_End(hWnd)
   HWND hWnd;    /* window handle */
{
   HCURSOR hNewCur,            /* new (hourglass) cursor */
            hOldCur;           /* old (arrow) cursor */
   int    err, brd;
   HANDLE  hMem;



   /* call DLL function */

            brd = 1;

            err = WFM_Group_Control(brd, 1, 0);

}
/************************************************************************
   MainWndProc(HWND, unsigned, WORD, LONG)
   -- Processes messages
************************************************************************/

long FAR PASCAL MainWndProc(hWnd, message, wParam, lParam)
   HWND hWnd;           /* window handle */
   unsigned message;    /* type of message */
```

```
  WORD wParam;          /* additional information */
  LONG lParam;          /* additional information */
{
  FARPROC lpProcAbout;          /* pointer to the "About" function */

  switch (message)
    {
    case WM_COMMAND:
          switch (wParam)
            {
             case IDM_ABOUT:
                   lpProcAbout = MakeProcInstance(About, hInst);

                   DialogBox(hInst,              /* current instance        */
                     "AboutBox",                 /* resource to use         */
                     hWnd,                  /* parent handle          */
                     lpProcAbout);               /* About() instance address */

                   FreeProcInstance(lpProcAbout);
                   break;


            case PB_QUIT:          /* quit the application */
              PostQuitMessage(0);
              break;

              case PB_END:      /* execute the AO_VWrite function */
              Execute_AO_End(hWnd);
              break;

          case PB_WRITE:    /* execute the AO_VWrite function */
              Execute_AO_VWrite(hWnd);
              break;
            default:
              return(DefWindowProc(hWnd,message,wParam,lParam));
            }
          break;
    case WM_DESTROY:       /* destroy window */
          PostQuitMessage(0);
          break;
    case WM_PAINT:         /* draw labels */
          DrawScreen(hWnd);
          break;
    default:         /* Passes it on if not processed */
          return (DefWindowProc(hWnd, message, wParam, lParam));
    }
  return (NULL);
}

/************************************************************************
```

```
   FUNCTION: About(HWND, unsigned, WORD, LONG)

   PURPOSE:  Processes messages for "About" dialog box

   MESSAGES:

        WM_INITDIALOG - initialize dialog box
        WM_COMMAND    - Input received

   COMMENTS:

        No initialization is needed for this particular dialog box, but TRUE
        must be returned to Windows.

        Wait for user to click on "Ok" button, then close the dialog box.

*************************************************************************/

BOOL FAR PASCAL About(hDlg, message, wParam, lParam)
HWND hDlg;                      /* window handle of the dialog box */
unsigned message;               /* type of message                 */
WORD wParam;                    /* message-specific information    */
LONG lParam;
{
   switch (message) {
        case WM_INITDIALOG:             /* message: initialize dialog box */
          return (TRUE);

        case WM_COMMAND:                /* message: received a command */
          if (wParam == IDOK            /* "OK" box selected?          */
              || wParam == IDCANCEL) {  /* System menu close command? */
              EndDialog(hDlg, TRUE);    /* Exits the dialog box        */
              return (TRUE);
          }
          break;
   }
   return (FALSE);                      /* Didn't process a message    */
}
```

2. The header file

```
/*************************************************************************
  Header file for NI-DAQ for Windows AIAO example using Windows SDK
 *************************************************************************/

/*************************************************************************
  constant definitions
 *************************************************************************/

#define IDM_ABOUT   100
```

```
#define PB_QUIT             101       /* id for quit application push button */
#define PB_END    102       /* id for execute mode_VRead push button */
#define PB_WRITE   103      /* id for execute mode_VWrite push button */
#define MAXSTRINGLENGTH 80   /* maximum length of character string */

/************************************************************************
  function prototypes
 ************************************************************************/

int PASCAL WinMain(HANDLE, HANDLE, LPSTR, int);
BOOL InitApplication(HANDLE);
BOOL InitInstance(HANDLE, int);
long FAR PASCAL MainWndProc(HWND, unsigned, WORD, LONG);
BOOL FAR PASCAL About(HWND, unsigned, WORD, LONG);
```

3. The Resource-definition file

```
ding ICON "ding.ico"
```

4. The module-definition file

```
; module definition file for NI-DAQ for Windows DLL example
;   using Windows SDK

NAME       DING_C
EXETYPE    WINDOWS
STUB       'WINSTUB.EXE'
CODE  PRELOAD MOVEABLE DISCARDABLE
DATA  PRELOAD MOVEABLE MULTIPLE
HEAPSIZE    4096
STACKSIZE   20480
EXPORTS
        MainWndProc   @1   ; name of window processing function
        About         @2   ; name of "About" processing function
```

5. The makefile

```
# make file for NI-DAQ for Windows example using Windows SDK

all : ding_c.exe

ding_c.res: ding_c.h ding_c_a.res


ding_c.obj: ding_c.c ding_c.h
   cl -c -AL -Gsw -Oas -Zpe ding_c.c

ding_c.exe: ding_c.obj ding_c.def ding_c.res
   link /NOD ding_c,,, ..\lib\atwdaq libw llibcew, ding_c.def
   rc ding_c.res
```

B.4 Flow Response to Excitation Signal

The correlation between the excitation signal and the measured velocity is shown in Figure B.4. The data was acquired using hot wire located at the center of the circular jet at a distance of Z/D = 1 from the nozzle with actuators running. The setup of the actuators is shown in Figure 3.1. The velocity speed used for this testing was 20m/s which was the speed used for this study. The signal output was 80 Hz sine waves. As seen, the correlation between the signal output and the measured velocity is 0.96.

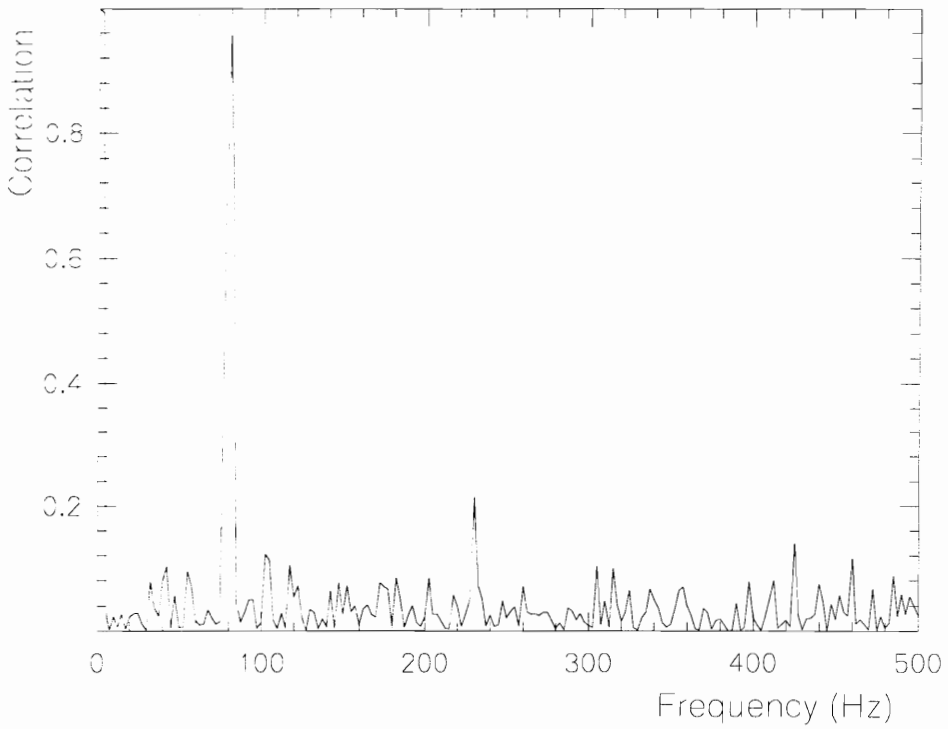

Figure B.4 Correlation between the signal output and the measured velocity

Appendix C: Excited Three Dimensional Flow Field Measurements Using A Six-Orientation Hot-Wire Probe Technique

In this appendix, a three dimensional hot wire measurements method using a single hot wire is discussed. This method was originally developed by Janjua, S. I. and Mclaughlin, D. D. (1982). However, additional improvements have been made on the following area:

1. In data sampling technique, DMA data acquisition and conditional data sampling method was used instead of the root mean square method.
2. In data preprocessing technique, the organized fluctuation component of the velocity was added so that the influence of periodical excitation of the flow could be taken into account.

Turbulence measurement in a complex flow field has always been a complicated issue encountered by engineers. In the past, turbulence phenomena have been discussed by various authors in detail, various methods of turbulence measurements have been suggested. One of the most widely used instruments to obtain turbulent quantities is the hot-wire. When used at a single orientation or in a two-dimensional flow with a predominant flow direction, a single hot-wire can measure the streamwise components of the time-mean velocity and the root-mean-square velocity fluctuation at a particular location in the flow field. A two-wire probe can be use to determine the time-mean velocities, streamwise and cross stream turbulence intensities, and the cross correlation between the two components of the velocity fluctuations.

Hot-wire measurements in complex three-dimensional flow fields are considerably more difficult than in one- or two-dimensional flow fields in which the mean flow is predominantly in one direction. To measure the three velocities and their corresponding fluctuating components in a three-dimensional flow field such as

encountered in combustor simulators, there are two methods that can be employed at a point in the flow field:

1 A three-wire probe used with a single orientation

2 A single- or double-wire probe used with multi-orientation

The three-wire probe technique permits the necessary simultaneous measurements from which three instantaneous velocity components can be determined. The appropriate signal processing can produce estimates of mean velocity components and normal and shear turbulent stresses (such as $\overline{u'^2}$ and $\overline{u'v'}$).

The three-hot-wire probe technique is significantly more complex than the single wire multi-orientation techniques. A multi-dimensional probe drive is required to orient the probe in approximately the mean flow direction. Also, sophisticated signal processing electronics is required to handle the three instantaneous hot-wire voltages. Finally, the three-wire probe typically has less spatial resolution in comparison with a single wire probe.

Multi-orientation of a single hot-wire is a novel way to measure the three components of a velocity vector and their fluctuating components. A method devised by Dvorak and Syred uses a single normal hot-wire oriented at three different positions such that the center one is separated by 45 degrees from the other two. The velocity vector at a location is related to the three orthogonal components using pitch and yaw factors in the form of mean and root-mean-square voltages. A single wire do not supple all the information needed to obtain the turbulence quantities. Therefore, in addition to a single wire, Dvorak and Syred used a cross-wire probe to obtain the covariance between the voltages obtained at adjacent hot-wire orientations.

King modified the technique developed by Dvorak and Syred. His method calls for a normal hot-wire to be oriented through six different positions, each orientation separated by 30 degrees from the adjacent one. Mean and root-mean-square voltages are measured at each orientation. The data reduction is performed using some assumptions

regarding the statistical nature of turbulence, making it possible to solve for the three time mean velocities, the three normal turbulent stresses, and the three turbulent shear stresses.

The six-orientation hot-wire technique requires a single, straight, hot-wire to be calibrated for three different flow directions in order to determine the directional sensitivity of such a probe. The calibration curves demonstrate that the hot-wire is most efficiently cooled when the flow is in the direction of the $\tilde{u}$ component, whereas, the wire is most inefficiently cooled when the flow is in the direction of the $\tilde{w}$ component. Each of the calibration curves follows a second order, least square fit of the form:

$$E_i^2 = A_i + B_i \tilde{u}^{1/2} + C_i \tilde{u}_i \qquad (i = 1, 2, 3) \qquad (c.1)$$

which is an extension of the commonly used King's Law. In this equation, Ai, Bi and Ci are calibration curves respectively.

When the wire is placed in a three dimensional flow field, the effective cooling velocity experienced by the hot-wire is:

$$Z^2 = \tilde{V}^2 + G^2 \tilde{u}^2 + K^2 \tilde{w}^2 \qquad (c.2)$$

where G and K are the pitch and yaw factors defined by Jorgensen to be:

$$G = \frac{\tilde{v}(\tilde{u}, \tilde{w} = 0)}{\tilde{u}(\tilde{v}, \tilde{w} = 0)} \quad \text{, and}$$

$$K = \frac{\tilde{v}(\tilde{u}, \tilde{w} = 0)}{\tilde{w}(\tilde{u}, \tilde{v} = 0)} \qquad (c.3)$$

which are evaluated from the three calibration curves for a constant value of E^2. Equation (c.3) shows that the pitch and yaw factors are calculated with the component i =2 in equation (c.1) of the effective cooling velocity as the reference. Therefore, the calibration constants used in equation (c.1) are the coefficients in the E vs. calibration curve, i.e., in a general flow field:

$$E^2 = A_2 + B_2 Z^{1/2} + C_2 Z$$

with Z as given in Equation (c.2) above.

Both pitch and yaw factors are function of hot-wire voltage determined from the calibration curve which shows that the yaw factor is far more sensitive. The sensitivity analysis discussed by Janjua, S. I. and Mclaughlin, D. D. (1982) demonstrates that uncertainties associated with the varying pitch and yaw factors do not seriously affect the accuracy of the estimated flow quantities.

To carry out measurements in the jet flow field, the wire is aligned in the flow in such a way that in the first orientation, the wire is normal to the flow in the axial direction and the probe coordinates coincide with the coordinates of the experimental facility. Thus, the six equations for the instantaneous cooling velocities at the six orientations, as given by King are:

$$
\begin{aligned}
Z_1^2 &= v^2 + G^2 u^2 + K^2 w^2 \, Z \\
Z_2^2 &= v^2 + G^2 \left(u\cos 30° + w \sin 30°\right)^2 + K^2 \left(w \cos 30° - u \sin 30°\right)^2 \\
Z_3^2 &= v^2 + G^2 \left(u\cos 60° + w \sin 60°\right)^2 + K^2 \left(w \cos 60° - u \sin 60°\right)^2 \\
Z_4^2 &= v^2 + G^2 w^2 + K^2 u^2 \qquad \text{(c.4)} \\
Z_5^2 &= v^2 + G^2 \left(w\sin 120° + u\cos 120°\right)^2 + K^2 \left(u\sin 120° - w\cos 120°\right)^2 \\
Z_6^2 &= v^2 + G^2 \left(w\sin 150° + u\cos 150°\right)^2 + K^2 \left(u\sin 150° - w\cos 150°\right)^2
\end{aligned}
$$

Solving simultaneously any three adjacent equations provide expressions for the instantaneous values of the three velocity components, u, w, and v in terms of the equivalent cooling velocities (Z_1, Z_2 and Z_3) for example, when the first three equations are chosen). Thus, the general form of the instantaneous velocity components is given as:

$$
U = \left[\left\{ AO + \left(AO^2 + \frac{BO^2}{3} \right)^{1/2} \right\} \frac{1}{\left(G^2 - K^2\right)} \right]^{\frac{1}{2}}
$$

$$= \left[\left\{ -AO + \left(AO^2 + \frac{BO^2}{3} \right)^{1/2} \right\} \frac{1}{\left(G^2 - K^2 \right)} \right]^{\frac{1}{2}} \qquad \text{(c.5)}$$

$$= \left[CO - \frac{\left(G^2 + K^2 \right)}{\left(G^2 - K^2 \right)} \left(AO^2 + \frac{BO^2}{3} \right)^{1/2} \right]^{\frac{1}{2}}$$

The values of AO, BO and CO depend on the set of the three equations chosen and are given in table c.1 for appropriate equation sets.

Table c.1 Values of AO, BO, and CO in Various Equation Sets

Equation Set P,Q,R Choice	AO	BO	CO
6, 1, 2	$\left(-Z_6^2 + 2Z_1^2 - Z_2^2 \right)$	$\left(-Z_6^2 + Z_2^2 \right)$	$\left(Z_6^2 - Z_1^2 + Z_2^2 \right)$

However, these equations can not be directly used since it is impossible to obtain Z_1, Z_2 *and* Z_3 at a single instant in time with a single wire probe. Therefore, Equations (c.5) must be expressed in terms of mean and root-mean-square values.

In the excited flow, the phase mean of the effective velocity can be expressed as an ensemble averaged quantity:

$$\langle Z \rangle = \lim_{n \to \infty} Z \left(x, n\omega\tau + \phi_0 \right) \quad 0 \le \phi_0 \le \pi \qquad \text{(c.6)}$$

where ω is the angular frequency, f_0 the initial phase angle and τ the time. If the total data sets in time are NI and in phase are NJ then

$$\langle Z_p \rangle = \frac{1}{NI} \sum_{i=1}^{NI} Z_{p,i}, \quad \langle Z'_p \rangle^2 = \frac{1}{NI} \sum_{i=1}^{NI} \left(Z_{p,i} - \langle Z_p \rangle \right)^2, \quad \overline{Z'^2} = \frac{1}{NJ} \sum_{j=1}^{NJ} \langle Z'_p \rangle_j^2$$

equation (c.1) can be written as:

$$Z_{i,p} = \left[-B_2 + \left\{ B_2^2 + 4C_2 \left(A_2 - E_{i,p}^2 \right) \right\}^{1/2} \right]^2 \qquad \text{(c.7)}$$

where p represent the phase. For simplicity, the subscript p will be omitted from hereafter.

In a 3-dimensional flow, it is usually desirable to obtain the mean and variance for the individual velocity components in axial, azimuthal, and radial directions and also their cross correlations. The procedure to obtain the mean and variance of the individual velocity components is the same as for the effective cooling velocities. However in this case, u, w and v are functions of three random variables and there are extra terms in the Taylor expansion to account for the covariances of the cooling velocities. Thus, the axial mean velocity component as given by Dvorak and Syred, and King is:

$$\bar{u} = U\left(\bar{Z}_P, \bar{Z}_Q, \bar{Z}_R\right) + \frac{1}{2}\sum_{i=1}^{3}\frac{\partial^2 U}{\partial Z_i^2}\sigma_{Z_i}^2 + \sum_{i<j}^{3}\frac{\partial^2 U}{\partial Z_i \partial Z_j} \bullet K_{Z_i Z_j} \qquad \text{(c.8)}$$

where $K_{Z_i Z_j}$ is the covariance of the cooling velocities. Z_i *and* Z_j and is defined as:

$$K_{Z_i Z_j} = \frac{1}{T}\int_0^T \left(Z_i - \bar{Z}_j\right)\left(Z_j - \bar{Z}_j\right)dt \qquad \text{(c.9)}$$

identical expressions for $\bar{w}$ *and* $\bar{v}$ can also be obtained in terms of W and V, respectively. Derivatives of the form $\partial^2 U / \partial Z_i \partial Z_j$ are determined analytically from equation (c.5) and table c.1.

The normal stresses are given as:

$$\overline{u'^2} = \sum_{i=1}^{3}\left(\frac{\partial U}{\partial Z_i}\right)^2 \bullet \sigma_{Z_i}{}^2 + \sum_{i}^{3}\sum_{i\neq j}^{3}\sum_{j}^{3}\frac{\partial U}{\partial Z_i} \bullet \frac{\partial U}{\partial Z_j} \bullet K_{Z_i Z_j} - \left[\frac{1}{2}\sum_{i=1}^{3}\frac{\partial^2 U}{\partial Z_i^2} \bullet \sigma_{Z_i}^2 + \sum_{i<j}^{3}\frac{\partial^2 U}{\partial Z_i \partial Z_j} \bullet K_{Z_i Z_j}\right]^2 \qquad \text{(c.10)}$$

with similar expressions for $\overline{w'^2}$ *and* $\overline{v'^2}$.

Finally, the expressions for shear stresses as given by Dvorak and Syred are of the form:

$$\begin{aligned}\overline{u'v'} = &\sum_{i=1}^{3}\frac{\partial U}{\partial Z_i}\frac{\partial V}{\partial Zi}\sigma_{Z_i}^2 + \sum_{i}^{3}\sum_{i\neq j}^{3}\sum_{j}^{3}\frac{\partial U}{\partial Z_i}\frac{\partial V}{\partial Z_j}K_{Z_i Z_j} \\ &-\left[\tfrac{1}{2}\sum_{i=1}^{3}\frac{\partial^2 U}{\partial Z_i^2}\sigma_{Z_i}^2 + \sum_{i}^{3}\sum_{i<j}^{3}\frac{\partial^2 V}{\partial Z_i \partial Z_j} \bullet K_{Z_i Z_j}\right] \\ &\bullet\left[\tfrac{1}{2}\sum_{i=1}^{3}\frac{\partial^2 V}{\partial Z_i^2} \bullet \sigma_{Z_i}^2 + \sum_{i}^{3}\sum_{i<j}\frac{\partial^2 V}{\partial Z_i \partial Z_j} \bullet K_{Z_i Z_j}\right]\end{aligned} \qquad \text{(c.11)}$$

Expressions for $\overline{u'w'}$ *and* $\overline{v'w'}$ can also be obtained in a similar manner.

The informations needed to program the above equations are listed as follows:

1. Calculation of the pitch and yaw factors:

a) Assume a temporary G and K;

b) Using equation (c.7) to calculate $\tilde{u}_1$, $\tilde{v}_1$ *and* $\tilde{w}_1$ (note: since the second and third term in equation (c.7) are very small, using equation (c.5) is recommended);

c) Equation (c.1) is then employed to calculate the calibrated voltage $F_i = f(\tilde{u}_i)$;

d) Then calculate $G = \dfrac{\tilde{v}(F_2)}{\tilde{u}(F_1)}$ and $K = \dfrac{\tilde{v}(F_2)}{\tilde{w}(F_3)}$;

e) Check $(\tilde{u}_2 - \tilde{u}_1)\langle 0.001$, go to b). and repeat step b). - e). until convergence is reached.

2. Derivation of the first and second derivatives in equation (c.7), (c.9) and (c.10):

a) $\dfrac{\partial U}{\partial Z_6}, \dfrac{\partial U}{\partial Z_1}, \dfrac{\partial U}{\partial Z_2}$

$$\frac{\partial U}{\partial Z_6} = -\left[\frac{1}{\left(G^2 - K^2\right)}\right]^{1/2}\left\{AO + \left(AO^2 + \frac{B0^2}{3}\right)^{1/2}\right\}^{-1/2}\left\{Z_6 + \left(AO^2 + \frac{B0^2}{3}\right)^{-1/2}\left(Z_6 AO + \frac{1}{3}Z_6 BO\right)\right\}$$

$$= \frac{1}{2}\left[\frac{1}{\left(G^2 - K^2\right)}\right]\frac{\left\{\dfrac{\partial(AO)}{\partial Z_6} + \left(AO^2 + \dfrac{B0^2}{3}\right)^{-1/2}\left(\dfrac{\partial(AO)}{\partial Z_6}AO + \dfrac{1}{3}\dfrac{\partial(BO)}{\partial Z_6}BO\right)\right\}}{U}$$

$$\frac{\partial U}{\partial Z_2} = \frac{1}{2}\left[\frac{1}{\left(G^2 - K^2\right)}\right]^{1/2}\left\{AO + \left(AO^2 + \frac{B0^2}{3}\right)^{1/2}\right\}^{-1/2}\left\{-2Z_2 + 2\left(AO^2 + \frac{B0^2}{3}\right)^{-1/2}\left(-Z_2 AO + \frac{1}{3}BOZ_2\right)\right\}$$

$$= \frac{1}{2}\left[\frac{1}{\left(G^2 - K^2\right)}\right]\frac{\left\{\dfrac{\partial(AO)}{\partial Z_2} + \left(AO^2 + \dfrac{B0^2}{3}\right)^{-1/2}\left(\dfrac{\partial(AO)}{\partial Z_2}AO + \dfrac{1}{3}BO\dfrac{\partial(BO)}{\partial Z_2}\right)\right\}}{U}$$

$$\frac{\partial U}{\partial Z_1} = \frac{1}{2}\left[\frac{1}{\left(G^2 - K^2\right)}\right]^{1/2}\left\{AO + \left(AO^2 + \frac{B0^2}{3}\right)^{1/2}\right\}^{-1/2}\left\{4Z_1 + \left(AO^2 + \frac{B0^2}{3}\right)^{-1/2}\left(2Z_1 AO\right)\right\}$$

$$= \frac{1}{2}\left[\frac{1}{\left(G^2 - K^2\right)}\right]\frac{\left\{\dfrac{\partial(AO)}{\partial Z_1} + \left(AO^2 + \dfrac{B0^2}{3}\right)^{-1/2}\left(\dfrac{\partial(AO)}{\partial Z_1}AO + \dfrac{1}{3}\dfrac{\partial(BO)}{\partial Z_1}BO\right)\right\}}{U}$$

b) $\dfrac{\partial W}{\partial Z_6}, \dfrac{\partial W}{\partial Z_2}, \dfrac{\partial W}{\partial Z_1}$

$$\frac{\partial W}{\partial Z_6} = -\left[\frac{1}{\left(G^2 - K^2\right)}\right]^{1/2}\left\{-AO + \left(AO^2 + \frac{B0^2}{3}\right)^{1/2}\right\}^{-1/2}\left\{-Z_6 + \left(AO^2 + \frac{B0^2}{3}\right)^{-1/2}\left(Z_6 AO + \frac{1}{3}Z_6 BO\right)\right\}$$

$$= \frac{1}{2}\left[\frac{1}{\left(G^2 - K^2\right)}\right]\frac{\left\{-\dfrac{\partial(AO)}{\partial Z_6} + \left(AO^2 + \dfrac{B0^2}{3}\right)^{-1/2}\left(-\dfrac{\partial(AO)}{\partial Z_6}AO + \dfrac{1}{3}BO\dfrac{\partial(BO)}{\partial Z_6}\right)\right\}}{W}$$

$$\frac{\partial W}{\partial Z_2} = \frac{1}{2}\left[\frac{1}{\left(G^2 - K^2\right)}\right]^{1/2}\left\{-AO + \left(AO^2 + \frac{B0^2}{3}\right)^{1/2}\right\}^{-1/2}\left\{-\left(-2Z_2\right) + 2\left(AO^2 + \frac{B0^2}{3}\right)^{-1/2}\left(-Z_2 AO + \frac{1}{3}BOZ_2\right)\right\}$$

$$= \frac{1}{2}\left[\frac{1}{\left(G^2 - K^2\right)}\right]\frac{\left\{-\left(-2Z_2\right)+\left(AO^2+\frac{B0^2}{3}\right)^{-1/2}\left(\left(-2Z_2\right)AO+\frac{1}{3}BO\left(2Z_2\right)\right)\right\}}{W}$$

$$\frac{\partial W}{\partial Z_1} = \frac{1}{2}\left[\frac{1}{\left(G^2-K^2\right)}\right]^{1/2}\left\{-AO+\left(AO^2+\frac{B0^2}{3}\right)^{1/2}\right\}^{-1/2}\left\{-4Z_1+\left(AO^2+\frac{B0^2}{3}\right)^{-1/2}\left(2Z_1 AO\right)\right\}$$

$$= \frac{1}{2}\left[\frac{1}{\left(G^2 - K^2\right)}\right]\frac{\left\{-\frac{\partial(AO)}{\partial Z_1}+\left(AO^2+\frac{B0^2}{3}\right)^{-1/2}\left(\frac{\partial(AO)}{\partial Z_1}AO+\frac{1}{3}\frac{\partial(BO)}{\partial Z_1}\right)\right\}}{W}$$

c) $\frac{\partial V}{\partial Z_6},\ \frac{\partial V}{\partial Z_2},\ \frac{\partial V}{\partial Z_1}$

$$\frac{\partial V}{\partial Z_6} = \left[CO-\frac{\left(G^2+K^2\right)}{\left(G^2-K^2\right)}\left(AO^2+\frac{BO^2}{3}\right)^{\frac{1}{2}}\right]^{-\frac{1}{2}}\left[Z_6+\frac{\left(G^2+K^2\right)}{\left(G^2-K^2\right)}\left(AO^2+\frac{BO^2}{3}\right)^{-\frac{1}{2}}\left(Z_6 AO+\frac{1}{3}Z_6 BO\right)\right]$$

$$= \frac{1}{2}\frac{\left[\frac{\partial(CO)}{\partial Z_6}-\frac{\left(G^2+K^2\right)}{\left(G^2-K^2\right)}\left(AO^2+\frac{BO^2}{3}\right)^{-\frac{1}{2}}\left(\frac{\partial(AO)}{\partial Z_6}AO+\frac{1}{3}BO\frac{\partial(BO)}{\partial Z_6}\right)\right]}{V}$$

$$\frac{\partial V}{\partial Z_2} = \frac{1}{2}\left[CO-\frac{\left(G^2+K^2\right)}{\left(G^2-K^2\right)}\left(AO^2+\frac{BO^2}{3}\right)^{\frac{1}{2}}\right]^{-\frac{1}{2}}\left[2Z_2-\frac{1}{2}\frac{\left(G^2+K^2\right)}{\left(G^2-K^2\right)}\left(AO^2+\frac{BO^2}{3}\right)^{-\frac{1}{2}}\left(-4Z_2 AO+\frac{4}{3}Z_2 BO\right)\right]$$

$$= \frac{1}{2}\frac{\left[\dfrac{\partial(CO)}{\partial Z_2} - \dfrac{1}{2}\dfrac{\left(G^2+K^2\right)}{\left(G^2-K^2\right)}\left(AO^2+\dfrac{BO^2}{3}\right)^{-\frac{1}{2}}\left(\dfrac{\partial(AO)}{\partial Z_2}AO+\dfrac{1}{3}BO\dfrac{\partial(BO)}{\partial Z_2}\right)\right]}{V}$$

$$\frac{\partial V}{\partial Z_1} = \frac{1}{2}\left[CO - \frac{\left(G^2+K^2\right)}{\left(G^2-K^2\right)}\left(AO^2+\frac{BO^2}{3}\right)^{\frac{1}{2}}\right]^{-\frac{1}{2}}\left[-2Z_1 - \frac{\left(G^2+K^2\right)}{\left(G^2-K^2\right)}\left(AO^2+\frac{BO^2}{3}\right)^{-\frac{1}{2}}\left(4Z_1 AO\right)\right]$$

$$= \frac{1}{2}\frac{\left[\dfrac{\partial(CO)}{\partial Z_1} - \dfrac{\left(G^2+K^2\right)}{\left(G^2-K^2\right)}\left(AO^2+\dfrac{BO^2}{3}\right)^{-\frac{1}{2}}\left(\dfrac{\partial(AO)}{\partial Z_1}AO+\dfrac{1}{3}\dfrac{\partial(BO)}{\partial Z_1}BO\right)\right]}{V}$$

d) $\dfrac{\partial^2 U}{\partial Z_6^2}$, $\dfrac{\partial^2 U}{\partial Z_2^2}$ *and* $\dfrac{\partial^2 U}{\partial Z_1^2}$

$$\frac{\partial^2 U}{\partial Z_6^2} = \frac{1}{2}\left[\frac{1}{\left(G^2-K^2\right)}\right]\left[U\frac{\partial}{\partial Z_6}\left\{\frac{\partial(AO)}{\partial Z_6}+\left(AO^2+\frac{BO^2}{3}\right)^{-1/2}\left(\frac{\partial(AO)}{\partial Z_6}AO+\frac{1}{3}\frac{\partial(BO)}{\partial Z_6}BO\right)\right\} - \left\{\frac{\partial(AO)}{\partial Z_6}+\left(AO^2+\frac{BO^2}{3}\right)^{-1/2}\left(\frac{\partial(AO)}{\partial Z_6}AO+\frac{1}{3}\frac{\partial(BO)}{\partial Z_6}BO\right)\right\}\frac{\partial U}{\partial Z_6}\right] \Big/ U^2$$

$$= \left\langle\left[\frac{1}{\left(G^2-K^2\right)}\right]\frac{\partial}{\partial Z_6}\left\{\frac{\partial(AO)}{\partial Z_6}+\left(AO^2+\frac{BO^2}{3}\right)^{-1/2}\left(\frac{\partial(AO)}{\partial Z_6}AO+\frac{1}{3}\frac{\partial(BO)}{\partial Z_6}BO\right)\right\} - 2\frac{\partial U}{\partial Z_6}\frac{\partial U}{\partial Z_6}\right\rangle \Big/ [2U]$$

where

$$\frac{\partial}{\partial Z_6}\left\{\frac{\partial(AO)}{\partial Z_6}+\left(AO^2+\frac{B0^2}{3}\right)^{-1/2}\left(\frac{\partial(AO)}{\partial Z_6}AO+\frac{1}{3}\frac{\partial(BO)}{\partial Z_6}BO\right)\right\}=$$

$$\frac{\partial^2(AO)}{\partial Z_6^2}+\left(AO^2+\frac{B0^2}{3}\right)^{-1/2}\left(\frac{\partial^2(AO)}{\partial Z_6^2}AO+\left(\frac{\partial(AO)}{\partial Z_6}\right)^2+\frac{1}{3}\frac{\partial^2(BO)}{\partial Z_6^2}BO+\frac{1}{3}\left(\frac{\partial(AO)}{\partial Z_6}\right)^2\right)$$

$$-\left(AO^2+\frac{B0^2}{3}\right)^{-\frac{3}{2}}\left(\frac{\partial(AO)}{\partial Z_6}AO+\frac{1}{3}\frac{\partial(BO)}{\partial Z_6}BO\right)^2$$

$$\frac{\partial}{\partial Z_6}\left\{\frac{\partial(AO)}{\partial Z_6}+\left(AO^2+\frac{B0^2}{3}\right)^{-1/2}\left(\frac{\partial(AO)}{\partial Z_6}AO+\frac{1}{3}\frac{\partial(BO)}{\partial Z_6}BO\right)\right\}=$$

$$\frac{\partial^2(AO)}{\partial Z_6^2}+\left(AO^2+\frac{B0^2}{3}\right)^{-1/2}\left[\left(\frac{\partial^2(AO)}{\partial Z_6^2}AO+\left(\frac{\partial(AO)}{\partial Z_6}\right)^2+\frac{1}{3}\frac{\partial^2(BO)}{\partial Z_6^2}BO+\frac{1}{3}\left(\frac{\partial(AO)}{\partial Z_6}\right)^2\right)\right.$$

$$\left.-\left(AO^2+\frac{B0^2}{3}\right)^{-1}\left(\frac{\partial(AO)}{\partial Z_6}AO+\frac{1}{3}\frac{\partial(BO)}{\partial Z_6}BO\right)^2\right]$$

$$\frac{\partial^2 U}{\partial Z_2^2}=\frac{\left[\frac{1}{\left(G^2-K^2\right)}\right]\frac{\partial}{\partial Z_2}\left\{\frac{\partial(AO)}{\partial Z_2}+\left(AO^2+\frac{B0^2}{3}\right)^{-1/2}\left(\frac{\partial(AO)}{\partial Z_2}AO+\frac{1}{3}BO\frac{\partial(BO)}{\partial Z_2}\right)\right\}-2\frac{\partial U}{\partial Z_2}\frac{\partial U}{\partial Z_2}}{2U}$$

where

$$\frac{\partial}{\partial Z_2}\left\{\frac{\partial(AO)}{\partial Z_2}+\left(AO^2+\frac{B0^2}{3}\right)^{-1/2}\left(\frac{\partial(AO)}{\partial Z_2}AO+\frac{1}{3}BO\frac{\partial(BO)}{\partial Z_2}\right)\right\}=$$

$$= \frac{\partial^2(AO)}{\partial Z_2^2} + \left(AO^2 + \frac{B0^2}{3} \right)^{-1/2} \left[\left(\frac{\partial^2(AO)}{\partial Z_2^2} AO + \left(\frac{\partial(AO)}{\partial Z_2} \right)^2 + \frac{1}{3} BO \frac{\partial^2(BO)}{\partial Z_2^2} + \frac{1}{3} \left(\frac{\partial(AO)}{\partial Z_2} \right)^2 \right) \right.$$

$$\left. - \left(AO^2 + \frac{B0^2}{3} \right)^{-1} \left(\frac{\partial^2(AO)}{\partial Z_2^2} AO + \frac{1}{3} BO \frac{\partial^2(BO)}{\partial Z_2^2} \right)^2 \right]$$

$$\frac{\partial^2 U}{\partial Z_1^2} = \frac{1}{2} \left[\frac{1}{(G^2 - K^2)} \right] \left[U \frac{\partial}{\partial Z_1} \left\{ \frac{\partial(AO)}{\partial Z_1} + \left(AO^2 + \frac{B0^2}{3} \right)^{-1/2} \left(\frac{\partial(AO)}{\partial Z_1} AO + \frac{1}{3} \frac{\partial(BO)}{\partial Z_1} BO \right) \right\} - \left\{ \frac{\partial(AO)}{\partial Z_1} + \left(AO^2 + \frac{B0^2}{3} \right)^{-1/2} \left(\frac{\partial(AO)}{\partial Z_1} AO + \frac{1}{3} \frac{\partial(BO)}{\partial Z_1} BO \right) \right\} \frac{\partial U}{\partial Z_1} \right] \Big/ U^2$$

$$= \left[\left[\frac{1}{(G^2 - K^2)} \right] \frac{\partial}{\partial Z_1} \left\{ \frac{\partial(AO)}{\partial Z_1} + \left(AO^2 + \frac{B0^2}{3} \right)^{-1/2} \left(\frac{\partial(AO)}{\partial Z_1} AO + \frac{1}{3} \frac{\partial(BO)}{\partial Z_1} BO \right) \right\} - 2 \frac{\partial U}{\partial Z_1} \frac{\partial U}{\partial Z_1} \right] \Big/ [2U]$$

where

$$\frac{\partial}{\partial Z_1} \left\{ \frac{\partial(AO)}{\partial Z_1} + \left(AO^2 + \frac{B0^2}{3} \right)^{-1/2} \left(\frac{\partial(AO)}{\partial Z_1} AO + \frac{1}{3} \frac{\partial(BO)}{\partial Z_1} BO \right) \right\} =$$

e)

$$= \frac{\partial^2(AO)}{\partial Z_1^2} + \left(AO^2 + \frac{B0^2}{3} \right)^{-1/2} \left[\left(\frac{\partial^2(AO)}{\partial Z_1^2} AO + \left(\frac{\partial(AO)}{\partial Z_1} \right)^2 + \frac{1}{3} \frac{\partial^2(BO)}{\partial Z_1^2} BO + \frac{1}{3} \left(\frac{\partial(BO)}{\partial Z_1} \right)^2 \right) \right.$$

$$\left. - \left(AO^2 + \frac{B0^2}{3} \right)^{-1} \left(\frac{\partial^2(AO)}{\partial Z_1^2} AO + \frac{1}{3} \frac{\partial^2(BO)}{\partial Z_1^2} BO \right)^2 \right]$$

$$\frac{\partial^2 U}{\partial Z_6 \partial Z_1}, \quad \frac{\partial^2 U}{\partial Z_6 \partial Z_2}, \quad \frac{\partial^2 U}{\partial Z_2 \partial Z_1}$$

$$\frac{\partial^2 U}{\partial Z_6 \partial Z_1} = \left\langle \left[\frac{1}{(G^2 - K^2)} \right] \frac{\partial}{\partial Z_1} \left\{ \frac{\partial(AO)}{\partial Z_6} + \left(AO^2 + \frac{B0^2}{3} \right)^{-1/2} \left(\frac{\partial(AO)}{\partial Z_6} AO + \frac{1}{3} \frac{\partial(BO)}{\partial Z_6} BO \right) \right\} - 2 \frac{\partial U}{\partial Z_1} \frac{\partial U}{\partial Z_6} \right\rangle \Big/ \langle 2U \rangle$$

where

$$\frac{\partial}{\partial Z_1}\left\{\frac{\partial(AO)}{\partial Z_6}+\left(AO^2+\frac{B0^2}{3}\right)^{-1/2}\left(\frac{\partial(AO)}{\partial Z_6}AO+\tfrac{1}{3}\frac{\partial(BO)}{\partial Z_6}BO\right)\right\}=$$

$$=\frac{\partial^2(AO)}{\partial Z_6\partial Z_1}+\left(AO^2+\frac{B0^2}{3}\right)^{-1/2}\left\langle\left(\frac{\partial^2(AO)}{\partial Z_6\partial Z_1}AO+\frac{\partial(AO)}{\partial Z_6}\frac{\partial(AO)}{\partial Z_1}+\frac{1}{3}\frac{\partial^2(BO)}{\partial Z_6\partial Z_1}BO+\frac{\partial(BO)}{\partial Z_6}\frac{\partial(BO)}{\partial Z_1}\right)-\right.$$

$$\left.-\left(AO^2+\frac{B0^2}{3}\right)^{-1}\left(\frac{\partial(AO)}{\partial Z_6}AO+\frac{\partial(BO)}{\partial Z_6}BO\right)\left(\frac{\partial(AO)}{\partial Z_1}AO+\frac{\partial(BO)}{\partial Z_1}BO\right)\right\rangle$$

$$note:\frac{\partial^2}{\partial Z_i\partial Z_j}(BO\ \ or\ \ AO)\equiv 0$$

$$\frac{\partial^2 U}{\partial Z_6\partial Z_2}=\left\langle\left[\frac{1}{\left(G^2-K^2\right)}\right]\frac{\partial}{\partial Z_2}\left\{\frac{\partial(AO)}{\partial Z_6}+\left(AO^2+\frac{B0^2}{3}\right)^{-1/2}\left(\frac{\partial(AO)}{\partial Z_6}AO+\frac{1}{3}\frac{\partial(BO)}{\partial Z_6}BO\right)\right\}-2\frac{\partial U}{\partial Z_1}\frac{\partial U}{\partial Z_6}\right\rangle\Big/\langle 2U\rangle$$

where

$$\frac{\partial}{\partial Z_2}\left\{\frac{\partial(AO)}{\partial Z_6}+\left(AO^2+\frac{B0^2}{3}\right)^{-1/2}\left(\frac{\partial(AO)}{\partial Z_6}AO+\tfrac{1}{3}\frac{\partial(BO)}{\partial Z_6}BO\right)\right\}=$$

$$=\frac{\partial^2(AO)}{\partial Z_6\partial Z_2}+\left(AO^2+\frac{B0^2}{3}\right)^{-1/2}\left\langle\left(\frac{\partial^2(AO)}{\partial Z_6\partial Z_2}AO+\frac{\partial(AO)}{\partial Z_6}\frac{\partial(AO)}{\partial Z_2}+\frac{1}{3}\frac{\partial^2(BO)}{\partial Z_6\partial Z_2}BO+\frac{\partial(BO)}{\partial Z_6}\frac{\partial(BO)}{\partial Z_2}\right)-\right.$$

$$\left.-\left(AO^2+\frac{B0^2}{3}\right)^{-1}\left(\frac{\partial(AO)}{\partial Z_6}AO+\frac{\partial(BO)}{\partial Z_6}BO\right)\left(\frac{\partial(AO)}{\partial Z_2}AO+\frac{\partial(BO)}{\partial Z_2}BO\right)\right\rangle$$

$$\frac{\partial^2 U}{\partial Z_1\partial Z_2}=\left\langle\left[\frac{1}{\left(G^2-K^2\right)}\right]\frac{\partial}{\partial Z_2}\left\{\frac{\partial(AO)}{\partial Z_1}+\left(AO^2+\frac{B0^2}{3}\right)^{-1/2}\left(\frac{\partial(AO)}{\partial Z_1}AO+\frac{1}{3}\frac{\partial(BO)}{\partial Z_1}BO\right)\right\}-2\frac{\partial U}{\partial Z_1}\frac{\partial U}{\partial Z_1}\right\rangle\Big/\langle 2U\rangle$$

where

$$\frac{\partial}{\partial Z_2}\left\{\frac{\partial(AO)}{\partial Z_1}+\left(AO^2+\frac{B0^2}{3}\right)^{-1/2}\left(\frac{\partial(AO)}{\partial Z_1}AO+\tfrac{1}{3}\frac{\partial(BO)}{\partial Z_1}BO\right)\right\}=$$

$$=\frac{\partial^2(AO)}{\partial Z_1\partial Z_2}+\left(AO^2+\frac{B0^2}{3}\right)^{-1/2}\left\langle\left(\frac{\partial^2(AO)}{\partial Z_1\partial Z_2}AO+\frac{\partial(AO)}{\partial Z_1}\frac{\partial(AO)}{\partial Z_2}+\frac{1}{3}\frac{\partial^2(BO)}{\partial Z_1\partial Z_2}BO+\frac{\partial(BO)}{\partial Z_1}\frac{\partial(BO)}{\partial Z_2}\right)-\right.$$

$$\left.-\left(AO^2+\frac{B0^2}{3}\right)^{-1}\left(\frac{\partial(AO)}{\partial Z_1}AO+\frac{\partial(BO)}{\partial Z_1}BO\right)\left(\frac{\partial(AO)}{\partial Z_2}AO+\frac{\partial(BO)}{\partial Z_2}BO\right)\right\rangle$$

or

$$\frac{\partial^2U}{\partial Z_i\partial Z_j}=\left\langle\left[\frac{1}{\left(G^2-K^2\right)}\right]\frac{\partial}{\partial Z_i}\left\{\frac{\partial(AO)}{\partial Z_j}+\left(AO^2+\frac{B0^2}{3}\right)^{-1/2}\left(\frac{\partial(AO)}{\partial Z_j}AO+\frac{1}{3}\frac{\partial(BO)}{\partial Z_j}BO\right)\right\}-2\frac{\partial U}{\partial Z_j}\frac{\partial U}{\partial Z_j}\right\rangle\Big/\langle 2U\rangle$$

where $i\langle j$ and the combination is: $\langle 6,1\rangle,\langle 6,2\rangle\langle 2,1\rangle$ and:

$$\frac{\partial}{\partial Z_i}\left\{\frac{\partial(AO)}{\partial Z_j}+\left(AO^2+\frac{B0^2}{3}\right)^{-1/2}\left(\frac{\partial(AO)}{\partial Z_j}AO+\tfrac{1}{3}\frac{\partial(BO)}{\partial Z_j}BO\right)\right\}=$$

$$=\frac{\partial^2(AO)}{\partial Z_i\partial Z_j}+\left(AO^2+\frac{B0^2}{3}\right)^{-1/2}\left\langle\left(\frac{\partial^2(AO)}{\partial Z_i\partial Z_j}AO+\frac{\partial(AO)}{\partial Z_i}\frac{\partial(AO)}{\partial Z_j}+\frac{1}{3}\frac{\partial^2(BO)}{\partial Z_i\partial Z_j}BO+\frac{\partial(BO)}{\partial Z_i}\frac{\partial(BO)}{\partial Z_j}\right)-\right.$$

$$\left.-\left(AO^2+\frac{B0^2}{3}\right)^{-1}\left(\frac{\partial(AO)}{\partial Z_i}AO+\frac{\partial(BO)}{\partial Z_i}BO\right)\left(\frac{\partial(AO)}{\partial Z_j}AO+\frac{\partial(BO)}{\partial Z_j}BO\right)\right\rangle$$

f) $\dfrac{\partial^2 W}{\partial Z_i^2}$, i = 6,2,1

$$\frac{\partial^2W}{\partial Z_1^2}=\frac{1}{2}\left[\frac{1}{\left(G^2-K^2\right)}\right]$$

$$\left[W\frac{\partial}{\partial Z_1}\left\{-\frac{\partial(AO)}{\partial Z_1}+\left(AO^2+\frac{B0^2}{3}\right)^{-1/2}\left(\frac{\partial(AO)}{\partial Z_1}AO+\frac{1}{3}\frac{\partial(BO)}{\partial Z_1}BO\right)\right\}-\left\{-\frac{\partial(AO)}{\partial Z_1}+\left(AO^2+\frac{B0^2}{3}\right)^{-1/2}\left(\frac{\partial(AO)}{\partial Z_1}AO+\frac{1}{3}\frac{\partial(BO)}{\partial Z_1}BO\right)\right\}\frac{\partial W}{\partial Z_1}\right]\Big/W^2$$

$$=\left[\left[\frac{1}{\left(G^2-K^2\right)}\right]\frac{\partial}{\partial Z_i}\left\{-\frac{\partial(AO)}{\partial Z_i}+\left(AO^2+\frac{B0^2}{3}\right)^{-1/2}\left(\frac{\partial(AO)}{\partial Z_i}AO+\frac{1}{3}\frac{\partial(BO)}{\partial Z_i}BO\right)\right\}-2\frac{\partial W}{\partial Z_i}\frac{\partial W}{\partial Z_i}\right]\Big/[2W]$$

where

$$\frac{\partial}{\partial Z_i}\left\{\frac{\partial(AO)}{\partial Z_i}+\left(AO^2+\frac{B0^2}{3}\right)^{-1/2}\left(\frac{\partial(AO)}{\partial Z_i}AO+\tfrac{1}{3}\frac{\partial(BO)}{\partial Z_i}BO\right)\right\}=$$

$$=\frac{\partial^2(AO)}{\partial Z_i^2}+\left(AO^2+\frac{B0^2}{3}\right)^{-1/2}\left[\left(\frac{\partial^2(AO)}{\partial Z_i^2}AO+\left(\frac{\partial(AO)}{\partial Z_i}\right)^2+\frac{1}{3}\frac{\partial^2(BO)}{\partial Z_i^2}BO+\frac{1}{3}\left(\frac{\partial(BO)}{\partial Z_i}\right)^2\right)\right.$$

$$\left.-\left(AO^2+\frac{B0^2}{3}\right)^{-1}\left(\frac{\partial^2(AO)}{\partial Z_i^2}AO+\frac{1}{3}\frac{\partial^2(BO)}{\partial Z_i^2}BO\right)^2\right]$$

g) $\frac{\partial^2 W}{\partial Z_i \partial Z_j}\frac{\partial^2 W}{\partial Z_i \partial Z_j}$, where $i\langle j$ and the combination is: $\langle 6,1\rangle,\langle 6,2\rangle\langle 2,1\rangle$, similarly as the above we have:

$$\frac{\partial^2 W}{\partial Z_i \partial Z_j}=\left\langle\left[\frac{1}{\left(G^2-K^2\right)}\right]\frac{\partial}{\partial Z_i}\left\{-\frac{\partial(AO)}{\partial Z_j}+\left(AO^2+\frac{B0^2}{3}\right)^{-1/2}\left(\frac{\partial(AO)}{\partial Z_j}AO+\frac{1}{3}\frac{\partial(BO)}{\partial Z_j}BO\right)\right\}-2\frac{\partial W}{\partial Z_j}\frac{\partial W}{\partial Z_j}\right\rangle\Big/\langle 2W\rangle$$

and

$$\frac{\partial}{\partial Z_i}\left\{-\frac{\partial(AO)}{\partial Z_j}+\left(AO^2+\frac{B0^2}{3}\right)^{-1/2}\left(\frac{\partial(AO)}{\partial Z_j}AO+\tfrac{1}{3}\frac{\partial(BO)}{\partial Z_j}BO\right)\right\}=$$

$$=-\frac{\partial^2(AO)}{\partial Z_i \partial Z_j}+\left(AO^2+\frac{B0^2}{3}\right)^{-1/2}\left\langle\left(\frac{\partial^2(AO)}{\partial Z_i \partial Z_j}AO+\frac{\partial(AO)}{\partial Z_i}\frac{\partial(AO)}{\partial Z_j}+\frac{1}{3}\frac{\partial^2(BO)}{\partial Z_i \partial Z_j}BO+\frac{\partial(BO)}{\partial Z_i}\frac{\partial(BO)}{\partial Z_j}\right)-\right.$$

$$\left.-\left(AO^2+\frac{B0^2}{3}\right)^{-1}\left(\frac{\partial(AO)}{\partial Z_i}AO+\frac{\partial(BO)}{\partial Z_i}BO\right)\left(\frac{\partial(AO)}{\partial Z_j}AO+\frac{\partial(BO)}{\partial Z_j}BO\right)\right\rangle$$

h) $\frac{\partial^2 V}{\partial Z_i^2}$, i = 6,2,1

$$\frac{\partial^2 V}{\partial Z_i^2} = \frac{\partial}{\partial Z_i}\left(\frac{\partial V}{\partial Z_i}\right) =$$

$$= \left\{ V \frac{\partial}{\partial Z_i}\left[\frac{\partial(CO)}{\partial Z_i} - \frac{\left(G^2+K^2\right)}{\left(G^2-K^2\right)}\left(AO^2 + \frac{BO^2}{3}\right)^{-\frac{1}{2}}\left(\frac{\partial(AO)}{\partial Z_i} AO + \frac{1}{3}\frac{\partial(BO)}{\partial Z_i} BO\right)\right] - 2\frac{\partial V}{\partial Z_i}\frac{\partial V}{\partial Z_i}\right\} \Big/ [2V]$$

where

$$\frac{\partial}{\partial Z_i}\left[\frac{\partial(CO)}{\partial Z_i} - \frac{\left(G^2+K^2\right)}{\left(G^2-K^2\right)}\left(AO^2 + \frac{BO^2}{3}\right)^{-\frac{1}{2}}\left(\frac{\partial(AO)}{\partial Z_i} AO + \frac{1}{3}\frac{\partial(BO)}{\partial Z_i} BO\right)\right] =$$

$$\frac{\partial^2(CO)}{\partial Z_i^2} - \frac{\left(G^2+K^2\right)}{\left(G^2-K^2\right)}\left(AO^2 + \frac{BO^2}{3}\right)^{-\frac{1}{2}} \bullet \left[\left(\frac{\partial^2(AO)}{\partial Z_i^2} AO + \left(\frac{\partial(AO)}{\partial Z_i}\right)^2 + \frac{1}{3}\frac{\partial^2(BO)}{\partial Z_i^2} BO + \frac{1}{3}\left(\frac{\partial(BO)}{\partial Z_i}\right)^2 \right) \right.$$

$$\left. - \left(AO^2 + \frac{BO^2}{3}\right)^{-1}\left(\frac{\partial(AO)}{\partial Z_i} AO + \frac{1}{3}\frac{\partial(BO)}{\partial Z_i} BO\right)^2 \right]$$

j) $\dfrac{\partial^2 V}{\partial Z_i \partial Z_j}$, where $i\langle j$ and it is a combination of $\langle 1,6\rangle$, $\langle 2,6\rangle$, $\langle 2,1\rangle$

$$\frac{\partial^2 V}{\partial Z_i \partial Z_j} = \left[V \frac{\partial}{\partial Z_i}\left[\frac{\partial(CO)}{\partial Z_j} - \frac{\left(G^2+K^2\right)}{\left(G^2-K^2\right)}\left(AO^2 + \frac{BO^2}{3}\right)^{-\frac{1}{2}}\left(\frac{\partial(AO)}{\partial Z_j} AO + \frac{1}{3}\frac{\partial(BO)}{\partial Z_j} BO\right)\right] - 2\frac{\partial V}{\partial Z_i}\frac{\partial V}{\partial Z_j}\right] \Big/ [2V]$$

where

$$\frac{\partial}{\partial Z_i}\left[\frac{\partial(CO)}{\partial Z_j} - \frac{\left(G^2+K^2\right)}{\left(G^2-K^2\right)}\left(AO^2 + \frac{BO^2}{3}\right)^{-\frac{1}{2}}\left(\frac{\partial(AO)}{\partial Z_j} AO + \frac{1}{3}\frac{\partial(BO)}{\partial Z_j} BO\right)\right] =$$

$$\frac{\partial^2(CO)}{\partial Z_i \partial Z_j} - \frac{\left(G^2+K^2\right)}{\left(G^2-K^2\right)}\left(AO^2 + \frac{BO^2}{3}\right)^{-\frac{1}{2}} \bullet \left[\left(\frac{\partial^2(AO)}{\partial Z_i} AO + \left(\frac{\partial(AO)}{\partial Z_i}\right)^2 + \frac{1}{3}\frac{\partial^2(BO)}{\partial Z_i^2} BO + \frac{1}{3}\left(\frac{\partial(BO)}{\partial Z_i}\right)^2 \right) \right.$$

$$\left. - \left(AO^2 + \frac{BO^2}{3}\right)^{-1}\left(\frac{\partial(AO)}{\partial Z_i} AO + \frac{1}{3}\frac{\partial(BO)}{\partial Z_i} BO\right)^2 \right]$$

$$\frac{\partial^2(CO)}{\partial Z_i \partial Z_j} - \frac{\left(G^2+K^2\right)}{\left(G^2-K^2\right)}\left(AO^2+\frac{BO^2}{3}\right)^{-\frac{1}{2}} \bullet \left[\left(\frac{\partial^2(AO)}{\partial Z_i \partial Z_j}AO + \frac{\partial(AO)}{\partial Z_i}\frac{\partial(AO)}{\partial Z_j} + \frac{1}{3}\frac{\partial^2(BO)}{\partial Z_i^2}BO + \frac{1}{3}\frac{\partial(BO)}{\partial Z_i}\frac{\partial(BO)}{\partial Z_j}\right)\right.$$

$$\left. -\left(AO^2+\frac{BO^2}{3}\right)^{-1}\left(\frac{\partial(AO)}{\partial Z_i}AO + \frac{1}{3}\frac{\partial(BO)}{\partial Z_i}BO\right)\left(\frac{\partial(AO)}{\partial Z_j}AO + \frac{1}{3}\frac{\partial(BO)}{\partial Z_j}BO\right)\right]$$

where $\dfrac{\partial^2\left(AO, CO \text{ or } BO\right)}{\partial Z_i \partial Z_j} \equiv 0$

$$\frac{\partial}{\partial Z_6}\langle AO\rangle = -2Z_6, \frac{\partial}{\partial Z_2}\langle AO\rangle = -2Z_2, \frac{\partial}{\partial Z_1}\langle AO\rangle = 4Z_1,$$

$$\frac{\partial}{\partial Z_6}\langle BO\rangle = -2Z_6, \frac{\partial}{\partial Z_2}\langle BO\rangle = 2Z_2, \frac{\partial}{\partial Z_1}\langle BO\rangle = 0$$

$$\frac{\partial}{\partial Z_6}\langle CO\rangle = 2Z_6, \frac{\partial}{\partial Z_2}\langle CO\rangle = 2Z_2, \frac{\partial}{\partial Z_1}\langle CO\rangle = -2Z_1$$

$$\frac{\partial^2}{\partial Z_6^2}\langle AO\rangle = -2, \frac{\partial^2}{\partial Z_2^2}\langle AO\rangle = -2, \frac{\partial^2}{\partial Z_1^2}\langle AO\rangle = 4$$

$$\frac{\partial^2}{\partial Z_6^2}\langle BO\rangle = -2, \frac{\partial^2}{\partial Z_2^2}\langle BO\rangle = 2, \frac{\partial^2}{\partial Z_1^2}\langle BO\rangle = 0$$

$$\frac{\partial^2}{\partial Z_6^2}\langle CO\rangle = 2, \frac{\partial^2}{\partial Z_2^2}\langle CO\rangle = 2, \frac{\partial^2}{\partial Z_1^2}\langle CO\rangle = -2$$

The following is an Fortran program implementing the above algorithm. The program was tested over a triangular nozzle. It was found that the phase mean data was

the most accurate measure. Deviation of the streamwise velocity was below 5%. The results of root mean value of the turbulent were not accurate, deviation of more than 30% was observed. More effort is, therefor, needed, to improve its accuracy (such as adjustment in calibration procedure). The Renolds stress results were not presentable because of the lack of accurate correlation results. The assumption adopted by Janjua, S. I. and Mclaughlin, D. D. (1982) was found not valid.

```
CCCCCCCCCCCCCCCCCCCCCCCCCCCCCCCCCCCCCCCCCCCCCCCCCCCCCCCCCCCCCCCCCCCCCCC
      Three dimensional Conditioning data sampling program using single straight hot wire   C
CCCCCCCCCCCCCCCCCCCCCCCCCCCCCCCCCCCCCCCCCCCCCCCCCCCCCCCCCCCCCCCCCCCCCCC

      DIMENSION DZ(20),DX(20),DY(20),RRI(9)
C
      DATA DZ(1), DZ(2), DZ(3), DZ(4), DZ(5)/5,5,5,5,5/
      DATA DZ(6), DZ(7), DZ(8), DZ(9), DZ(10)/6,6,7,7,8/
      DATA DZ(11),DZ(12),DZ(13),DZ(14),DZ(15)/9,9,9,9,9/
      DATA DZ(16),DZ(17),DZ(18),DZ(19),DZ(20)/9,9,9,9,9/
C
      DATA DX(1), DX(2), DX(3), DX(4), DX(5)/4,4,4,4,4/
      DATA DX(6), DX(7), DX(8), DX(9), DX(10)/1,1,1,1,2/
      DATA DX(11),DX(12),DX(13),DX(14),DX(15)/2,2,2,2,2/
      DATA DX(16),DX(17),DX(18),DX(19),DX(20)/2,2,3,3,3/
C
      DATA DY(1), DY(2), DY(3), DY(4), DY(5)/4,4,4,4,4/
      DATA DY(6), DY(7), DY(8), DY(9), DY(10)/1,1,1,1,2/
      DATA DY(11),DY(12),DY(13),DY(14),DY(15)/2,2,2,2,2/
      DATA DY(16),DY(17),DY(18),DY(19),DY(20)/2,2,3,3,3/
C
      OPEN(6,FILE='DATA',STATUS='NEW')
C
      IO=0
C
C
150    WRITE(*,300)
300    FORMAT(1X,' STEP? (One step equals 1mm)')
      READ(*,*)STEP
      WRITE(*,310)
310    FORMAT(1X,'FORWARD OR BACKWARD ? (0=F,1=B)')
      READ(*,*)NB
      WRITE(*,320)
      WRITE(*,125)
320    FORMAT(1X,'WHICH STAGE ?')
125    FORMAT(1X,'(TOP,BOTTOM OR MIDDLE,0=TOP,1=BOTTOM,2=MID)')
      READ(*,*) NC
C     NA:NUMBER OF STEPS, NB:FORWARD OF BACKWARD DIRECTION, NC:WHICH STAGE
      CALL SM(STEP,NB,NC,1.0)
      WRITE(*,340)
```

```
340    FORMAT(1X,'SATISFIED ? (0=YES)')
      CALL SM(0,0,0,0)
      CALL SM(0,0,2,0)
      READ(*,*) ND
      IF (ND.NE.0) GOTO 150
C
C     READ THE ORIGINAL IN X DIRECTION
C
      WRITE(*,360)
360    FORMAT(1X,'INPUT THE THE FIRST POSIOTION OF MEASUREMENTS ZO=?')
      READ(*,*)ZO
C
C     data sampling point per time
C
      NS=17
C     DATA SAMPLING AVERAGE NUMBER( TOTAL TIME)
      ND=128
C
C     NTG IS THE TRIGGER MODE
      NTG=0
C     WHICH MEANS EXT TRI AND EXT CLK
C
C     Hot Wire Caliberation Point:
      NN=10
      NCK=200
C
C     Z Step:
      NZ=1
C     THE X AND Y STEP SHOULD BE SINGULAR LIKE 5,7,9, ETC.
C     Y Step:
      NY=1
C     X Step:
      NX=1
C
      DO 1 I=1,1000
1     CALL SM(0.0,0,3,1.0)
      CALL SM(33.0,0,3,1.0)
C
      VM=0.0
      CALL SAMP(NCK,NN,NTG,NS,ND,RRI,VM)
      VM=RRI(1)
      CALL SM((NY-1)*DY(1)/2,1,1,1.0)
      CALL SM((NX-1)*DX(1)/2,1,2,1.0)
      WRITE(*,*)VM
      DO 10 JZ=1,NZ
      DO 20 JX=1,NX
      DO 30 JY=1,NY
      CALL SAMP(NCK,NN,NTG,NS,ND,RRI,VM)
      WRITE(*,*)JX,JY,JZ
      WRITE(*,200)(RRI(I),I=0,5)
      XN=DX(JZ)*(JX-1)
```

```
      YN=DY(JZ)*(JY-1)
      ZN=DZ(JZ)*(JZ-1)+ZO
      WRITE(6,210) XN,YN,ZN
      IF(JY.EQ.NY) GOTO 35
30     CALL SM(DY(JZ),0,2,1.0)
35     CALL SM((NY-1)*DY(JZ),1,2,1.0)
      IF(JX.EQ.NX) GOTO 36
20     CALL SM(DX(JZ),0,1,1.0)
36     CALL SM((NX-1)*DX(JZ),1,1,1.0)
      IF(JZ.EQ.NZ) GOTO 38
      CALL SM(DZ(JZ),1,0,1.0)
38     CALL SM((NX-1)/2*(DX(JZ+1)-DX(JZ)),1,1,1.0)
      CALL SM((NY-1)/2*(DY(JZ+1)-DY(JZ)),1,2,1.0)
10     CONTINUE
200    FORMAT(1X,6(F9.5,1X))
210    FORMAT(1X,3(F9.3,1X))
220    FORMAT(1X,I3,2X,I3,2X,I3,/,2X,6(F8.3,2X))
230    FORMAT(1X,/)
      CALL SM(0,0,0,0)
      CALL SM(0,0,2,0)
      STOP
      END
      SUBROUTINE SAMP(NCK,NN,NTG,NS,ND,RRI,VM)
      COMMON /A2/XR(48),XI(48)
      DIMENSION V(200,3),RZ(200,3),U2(200,512),U(3),U1(3)
      DIMENSION RRI(9)
25     CALL SM(0.0,0,3,0.0)
      CALL ADS(NCK,NS,NTG)
      DO 500 JS=1,3
      DO 40 I1=1,NS
40     V(I1,JS)=0.0
      DO 50 I2=1,ND
      CALL ADS(NCK,NS,NTG)
      DO 60 I1=1,NS
      XR(I1)=XR(I1)+0.035
      CALL LI(NN,XR(I1),P,2,1)
60     U2(I1,I2)=P
      DO 70 I1=1,NS
      V(I1,JS)=V(I1,JS)+U2(I1,I2)
70     CONTINUE
50     CONTINUE
      CALL ADS(NCK,NS,NTG)
      DO 80 I1=1,NS
80     V(I1,JS)=V(I1,JS)/ND
      DO 90 I1=1,NS
90     RZ(I1,JS)=0.0
      DO 100 I2=1,ND
      DO 100 I1=1,NS
      AA=U2(I1,I2)-V(I1,JS)
100    RZ(I1,JS)=RZ(I1,JS)+AA*AA
      DO 110 I1=1,NS
```

```
110    RZ(I1,JS)=RZ(I1,JS)/ND/ND
       IF(JS.EQ.3) GOTO 500
       CALL SM(17.0,0,3,1.0)
500    CONTINUE
       CALL SM(34.0,1,3,1.0)
       DO 510 IS=1,NS
       DO 520 JS=1,3
       U(JS-1)=V(IS,JS)
520    U1(JS-1)=RZ(IS,JS)
       CALL IIIHWM(U,U1,RRI,NN,ERR)
       IF(ERR.EQ.0.0) GOTO 525
       GOTO 25
525    RRI(1)=RRI(1)-0.9*VM
       WRITE(6,200)(RRI(I),I=0,5)
510    CONTINUE
515    CONTINUE
200    FORMAT(1X,6(F10.6,2X))
       RETURN
       END
       SUBROUTINE ADS(NCK,NN,TIMING)
       COMMON /A2/XR(48),XI(48)
       INTEGER*2 STATUS,STARTC,ENDCHA,GAIN,TIMING,SAMPLE,COUNT
       INTEGER*2 XINIT,XTERM,XSB,XST,XSCD,DATPTS,ANALOG(2048)
       INTEGER*2 XDLY,XSTB,XWD,XSC,XGC,XCEV,XREV,XGF,CHANLS
       INTEGER*2 XAV,XAOT,XSA,XAS,XBAD,XCAD,XTAD,XWAD,XSAD
       INTEGER*2 XDV,XDOT,XSD,XDS,XBDD,XCDD,XTDD,XWDD,XSDD
       INTEGER*2 XEFO,XEFI,XODV,XODOT,XIDV,XIDOT,XIXR,XIXW
       INTEGER*2 XSECW,XGDE,XRD,XFDL,XESC,XDSC,PLOTS,PLTPNT
       INTEGER*4 CLOCKD
       EXTERNAL XINIT,XTERM,XSAD,XSDD,XWD,XSC,XCEV,XESC,XDSC
C   end of PCLAB subroutines definition
       STATUS=0
       DATPTS=NN
       CLOCKD=NCK
C      DEFINITION OF 'TIMING' SEE PAGE 6-8
C      EACH CLOCK TICK = .0000125 SEC., MINIMUM CLOCK TICKS = 30
       STARTC=0
       ENDCHA=0
       GAIN=4
       CHANLS=(ENDCHA+1)-STARTC
       SAMPLE=CHANLS*DATPTS
       ANALOG(1)=SAMPLE
       STATUS=XDSC
       STATUS=XRD
       STATUS=XINIT
       STATUS=XSCD(CLOCKD)
       STATUS=XSA(TIMING, STARTC, ENDCHA, GAIN)
       STATUS=XDSC
       STATUS=XBAD(SAMPLE, ANALOG(1))
       STATUS=XTAD(COUNT)
       STATUS=XWAD(ANALOG(NN))
```

```
      DO 10 I=1,NN
10     XR(I)=(FLOAT(ANALOG(I))*5.0/4096.0-2.5)
      RETURN
      END
      SUBROUTINE SM(STEP,NB,NC,FN)
     INTEGER*2 STATUS,STARTC,ENDCHA,GAIN,TIMING,SAMPLE,COUNT
     INTEGER*2 XINIT,XTERM,XSB,XST,XSCD,DATPTS,ANALOG(512)
     INTEGER*2 XDLY,XSTB,XWD,XSC,XGC,XCEV,XREV,XGF,CHANLS
     INTEGER*2 XAV,XAOT,XSA,XAS,XBAD,XCAD,XTAD,XWAD,XSAD
     INTEGER*2 XDV,XDOT,XSD,XDS,XBDD,XCDD,XTDD,XWDD,XSDD
     INTEGER*2 XEFO,XEFI,XODV,XODOT,XIDV,XIDOT,XIXR,XIXW
     INTEGER*2 XSECW,XGDE,XRD,XFDL,XESC,XDSC,PLOTS,PLTPNT
     INTEGER*4 CLOCKD
     EXTERNAL XEFO,XODV
      DIMENSION N(2,4)
      IO=0
      IF (NC.EQ.2.OR.NC.EQ.3) IO=1
      STATUS=XEFO(IO)
C
C: ENABLE THE FIRST FOUR LINE
      N(1,1)=128
      N(1,2)=130
      N(1,3)=132
      N(1,4)=134
C
C: ENABLE THE SECOND FOUR LINE
      N(2,1)=8
      N(2,2)=40
      N(2,3)=72
      N(2,4)=104
      I1=INT(STEP*126)
      IF(NC.NE.1) GOTO 1
      I1=INT(STEP*40)
1      IF(NC.NE.3) GOTO 2
      I1=INT(STEP)
2      IC=1
      II=2
      IF (NC.NE.1.AND.NC.NE.3) GOTO 111
      IC=2
      II=3
111     J1=N(IC,1)
      J2=N(IC,2)
      J3=N(IC,3)
      J4=N(IC,4)
      IF(NB.NE.0) GOTO 120
C      CW DIRECTION
      DO 30 J=1,I1
      DO 10 I=1,II
10     STATUS=XODV(IO,255,J1)
     DO 20 I=1,II
20     STATUS=XODV(IO,255,J2)
```

```
 30    CONTINUE
       goto 140
 120   CONTINUE
C
C      CCW DIRECTION
C
       DO 60 J=1,I1
       DO 40 I=1,II
 40    STATUS=XODV(IO,255,J3)
       DO 50 I=1,II
 50    STATUS=XODV(IO,255,J4)
 60    CONTINUE
 140   CONTINUE
       IF (FN.NE.0.0) GOTO 150
       STATUS=XODV(IO,255,136)
 150   IF(IO.EQ.0) THEN
       STATUS=XODV(1,255,136)
       ELSE
       STATUS=XODV(0,255,136)
       END IF
       RETURN
       END
       SUBROUTINE IIIHWM(V,RZ,RRI,NN,ERR)
       DIMENSION RRI(9),U(6)
       DIMENSION E(3),V(3),F(3)
       DIMENSION Y(3,3),DU(3,3),DV(3,3),DW(3,3),T(3,3),X(3,3)
       DIMENSION YU(3,3),YV(3,3),KR(3),RZ(3)
       REAL*4 XN,RN,R(3),GO,KO,H(3,3)
C
C      THE REQUIRED INPUT IS THE  EFFECTIVE COOLING VELOCITY V(J) WHICH
C      IS CACULATED BY SUBOUTINE LI(NN,E(I),V(I),JE). SINCE V(0-2) CAN
C      NOT BE SAMPLED SIMULTANEOUSLY, THE AVERAGE VALUE V(J) AND ITS ROOT
C      MEAN SQUARE VALUE RZ(J) ARE REQURED FOR INPUT.
C
C      NOTE RZ(I) IS THE SQUARE OF THE ROOT MEAN SQUARE OF THE FLUCTUATION
C
C      ASSUME THE FIRST PITCH AND YAW VALUE
      GO=1.05
      KO=0.12
      ERR=0.0
C
C      ENTER TRY & ERROR ITERATION LOOP TO GET THE CORRECT GO AND KO
C
      OPEN(9,FILE='DATA.DAT',STATUS='NEW')
      WRITE(9,*)(V(I),I=0,2)
      WRITE(9,*)(RZ(K),I=0,2)
      CLOSE (9)
      AO=-V(0)*V(0)+2.0*V(1)*V(1)-V(2)*V(2)
      BO=-V(0)*V(0)+V(2)*V(2)
      CO=V(0)*V(0)-V(1)*V(1)+V(2)*V(2)
      XN=AO*AO+BO*BO/3.0
```

```
      RN=SQRT(XN)
      XN=GO*GO-KO*KO
      U(0)=((AO+RN)/XN)
      U(0)=SQRT(U(0))
      XN=(GO*GO+KO*KO)/(GO*GO-KO*KO)
      U(1)=CO-RN*XN
      IF(U(1).GE.0.0) GOTO 10
      WRITE(*,15)
15     FORMAT(1X,'ERROR MEASUREING, REPEAT')
      ERR=1.0
      GOTO 5000
10     U(1)=SQRT(XN)
      XN=GO*GO-KO*KO
      U(2)=((-AO+RN)/XN)
      U(2)=SQRT(U(2))
      DO 40 K=0,2
40     R(K)=U(K)
C
C      U(0-2) IS THE FIRST TRYING VELOCITY
      IK=0
C
1300   CONTINUE
C
C: USING THE FIRST CACULATED VELOCITY TO FIND THE CURVE FITTING VOLTAGE
      DO 50 K=0,2
50     CALL LI(NN,U(K),F(K),K+1,2)
C  WHERE "2" MEANS VELOCITY TO VOLTAGE TRANSFORMATION, SO BY FINDING
C  THE FIRST TRYING VELOCITY U,V,W WE CAN FIND THE CORRESPONDING VOLTAGE
C  FROM FIG. 5.
      IK=IK+1
C
C: FIND THE NEW "GO" AND "KO" USING EQN. (2) AND NOTE THAT WHEN V AND W =0
C  EQN.(2) BECOMES Z=GO*U(0), SO GO=Z/U(0) WITH E(0) AS THE REFERENCE. AND
C  IN EQN. GO=Z(1)/Z(0), Z(1) REPRESENTS V AND Z(0) REPRESENTS U VELOCITY
C  COMPONENTS.
C
      DO 60 K=0,1
60     CALL LI(NN,F(0),E(K),K+1,1)
      IF(E(0).NE.0.0) GOTO 65
      GO=1.0E+10
      IF(E(1).EQ.0.0) GO=1.0
      GOTO 75
65     GO=E(1)/E(0)
75     DO 70 K=1,2
70     CALL LI(NN,F(2),E(K),K+1,1)
      KO=E(1)/E(2)
      XN=AO*AO+BO*BO/3.0
      RN=SQRT(XN)
      U(0)=((AO+RN)/(GO*GO-KO*KO))
      U(0)=SQRT(U(0))
      U(1)=CO-RN*(GO*GO+KO*KO)/(GO*GO-KO*KO)
```

```
      IF(U(1).GE.0.0) GOTO 85
      ERR=1.0
      WRITE(*,15)
      GOTO 5000
 85     U(1)=SQRT(U(1))
      U(2)=(-AO+RN)/(GO*GO-KO*KO)
      U(2)=SQRT(U(2))
      XN=GO*GO-KO*KO
      C1=1.0/SQRT(XN)
      C2=(GO*GO+KO*KO)*C1*C1
      XN=AO*AO+BO*BO/3.0
      X2=SQRT(XN)
      H(0,0)=-2.0*V(0)
      H(0,1)=4.0*V(1)
      H(0,2)=-2.0*V(2)
      H(0,3)=-2.0
      H(0,4)=4.0
      H(0,5)=-2.0
      H(1,0)=-2.0*V(0)
      H(1,1)=0.0
      H(1,2)=2.0*V(2)
      H(1,3)=-2.0
      H(1,4)=0.0
      H(1,5)=2.0
      H(2,0)=2.0*V(0)
      H(2,1)=-2.0*V(1)
      H(2,2)=2.0*V(2)
      H(2,3)=2.0
      H(2,4)=-2.0
      H(2,5)=2.0
      DO 100 K=0,2
      X(0,K)=(AO*H(0,K)+BO*H(1,K)/3.0)/X2
      RN=H(0,K)*H(0,K)+AO*H(0,K+3)
      XN=H(1,K)*H(1,K)/3.0
100     X(1,K)=(XN+RN+BO*H(1,K+3)/3.0-X(0,K)*X(0,K))/X2
      DO 110 K=1,2
      XN=H(0,0)*X(0,K)+H(1,0)*H(1,K)/3.0
110     X(2,K-1)=(XN-X(0,0)*X(0,K))/X2
      XN=H(0,2)*H(0,1)+H(1,1)*H(1,2)/3.0
      X(2,2)=(XN-X(0,1)*X(0,2))/X2
      DO 120 K=0,2
      IF(ABS(U(0)).GT.0.01) GOTO 121
      DU(0,K)=0.0
      DU(1,K)=0.0
      GOTO 122
121     DU(0,K)=C1*C1*(H(0,K)+X(0,K))/2.0/U(0)
      XN=C1*C1*(H(0,K+3)+X(1,K))
      DU(1,K)=(XN-2.0*DU(0,K)*DU(0,K))/2.0/U(0)
122     IF(ABS(U(1)).GT.0.01) GOTO 123
      DV(0,K)=0.0
      DV(1,K)=0.0
```

```
      GOTO 124
  123   DV(0,K)=(H(2,K)-C2*X(0,K))/2.0/U(1)
      XN=H(2,K+3)-C2*X(1,K)
      DV(1,K)=(XN-2.0*DV(0,K)*DV(0,K))/2.0/U(1)
  124   IF(ABS(U(2)).GT.0.01) GOTO 125
      DW(0,K)=0.0
      DW(1,K)=0.0
      GOTO 120
  125   DW(0,K)=C1*C1*(-H(0,K)+X(0,K))/2.0/U(2)
      XN=C1*C1*(-H(0,K+3)+X(1,K))
      DW(1,K)=(XN-2.0*DW(0,K)*DW(0,K))/2.0/U(2)
  120   CONTINUE
      DO 130 K=0,1
      IF(ABS(U(0)).GT.0.01) GOTO 131
      DU(2,K)=0.0
      GOTO 132
  131   DU(2,K)=(C1*C1*X(2,K)-2.0*DU(0,0)*DU(0,K+1))/2.0/U(0)
  132   IF(ABS(U(1)).GT.0.01) GOTO 133
      DV(2,K)=0.0
      GOTO 134
  133   DV(2,K)=(-C2*X(2,K)-2.0*DV(0,0)*DV(0,K+1))/2.0/U(1)
  134   IF(ABS(U(2)).GT.0.01) GOTO 135
      DU(2,K)=0.0
      GOTO 130
  135   DW(2,K)=(C1*C1*X(2,K)-2.0*DW(0,0)*DW(0,K+1))/2.0/U(2)
  130   CONTINUE
      XN=RZ(0)*RZ(1)
      RN=SQRT(XN)
      KR(0)=0.9*RN
      XN=RZ(0)*RZ(2)
      RN=SQRT(XN)
      KR(1)=0.65*RN
      XN=RZ(1)*RZ(2)
      RN=SQRT(XN)
      KR(2)=0.9*RN
      IF(ABS(U(0)).GT.0.01) GOTO 141
      DU(2,2)=0.0
      GOTO 142
  141   DU(2,2)=(C1*C1*X(2,2)-2.0*DU(0,1)*DU(0,2))/2.0/U(0)
  142   IF(ABS(U(1)).GT.0.01) GOTO 143
      DV(2,2)=0.0
      GOTO 144
  143   DV(2,2)=(-C2*X(2,2)-2.0*DV(0,1)*DV(0,2))/2.0/U(1)
  144   IF(ABS(U(2)).GT.0.01) GOTO 145
      DW(2,2)=0.0
      GOTO 146
  145   DW(2,2)=(C1*C1*X(2,2)-2.0*DW(0,1)*DW(0,2))/2.0/U(2)
  146   XN=(DU(1,0)*RZ(0)+DU(1,1)*RZ(1)+DU(1,2)*RZ(2))/2.0
      U(3)=XN+DU(2,0)*KR(0)+DU(2,1)*KR(1)+DU(2,2)*KR(2)
      XN=(DV(1,0)*RZ(0)+DV(1,1)*RZ(1)+DV(1,2)*RZ(2))/2.0
      U(4)=XN+DV(2,0)*KR(0)+DV(2,1)*KR(1)+DV(2,2)*KR(2)
```

```
      XN=(DW(1,0)*RZ(0)+DW(1,1)*RZ(1)+DW(1,2)*RZ(2))/2.0
      U(5)=XN+DW(2,0)*KR(0)+DW(2,1)*KR(1)+DW(2,2)*KR(2)
      DO 89 K=0,2
 89     U(K)=U(K)+U(K+3)
      RN=0.0
      DO 80 K=0,2
      IF(R(K).EQ.0.0) GOTO 80
      XN=(U(K)-R(K))/R(K)
      IF(ABS(XN).LT.RN) GOTO 80
      RN=XN
 80     CONTINUE
      IF(ABS(RN).LT.0.001) GOTO 1200
      DO 90 K=0,2
 90     R(K)=U(K)
      IF(IK.LT.500) GOTO 1400
      WRITE(*,95)
 95     FORMAT(1X,'TOO MUCH ITERATION')
      ERR=1.0
      GOTO 5000
1400    GOTO 1300
1200    CONTINUE

      DO 140 K=0,2
      DO 140 J=0,2
140     Y(K,J)=DU(K,J)
      CALL TUI(Y,KR,RZ,TU)
      T(0,0)=TU
      DO 150 K=0,2
      DO 150 J=0,2
150     Y(K,J)=DV(K,J)
      CALL TUI(Y,KR,RZ,TU)
      T(0,1)=TU
      DO 160 K=0,2
      DO 160 J=0,2
160     Y(K,J)=DW(K,J)
      CALL TUI(Y,KR,RZ,TU)
      T(0,2)=TU
      DO 170 K=0,2
      DO 170 J=0,2
      YU(K,J)=DU(K,J)
170     YV(K,J)=DV(K,J)
      CALL TTI(YU,YV,KR,RZ,TT)
      T(1,0)=TT
      DO 180 K=0,2
      DO 180 J=0,2
      YU(K,J)=DU(K,J)
180     YV(K,J)=DW(K,J)
      CALL TTI(YU,YV,KR,RZ,TT)
      T(1,1)=TT
      DO 190 K=0,2
      DO 190 J=0,2
```

```
      YU(K,J)=DV(K,J)
190    YV(K,J)=DW(K,J)
      CALL TTI(YU,YV,KR,RZ,TT)
      T(1,2)=TT
C
C      THE THREE CONPONENT OF VELOCITY IS U(0-2), NORMAL STRESS ARE
C      T(0,0-2) AND SHEAR STRESS ARE T(1,0-2)
C
      DO 200 I5=0,2
      RRI(I5)=U(I5)
      RRI(I5+3)=T(0,I5)
200    RRI(I5+6)=T(1,I5)
5000   CONTINUE
      RETURN
      END
      SUBROUTINE TUI(Y,KR,RZ,TU)
      DIMENSION Y(3,3),KR(3),RZ(3)
      TU=Y(0,0)*Y(0,0)*RZ(0)+Y(0,1)*Y(0,1)*RZ(1)
      TU=TU+Y(0,2)*Y(0,2)*RZ(2)
      TU=TU+2.0*(Y(0,0)*Y(0,1)*KR(0)+Y(0,0)*Y(0,2)*KR(1)
     1   +Y(0,1)*Y(0,2)*KR(2))
      TUO=(Y(1,0)*RZ(0)+Y(1,1)*RZ(1)+Y(1,2)*RZ(2))/2.0
      KX=TUO+Y(2,0)*KR(0)+Y(2,1)*KR(1)+Y(2,2)*KR(2)
      TU=TU-KX*KX
      RETURN
      END
      SUBROUTINE TTI(YU,YV,KR,RZ,TT)
      DIMENSION YU(3,3),YV(3,3),KR(3),RZ(3)
      T1=0.0
      DO 10 K=0,2
      TO=YU(0,K)*YV(0,K)*RZ(K)+T1
10     T1=TO
      Y1=0.0
      DO 20 K=0,1
      YO=Y1+KR(K)*(YU(0,0)*YV(0,K+1)+YU(0,K+1)*YV(0,0))
20     Y1=YO
      YO=YO+KR(2)*(YU(0,1)*YV(0,2)+YU(0,2)*YV(0,1))
      Y2=(YU(1,0)*RZ(0)+YU(1,1)*RZ(1)+YU(1,2)*RZ(2))/2.0
      Y2=Y2+(YU(2,0)*KR(0)+YU(2,1)*KR(1)+YU(2,2)*KR(2))
      Y3=(YV(1,0)*RZ(0)+YV(1,1)*RZ(1)+YV(1,2)*RZ(2))/2.0
      Y3=Y3+(YV(2,0)*KR(0)+YV(2,1)*KR(1)+YV(2,2)*KR(2))
      TT=TO+YO-Y2*Y3
      RETURN
      END
      SUBROUTINE LI(NN,EI,P,JE,IC)
      DIMENSION V(10,3),E(10,3),A(10,3)
      DIMENSION PL(10)
      DATA V /0.0,3.77,5.85,7.92,9.98,11.96,13.99,15.95,18.00
     1      ,20.01
     3      ,0.0,4.0,6.00,8.13,9.93,12.27,13.87,15.9,18.13
     4      ,20.14
```

```
     6       ,0.0,3.77,5.85,7.92,9.98,11.96,13.99,15.95,18.00
     7       ,20.01/
      DATA E /0.782,1.059,1.104,1.150,1.188,1.220,1.247,1.170,1.291
     1       ,1.313
     3       ,0.782,1.054,1.099,1.139,1.171,1.206,1.227,1.250,1.274
     4       ,1.295
     6       ,0.782,0.911,0.931,0.950,0.976,0.978,0.980,0.982,0.988
     7       ,0.995/
        P=0.0
        IF(IC.EQ.2) GOTO 100
        DO 2 I=1,NN
2        A(I,JE)=E(I,JE)
        GOTO 200
100      DO 3 I=1,NN
3        A(I,JE)=V(I,JE)
200      DO 5 II=1,NN
        IF(EI-A(II,JE))15,15,5
5        CONTINUE
15       IF(II+1.GT.NN) GOTO 25
        IF(II.GT.2) GOTO 16
        IF(II.NE.1) GOTO 17
        I1=II
        I2=II
        GOTO 35
17       I1=II-1
        I2=II
        GOTO 35
16       I1=II-1
        I2=II+1
        GOTO 35
25       I1=II-2
        I2=II
35       DO 10 I=I1,I2
        PL(I)=1.0
        DO 20 J=I1,I2
        IF(I.EQ.J) GOTO 20
        PL(I)=PL(I)*(EI-A(J,JE))/(A(I,JE)-A(J,JE))
20       CONTINUE
10       CONTINUE
        P=0.0
        IF(IC.EQ.1) GOTO 300
        DO 30 I=I1,I2
30       P=P+E(I,JE)*PL(I)
        GOTO 400
300      DO 40 I=I1,I2
40       P=P+V(I,JE)*PL(I)
400      CONTINUE
        RETURN

        END
```

Vita

The author was born to ShiChai Ding and XiuLang Lue on April 15, 1956 in Nanjing China. He spent his childhood and received his pre-college education there. In 1977, the author became a student in the University of Astronautics and Aeronautics of Nanjing, in Nanjing, China. In 1980, He obtained a Bachelor of Science in Mechanical Engineering there. In the same year, he was accepted for graduate study in the same University. In the two years that followed, he developed experimental methods for measuring and evaluating the dynamic characteristics of a transonic diffuser. He obtained a Master of Science in Engineering there in 1982. From then to 1990, he was a Lecturer in the Institute of Technology of Nanjing. In the seven years afterwards, he taught undergraduate courses and completed many projects in Fluid Mechanics and Laboratory automation. The projects he completed include: the implementation of the hardware and software of a conditional data sampling system; a computation code for computing the air organization in a room environment; the computation of a hydraulic water supply pipe network system. In 1990, he began his Ph. D. study in the Mechanical Engineering Department of Virginia Polytechnic Institute and State University and carried out an experimental study on methodologies for active control of free shear flows. After his Ph. D. Study, the author will become an engineer in Premier Solutions Ltd. in Pennsylvania, Philadelphia.